

**Studies on the nephroprotective potential of the  
nanoformulations of curcumin, catechin,  
extracts of *Pueraria tuberosa* and *Pterocarpus  
santalinus***

Thesis Submitted

By

**GYAMCHO TSHERING BHUTIA**

**Doctor of Philosophy (Pharmacy)**

**Department of Pharmaceutical Technology  
Faculty Council of Engineering and Technology  
Jadavpur University  
Kolkata, India**

**2024**

**JADAVPUR UNIVERSITY  
KOLKATA-700 032, INDIA**

**1. Title of the thesis:**

Studies on the nephroprotective potential of the nanoformulations of curcumin, catechin, extracts of *Pueraria tuberosa* and *Pterocarpus santalinus*

**2. Name, Designation & Institution of the Supervisor:**

**a) Supervisor/guide:**

Dr. Tanmoy Bera

Professor,

Department of Pharmaceutical Technology,

Jadavpur University,

Kolkata 700 032, India.

**b) Co-supervisor/co-guide:**

Dr. Manas Bhowmik

Associate Professor,

Department of Pharmaceutical Technology,

Jadavpur University,

Kolkata 700 032, India.

**3. List of Publications:**

(i) **Gyamcho Tshering Bhutia**, Asit Kumar De, Tanmoy Bera, Validation, Stability Studies, and Simultaneous Estimation of Co-Encapsulated Curcumin, Epigallocatechin Gallate Nanoformulation by RP-HPLC Method, Int. J. Appl. Pharm. 14 (2022) 186-195. <https://doi.org/10.22159/ijap.2022v14i6.45818>

(ii) **Gyamcho Tshering Bhutia**, Asit Kumar De, Manas Bhowmik, Tanmoy Bera, Shellac and Locust Bean Gum Coacervated Curcumin, Epigallocatechin Gallate Nanoparticle Ameliorates Diabetic Nephropathy in a Streptozotocin-Induced Mouse Model, Int. J. Biol. Macromol. 271 (2024) 132369. <https://doi.org/10.1016/j.ijbiomac.2024.132369>

- iii) **Gyamcho Tshering Bhutia**, Asit Kumar De, Manas Bhowmik, Tanmoy Bera, Evaluation of the antidiabetic and antinephritic effects of *Pueraria tuberosa* and *Pterocarpus santalinus* extracts co-encapsulated in nanostructured lipid carriers in streptozotocin-induced mouse model, *Phytomedicine Plus* 5 (2025) 100742. <https://doi.org/10.1016/j.phyplu.2025.100742>

#### 4. List of Patents: Nil

#### 5. List of Presentation in National /International:

(i) **Gyamcho Tshering Bhutia**, Tanmoy Bera, entitled “Evaluation of the nephroprotective efficacy of nanoformulation of curcumin and catechin in diabetic nephropathy” at 6<sup>th</sup> International Conference on “Current Issues in Agricultural, Biological & Applied Sciences for Sustainable Development (CIABASSD-2022)” held on 11<sup>th</sup>-13<sup>th</sup> June 2022, at Kalimpong Science Centre, Deolo, Kalimpong, West Bengal.

(ii) **Gyamcho Tshering Bhutia**, Asit Kumar De, Tanmoy Bera, entitled “A validated stability studies indicating RP-HPLC method development for simultaneous determination of EGCG and curcumin in nanoformulation” at International Conference on “Bioprocess for Sustainable Environment and Energy ICBSEE-INDIA-2022” held on 20<sup>th</sup>-24<sup>th</sup> June, at NIT Rourkela, Odisha.

(iii) **Gyamcho Tshering Bhutia**, Tanmoy Bera, entitled “Alleviation of diabetic nephropathy by the co-encapsulated nanoformulation of *Pueraria tuberosa* and *Pterocarpus santalinus* extracts in diabetic mice” at international seminar on “Emerging fields of research in biotechnology and biomedicine” held on 16th November 2022, at Jadavpur University, Kolkata, West Bengal.

#### 5. Book Chapters:

i) **Gyamcho Tshering Bhutia**, Asit Kumar De, Tanmoy Bera. Validation, Stability Studies, and Simultaneous Estimation of Co-Encapsulated Curcumin, Epigallocatechin Gallate Nanoformulation by RP-HPLC Method. *Innovare Academic Sciences Pvt Ltd., Recent Advances in Pharmaceutical Sciences, Vol-17, Chapter 3, Pages 33-66.*

## STATEMENT OF ORIGINALITY

I, **Gyamcho Tshering Bhutia** registered on **4<sup>th</sup> December, 2020**, do hereby declare that this thesis entitled “**Studies on the nephroprotective potential of the nanoformulations of curcumin, catechin, extracts of *Pueraria tuberosa* and *Pterocarpus santalinus***” contains literature survey and original research work done by the undersigned candidate as part of Doctoral studies. All information in this thesis have been obtained and presented in accordance with existing academic rules and ethical conduct. I declare that, as required by these rules and conduct, I have fully cited and referred all materials and results that are not original to this work. I also declare that I have checked this thesis as per the “Policy on Anti Plagiarism, Jadavpur University, 2019”, and the level of similarity as checked by iThenticate software is **5%**.

Signature of Candidate:

*Gyamcho Tshering Bhutia*

Date: 05/11/24

Certified by Supervisor(s):

(Signature with date, seal)

1. *[Signature]* 05/11/24

**Janmoy Bera, M. Pharm., Ph.D.**  
*Professor*


Division of Medicinal Biochemistry  
Department of Pharmaceutical Tech.  
Jadavpur University, Kolkata - 700 032

2. *[Signature]*  
05/11/2024

**Dr. Manas Bhowmik**  
Associate Professor  
Dept. of Pharmaceutical Technology  
Jadavpur University, Kol-700 032  
West Bengal, India

## CERTIFICATE FROM THE SUPERVISORS

This is to certify that the thesis entitled “**Studies on the nephroprotective potential of the nanoformulations of curcumin, catechin, extracts of *Pueraria tuberosa* and *Pterocarpus santalinus***” submitted by Shri **Gyamcho Tshering Bhutia**, who got his name registered on **4<sup>th</sup> December, 2020**, for the award of Ph. D. (Pharmacy) degree of Jadavpur University is absolutely based upon his own work under the supervision of **Prof. Tanmoy Bera, Department of Pharmaceutical Technology, Jadavpur University, Kolkata, 700032, India** and co-supervision of **Assoc. Prof. Manas Bhowmik, Department of Pharmaceutical Technology, Jadavpur University, Kolkata, 700032, India** and that neither his thesis nor any part of the thesis has been submitted for any degree/diploma or any other academic award anywhere before.

1.  11/24

Signature of the Supervisor

and date with Office Seal

**Tanmoy Bera, M. Pharm., Ph.D.**  
*Professor*

Division of Medicinal Biochemistry  
Department of Pharmaceutical Tech.  
Jadavpur University, Kolkata - 700 032

2.  05/11/2024

Signature of the Co-supervisor

and date with Office Seal

**Dr. Manas Bhowmik**  
Associate Professor  
Dept. of Pharmaceutical Technology  
Jadavpur University, Kol-700 032  
West Bengal, India

*Dedicated to  
my amma and  
my appa*

## Acknowledgement

*As I conclude this chapter of my PhD journey, I am deeply grateful for the invaluable experiences and support I have received along the way. This research has been a transformative process, filled with both challenges and triumphs that have shaped me both personally and professionally.*

*I would like to express my deepest gratitude to my thesis supervisor, **Prof. (Dr.) Tanmoy Bera**, Department of Pharmaceutical Technology, Jadavpur University, for allowing me the opportunity to work in his laboratory. His unwavering support, insightful ideas, and constant encouragement propelled me forward.*

*I am also indebted to my co-supervisor, **Assoc. Prof. (Dr.) Manas Bhowmik**, for his invaluable support and contributions. His expertise and willingness to share his knowledge have been invaluable to my research endeavours.*

*With immense pleasure, I express my gratitude and respect to the Registrar and Vice Chancellor of Jadavpur University, Kolkata.*

*I would like to acknowledge the financial support provided by the National Doctoral Fellowship (NDF) from the AICTE, New Delhi, which has enabled me to pursue this research.*

*My sincere thanks go to Mrs. Champa Bag from the Indian Association for the Cultivation of Science (IACS), Ms. Urmi Chakrabarty, Mr. Amit Kumar Chanda, Mr. Joy Bandopadhyay from the S. N. Bose National Centre for Basic Sciences, and Mr. Manna from Jadavpur University, for their technical assistance and support with instrumentation and analysis.*

*I am also deeply indebted to my senior, Dr. Asit Kumar De, and my juniors in the laboratory—Jigme Sangay Tamang, Rinchen Palzong Bhutia, Mahesh Kumar, and Sagar Roy—for their constant support and assistance throughout this journey.*

*I extend my deepest gratitude to my special friend, Zeno Lepcha, for always being there, offering constant support, motivation, and encouragement during the most challenging times.*

*Lastly, I dedicate this work to my parents, especially my beloved mother, whose absence is deeply felt at this moment. Her love and belief in me continue to guide and inspire me. I am also profoundly grateful to the **Almighty** for granting me the wisdom, strength, and opportunities that made this PhD journey possible.*

Signature of Candidate:

*Gyamcho Tshering Bhutia.*

Date: 05/11/24

যাদবপুর বিশ্ববিদ্যালয়  
কলকাতা-৭০০০৩২, ভারত



\*JADAVPUR UNIVERSITY  
KOLKATA-700 032, INDIA

FACULTY OF ENGINEERING & TECHNOLOGY  
DEPARTMENT OF PHARMACEUTICAL TECHNOLOGY

## Certificate

This is to certify that the project proposal no. **JU/IAEC-22/02** entitled “**Studies on the nephroprotective potential of nanoformulations of curcumin, catechin, the extracts of Pueraria tubarosa, and Pterocarpus santalinus**”, submitted by **Dr. Tanmoy Bera** has been approved/recommended by the IAEC of Department of Pharmaceutical Technology, Jadavpur University, in its meeting held on 01.06.2022 and <sup>Swiss albino</sup> 25).....mice.... (Number and Species of animals) have been sanctioned under this proposal for a duration of next .....12..... months.

Authorized by	Name	Signature	Date
Chairman	Prof. Sanmoy Karmakar		01/6/22
Member Secretary	Prof. Pallab Kanti Halder		01/6/22
Main nominee of CPCSEA	Dr. Sankar Maiti		01-06-2022

\* Established on and from 24<sup>th</sup> December, 1955 vide Notification No.10986-Edn/IU-42/55 dated 6<sup>th</sup> December, 1955 under Jadavpur University Act, 1955 (West Bengal Act XXIII of 1955) followed by Jadavpur University Act, 1981 (West Bengal Act XXIV of 1981)

Website :www.jadavpur.edu  
Telephone :+91-33-2457-2274  
E-mail :hodpharmacy@jadavpuruniversity.in

## List of Abbreviations

<b>Abbreviation</b>	<b>Full form</b>	<b>Abbreviation</b>	<b>Full form</b>
<b>ACE</b>	Angiotensin converting enzyme	<b>ADA</b>	American Diabetes Association
<b>AFM</b>	Atomic force microscopy	<b>AGES</b>	Advanced glycation end products
<b>Alb</b>	albumin	<b>ANG-II</b>	Angiotensin II
<b>ANOVA</b>	Analysis of variance	<b>AR</b>	aldose reductase
<b>ARB</b>	Angiotensin receptor blockers	<b>BBB</b>	Blood brain barrier
<b>BSA</b>	Bovine Serum Albumin	<b>BUN</b>	Blood urea nitrogen
<b>CESL-NP</b>	Curcumin and epigallocatechin gallate-loaded shellac and locust bean gum nanoparticle	<b>CSL-NP</b>	Curcumin-loaded shellac and locust bean gum nanoparticle
<b>CTAB</b>	Cetyltrimethyl ammonium bromide	<b>CTASB</b>	Cetyltrimethyl ammonium silver bromide
<b>CTGF</b>	Connective tissue growth factor	<b>CUR</b>	Curcumin
<b>CVD</b>	Cardiovascular disease	<b>Cxb</b>	Celecoxib
<b>DAD</b>	Diode array detector	<b>DAG</b>	Diacylglycerol
<b>DAM</b>	Diazomethane	<b>DEGEE</b>	Diethylene glycol monoethyl ether
<b>DL</b>	Drug loading	<b>DLS</b>	Dynamic light scattering
<b>DM</b>	Diabetes mellitus	<b>DMSO</b>	Dimethoxy sulfoxide
<b>DN</b>	Diabetic nephropathy	<b>DPP-4</b>	Dipeptidyl peptidase-4
<b>DSC</b>	Differential scanning calorimetry	<b>DTA</b>	Data Transfer Assistance
<b>EC</b>	Epicatechin	<b>ECG</b>	Epicatechin-3-gallate
<b>ECM</b>	Extracellular matrix	<b>EE</b>	Entrapment efficiency
<b>EGC</b>	Epigallocatechin	<b>EGCG</b>	epigallocatechin-3-gallate
<b>EGCG</b>	epigallocatechin-3-gallate	<b>ESL-NP</b>	Epigallocatechin gallate-loaded shellac and locust bean gum nanoparticle
<b>ESRD</b>	End-stage renal disease	<b>ET</b>	Endothelin
<b>FBGL</b>	fasting blood glucose level	<b>FDA</b>	Food and drug administration
<b>FESEM</b>	Field emission scanning electron microscopy	<b>FTIR</b>	fourier transform infrared spectroscopy

<b>GDM</b>	Gestational diabetes mellitus	<b>GFR</b>	Glomerular filtration rate
<b>GH</b>	Growth hormone	<b>GLP-1</b>	Glucagon-like peptide-1
<b>GRAS</b>	Generally recognized as safe	<b>H&amp;E</b>	Hematoxylin and eosin
<b>H<sub>2</sub>O<sub>2</sub></b>	Hydrogen peroxide	<b>HLB</b>	Hydrophilic lipophilic balance
<b>HO<sup>•</sup></b>	Hydroxyl radical	<b>HOCl-</b>	Hypochlorous acid
<b>HPH</b>	High pressure homogenization	<b>HRTEM</b>	High-resolution transmission electron microscopy
<b>HSH</b>	High sheer homogenization	<b>IAEC</b>	Institutional Animal Ethics Committee
<b>ICH</b>	International Council for Harmonisation	<b>IDF</b>	International Diabetes Federation
<b>IGFS</b>	Insulin-like growth factors	<b>IL-1</b>	Interleukin-1
<b>KHI</b>	Kidney hypertrophy index	<b>LBG</b>	Locust bean gum
<b>LDL</b>	Low-density lipoprotein	<b>LOD</b>	Limit of detection
<b>LOQ</b>	Limit of quantification	<b>MAPKs</b>	Mitogen-activated protein kinases
<b>MCP-1</b>	Monocyte chemoattractant protein-1	<b>MIC</b>	Minimum inhibitory concentration
<b>NaDC</b>	Sodium deoxycholate	<b>NADPH</b>	Nicotinamide adenine dinucleotide phosphate
<b>NF- κB</b>	Nuclear factor kappa B	<b>NLCs</b>	Nanostructured lipid carriers
<b>NO</b>	Nitric oxide	<b>NSAIDs</b>	Non-steroidal anti-inflammatory drugs
<b>OHAs</b>	Oral hypoglycaemic agents	<b>ONOO<sup>•</sup></b>	Peroxynitrite
<b>OS</b>	Oxidative stress	<b>PCL</b>	Polycaprolactone
<b>PDGF</b>	Platelet-derived growth factor	<b>PDI</b>	Polydispersity index
<b>PEBBLES</b>	Probes encapsulated by biologically localized embedding	<b>PEG</b>	Polyethyleneglycol
<b>PEI</b>	Polyethylenimine	<b>PGA</b>	Polyglycolides
<b>PKC</b>	Protein kinase C	<b>PLA</b>	Poly lactides
<b>PLGA</b>	Poly lactide-co-glycolides	<b>PNLC</b>	Polycation nanostructured lipid carrier

<b>PNPs</b>	Polymeric nanoparticles	<b>PPAR</b>	Peroxisome proliferator activated receptor
<b>PSE</b>	<i>Pterocarpus santalinus</i> extract	<b>PSE-NLC</b>	<i>Pterocarpus santalinus</i> extract- loaded nanostructured lipid carrier
<b>PTE</b>	<i>Pueraria tuberosa</i> extract	<b>PTE+PSE</b>	<i>Pueraria tuberosa</i> and
		<b>-NLC</b>	<i>Pterocarpus santalinus</i> extracts- loaded nanostructured lipid carrier
<b>PTE-NLC</b>	<i>Pueraria tuberosa</i> extract-loaded nanostructured lipid carrier	<b>RAAS</b>	Renin-angiotensin-aldosterone system
<b>ROS</b>	Reactive oxygen species	<b>RSD</b>	Relative standard deviation
<b>SCF</b>	Supercritical fluid technology	<b>Scr</b>	Serum creatinine
<b>SGCs</b>	Satellite glial cells	<b>SGF</b>	Simulated gastric fluid
<b>SIF</b>	Simulated intestinal fluid	<b>SLNs</b>	Solid lipid nanoparticles
<b>SMEDDS</b>	Self-microemulsifying drug delivery systems	<b>SNEDDS</b>	Self-nanoemulsifying drug delivery system
<b>STZ</b>	Streptozotocin	<b>SUs</b>	Sulphonylureas
<b>T1DM</b>	Type 1 diabetes mellitus	<b>T2DM</b>	Type 2 diabetes mellitus
<b>TGF-<math>\beta</math></b>	Transforming growth factor $\beta$	<b>TQ</b>	Thymoquinone
<b>TZD</b>	Thiazolidinediones	<b>VEGF</b>	Vascular endothelial growth factor
<b>WHO</b>	World Health Organization	<b>XRD</b>	X-ray diffraction

# Table of Contents

<b>CHAPTER I</b>	<b>1</b>
<b>1. INTRODUCTION</b>	<b>2</b>
1.1. Diabetes mellitus	2
1.2. Classification of diabetes mellitus	2
1.2.1. Type 1 diabetes mellitus	2
1.2.2. Type 2 diabetes mellitus	3
1.2.3. Gestational diabetes mellitus	4
1.3. Pathophysiology of diabetes mellitus	5
1.4. Complications of diabetes mellitus	5
1.4.1. Macrovascular complications	6
1.4.2. Microvascular complications	7
1.5. Diabetic nephropathy	7
1.5.1. Stages of diabetic nephropathy	9
1.5.2. Symptoms and indicators of diabetic nephropathy	10
1.5.3. Risk factors of diabetic nephropathy	10
1.5.4. Structural and functional alterations during diabetic nephropathy	11
1.5.5. Pathogenesis of diabetic nephropathy	12
1.5.5.1.1. Renin angiotensin aldosterone system	14
1.5.5.1.2. Endothelien	14
1.5.5.2. Role of metabolic factors in diabetic nephropathy	15
1.5.5.2.1. Advanced glycation end products	15
1.5.5.2.2. Aldose reductase and the polyol pathway	16
1.5.5.3. Role of intracellular factors in diabetic nephropathy	17
1.5.5.3.1. Protein kinase C	17
1.5.5.3.2. Mitogen-activated protein kinase	17
1.5.5.3.3. Nuclear factor kappa B	18
1.5.5.4. Role of growth factors and cytokines in diabetic nephropathy	18
1.5.5.4.1. Transforming growth factor $\beta$	19
1.5.5.4.2. Platelet-derived growth factor	19
1.5.5.4.3. Vascular endothelial growth factor	20
1.5.5.5. Role of reactive oxidative species in diabetic nephropathy	20
1.5.5.6. Role of streptozotocin in diabetic nephropathy	21
1.5.6. Available drugs for treatment of diabetic nephropathy	23
1.5.6.1. Oral hypoglycaemic agents	23
1.5.6.1.1. Biguanides	23
1.5.6.1.2. Sulphonylureas	24
1.5.6.1.3. Non-sulphonylurea secretagogues	24
1.5.6.1.4. Dipeptidyl peptidase-4 inhibitor	24
1.5.6.1.5. Thiazolidinediones	24
1.5.6.1.6. $\alpha$ -Glucosidase inhibitors	25
1.5.6.2. Insulin	25
1.5.6.3. Angiotensin converting enzyme inhibitors and angiotensin II receptor blockers	26

1.5.6.4. Limitaions of oral hypoglycemic agents	26
1.5.7. Natural products in the treatment of diabetic nephropathy	27
1.5.7.1. Curcumin	28
1.5.7.2. Catechin	28
1.5.7.3. <i>Pueraria tuberosa</i>	29
1.5.7.4. <i>Pterocarpus santalinus</i>	29
1.6. Nanotechnology-based drug delivery system	30
1.6.1. Polymeric nanoparticles	31
1.6.1.1. Methods for fabrication of nanoparticles from biopolymers	31
1.6.1.1.1. Emulsification	32
1.6.1.1.2. Anti-solvent precipitation	32
1.6.1.1.3. Coacervation	32
1.6.1.1.4. Electrospray drying	32
1.6.1.2. Methods for fabricating nanoparticles from synthetic polymer dispersions	33
1.6.2. Nanostructure lipid carriers	33
1.6.2.1. Methods for fabrication of nanostructured lipid carriers	34
1.6.2.1.1. High-pressure homogenization method	34
1.6.2.1.2. High-shear homogenization and ultrasonication method	35
1.6.2.1.3. Solvent emulsification evaporation technique	35
1.6.2.1.4. Microemulsion method	36
<b>CHAPTER II</b>	<b>37</b>
<b>2. LITERATURE REVIEW</b>	<b>38</b>
2.1. Diverse applications of nanotechnology	38
2.2. Nanotechnology and medicine	39
2.3. Nanoparticles used in the treatment of diabetic nephropathy	40
2.4. Polymeric nanoparticles	41
2.4.1. Shellac	42
2.4.2. Locust bean gum	44
2.4.3. Ascorbyl palmitate	46
2.4.4. Hydroxypropyl methylcellulose	47
2.4.5. Transcutol®	48
2.4.6. Aerosil 200	49
2.4.7. Curcumin	50
2.4.7.1. Source and physical appearance	50
2.4.7.2. Structural characteristics of curcumin	51
2.4.7.3. Solubility of curcumin	51
2.4.7.4. Biological activities of curcumin	52
2.4.7.5. Safety and toxicity of curcumin	53
2.4.8. Epigallocatechin-3-gallate	53
2.4.8.1. Source and physical appearance	53
2.4.8.2. Structural characteristics of EGCG	54
2.4.8.3. Solubility of EGCG	55
2.4.8.4. Biological activities of EGCG	55
2.4.8.5. Safety and toxicity of EGCG	56
2.4.9. Methods for preparation of biopolymer nanoparticles	57
2.4.9.1. Emulsification	57

2.4.9.2. Anti-solvent precipitation	57
2.4.9.3. Coacervation	58
2.4.9.4. Electrospray drying	59
2.5. Nanostructured lipid carriers	59
2.5.1. Compritol 888 ATO	61
2.5.2. Triolein	62
2.5.3. Soybean lecithin	63
2.5.4. Sodium deoxycholate	65
2.5.5. Cetyltrimethylammonium bromide	66
2.5.6. <i>Pueraria tuberosa</i>	67
2.5.6.1. Scientific classification of <i>Pueraria tuberosa</i>	67
2.5.6.2. Phytochemistry of <i>Pueraria tuberosa</i> extract	68
2.5.6.3. Biological activities of <i>Pueraria tuberosa</i> extract	69
2.5.6.4. Safety and toxicity of <i>Pueraria tuberosa</i> extract	71
2.5.7. <i>Pterocarpus santalinus</i> extract	71
2.5.7.1. Scientific classification of <i>Pterocarpus santalinus</i>	71
2.5.7.2. Phytochemistry of <i>Pterocarpus santalinus</i> extract	72
2.5.7.3. Biological activities of <i>Pterocarpus santalinus</i> extract	73
2.5.7.4. Safety and toxicity of <i>Pterocarpus santalinus</i> extract	75
2.5.8. Methods for preparation of nanostructured lipid carriers	75
2.5.8.1. High-pressure homogenization method	75
2.5.8.2. High-shear homogenization and ultrasonication method	76
2.5.8.3. Solvent emulsification evaporation technique	76
2.5.8.4. Microemulsion method	77
2.6. Streptozotocin	78
2.7. Glibenclamide	78
<b>CHAPTER III</b>	<b>80</b>
<b>3. OBJECTIVES AND PLAN OF STUDY</b>	<b>81</b>
3.1. Objectives	81
3.2. Plan of study for curcumin and epigallocatechin gallate coacervated nanoparticles	81
3.3. Plan of study for <i>Pueraria tuberosa</i> and <i>Pterocarpus santalinus</i> extracts co-encapsulated nanoparticles	83
<b>CHAPTER IV</b>	<b>85</b>
<b>4. STUDIES ON CURCUMIN AND EPIGALLOCATECHIN GALLATE</b>	<b>86</b>
4.A. MATERIALS AND METHODS	86
4.A.1. Materials	86
4.A.1.1. Chemicals and reagents used for the study	86
4.A.1.2. Instruments used for the study	87
4.A.2. Methods	88
4.A.2.1. Preparation procedures for buffers and reagents used in the study	88
4.A.2.1.1. Preparation of enzyme-free simulated gastric fluid buffer at pH 1.2	88
4.A.2.1.2. Preparation of enzyme-free simulated intestinal fluid buffer at pH 7.4	88
4.A.2.1.3. Preparation of citrate buffer at pH 4.5	89

4.A.2.2. Synthesis of ammonium salt of hydrolyzed shellac	89
4.A.2.3. Synthesis of colloidal complex coacervate nanoparticles (CSL, ESL, and CESL)	89
4.A.2.4. Solidification of CSL, ESL, and CESL colloidal nanoparticles	90
4.A.2.5. RP-HPLC analytical method for estimation of curcumin and epigallocatechin gallate	91
4.A.2.5.1. Selection of UV wavelength for HPLC analysis	92
4.A.2.5.2. Instrumentation and chromatographic conditions for HPLC analysis	92
4.A.2.5.3. Preparation of stock standards and sample solutions	93
4.A.2.5.4. Method validation	94
4.A.2.5.4.1. Specificity	94
4.A.2.5.4.2. Linearity	94
4.A.2.5.4.3. Accuracy	94
4.A.2.5.4.4. Precision	94
4.A.2.5.4.5. Sensitivity	95
4.A.2.5.4.6. Robustness	95
4.A.2.5.5. System suitability	95
4.A.2.5.6. Forced degradation studies	95
4.A.2.5.7. Assessment of drug loading and entrapment efficiency	96
4.A.2.6. Characterization of the formulated nanoparticles	96
4.A.2.6.1. DLS analysis	96
4.A.2.6.2. FTIR analysis	97
4.A.2.6.3. DSC analysis	97
4.A.2.6.4. XRD analysis	97
4.A.2.6.5. AFM analysis	98
4.A.2.6.6. HRTEM analysis	98
4.A.2.6.7. FESEM analysis	98
4.A.2.7. Solubility study of CESL-NP	98
4.A.2.8. Stability study of CESL-NP	99
4.A.2.9. <i>In vitro</i> release of CESL-NP	99
4.A.2.10. <i>In vitro</i> drug release kinetic models	99
4.A.2.11. <i>In vivo</i> antidiabetic and antinephritic studies	101
4.A.2.11.1. Experimental animals	101
4.A.2.11.2. Induction of diabetes	101
4.A.2.11.3. Experimental design and animal treatment	101
4.A.2.11.4. Collection of serum and tissue samples	102
4.A.2.11.5. Histopathological analysis	103
4.A.2.11.6. Statistical analysis	103
4.B. RESULTS	104
4.B.1. Preformulation study of CESL-NP	104
4.B.2. RP-HPLC analytical method for estimation of CUR and EGCG	104
4.B.2.1. Method development	104
4.B.2.2. Method validation	105
4.B.2.2.1. Specificity	105
4.B.2.2.2. Linearity	106
4.B.2.2.3. Accuracy	107
4.B.2.2.4. Precision	108
4.B.2.2.5. Sensitivity	109
4.B.2.2.6. Robustness	109

4.B.2.3. System suitability	110
4.B.2.5. Drug loading and entrapment efficiency of formulated nanoparticles	118
4.B.3. Characterization of formulated nanoparticles	119
4.B.3.1. DLS analysis	119
4.B.3.2. FTIR analysis	121
4.B.3.3. DSC analysis	123
4.B.3.4. XRD analysis	124
4.B.3.5. AFM analysis	125
4.B.3.6. HRTEM analysis	126
4.B.3.7. FESEM analysis	127
4.B.4. Solubility study of CESL-NP	127
4.B.5. Stability study of CESL-NP	128
4.B.6. <i>In vitro</i> drug release study of CESL-NP	129
4.B.7. Drug release kinetics of CESL-NP	130
4.B.8. <i>In vivo</i> antidiabetic and antinephritic studies	132
4.B.8.1. Effects of CESL-NP on glycemic control in STZ-induced diabetic mice	132
4.B.8.2. Effects of CESL-NP on renal parameters in mice with early diabetic nephropathy	135
4.B.8.3. Effects of CESL-NP on renal biomarkers in early diabetic nephropathy in mice	137
4.B.8.4. Effects of CESL-NP on pancreatic and renal tissue in mice with early diabetic nephropathy	138
4.C. DISCUSSION	141
4.D. CONCLUSION	144
<b>CHAPTER V</b>	
<b>5. STUDIES ON <i>PUERARIA TUBEROSA</i> AND <i>PTEROCARPUS SANTALINUS</i> EXTRACTS</b>	146
5.A. MATERIALS AND METHODS	146
5.A.1. Materials	146
5.A.1.1. Chemicals and reagents used in the study	146
5.A.1.2. Instruments used in the study	147
5.A.2. Methods	148
5.A.2.1. Preparation procedures for buffers and reagents used in the study	148
5.A.2.1.1. Preparation of enzyme-free simulated gastric fluid buffer at pH 1.2	148
5.A.2.1.3. Preparation of citrate buffer at pH 4.5	149
5.A.2.2. Preparation of <i>Pueraria tuberosa</i> and <i>Pterocarpus santalinus</i> extracts	149
5.A.2.3. Preparation of NLCs loaded with <i>Pueraria tuberosa</i> extract, <i>Pterocarpus santalinus</i> extract, and their combination	150
5.A.2.4. Solidification of the formulated liquid nanostructured lipid carriers	150
5.A.2.5. RP-HPLC analytical method for estimation of puerarin and pterostilbene	152
5.A.2.5.1. Determination of UV wavelength for HPLC analysis	152
5.A.2.5.2. Instrumentation and chromatographic conditions	153
5.A.2.5.3. Preparation of standard-stock and sample-solutions	154
5.A.2.5.4. Validation of the developed RP-HPLC analytical method	154
5.A.2.5.4.1. Accuracy	154
5.A.2.5.4.2. Linearity	155
5.A.2.5.4.3. Precision	155
5.A.2.5.4.4. Sensitivity	155
5.A.2.5.4.5. Robustness	155

5.A.2.5.4.6. Selectivity	156
5.A.2.5.5. System suitability	156
5.A.2.5.6. Estimation of loading capacity and entrapment efficiency	156
5.A.2.6 Characterization of the prepared nanostructured lipid carriers	157
5.A.2.6.1. Dynamic Light Scattering analysis	157
5.A.2.6.2. Fourier transform infrared analysis	157
5.A.2.6.3. Differential scanning calorimeter analysis	158
5.A.2.6.4. X-ray diffraction analysis	158
5.A.2.6.5. Atomic force microscopy analysis	158
5.A.2.6.6. High-resolution transmission electron microscopy analysis	159
5.A.2.6.7. Field emission scanning electron microscopy analysis	159
5.A.2.7. Stability study of (PTE+PSE)-NLC	159
5.A.2.8. <i>In vitro</i> release of (PTE+PSE)-NLC	159
5.A.2.9. <i>In vitro</i> drug release kinetic models	160
5.A.2.10. <i>In vivo</i> antidiabetic and antinephritic studies	161
5.A.2.10.1. Experimental animals	161
5.A.2.10.2. Induction of diabetes	161
5.A.2.10.3. Experimental design and animal treatment	161
5.A.2.10.4. Serum collection and tissue preparation	162
5.A.2.10.5. Histopathological analysis for pancreas and kidney tissues	163
5.A.2.10.6. Statistical analysis	163
5.B. RESULTS	164
5.B.1. Preformulation study of (PTE+PSE)-NLC	164
5.B.2. RP-HPLC analytical method for estimation of puerarin and pterostilbene	165
5.B.2.1. Validation of method	165
5.B.2.1.1. Accuracy	165
5.B.2.1.2. Linearity	165
5.B.2.1.3. Precision	167
5.B.2.1.4. Sensitivity	168
5.B.2.1.5. Robustness	168
5.B.2.1.6. Selectivity	169
5.B.2.2. System suitability	169
5.B.2.3. Quantification of active constituents in herbal extracts and formulated NLCs using HPLC	170
5.B.2.4. Loading capacity and entrapment efficiency	174
5.B.3. Characterization of formulated NLCs	174
5.B.3.1. DLS analysis	174
5.B.3.2. FTIR analysis	176
5.B.3.3. DSC analysis	178
5.B.3.4. XRD analysis	179
5.B.3.5. AFM analysis	181
5.B.3.6. HRTEM analysis	181
5.B.3.7. FESEM analysis	182
5.B.4. Stability study of (PTE+PSE)-NLC	183
5.B.5. <i>In vitro</i> drug release study of (PTE+PSE)-NLC	184
5.B.6. Drug release kinetic study of (PTE+PSE)-NLC	185
5.B.7. <i>In vivo</i> antidiabetic and antinephritic studies	186
5.B.7.1. Effects of (PTE+PSE)-NLC on glycemic control in STZ-induced diabetic mice	186

5.B.7.2. Effects of (PTE+PSE)-NLC on renal parameters in mice with early diabetic nephropathy	190
5.B.7.3. Effects of (PTE+PSE)-NLC on renal biochemical markers in mice with early-stage diabetic nephropathy	192
5.B.7.4. Effects of (PTE+PSE)-NLC on pancreatic and renal tissue in mice with early diabetic nephropathy	194
5.C. DISCUSSION	197
5.D. CONCLUSION	201
<b>CHAPTER VI</b>	<b>202</b>
<b>6. SUMMARY</b>	<b>203</b>
<b>REFERENCES</b>	<b>206</b>

# List of Tables and Figures

## List of Tables

<b>Table 4. 1:</b> List of chemicals with their respective sources used in the study	86
<b>Table 4. 2:</b> List of all the equipment and instruments used in the study	87
<b>Table 4. 3:</b> Optimized chromatographic parameters of the validated RP-HPLC method	93
<b>Table 4. 4:</b> Optimized parameters for CUR and EGCG forced degradation study	96
<b>Table 4. 5:</b> Ingredients of CUR and EGCG-loaded nanoparticles	104
<b>Table 4. 6:</b> Accuracy findings by the validated HPLC method	108
<b>Table 4. 7:</b> Intraday precision findings by the validated HPLC method	108
<b>Table 4. 8:</b> Interday precision findings by the validated HPLC method	109
<b>Table 4. 9:</b> Robustness parameter of the validated method	110
<b>Table 4. 10:</b> System suitability parameters of the validated HPLC method	111
<b>Table 4. 11:</b> Percentage recovery and degradation of CUR and EGCG following stress conditions	112
<b>Table 4. 12:</b> Drug loading and entrapment efficiency of formulated nanoparticles	119
<b>Table 4. 13:</b> Mean particle size, polydispersity-index, and zeta potential of formulated nanoparticles	120
<b>Table 4. 14:</b> Characterization of CESL-NP after 90 days: stability studies	129
<b>Table 4. 15:</b> In vitro drug release kinetics of CUR and EGCG	131
<b>Table 4. 16:</b> Antidiabetic activity of glibenclamide, free (C+E), CESL-NP, CSL-NP, and ESL-NP on STZ-induced diabetic mice	133
<b>Table 4. 17:</b> Antinephritic effects of glibenclamide, free (C+E) and CESL-NP on renal parameters in mice with early diabetic nephropathy	136
<b>Table 4. 18:</b> Effect of glibenclamide, free (C+E) and CESL-NP on serum albumin, serum creatinine, and blood urea nitrogen (BUN) of diabetic mice	137
<b>Table 5. 1:</b> List of chemicals with their respective sources used in the study	146
<b>Table 5. 2:</b> List of all the equipment and instruments used in the study	147
<b>Table 5. 3:</b> Validated RP-HPLC method: optimized conditions	154
<b>Table 5. 4:</b> Composition of PTE and PSE-loaded NLC	164
<b>Table 5. 5:</b> Accuracy assessment of the validated HPLC method	165
<b>Table 5. 6:</b> Intraday precision data of the analytical method	167
<b>Table 5. 7:</b> Interday precision data of the analytical method	167
<b>Table 5. 8:</b> Robustness parameters of the validated HPLC method	168
<b>Table 5. 9:</b> System suitability parameters of the analytical HPLC method	169
<b>Table 5. 10:</b> Loading capacity and entrapment efficiency of the formulated NLCs	174
<b>Table 5. 11:</b> Average particle size, polydispersity index, and zeta potential of formulated NLCs	175
<b>Table 5. 12:</b> Characterization of (PTE+PSE)-NLC at 4 °C after 90 days: stability studies	183
<b>Table 5. 13:</b> In vitro drug release kinetics of PTE and PSE	186

<b>Table 5. 14:</b> Antidiabetic activity of glibenclamide, plant extracts (PTE+PSE), (PTE+PSE)-NLC, PTE-NLC, PSE-NLC on STZ-induced diabetic mice	188
<b>Table 5. 15:</b> Antinephritic effects of glibenclamide, plant extracts (PTE+PSE) and (PTE+PSE)-NLC on renal parameters in mice with early diabetic nephropathy	191
<b>Table 5. 16:</b> Antinephritic effects of glibenclamide, plant extracts (PTE+PSE) and (PTE+PSE)-NLC on renal parameters in mice with early diabetic nephropathy	193

## List of Figures

<b>Figure 1. 1:</b> Global projections of diabetes (2013 and 2035).	4
<b>Figure 1. 2:</b> Pathophysiology of diabetes mellitus	5
<b>Figure 1. 3:</b> Complications of diabetes mellitus	6
<b>Figure 1. 4:</b> Normal anatomy of kidney	8
<b>Figure 1. 5:</b> Normal and diabetic kidney	9
<b>Figure 1. 6:</b> Various pathways leading to the progression of diabetic nephropathy	13
<b>Figure 1. 7:</b> Chemical structure of streptozotocin	22
<b>Figure 1. 8:</b> Structure of polymeric nanoparticle	31
<b>Figure 1. 9:</b> Comparison of SLN and NLC structures	34
<b>Figure 2. 1:</b> Nanotechnology and its application in various fields	38
<b>Figure 2. 2:</b> (A) Lac tubes produced by <i>Kerria lacca</i> and (B) shellac in different colours	42
<b>Figure 2. 3:</b> Chemical composition of a typical structural unit of shellac	43
<b>Figure 2. 4:</b> Locust bean gum derived from carob fruit	44
<b>Figure 2. 5:</b> Molecular composition of locust bean gum	45
<b>Figure 2. 6:</b> Molecular structure of ascorbyl palmitate	46
<b>Figure 2. 7:</b> Molecular structure of hydroxypropyl methylcellulose	47
<b>Figure 2. 8:</b> Chemical structure of Transcutol®	48
<b>Figure 2. 9:</b> Chemical structure of Aerosil 200	50
<b>Figure 2. 10:</b> (A) Rhizomes of turmeric and (B) turmeric powder containing curcumin	51
<b>Figure 2. 11:</b> Chemical structure of curcumin	51
<b>Figure 2. 12:</b> (A) Leaves of <i>Camellia sinensis</i> and (B) EGCG in powder form	54
<b>Figure 2. 13:</b> Chemical structure of epigallocatechin gallate	55
<b>Figure 2. 14:</b> Structures of glyceryl mono-, di- and tri-behenate	61
<b>Figure 2. 15:</b> Chemical structure of triolein	63
<b>Figure 2. 16:</b> Chemical structure of soybean lecithin	64
<b>Figure 2. 17:</b> Chemical structure of sodium deoxycholate	66
<b>Figure 2. 18:</b> Chemical structure of cetyltrimethylammonium bromide	67
<b>Figure 2. 19:</b> <i>Pueraria tuberosa</i> : (A) whole plant, (B) flower, (C) tubers, and (D) leaves	68
<b>Figure 2. 20:</b> (A) <i>Pueraria tuberosa</i> extract and (B) chemical structure of puerarin	69
<b>Figure 2. 21:</b> <i>Pterocarpus santalinus</i> : (A) tree, (B) heartwood, and (C) heartwood chips	72
<b>Figure 2. 22:</b> (A) <i>Pterocarpus santalinus</i> extract and (B) chemical structure of pterostilbene	73
<b>Figure 2. 23:</b> Chemical structure of glibenclamide	79
<b>Figure 4. 1:</b> Schematic diagram for preparation of CESL-NP	91
<b>Figure 4. 2:</b> Overlay of UV spectra for curcumin and epigallocatechin gallate	92

<b>Figure 4. 3:</b> HPLC chromatograms of (A) standard curcumin, (B) standard epigallocatechin gallate, and (C) optimized chromatogram of a mixture of curcumin and epigallocatechin gallate	105
<b>Figure 4. 4:</b> Calibration curve of standard curcumin	107
<b>Figure 4. 5:</b> Calibration curve of standard EGCG	107
<b>Figure 4. 6:</b> Standard CUR degradation profile in 0.1 M NaOH under forced conditions	112
<b>Figure 4. 7:</b> Standard CUR degradation profile in 10% (v/v) H <sub>2</sub> O <sub>2</sub> under forced conditions	113
<b>Figure 4. 8:</b> Standard CUR degradation profile in 0.1 M HCl under forced conditions	113
<b>Figure 4. 9:</b> Standard CUR degradation profile under heat stress conditions	114
<b>Figure 4. 10:</b> Standard CUR degradation profile under photolytic stress conditions	114
<b>Figure 4. 11:</b> Standard CUR degradation profile under UV light exposure	115
<b>Figure 4. 12:</b> Standard EGCG degradation profile in 0.1 M NaOH under forced conditions	116
<b>Figure 4. 13:</b> Standard EGCG degradation profile in 10% (v/v) H <sub>2</sub> O <sub>2</sub> under forced conditions	116
<b>Figure 4. 14:</b> Standard EGCG degradation profile in 0.1 M HCl under forced conditions	117
<b>Figure 4. 15:</b> Standard EGCG degradation profile under heat stress conditions	117
<b>Figure 4. 16:</b> Standard EGCG degradation profile under photolytic stress conditions	117
<b>Figure 4. 17:</b> Standard EGCG degradation profile under UV light exposure	118
<b>Figure 4. 18:</b> HPLC chromatogram of CUR and EGCG in drug-loaded nanoparticles	119
<b>Figure 4. 19:</b> Particle size distribution of formulated CESL-NP	120
<b>Figure 4. 20:</b> FTIR spectra of pure drugs, nanoparticles, blank and physical mixture	122
<b>Figure 4. 21:</b> DSC thermograms of pure drugs, nanoparticles, blank and physical mixture	123
<b>Figure 4. 22:</b> XRD patterns of pure drugs, nanoparticles, blank and physical mixture	125
<b>Figure 4. 23:</b> AFM images of CESL-NP	126
<b>Figure 4. 24:</b> TEM image of CESL-NP	126
<b>Figure 4. 25:</b> FESEM image of CESL-NP	127
<b>Figure 4. 26:</b> Solubility assessment of free CUR and CESL-NP	128
<b>Figure 4. 27:</b> <i>In vitro</i> release of CUR and EGCG from CESL-NP at pH 1.2 and 7.4.	130
<b>Figure 4. 28:</b> Effects of glibenclamide, free (C+E), CESL-NP, CSL-NP, and ESL-NP on blood glucose in STZ-diabetic mice.	134
<b>Figure 4. 29:</b> Effects of glibenclamide, free (C+E), CESL-NP, CSL-NP, and ESL-NP on fasting blood glucose inhibition in STZ-diabetic mice.	135
<b>Figure 4. 30:</b> Impact of different treatments on kidney structure	136
<b>Figure 4. 31:</b> Antinephritic effects of glibenclamide, free (C+E), and CESL-NP on: (A) serum albumin, (B) serum creatinine, and (C) blood urea nitrogen levels in mice with early diabetic nephropathy	138
<b>Figure 4. 32:</b> Histopathological photomicrographs of pancreatic islet sections	139
<b>Figure 4. 33:</b> Histopathological photomicrographs of kidney sections 50 μm)	140
<b>Figure 5. 1:</b> Schematic diagram for preparation of PTE and PSE-loaded NLC	151

---

<b>Figure 5. 2:</b> UV overlay spectrum of puerarin and pterostilbene	152
<b>Figure 5. 3:</b> Linearity curve of puerarin of the analytical HPLC method	166
<b>Figure 5. 4:</b> Linearity curve of pterostilbene of the analytical HPLC method	166
<b>Figure 5. 5:</b> HPLC chromatogram of standard puerarin	171
<b>Figure 5. 6:</b> HPLC chromatogram of <i>Pueraria tuberosa</i> extract	171
<b>Figure 5. 7:</b> HPLC chromatogram of standard pterostilbene	172
<b>Figure 5. 8:</b> HPLC chromatogram of <i>Pterocarpus santalinus</i> extract	172
<b>Figure 5. 9:</b> HPLC chromatogram of puerarin and pterostilbene in mixed standard	173
<b>Figure 5. 10:</b> HPLC chromatogram of formulated (PTE+PSE)-NLC depicting distinct peaks of puerarin and pterostilbene by the detection at 284 nm	173
<b>Figure 5. 11:</b> Particle size distribution graph of (PTE+PSE)-NLC	176
<b>Figure 5. 12:</b> FTIR of PTE, PSE, (PTE+PSE)-NLC, physical mixture, and blank	177
<b>Figure 5. 13:</b> DSC thermograms of PTE, PSE, physical mixture, (PTE+PSE)-NLC, and blank	179
<b>Figure 5. 14:</b> XRD patterns of PTE, PSE, physical mixture, (PTE+PSE)-NLC, and blank	180
<b>Figure 5. 15:</b> AFM analysis of (PTE+PSE)-NLC	181
<b>Figure 5. 16:</b> TEM image of (PTE+PSE)-NLC	182
<b>Figure 5. 17:</b> FESEM of (PTE+PSE)-NLC	183
<b>Figure 5. 18:</b> <i>In vitro</i> cumulative drug release study of PTE and PSE from NLC formulation at pH 1.2 and 7.4	185
<b>Figure 5. 19:</b> Effects of glibenclamide, plant extracts (PTE+PSE), (PTE+PSE)-NLC, PTE-NLC, and PSE-NLC on blood glucose in STZ-diabetic mice	189
<b>Figure 5. 20:</b> Effects of glibenclamide, plant extracts (PTE+PSE), (PTE+PSE)-NLC, PTE-NLC, and PSE-NLC on the percentage inhibition of fasting blood glucose in streptozotocin-induced diabetic mice	190
<b>Figure 5. 21:</b> Effect of various treatments on kidney structure: glibenclamide (1 mg/kg), plant extracts (PTE+PSE) (1000 mg/kg), and (PTE+PSE)-NLC (200 mg/kg)	192
<b>Figure 5. 22:</b> Antinephritic effects of glibenclamide (1 mg/kg), plant extracts (1000 mg/kg), and (PTE+PSE)-NLC (200 mg/kg) on: (A) serum albumin, (B) serum creatinine, and (C) blood urea nitrogen levels in mice with early diabetic nephropathy	194
<b>Figure 5. 23:</b> Microscopic images of pancreatic tissue	195
<b>Figure 5. 24:</b> Photomicrographs of kidney histological sections	196

# Chapter I

## Introduction

## **1. INTRODUCTION**

### **1.1. Diabetes mellitus**

Diabetes, initially recorded by the Egyptians, is marked by symptoms such as polyuria and weight loss. The term "diabetes mellitus" was later introduced by the Greek physician Aetaeus. In Greek, "diabetes" translates to "to pass through," while "mellitus," derived from Latin, means honey, indicating sweetness (Kaul et al., 2013). Diabetes mellitus (DM), commonly known as diabetes, refers to a group of metabolic disorders characterized by elevated blood glucose levels. This hyperglycemic condition results from either a relative or absolute lack of insulin secretion, impaired insulin action, or a combination of both factors (Skyler, 2004). DM represents one of the most significant global health crises, affecting both developed and developing countries. Over the past 20 years, the global prevalence of DM has more than doubled. According to the most recent estimates from the International Diabetes Federation (IDF), there were 415 million individuals with DM in 2015, and this number is projected to reach 642 million by 2040 (Zimmet et al., 2016).

### **1.2. Classification of diabetes mellitus**

The current classification of diabetes was first introduced by the American Diabetes Association (ADA) and subsequently updated by the World Health Organization (WHO). This revised classification focuses on the underlying mechanisms of the disease rather than its treatment. It includes four main categories: It encompasses four primary categories: Type 1 diabetes mellitus (T1DM), Type 2 diabetes mellitus (T2DM), other specific forms of diabetes, and gestational diabetes (Maraschin, 2013).

#### **1.2.1. Type 1 diabetes mellitus**

T1DM, previously referred to as insulin-dependent diabetes mellitus is a prevalent endocrine and metabolic disorder in children. In the majority of cases, approximately 70–90%, T1DM is

linked to autoimmune destruction of  $\beta$ -cells, often accompanied by the presence of T1DM-specific autoantibodies. This form of the disease is referred to as autoimmune T1DM. In a smaller group of patients, the cause of  $\beta$ -cell destruction remains unclear, as no autoimmune response or autoantibodies are detected. This variant, known as idiopathic T1DM and is believed to have a strong genetic component (Katsarou et al., 2017). While much of the focus has been on the rise of type 2 diabetes, type 1 diabetes has also seen an increase. Traditionally recognized as a childhood disease, recent epidemiological studies reveal that its incidence in adults is now comparable (Devendra et al., 2004). The classic symptoms of polydipsia, polyphagia, and polyuria, along with significant hyperglycemia, continue to be key diagnostic indicators in children and adolescents. Additionally, the need for immediate exogenous insulin replacement is a defining characteristic of type 1 diabetes, necessitating lifelong treatment (Atkinson et al., 2014).

### **1.2.2. Type 2 diabetes mellitus**

T2DM, previously called non-insulin-dependent diabetes mellitus, is a metabolic disorder marked by elevated blood glucose levels resulting from resistance of insulin and a relative lack of insulin. The primary symptoms of T2DM include fatigue, frequent urination, weight loss, and excessive thirst (Ginter and Simko, 2013). The pathophysiology of T2DM comprises peripheral insulin resistance, altered hepatic glucose production, and diminishing  $\beta$ -cell function, ultimately leading to  $\beta$ -cell failure (Mahler and Adler, 1999). According to estimates from the IDF, in 2013, approximately 382 million adults aged 20–70 worldwide were affected by T2DM, with 80% of these individuals residing in low- and middle-income countries. This number is projected to increase to 592 million by 2035. China and India, in particular, have shown a rapid increase in T2DM incidence despite relatively low obesity rates (DeFronzo et al., 2015). T2DM is primarily influenced by lifestyle factors and genetic predisposition. Key lifestyle factors contributing to the development of T2DM include physical inactivity, a

sedentary lifestyle, cigarette smoking, and excessive alcohol consumption. Additionally, obesity is a significant factor, accounting for approximately 55% of T2DM cases (Olokoba et al., 2012).

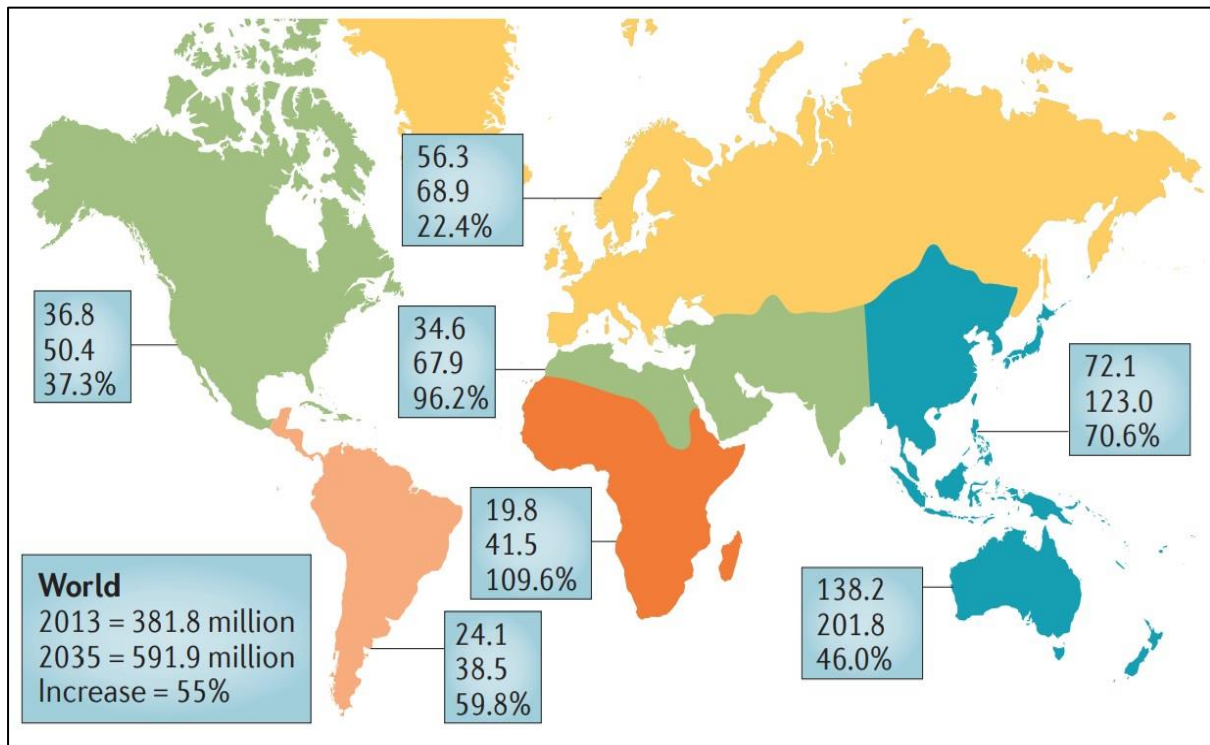


**Figure 1. 1:** Global projections of diabetes (2013 and 2035). In each box, the top values represent the number of individuals with T2DM (in millions) in 2013, while the values in middle, estimates the number of people expected to have T2DM in 2035. The bottom values show the percentage increase in T2DM cases from 2013 to 2035 (DeFronzo et al., 2015).

### 1.2.3. Gestational diabetes mellitus

Gestational diabetes mellitus (GDM) arises when women without a prior history of diabetes develop elevated blood sugar levels during pregnancy. This condition results from the release of diabetogenic hormones by the placenta, including placental lactogen, growth hormone, progesterone, and corticotropin-releasing hormone, which enhance insulin resistance. GDM develops when the  $\beta$ -cells are unable to overcome this increased insulin resistance during pregnancy, despite their proliferation (Bacon and Tomich, 2017).

### 1.3. Pathophysiology of diabetes mellitus

Genetic and environmental factors significantly influence autoimmunity, inflammation, and metabolic stress, which can impair the function or reduce the number of insulin-producing  $\beta$ -cells in the pancreas. When these cells are damaged or insufficient, the body struggles to produce adequate insulin, resulting in elevated blood sugar levels enough to diagnose diabetes. Genetic predispositions and environmental factors, such as diet and lifestyle, interact to worsen  $\beta$ -cell dysfunction. For instance, chronic inflammation or metabolic stress from obesity can further compromise  $\beta$ -cell performance. Ultimately, the interplay between these factors results in insufficient insulin production and the development of diabetes (Skyler et al., 2017).

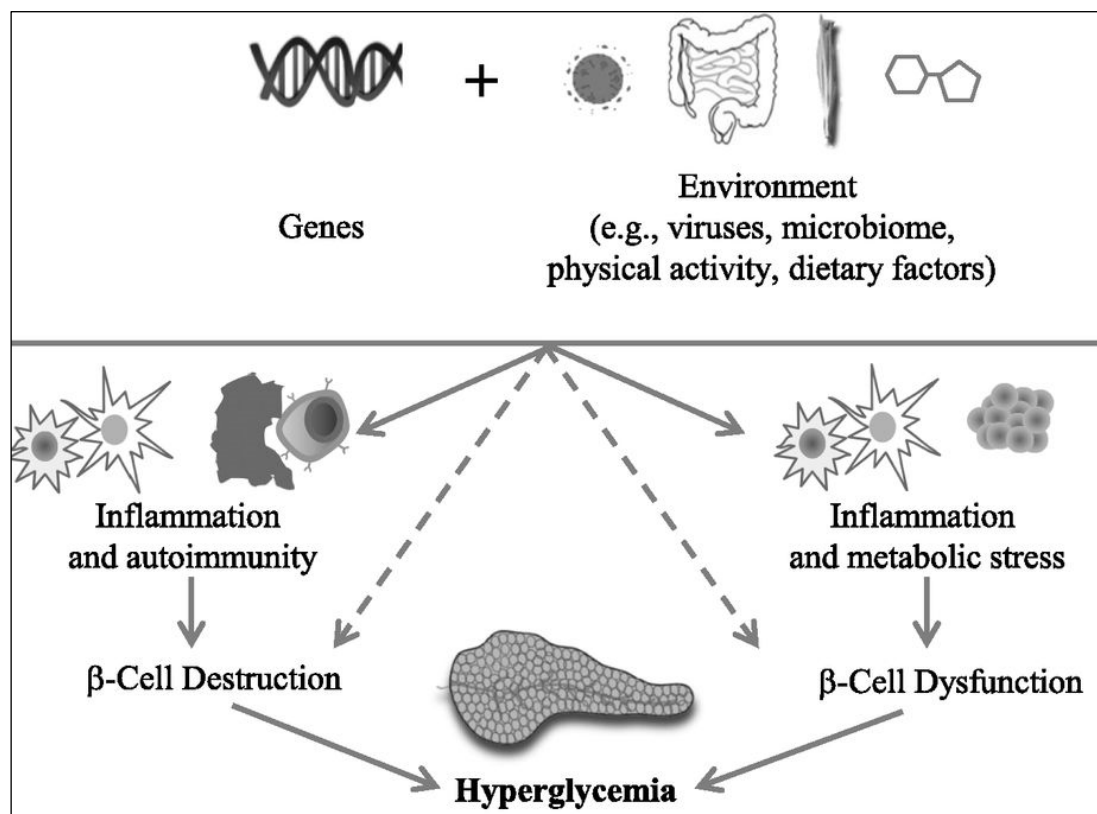


**Figure 1. 2:** Pathophysiology of diabetes mellitus (Skyler et al., 2017)

### 1.4. Complications of diabetes mellitus

Complications of diabetes are prevalent among patients with both type 1 and type 2 diabetes and are major contributors to significant morbidity and mortality (Papatheodorou et al., 2018).

These complications can be categorized into chronic and acute types (Figure 1.3). Chronic complications typically involve vascular damage and are generally classified into macrovascular and microvascular diseases (Verhulst et al., 2019). Macrovascular conditions, such as peripheral arterial disease, coronary heart disease, and stroke affect large blood vessels, while microvascular conditions, including diabetic retinopathy, nephropathy, and peripheral neuropathy, impact small blood vessels (Tomic et al., 2022). Although chronic complications develop gradually, there are three primary acute complications- diabetic ketoacidosis, nonketotic hyperosmolar syndrome, and hypoglycemia (Palk, 2018).

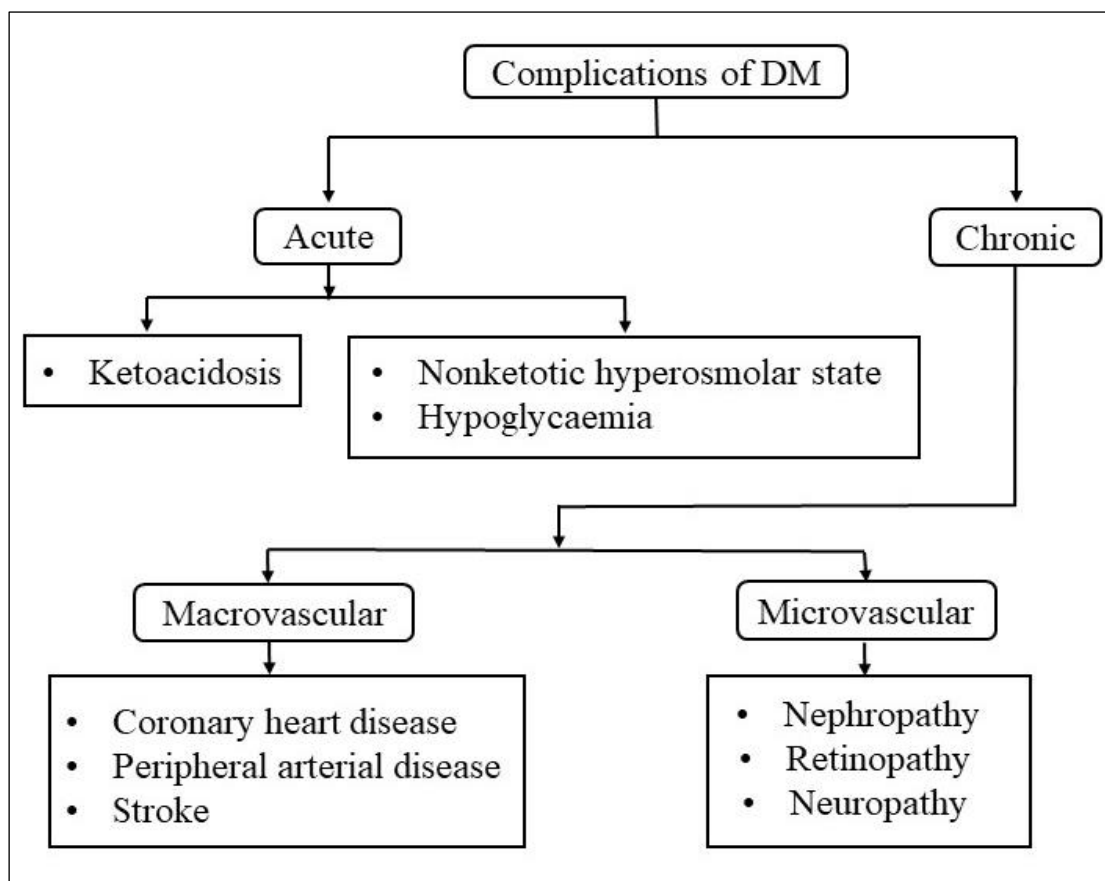


Figure 1. 3: Complications of diabetes mellitus

#### 1.4.1. Macrovascular complications

DM is a major contributor to macrovascular complications and is linked to accelerated atherosclerosis, often going undetected until the advanced stages of cardiovascular disease

(CVD). Numerous studies have observed a strong association between CVD and diabetes, regardless of other conventional cardiovascular risk factors. CVD is the most prevalent cause of mortality among diabetic patients, accounting for 52% of deaths in those with T2DM and 44% in those with T1DM (Huang et al., 2017).

#### **1.4.2. Microvascular complications**

Diabetes-related microvascular complications lead to pathological and functional changes in various tissues, including the kidneys, eyes, nerves, heart, and skin. These changes are commonly referred to as diabetic nephropathy, retinopathy, and neuropathy, depending on the affected tissues (He and King, 2004). Microvascular complications usually progress over many years but can be present at the time of diagnosis, especially in individuals with T2DM. While hyperglycemia is a crucial factor in causing microvascular disease, the specific mechanisms through which it affects the normal structure and function of microvessels are complex and not well fully understood (Crasto et al., 2021).

#### **1.5. Diabetic nephropathy**

Diabetic nephropathy (DN) is one of the most critical complications of diabetes and has become the primary cause of end-stage renal disease (ESRD) and cardiovascular-related deaths. This condition typically develops after several years following the onset of diabetes (Duran-Salgado, 2014). Approximately 20% to 40% of diabetes patients eventually develop DN. Clinically, DN is characterized by reduced kidney function, increased urinary albumin excretion, or both (Dronavalli et al., 2008; Thomas et al., 2015). The kidneys are crucial to the urinary system and play key roles in maintaining homeostasis, such as regulating electrolytes, maintaining acid-base balance, and controlling blood pressure. They act as natural filters for the blood, removing waste products, which are then expelled through the urinary bladder (Raghavendra et al., 2013).

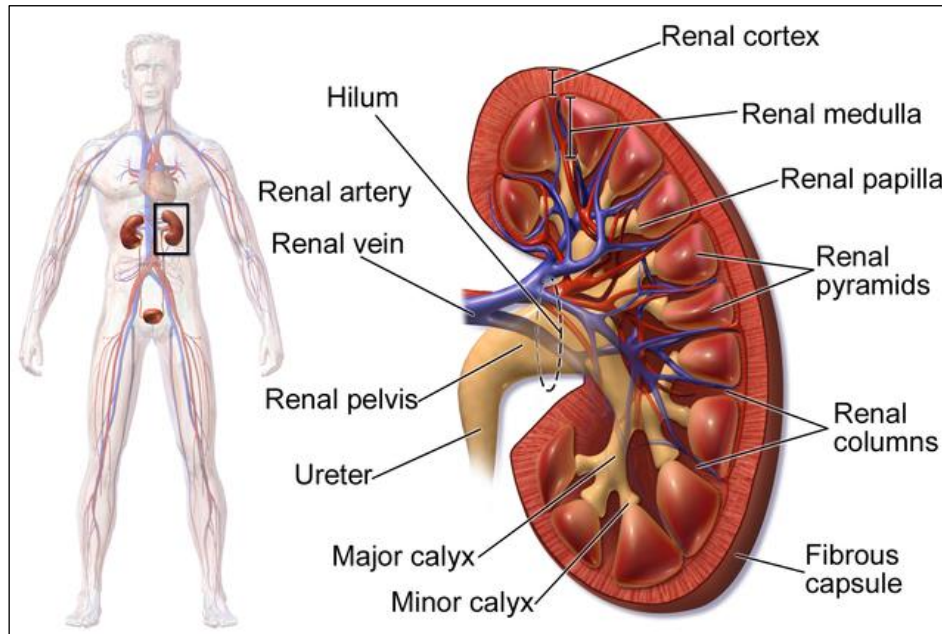


**Figure 1. 4:** Normal anatomy of kidney

Elevated glucose levels trigger specific cellular responses that impact various types of cells in the kidneys. Myofibroblasts, endothelial cells, smooth muscle cells, podocytes, inflammatory cells, tubular cells, and mesangial cells are all types of cells found in the kidney (Vallon and Komers, 2011). DN typically progresses through a defined clinical pathway, beginning with microalbuminuria and advancing to proteinuria, azotemia, and ultimately ESRD. Prior to the onset of noticeable proteinuria, several renal functional changes occur, including increased renal filtration, heightened blood flow, and greater capillary permeability to larger molecules. These functional changes are accompanied by ultrastructural alterations such as thickening of the glomerular basement membrane, glomerular hypertrophy, and mesangial expansion, which eventually lead to glomerulosclerosis and tubulointerstitial fibrosis. Basement membrane thickening is a well-established pathological feature of diabetes and can be detected within two years of diabetes diagnosis (Raptis and Viberti, 2001).

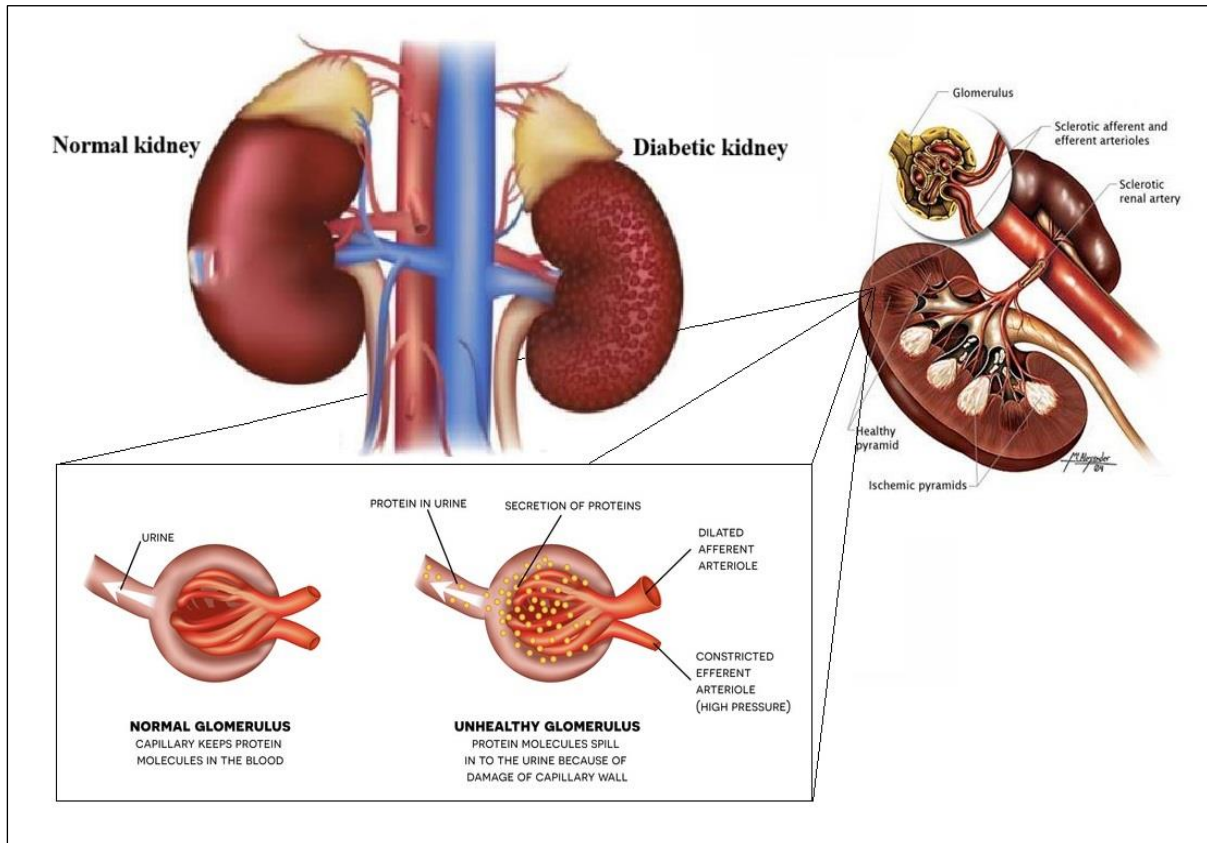


**Figure 1. 5:** Normal and diabetic kidney

### 1.5.1. Stages of diabetic nephropathy

DN is traditionally categorized into five stages based on the progression of kidney dysfunction. During Stage 1, the initial phase, the body experiences reversible glomerular hyperfiltration. In Stage 2, individuals have normoalbuminuria and normal glomerular filtration rate (GFR). By Stage 3, typically occurring approximately 5–10 years after the onset of diabetes, microalbuminuria becomes evident while GFR remains normal. Stage 4 is marked by the presence of proteinuria, which may reach nephrotic levels, usually occurring 10–15 years after the disease's onset. Finally, Stage 5 signifies chronic kidney disease progressing to ESRD, characterized by a GFR decline of less than 10 mL/min/year (Mansour and Thajudeen, 2017).

DN can also be classified into five functional stages. In Stage 1, there is hyperfunction and hypertrophy of the kidneys, often seen at diagnosis in T1DM, with exaggerated urinary albumin excretion that can be partially reversed with insulin treatment. Stage 2 features morphologic

lesions without clinical symptoms, with normal albumin excretion, though poor glycemic control and lack of exercise can reveal albuminuria. Stage 3, is marked by a rise in urinary albumin excretion from microalbuminuria (30–300 mg/day) to macroalbuminuria (>300 mg/day), often associated with increased blood pressure. Stage 4 of diabetic nephropathy is defined by the presence of persistent proteinuria (exceeding 0.5 g/day) and a decreased GFR. In Stage 5, the condition progresses to ESRD accompanied by uremia (waste buildup in the blood due to severe kidney dysfunction) (Mansour and Thajudeen, 2017).

### **1.5.2. Symptoms and indicators of diabetic nephropathy**

DN primarily manifests as hypertension and fluid accumulation in the body. Additional issues may include arteriosclerosis of the renal blood vessels and proteinuria. Symptoms may not be apparent in the initial stages, but as the condition progresses, significant protein loss through urine may occur due to renal impairment. Patients may experience edema, initially manifesting as swelling around the eyes in the morning and gradually extending to other parts of the body. Alongside this, they may observe increased nighttime urination, frothy urine due to proteinuria, and unintended weight gain from fluid retention. Additional signs and symptoms can include weakness, anemia, pale complexion, nausea, reduced appetite, and generalized itching. Laboratory tests often first detect microalbuminuria, and urine tests may reveal glucose, particularly if blood glucose management is inadequate. As kidney damage progresses, levels of serum creatinine and blood urea nitrogen (BUN) can rise. Kidney failure, driven by glomerulosclerosis, results in impaired fluid filtration and other functional issues (Ayodele et al., 2004).

### **1.5.3. Risk factors of diabetic nephropathy**

Risk factors for DN are categorized into modifiable and non-modifiable types. Modifiable factors include controlling hypertension, managing glycemic levels, and addressing

dyslipidemia. Additionally, the presence of other microvascular complications and smoking can heighten the risk of progressing to ESRD in individuals with type 2 diabetes. On average, diabetic patients who develop ESRD are around 60 years old. Factors that cannot be changed, such as age, sex, race, genetics, and pregnancy, can influence the risk of developing diabetic nephropathy. Individuals with a family history of this condition are more likely to develop it themselves. Male diabetes patients are more likely to develop DN compared to females. Several genes, such as CARS, VEGF, APOC1, eNOS, UNC13B, EPO, GREM1, HSPG2, APOE, ACE, CPVL/CHN2, FRMD3, and ALR2, have been associated with the genetic causes of DN. In diabetic patients, heightened levels of specific lifestyle habits, HbA1C, systolic blood pressure, and proteinuria raise the risk of developing diabetic nephropathy (Natesan and Kim, 2021).

#### **1.5.4. Structural and functional alterations during diabetic nephropathy**

The relationship between kidney structure and function is a two-way interaction throughout the stages of DN (Mogensen and Østerby, 1987). Renal failure develops over many years, starting with subtle functional changes and advancing to severe structural damage. Initially, the diabetic kidney may show increased glomerular filtration rate (GFR), microalbuminuria, and increased renal size (Mauer et al., 1984). The first significant structural change is the thickening of the glomerular basement membrane (GBM), nodular mesangial expansion, excessive extracellular matrix accumulation, and podocyte loss, disrupting glomerular integrity. Over 15-20 years, this progresses to overt proteinuria, hypertension, and a significant decline in GFR, potentially resulting in end-stage renal failure. Podocytes, crucial for maintaining glomerular structure and filtration, are damaged early, showing loss of foot processes, hypertrophy, shedding, and apoptosis before proteinuria appears (Liu et al., 2022). As the disease advances, clinical abnormalities such as elevated serum creatinine, BUN, serum urea, albuminuria, elevated blood pressure, and fluid retention become evident, eventually leading to end-stage renal disease (Wolf and Ziyadeh, 2007). At this stage, clinical features include overt proteinuria, decreased

GFR, hypertension, and glomerular occlusion, often reflecting advanced diabetic glomerulopathy with complete solidification of the glomerular tuft due to basement membrane accumulation (Mogensen and Østerby, 1987).

### **1.5.5. Pathogenesis of diabetic nephropathy**

Genetic factors may influence susceptibility to diabetic nephropathy, but chronic hyperglycemia is the primary instigator. Several mechanisms and factors can contribute to renal damage and the initiation or progression of diabetic nephropathy due to poor glycemic control (Parchwani and Upadhyah, 2012), as illustrated in Figure 1.6. Together, these factors increase extracellular matrix buildup and renal albumin permeability, which contribute to higher proteinuria, glomerulosclerosis, and eventually tubulointerstitial fibrosis (Soldatos and Cooper, 2008). The development and progression of DN are influenced not only by high blood glucose but also by various metabolic pathways. These pathways include growth factors and cytokines such as transforming growth factor  $\beta$  (TGF- $\beta$ ) (Lan, 2012), platelet-derived growth factor (PDGF) (Shen et al., 2020), connective tissue growth factor (CTGF) (Wahab et al., 2001), growth hormone (GH) and insulin-like growth factors (IGFS) (Poulaki et al., 2004), and vascular endothelial growth factor (VEGF) (Tufro and Veron, 2012). Hemodynamic factors, notably the renin-angiotensin-aldosterone system (RAAS) (Lozano-Maneiro and Puente-García, 2015) and endothelin (ET) (Chandrashekar and Juncos, 2014), also play a crucial role. Furthermore, metabolic factors like advanced glycation end products (AGES) (Singh et al., 2014) and the aldose reductase (AR)/polyol pathway (Dunlop, 2000), as well as intracellular mechanisms involving the diacylglycerol (DAG) – protein kinase C (PKC) (Noh and King, 2007), mitogen-activated protein kinases (MAPKs) (Wong et al., 2007), and nuclear transcription factors like nuclear factor kappa B (NF- $\kappa$ B) (Schmid et al., 2006), are the key factors to the development of diabetic nephropathy. Furthermore, growing evidence suggests

that the excessive production of reactive oxygen species (ROS) plays a crucial role in the onset of DN (Ha et al., 2008).

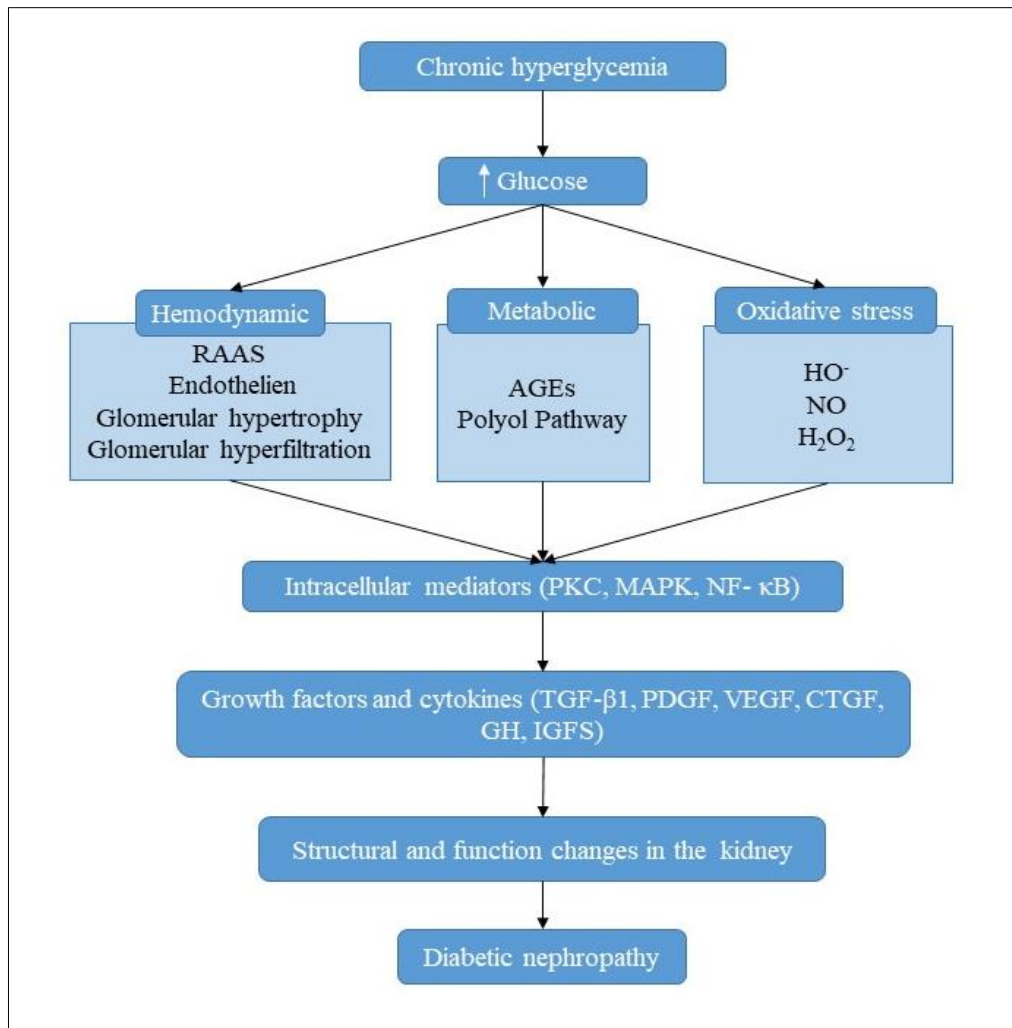


**Figure 1. 6:** Various pathways leading to the progression of diabetic nephropathy. RAAS: renin angiotensin aldosterone system, AGEs: advanced glycation end products, OH·: hydroxyl radical, H<sub>2</sub>O<sub>2</sub>: hydrogen peroxide, NO: nitric oxide, PKC: Protein Kinase C, MAPKs: Mitogen activated protein kinases, NF-κB: Nuclear factor kappa B, TGF-β: transforming growth factor β, PDGF: platelet derived growth factor, CTGF: connective tissue growth factor, GH: growth hormone, IGFS: insulin-like growth factors, VEGF: vascular endothelial growth factor.

#### 1.5.5.1. Role of hemodynamic factors in diabetic nephropathy

In DN, hemodynamic factors involve elevated intraglomerular and systemic pressure, along with the activation of vasoactive hormones, including the renin angiotensin-aldosterone system

(RAAS), and vasoconstrictors like endothelin, and nitric oxide. These changes, present early in the disease, exacerbate albumin leakage through glomerular capillaries and lead to mesangial matrix expansion, podocyte damage, and nephron loss (Satirapoj and Adler, 2014).

#### **1.5.5.1.1. Renin angiotensin aldosterone system**

Inappropriate activation of the RAAS can lead to hypertension, fluid accumulation, inflammation, blood clotting, and atherosclerosis, contributing to long-term kidney damage (Ruggenti et al., 2010). Renin, secreted by the kidney in response to decreased arterial blood pressure and sodium levels, regulates arteriolar constriction and overall blood pressure. It converts angiotensinogen into angiotensin (ANG) I, that is later converted into ANG II, an active peptide, by angiotensin-converting enzyme (ACE). This active peptide stimulates the adrenal glands to produce aldosterone, increasing sodium and water reabsorption in the kidney, leading to increased blood volume and pressure and potential cardiac complications (Zain and Awan, 2014).

#### **1.5.5.1.2. Endothelien**

In the kidney, similar to the renin-angiotensin-aldosterone system (RAAS), the endothelin (ET) system plays a crucial role in regulating water and sodium homeostasis. The ET system includes three distinct endothelins: ET-1, ET-2, and ET-3 (Forbes et al., 2007). Upon activation, ET-1 increases systemic and intraglomerular pressure, contributing to hypertension. It promotes renal cell proliferation and hypertrophy, leading to glomerular hypertrophy and mesangial matrix expansion. ET-1 also stimulates the release of pro-inflammatory cytokines, causing renal inflammation and leukocyte infiltration. Additionally, it induces the production of extracellular matrix components like collagen, contributing to glomerulosclerosis and interstitial fibrosis. ET-1 increases the permeability of the glomerular filtration barrier,

resulting in proteinuria, and generates reactive oxygen species, contributing to oxidative stress and further renal damage (Benz and Amann, 2011; Hocher et al., 2001).

### **1.5.5.2. Role of metabolic factors in diabetic nephropathy**

#### **1.5.5.2.1. Advanced glycation end products**

Hyperglycemia can lead to the irreversible formation of advanced glycation end products (AGEs). These AGEs are created when glucose react with free amino groups found in proteins, lipids, and nucleic acids (Forbes et al., 2003). In diabetes, chronic hyperglycemia leads to the formation of AGEs. Under normal conditions, the kidneys are responsible for the clearance of AGEs. However, in diabetes, renal impairment hinders this clearance process, resulting in the accumulation of AGEs. Proteins modified by AGEs exhibit increased resistance to enzymatic degradation, further promoting local tissue AGE accumulation. This accumulation is a hallmark DN, particularly evident in the mesangium and nodular lesions of kidneys. AGEs can act both receptor-independently and dependently, influencing cells internally or by binding to cell surface receptors like RAGEs. Advanced glycation targets long-lived proteins over extended periods, particularly affecting structural basement membrane components such as type IV collagen (Goh and Cooper, 2008).

ECM proteins are easily modified by AGEs because they are replaced slowly. When AGEs form crosslinks with collagen, it changes the structure of these proteins, making them stiffer and harder to break down. This modification leads to an increase in expression of ECM proteins, such as fibronectin, collagen and laminin. These changes are likely driven by increased levels of specific growth factors like TGF- $\beta$  and CTGF (Throckmorton et al., 1995; Twigg et al., 2002).

Animal studies have consistently shown that AGEs and their receptor, RAGE, play a pathogenic role in DN. In diabetic animals, there is a marked increase in renal AGEs, which

correlates with several structural abnormalities associated with DN. These include thickening of the glomerular basement membrane, expansion of the mesangium, glomerulosclerosis, and tubulointerstitial fibrosis (Twigg et al., 2002).

#### **1.5.5.2.2. Aldose reductase and the polyol pathway**

The polyol pathway consists of two key reactions: glucose is first reduced to sorbitol by aldose reductase (AR) with NADPH as a co-factor, and sorbitol is then oxidized to fructose by sorbitol dehydrogenase (SDH) using NAD<sup>+</sup> as a co-factor (Dunlop, 2000). The polyol pathway significantly contributes to oxidative stress in diabetes, particularly in the renal tissues. This pathway induces oxidative stress primarily through three mechanisms. One of these mechanisms involves the depletion of NADPH by aldose reductase activity. NADPH is essential for regenerating the antioxidant glutathione (GSH). During hyperglycemia, up to 30% of glucose is directed into the polyol pathway, leading to a marked reduction in NADPH and GSH levels, thus weakening the antioxidant defenses of the cell. Second, the oxidation of sorbitol to fructose by SDH converts NAD<sup>+</sup> to NADH, which fuels NADH oxidase, an enzyme that generates reactive oxygen species (ROS). Third, the pathway converts glucose into fructose and its byproducts, 3-deoxyglucosone and fructose-3-phosphate, that are further effective in forming advanced glycation end products (AGEs) than glucose itself. AGEs and their interactions with receptors are well-known contributors to oxidative stress (Chung et al., 2003).

The accelerated polyol pathway not only induces oxidative stress but also contributes to renal cell dysfunction by increasing prostaglandin production, activating PKC, enhancing DAG synthesis, and boosting the levels of TGF- $\beta$ 1 and ECM proteins (Iso et al., 2001).

### **1.5.5.3. Role of intracellular factors in diabetic nephropathy**

#### **1.5.5.3.1. Protein kinase C**

Among the different signaling kinases, Protein Kinase C (PKC) plays a crucial role in the pathogenesis of DN (Sun et al., 2013). Hyperglycemia triggers the de novo synthesis of diacylglycerol (DAG), leading to PKC activation. Additionally, elevated levels of glomerular thromboxane and prostaglandin endoperoxide in diabetes further activate PKC through the inositol phospholipid signaling pathway (Studer et al., 1995).

In vitro studies propose several roles for PKC in DN, such as mediating gene expression and synthesizing extracellular matrix proteins like fibronectin, collagens I and IV, and laminin via increased TGF- $\beta$  bioactivity. PKC also suppresses nitric oxide synthesis in glomeruli, enhances arachidonate release, promotes vasodilatory prostaglandin synthesis, down-regulates vasoconstrictor hormone receptors, and increases albumin permeability in epithelial and endothelial cells. Activators of PKC, including high glucose concentrations, LDL, ANG II, phorbol ester, and the thromboxane analogue U-46619, have been shown to increase extracellular matrix protein synthesis and TGF- $\beta$  bioactivity or mRNA expression in glomerular mesangial cells (Craven et al., 1995).

#### **1.5.5.3.2. Mitogen-activated protein kinase**

Mitogen-activated protein kinase (MAPK) is a key signaling molecule in the pathways activated by vasoactive substances like TGF- $\beta$ , ANG II, thromboxane A<sub>2</sub>, endothelin, fibroblast growth factor, insulin-like growth factor-1, and platelet-derived growth factor (Awazu et al., 1999). MAPKs are classified into three separate subfamilies: p38 kinases, c-Jun NH<sub>2</sub>-terminal kinases (JNK), and extracellular signal-regulated kinases (ERK) (Purves et al., 2001). Research has shown that factors associated with diabetes, including elevated glucose levels and AGEs, activate the p38 MAPK signaling pathway in renal cells. Increased glucose

levels and glycated albumin can specifically induce the phosphorylation of p38 MAPK in mesangial cells and fibroblasts, respectively (Wilmer et al., 2001; Daoud et al., 2001). This activation can lead to inflammation and cytokine production, further promoting p38 MAPK phosphorylation in diabetic kidneys and contributing to renal fibrosis. Additionally, p38 MAPK phosphorylation induced by hyperglycemia or mechanical stretch enhances TGF- $\beta$ 1 and fibronectin production in mesangial cells. TGF- $\beta$ 1, in turn, stimulates collagen and fibronectin synthesis through a p38 MAPK-dependent pathway, suggesting that p38 MAPK plays a significant role in renal fibrosis associated with diabetic nephropathy (Adhikary et al., 2004).

#### **1.5.5.3.3. Nuclear factor kappa B**

Various studies highlights the significant role of inflammation in the progression of DN, indicating that microinflammation is a key mechanism in diabetic complications (Fornoni et al., 2008; Lim and Tesch, 2012). Nuclear factor kappa B (NF- $\kappa$ B), a prevalent transcription factor, integrates multiple signaling pathways and regulates the transcription of genes involved in inflammatory responses. Elevated nuclear translocation of NF- $\kappa$ B has been observed in both human and experimental kidney diseases (Lim and Tesch, 2012). NF- $\kappa$ B is activated by various stress stimuli such as growth factors, vasoactive agents, cytokines, and oxidative stress. It regulates genes that encode proteins essential for immune and inflammatory responses, including cytokines, chemokines, and adhesion molecules (Schmid et al., 2006).

#### **1.5.5.4. Role of growth factors and cytokines in diabetic nephropathy**

Growth factors and cytokines are crucial in diabetes research due to their roles in promoting cell growth and proliferation, particularly in DN. Growth factor broadly refers to substances that induce cellular proliferation and differentiation, encompassing various peptides in the bloodstream and tissues like the kidney (Flyvbjerg, 2000).

#### **1.5.5.4.1. Transforming growth factor $\beta$**

Transforming growth factor (TGF)- $\beta$ 1 plays a crucial role as a mediator in DN. TGF- $\beta$  exists in three different forms: TGF - $\beta$ 1, - $\beta$ 2, and - $\beta$ 3. Of these, TGF- $\beta$ 1 is the primary factor involved in fibrosis. It stimulates extracellular matrix (ECM) production and suppresses ECM breakdown via the Smad-dependent pathway. TGF- $\beta$ 1 binds to TGF- $\beta$  receptor type II (T $\beta$ RII), activating TGF- $\beta$  receptor type I (T $\beta$ RI) and leading to the phosphorylation of Smad2 and Smad3. These phosphorylated Smads then form complexes with Smad4 to regulate gene transcription in the nucleus. In diabetic nephropathy, the overactivity of the TGF- $\beta$ /Smad signaling pathway occurs, demonstrated by the translocation of phosphorylated Smad2 and Smad3 into the nuclei of glomerular and tubulointerstitial cells. This overactivation, coupled with reduced levels of the inhibitory Smad7, contributes to glomerular and tubulointerstitial fibrosis. Consequently, the Smad signaling pathway in the diabetic kidney becomes dysregulated and imbalanced (Lan, 2012; Hata and Chen, 2016).

#### **1.5.5.4.2. Platelet-derived growth factor**

Platelet-derived growth factor (PDGF) is a polypeptide first isolated from human platelets known for stimulating fibroblasts, osteoblasts, smooth muscle, and mesangial cells. It triggers several cellular responses relevant to kidney disease, such as matrix production, cell movement, and proliferation. There are three PDGF isoforms (PDGF-AA, -BB, and -AB) along with two receptor types (PDGFR - $\alpha$ , and - $\beta$ ). Among them, PDGF-BB is more effective than PDGF-AA in promoting mesangial cell proliferation. It also stimulates TGF- $\beta$  production, which contributes to kidney fibrosis and hypertrophy, particularly in diabetes (Langham et al., 2003; Bessa et al., 2012). Research shows that PDGF-BB is highly expressed in DN and plays a crucial role in its development and progression by enhancing fibrosis with TGF- $\beta$  (Wang et al., 2009).

#### **1.5.5.4.3. Vascular endothelial growth factor**

Vascular endothelial growth factor (VEGF) is known for its role in promoting the formation of new blood vessels (neovascularization) and enhancing vascular permeability. In diabetic kidneys, VEGF protein levels are notably increased in glomerular cells. VEGF may contribute to matrix accumulation observed in DN and enhances the permeability of the glomerular filtration barrier to proteins. Although the precise role of VEGF in DN remains unclear, additional blood vessels have been noted in the vascular pole area of affected glomeruli. There is a significant correlation between VEGF mRNA expression in the glomeruli and mesangial matrix accumulation, suggesting that VEGF levels rise early in disease progression (Kanesaki et al., 2005).

#### **1.5.5.5. Role of reactive oxidative species in diabetic nephropathy**

Diabetic nephropathy involves multiple pathophysiological mechanisms, with elevated reactive oxygen species (ROS) recognized as the key and unifying factor initiating its progression. Consequently, ROS occupies a central role in the pathogenesis of DN (Sagoo and Gnudi, 2018). ROS encompass a variety of molecules, including molecular oxygen and its derivatives, such as Hypochlorous acid (HOCl), hydroxyl radical (HO<sup>-</sup>), nitric oxide (NO), lipid radicals, peroxynitrite (ONOO<sup>-</sup>), superoxide anion (O<sub>2</sub><sup>-</sup>), and hydrogen peroxide (H<sub>2</sub>O<sub>2</sub>). Many of these ROS are classified as free radicals due to their unpaired electrons, which make them highly reactive. When ROS levels exceed the capacity of endogenous antioxidant defenses, they oxidize critical tissue biomolecules, including carbohydrates, lipids, DNA, and proteins. This damaging condition is commonly known as oxidative stress (OS) (Kashihara et al., 2010).

Research has demonstrated that in the context of hyperglycemia, several factors contribute to the generation of ROS. These include the critical role of mitochondrial metabolism, the

involvement of multiple overlapping glucose metabolic pathways, and hemodynamic changes associated with hyperglycemia, all of which are closely linked to the production of oxidative stress (OS). Hyperglycemia leads to the diversion of glucose into alternative metabolic pathways, which are significant contributors to ROS generation and are critical in DN development. Notably, the following pathways have been implicated: (1) The polyol pathway, where sorbitol accumulates intracellularly, causing cellular damage and reducing antioxidant glutathione levels; (2) Activation of PKC through DAG, which influences neovascularization, blood flow, and vascular permeability, by activating factors such as TGF- $\beta$ , endothelin-1, and NF- $\kappa$ B; and (3) Formation of AGEs, which modify proteins, lipids, and nucleic acids, generating free radicals and activating cytokines like interleukin-1 (IL-1) and TGF- $\beta$  (Vasavada and Agarwal, 2005).

The interaction between AGEs and their receptor, RAGE, further exacerbates oxidative stress, contributing significantly to DN. This AGE-RAGE engagement leads to increased ROS production, which is cytotoxic to renal cells and drives inflammatory and fibrotic responses in the diabetic kidney. Additionally, ROS produced through the interaction between AGEs and RAGE promote the synthesis of pro-sclerotic growth factors, such as TGF- $\beta$  and CTGF. This occurs via the activation of signaling pathways including PKC, MAPK, and NF- $\kappa$ B, in both mesangial and renal tubulointerstitial cells (Yamagishi and Matsu, 2010).

Extensive research on glomerular injury has identified ROS as key mediators in the development of DN, highlighting the increased vulnerability of kidney to oxidative stress (Ha and Kim, 1999).

#### **1.5.5.6. Role of streptozotocin in diabetic nephropathy**

Streptozotocin (STZ), chemically identified as 2-deoxy-2(3-methyl-3-nitrosoureido)-D-glucopyranose, is an antibiotic produced by the bacterium *Streptomyces achromogens*. It

exhibits a broad range of antibiotic properties and is notable for its oncolytic, oncogenic, and diabetogenic effects (Rossini et al., 1977). The structure of STZ includes a deoxy glucose molecule attached to a highly reactive methylnitrosourea moiety (Figure 1.7).

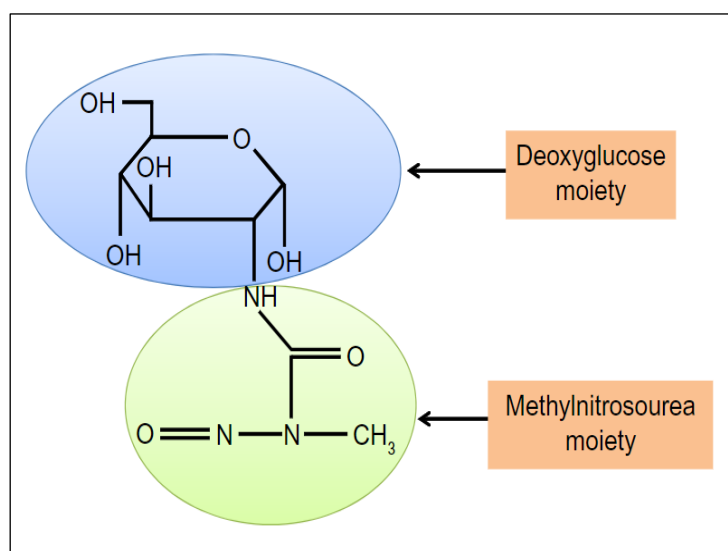


**Figure 1. 7:** Chemical structure of streptozotocin

The methylnitrosourea moiety is responsible for the cytotoxic effects of STZ, while the glucose moiety specifically targets pancreatic  $\beta$  cells by recognizing the GLUT2 receptor, which is abundant on the plasma membranes of these cells. Consequently, pancreatic  $\beta$  cells are the primary targets of STZ. However, since GLUT2 is also present, though to a lesser extent, in the liver and kidneys, high doses of STZ can impair the function of these organs as well. After administration, STZ is quickly metabolized in the liver and rapidly excreted by the kidneys, resulting in a short half-life of approximately 15 minutes in the serum following intravenous injection (Wu and Yan, 2015).

Once inside the cell, STZ is metabolized into diazomethane (DAM), an alkylating agent that causes DNA methylation, which contributes to its diabetogenic effects. Beyond DNA methylation, streptozotocin induces diabetes through various mechanisms. These mechanisms include increased NADPH levels due to glucose auto-oxidation or diacylglycerol production, elevated generation of oxygen-free radicals, activation of the protein kinase C pathway,

increased glucose flux through the polyol metabolic pathway, accumulation of advanced glycation end products, and the secretion of cytokines. These mechanisms collectively damage  $\beta$  cells, making STZ a unique compound for modeling diabetes in animals (Goyal et al., 2016).

### **1.5.6. Available drugs for treatment of diabetic nephropathy**

In patients with early-stage diabetic nephropathy, poor glycemic and blood pressure control is often observed and is associated with significant deterioration in clinical outcomes, increasing the risk of progression to kidney disease. Therefore, it is crucial to maintain both blood sugar and blood pressure levels within the appropriate ranges to minimize diabetic complications (Dounousi et al., 2015). The initial strategy for achieving better glycemic control and preventing both microvascular and macrovascular complications includes diet, exercise, and the use of oral hypoglycemic agents (OHAs) (Lorenzati et al., 2010). Additionally, most national guidelines recommend using ACE inhibitors and angiotensin receptor blockers (ARBs) over other antihypertensive agents for diabetic patients with micro- or macroalbuminuria (Strippoli et al., 2005).

#### **1.5.6.1. Oral hypoglycaemic agents**

##### **1.5.6.1.1. Biguanides**

Biguanides, notably metformin, are the first-line treatment for newly diagnosed type 2 diabetes, used in combination with diet and exercise. Metformin improves the body's ability to tolerate glucose by decreasing both baseline and post-meal blood sugar levels. It achieves this by reducing the liver's production of glucose, limiting glucose absorption from the intestines, and increasing insulin's effectiveness in promoting glucose uptake and utilization in peripheral tissues like muscles and fat cells. Common side effects include diarrhoea, vomiting, dyspepsia, flatulence, a metallic taste, and weight loss, while rare adverse reactions may include lactic acidosis and megaloblastic anaemia (Mane et al., 2012).

#### **1.5.6.1.2. Sulphonylureas**

Sulphonylureas (SUs) are traditionally categorized into first and second generations based on their duration of action. First-generation SUs, such as tolbutamide, acetohexamide, and chlorpropamide, have a shorter duration, while second-generation SUs, including glibenclamide, glipizide, and gliclazide, offer greater potency and improved safety, with effects lasting up to 48 hours. Notably, even the metabolites of second-generation SUs possess hypoglycemic activity. Glimepiride, classified as a third-generation SU, differs in that it operates through a glucose-independent mechanism, consistently inducing insulin release from beta cells by inhibiting ATP-dependent potassium channels, regardless of circulating glucose levels (Kaur et al., 2019).

#### **1.5.6.1.3. Non-sulphonylurea secretagogues**

Repaglinide is a fast-acting insulin secretagogue from the meglitinide class. Unlike sulphonylureas, it depends on the presence of glucose to close ATP-sensitive potassium channels, triggering calcium influx and promoting insulin release. (Kaur et al., 2019).

#### **1.5.6.1.4. Dipeptidyl peptidase-4 inhibitor**

Sitagliptin, the first available dipeptidyl peptidase-4 (DPP-4) inhibitor, works by preventing the breakdown of active glucagon-like peptide-1 (GLP-1) through DPP-4 enzyme inhibition. GLP-1, released from pancreatic  $\alpha$ -cells in response to food intake, plays a crucial role in blood glucose regulation. It enhances insulin secretion from the pancreas in a glucose-dependent manner, while also modulating glucagon release and reducing hepatic glucose production (Cheng and Fantus, 2005).

#### **1.5.6.1.5. Thiazolidinediones**

Thiazolidinediones (TZDs), like biguanides, enhance insulin action, with rosiglitazone and pioglitazone being key examples. TZDs act as agonists of peroxisome proliferator-activated

receptor (PPAR), promoting increased glucose uptake in various tissues such as adipose, muscle, and liver. Their mechanisms include reducing free fatty acid accumulation, lowering inflammatory cytokines, elevating adiponectin levels, and preserving  $\beta$ -cell integrity and function. Together, these effects improve insulin resistance and mitigate  $\beta$ -cell exhaustion (Chaudhury et al., 2017).

#### **1.5.6.1.6. $\alpha$ -Glucosidase inhibitors**

Acarbose and miglitol, which are  $\alpha$ -glucosidase inhibitors, target the  $\alpha$ -glucosidase enzyme found on the surface cells of the small intestine. This enzyme breaks down complex carbohydrates into simple sugars. By blocking this enzyme, these inhibitors prevent the breakdown and absorption of carbohydrates, but they don't interfere with the absorption of glucose and other simple sugars. As a result, the post-meal increase in blood sugar levels is reduced (Chaudhury et al., 2017).

#### **1.5.6.2. Insulin**

Insulin plays a vital role in regulating blood glucose levels by promoting the efficient use of glucose by cells, making it a cornerstone of diabetes management, particularly for patients with Type 1 Diabetes Mellitus (T1DM). In T1DM, where insulin production by the pancreas is either nonexistent or significantly reduced, patients often require a regimen of multiple daily injections. To closely replicate the body's natural blood glucose regulation, they may need both immediate-acting and long-acting insulin. Immediate-acting insulins, such as Novorapid, Apidra, or Humalog, are administered with meals to manage postprandial glucose levels, while long-acting insulins like Glargine or Determir are typically injected at dinner or bedtime to maintain basal glucose control (Wong et al., 2016).

### **1.5.6.3. Angiotensin converting enzyme inhibitors and angiotensin II receptor blockers**

In the management of DN, pharmacological interventions have been developed and investigated that either inhibit the synthesis of Angiotensin II (Ang-II) via angiotensin-converting enzyme (ACE) inhibitors or block its receptor-mediated effects using angiotensin II receptor blockers (ARBs). Numerous experimental and clinical studies have demonstrated the therapeutic potential of various ACE inhibitors—like captopril, lisinopril, cilazapril, imidapril, trandolapril, benazapril, fosinopril, perindopril, ramipril, and enalapril—and ARBs—including losartan, irbesartan, candesartan and olmesartan—in the management of DN (Balakumar et al., 2009).

Captopril has been observed to reduce microalbuminuria and inhibit lipid peroxidation in diabetic rats, and it has been found to extend the lifespan of patients with DN (Ha and Kim, 1992). Similarly, lisinopril has been observed to slow the advancement of DN and lower the frequency of proteinuria by inhibiting the renal expression of monocyte chemoattractant protein-1 (MCP1) (Amann et al., 2003). Losartan, a well-established ARB, has been found to reduce TGF- $\beta$  expression and suppress Ang-II-induced mesangial cell collagenase activity (Singh et al., 1999). Irbesartan, another ARB, has demonstrated effectiveness in reducing urinary protein excretion and providing renal protection against the progression of DN (Hunsicker, 2004).

### **1.5.6.4. Limitations of oral hypoglycemic agents**

In recent years, numerous oral and injectable medications have been developed to manage T2DM. These drugs, used either alone or in combination, target key pathophysiological issues like insulin resistance and inadequate insulin secretion, as well as related diabetic complications. However, long-term use of these pharmacological agents can be costly and often comes with significant side effects, including hypoglycemia, lactic acidosis,

gastrointestinal issues, weight gain, renal failure, and diarrhea (Blahova et al., 2021). Treating diabetic nephropathy with these drugs is further complicated by factors such as insulin resistance, hyperinsulinemia, hypertension, impaired insulin secretion, and cholesterol abnormalities. Despite their widespread use, many of these medications fail to significantly alter the progression of diabetic complications and are often accompanied by prominent side effects (Qi et al., 2010).

#### **1.5.7. Natural products in the treatment of diabetic nephropathy**

Natural products, originating from plants and other natural sources, are receiving increasing interest as alternative treatments for DN. This rise in interest is due to the limitations of traditional oral hypoglycemic agents and insulin therapy, which often face challenges related to patient adherence, systemic effectiveness, and adverse effects (Shafi et al., 2012). Recent advances in chemical and biological research have allowed several of these natural compounds to move from experimental research into clinical applications (Hu et al., 2021). Research has demonstrated that natural products can provide therapeutic effects by targeting key pathways involved in apoptosis, inflammation, cellular stress, and autophagy (Hu et al., 2023). Studies have shown that certain natural compounds can lower blood glucose and lipid levels and provide antioxidant benefits, which could help manage diabetes-related complications (Wu et al., 2024). As research into renal fibrosis and its treatment progresses, natural products are emerging as effective alternatives, offering potential anti-fibrotic benefits and supporting overall health and disease prevention (Chen et al., 2018). These compounds are valued for their antioxidant, anti-inflammatory, and antifibrotic properties, which makes them promising for managing DN (Wu et al., 2024). Moreover, some herbal agents are noted for their ability to regulate blood glucose and prevent complications associated with diabetes, with minimal side effects, thereby enhancing their use as both traditional and complementary therapies (Yaribeygi et al., 2019). There are over 400 plant species known for their antidiabetic properties,

highlighting the growing importance of herbal medicines. This is especially true in traditional medical systems, such as those in India, where many plants with potential kidney-protective benefits have yet to be fully scientifically validated (Shafi et al., 2012). Several bioactive compounds and herbs have been reported to be effective in treating diabetic nephropathy, including the following:

#### **1.5.7.1. Curcumin**

Curcumin, the yellow polyphenol found in turmeric (rhizomes of *Curcuma longa* from the ginger family, Zingiberaceae), has been widely studied over the past 60 years, with over 3,000 studies confirming its medicinal properties. This compound exhibits antioxidant, antibacterial, antifungal, antiviral, anti-inflammatory, antiproliferative, proapoptotic, and anti-atherosclerotic effects, benefiting a wide range of diseases. The multifaceted effects of curcumin stem from its ability to interact with and regulate various molecular targets (Parsamanesh et al., 2018; Soetikno et al., 2013). In diabetic rat models, curcumin has been shown to improve renal function and reduce oxidative stress, primarily due to its antioxidant properties (Parveen et al., 2018). Despite its potential benefits, curcumin's poor bioavailability remains a major obstacle. This is due to its low solubility in water, its breakdown in the digestive system under neutral and alkaline conditions, and its extensive metabolism in the intestinal wall before it enters the bloodstream (Joshi et al., 2013).

#### **1.5.7.2. Catechin**

Catechins, are primarily derived from the fresh leaves of *Camellia sinensis* (commonly known as green tea) belonging to the family Theaceae (Pedro et al., 2020). Green tea consumption has been associated with the prevention of diabetes, renal injury, oxidative stress, and hypertension (Parveen et al., 2018). Among the catechins, epigallocatechin-3-gallate (EGCG) is the most abundant and has been credited with many of green tea's health benefits (Yoon et al., 2014).

EGCG has demonstrated antihyperglycemic, antifibrotic effects, and protection against reactive oxygen species (ROS) production in diabetic nephropathy-induced mouse kidneys (Mohan et al., 2017). Despite its potential, the oral bioavailability of EGCG is relatively low, with maximum plasma concentrations of just 0.15  $\mu\text{M}$  after consuming two cups of green tea. This poor bioavailability of EGCG is likely due to sensitivity to digestive conditions, low intestinal absorption, and rapid degradation in the gastrointestinal tract (Zhang and Zhang, 2018).

#### **1.5.7.3. *Pueraria tuberosa***

*Pueraria tuberosa* Linn., a significant medicinal herb in Ayurvedic medicine and belonging to the Fabaceae family, is commonly known as Indian Kudzu or Vidarikanda. The tuber is renowned for its longevity, aphrodisiac, and rejuvenating properties (Maji et al., 2014b). *Pueraria tuberosa* exhibits a range of therapeutic activities, including DPP-IV enzyme inhibition, nephroprotective, antioxidant, anxiolytic, antihypoglycemic, anti-inflammatory, and antihypertensive effects. Puerarin, an active constituent of *Pueraria tuberosa*, is recognized as a potent hypoglycemic agent. Clinical and animal research has demonstrated that puerarin alleviates diabetic conditions by lowering blood glucose levels, increasing glucose uptake, safeguarding pancreatic beta cells, and decreasing insulin resistance (Pandey et al., 2019a). Although *Pueraria tuberosa* and its active components have low toxicity and minimal side effects, their short half-life and rapid metabolism via first-pass metabolism in the liver pose challenges for oral administration. Therefore, developing more suitable dosage forms is essential to enhance their efficacy (Deng et al., 2019; Chen et al., 2020).

#### **1.5.7.4. *Pterocarpus santalinus***

*Pterocarpus santalinus* Linn., also known as red sandalwood, belongs to the Fabaceae family and is predominantly found in Southern India (Azamthulla et al., 2015b). This plant has notable

antidiabetic effects, such as lowering blood glucose levels, improving hyperlipidemia, and stabilizing insulin levels (Nivedha et al., 2021). Treatment with *Pterocarpus santalinus* extract has also been shown to decrease lipid peroxidation, elevate antioxidant levels, and normalize serum creatinine and urine albumin levels (Shafi et al., 2012). Zhang et al., demonstrated pterostilbene, the principal bioactive compound in *Pterocarpus santalinus*, can alleviate renal damage in DN rats by inhibiting oxidative stress and inflammation and by modulating the NF- $\kappa$ B signaling pathway (Zhang et al., 2019). Although *Pterocarpus santalinus* demonstrates promising biological activities against diabetes, its clinical use is constrained by low bioavailability, poor solubility, and chemical instability. To improve its effectiveness, future strategies should emphasize targeted drug delivery to specific tissues (Wang et al., 2024).

#### **1.6. Nanotechnology-based drug delivery system**

Nanotechnology-based drug delivery systems offer precise and controlled release of drugs directly to target diseased cells. Nanoparticles, which range in size from 1 to 100 nm, can either chemically conjugate or physically encapsulate drugs. Due to their small size and large surface area, nanoparticles efficiently enter cells, interact with biomolecules, and traverse barriers such as the blood-brain barrier (BBB), pulmonary system, and tight junctions of the skin endothelial. These systems enhance drug concentration in targeted tissues while minimizing systemic side effects by optimizing pharmacokinetics and biodistribution. By improving absorption, bioavailability, and stability, nanotechnology overcomes the limitations of traditional drug delivery methods (Hami, 2021; Badar et al., 2019). Nanoparticles vary in size and shape and can be fabricated using various techniques, with polymeric nanoparticles, nanostructured lipid carriers, and liposomes being commonly employed in therapeutics (Patra et al., 2018).

### 1.6.1. Polymeric nanoparticles

Polymeric nanoparticles (PNPs) are made from biocompatible and biodegradable polymers, ranging in size from 10 to 1000 nm, with drugs either dissolved, encapsulated, entrapped, or attached to the nanoparticle matrix (Nagavarma et al., 2012). They significantly enhance efficacy and bioavailability compared to traditional intravenous and oral routes. Additionally, PNPs can be integrated into applications like tissue engineering and effectively deliver active ingredients to targeted tissues or organs, ensuring stability and prolonged activity for volatile compounds (El-Say and El-Sawy, 2017). PNPs are categorized mainly into two types: nanospheres and nanocapsules. Nanospheres are solid matrix particles that can carry biologically active molecules on their surface or within their structure, while nanocapsules feature an aqueous core surrounded by a polymeric shell (Lu et al., 2011). Figure 1.8 illustrates a schematic representation of polymer nanoparticles.

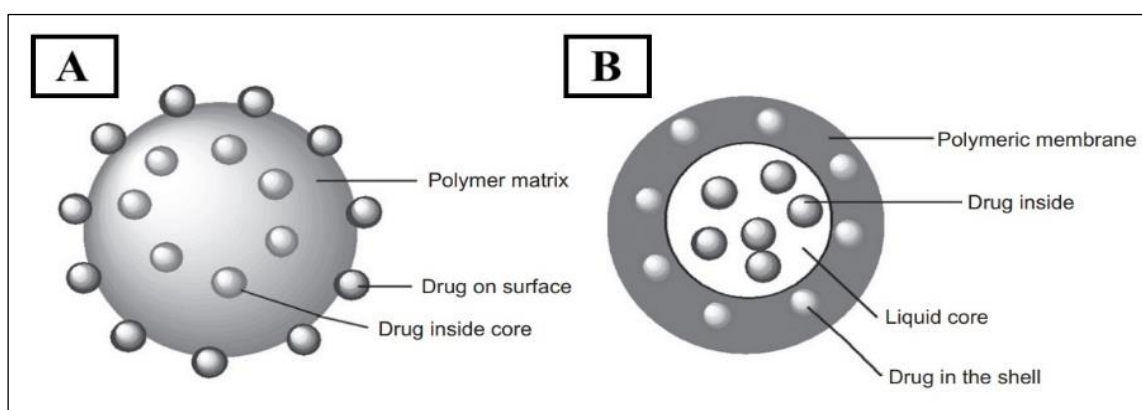


**Figure 1. 8:** Structure of polymeric nanoparticle: (A) polymer nanospheres and (B) polymer nanocapsules

#### 1.6.1.1. Methods for fabrication of nanoparticles from biopolymers

The four most common techniques for fabricating protein and polysaccharide-based nanoparticles are emulsification, anti-solvent precipitation, coacervation, and electrospray drying (Sundar et al., 2010).

#### **1.6.1.1.1. Emulsification**

Nano-emulsification occurs through the spontaneous formation of emulsions when the organic and aqueous phases are combined. The organic phase consists of oil, a water-miscible solvent, and a lipophilic surfactant, while the aqueous phase contains water and a hydrophilic surfactant. This method generates extremely small droplets, and the subsequent evaporation of the organic solvent produces stable dispersions of solid nanoparticles. (Sundar et al., 2010).

#### **1.6.1.1.2. Anti-solvent precipitation**

Anti-solvent precipitation reduces biopolymer solubility by adding a desolvation factor, causing supersaturation and solute precipitation. This process uses miscible solvents and anti-solvents like water, organic solvents, and supercritical CO<sub>2</sub>. It relies on molecular interaction imbalances, where strong solute–solute interactions drive precipitation. The process involves several critical stages: supersaturation, nucleation, particle growth, and coagulation. To ensure effective particle formation, it is essential to maintain enough repulsion to prevent aggregation (Joye and McClements, 2014).

#### **1.6.1.1.3. Coacervation**

Coacervates typically form when oppositely charged biopolymers interact through electrostatic attraction, though hydrophobic interactions and hydrogen bonds also play significant roles. These biopolymers can precipitate around an active ingredient, encapsulating it. To maintain the integrity of the shell, it can be covalently cross-linked (Joye and McClements, 2014).

#### **1.6.1.1.4. Electrospray drying**

Electrospray is a technique that transforms a leaky dielectric liquid, like a dilute polymer solution, into extremely small nanometer-sized droplets. By applying a high voltage to a needle electrode containing the liquid, electrohydrodynamic forces overcome the liquid's surface tension. This causes the liquid to form a cone shape at the needle's tip, from which a fine jet is

ejected. As this jet travels toward a grounded electrode, it breaks down into tiny nanoparticles (Luo et al., 2015).

#### **1.6.1.2. Methods for fabricating nanoparticles from synthetic polymer dispersions**

Nanoparticles can be created by dispersing drugs within preformed biodegradable polymers such as PLA, PLG, and PLGA. Several techniques are commonly used for this purpose, including solvent evaporation, nanoprecipitation, emulsification/solvent diffusion, salting out, dialysis, and supercritical fluid technology (SCF) (Nagavarma et al., 2012).

#### **1.6.2. Nanostructure lipid carriers**

Introduced in the early 1990s, solid lipid nanoparticles (SLNs) faced challenges like limited drug loading and drug loss during storage. To overcome these issues, nanostructured lipid carriers (NLCs) were developed. NLCs offer better drug loading due to higher drug solubility in liquid lipids compared to solid lipids (Parhi and Suresh, 2012). Unlike SLNs, NLCs have an unstructured solid lipid matrix of solid and liquid lipids, combined with an aqueous phase containing surfactants or surfactant mixtures (Beloqui et al., 2016). The liquid lipid does not incorporate into the crystalline structure of the solid lipid, resulting in the solid lipid crystals remaining undissolved in the liquid lipid. Instead, the liquid lipid forms nanoscale compartments within the solid crystalline matrix, maintaining homogeneity without phase separation below their melting point. NLCs are classified into three types: imperfect, amorphous, and multiple structure (Haider et al., 2020). Figure 1.9 represents the structure of SLN and NLC.

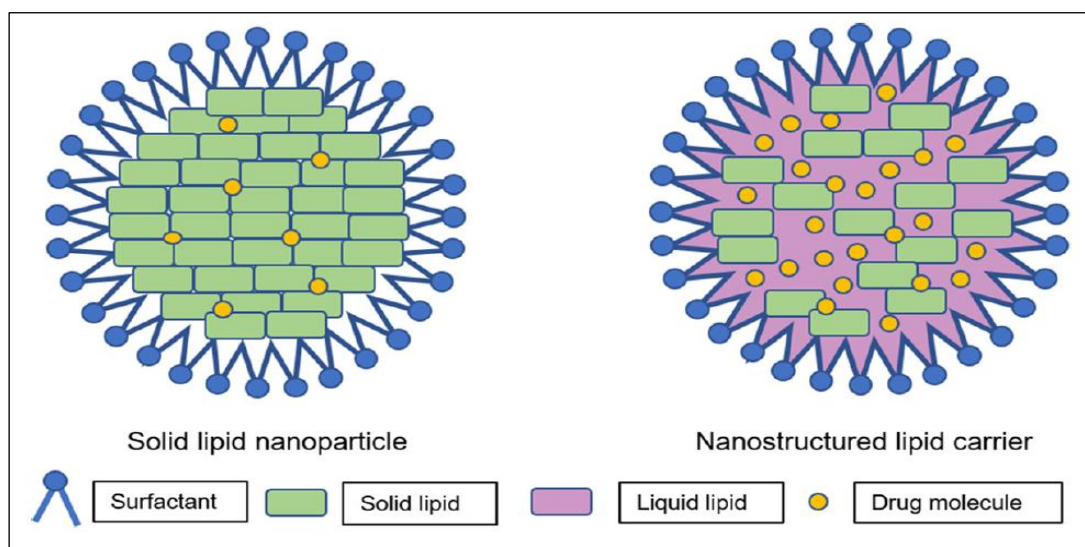


**Figure 1. 9:** Comparison of SLN and NLC structures

### 1.6.2.1. Methods for fabrication of nanostructured lipid carriers

Numerous techniques are employed for the preparation of NLCs. These include ultrasonic emulsion evaporation, high-pressure homogenization, and the film-ultrasonic method. Other methods are microemulsion, solvent dispersion, and high-temperature emulsion evaporation with subsequent low-temperature curing. Additionally, NLCs can be prepared using microchannel and microtube techniques, membrane contactors, and supercritical fluids (Li et al., 2017).

#### 1.6.2.1.1. High-pressure homogenization method

High-pressure homogenization (HPH) stands as a proven and reliable technique for producing lipid nanoparticles. It offers the advantage of large-scale NLC manufacturing without the use of organic solvents. HPH can be employed in two primary methods:

*Hot homogenization technique:* This method involves heating a mixture of liquid and solid lipids above the solid lipid's melting point and dissolving the drug in the melt. The drug-containing lipid melt is then dispersed in a hot aqueous surfactant solution using a high-speed stirrer. This coarse pre-emulsion is homogenized with a high-pressure homogenizer, usually in

one to three cycles. Subsequent cooling results in lipid crystallization and the formation of NLCs (Üner, 2006).

*Cold homogenization* technique: To prevent the potential for drug degradation associated with high temperatures in traditional hot homogenization, the cold homogenization technique was developed. In this method, lipids are heated above their melting point, and the drug is incorporated into the molten mixture. The resulting emulsion is then subjected to high-pressure homogenization and immediately cooled using extreme temperatures, such as liquid nitrogen or dry ice. This rapid cooling prevents thermal degradation of sensitive drugs. The solidified mass is subsequently ground into microparticles, which are then dispersed in a cold aqueous surfactant solution and subjected to additional homogenization or ultrasonication to produce NLCs (Salvi and Pawar, 2019).

#### **1.6.2.1.2. High-shear homogenization and ultrasonication method**

To prepare lipid nanoparticle dispersions, a solid lipid is melted to a temperature slightly exceeding its melting point, followed by dispersion into a warm aqueous solution containing surfactants. This mixture is subjected to high-shear homogenization (HSH) to break down droplets, followed by ultrasonication for further size reduction. As the emulsion cools below the lipid's crystallization temperature, lipid nanoparticles form within the aqueous dispersion (Ganesan and Narayanasamy, 2017).

#### **1.6.2.1.3. Solvent emulsification evaporation technique**

To prepare lipid nanoparticle dispersions, a water-insoluble organic solvent, such as chloroform, cyclohexane, toluene, or dichloromethane, is used to dissolve both the lipid and the hydrophobic drug. Using a high-speed homogenizer, this solution is then emulsified into an aqueous phase followed by the removal of the organic solvent through mechanical agitation

at ambient temperature, often under low pressure. This process results in the precipitation of lipid nanoparticles (Parhi and Suresh, 2012).

#### **1.6.2.1.4. Microemulsion method**

For this method, the drug is dissolved in a preheated mixture of melted lipid and oil, while a surfactant is dissolved in distilled water to create an aqueous phase. Both phases are heated to an elevated temperature and then combined under mechanical stirring, forming a microemulsion. This warm microemulsion is subsequently added to cold water (2-4 °C) while stirring. The rapid dilution in cold water causes the microemulsion globules to precipitate, resulting in the formation of NLCs (Üner, 2006).

# Chapter II

## Literature Review

## 2. LITERATURE REVIEW

### 2.1. Diverse applications of nanotechnology

Nanotechnology is an interdisciplinary field of science and technology that explores and manipulates phenomena at the nanoscale, integrating principles from biology, chemistry, colloidal science, physics, and other scientific disciplines (Mansoori and Soelaiman, 2005). Nanotechnology involves the self-assembly or manipulation of individual atoms, molecules, or molecular clusters to create materials and devices with novel or significantly altered properties (Manjunatha et al., 2016). Nanotechnology has captured considerable attention from the scientific community since its rise in the 2000s. It is already utilized in various daily and industrial applications, with many significant developments still in the research and development phase (Singh et al., 2020). Nanotechnology focuses on extremely small scales and finds application across various research and scientific disciplines, including informatics, energy, biology, engineering, chemistry, materials science, electronics, medicine, physics, and information technology (Kumar et al., 2023). Figure 2.1 illustrates the application of nanotechnology in multiple fields (Rao, 2019).

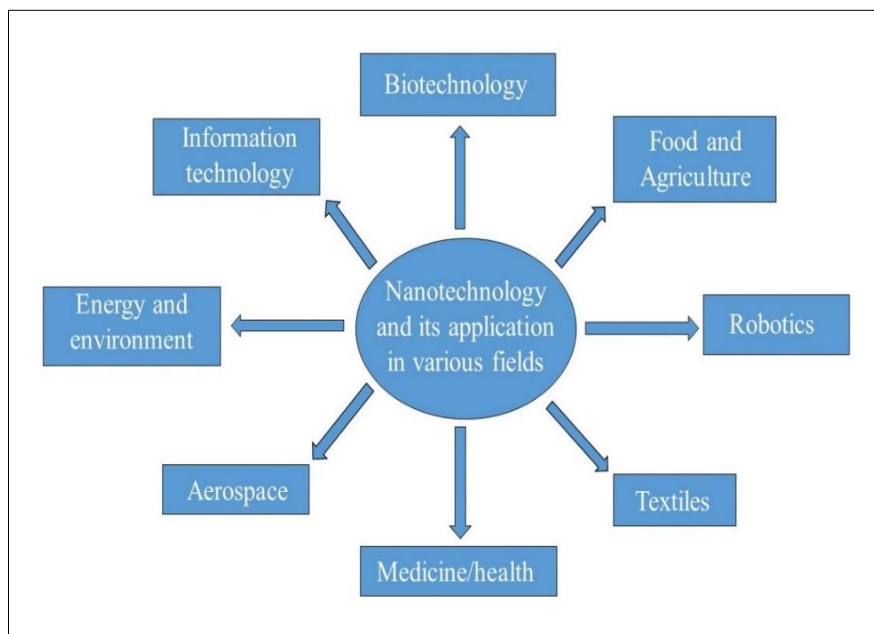


**Figure 2. 1:** Nanotechnology and its application in various fields

## **2.2. Nanotechnology and medicine**

Nanomedicine utilizes nanotechnology to improve human health. By developing nanoparticles ranging from 1 to 100 nm, it has advanced therapeutic methods and transformed medical treatments (Surendiran et al., 2009). The success of nanotechnology in healthcare is due to its capacity to work at the same scale as cellular mechanisms, organic molecules, and biological processes. As a result, medicine considers nanotechnology an ideal solution for diagnosing and treating numerous diseases (Morigi et al., 2012). Nanotechnology is transforming medical science with applications in artificial implants, gene delivery systems, targeted drug delivery, imaging, and sensing. Modern drugs often use nanoparticles made from metals, polymers, or ceramics to treat conditions like cancer and combat pathogens such as bacteria (Singh et al., 2008).

In the coming years, nanotechnology is likely to revolutionize pharmaceutical development. Nanoparticles are being used in drug delivery systems to enhance bioavailability, targeting, and controlled release. For instance, nanoscale polymer capsules can release drugs in response to specific conditions, such as low pH, enabling targeted delivery to tumor cells over normal tissues (Thrall, 2004).

Nanotechnology is set to improve fluorescent markers used in diagnostics and screening. Current markers face issues like fading, the need for specific lasers, and dye overlap. Fluorescent nanoparticles, like quantum dot nanocrystals, can address these problems by offering a wide range of distinct colors and better stability (Emerich and Thanos, 2003).

Raoul Kopelman developed the Probes Encapsulated by Biologically Localized Embedding (PEBBLES) technology, which uses dye-tagged nanoparticles to monitor cellular metabolism and disease. For example, this system has recently been used to measure zinc levels in living cells (Sumner et al., 2002).

Advancements in nanotechnology have facilitated the development of artificial receptors. Shi and Ratner, employed a radiofrequency-plasma glow-discharge process to imprint nanometer-sized pits onto a polysaccharide-like film, replicating the shapes of various proteins such as albumin, lysozyme, fibrinogen, and immunoglobulin (Shi and Ratner, 2000).

In the past decade, significant advancements in nanotechnology have had a profound impact on drug delivery. Nanotechnology provides new therapeutic options for agents with poor bioavailability in traditional oral formulations. Nanoparticles protect drugs from degradation in harsh pH environments and allow for sustained release. They can also penetrate membrane barriers, especially in the absorptive cells of the small intestine. Biodegradable nanospheres have been particularly effective in delivering small molecules, proteins, and other therapeutics. They enhance bioavailability by being absorbed into the system and gradually disappear from the system (Hillyer and Albrecht, 2001). Nanoparticles mostly used for drug delivery include polymeric nanoparticles, nanostructured lipid carriers (NLCs), liposomes, micelles, nanosuspensions, dendrimers, and hydrogel nanoparticles (Patra et al., 2018).

### **2.3. Nanoparticles used in the treatment of diabetic nephropathy**

Advances in nanotechnology have led to the development of nanopatform drug delivery systems that enhance the efficiency of antidiabetic drugs by breaking them down, encapsulating, or attaching them to nanoparticles. This approach improves drug delivery, reduces off-target effects, and enhances treatment outcomes (Liu et al., 2022). Alomari et al. found that gold nanoparticles significantly reduced albuminuria and podocyte injury in diabetic rats, indicating their potential to mitigate renal damage without side effects (Alomari et al., 2020). Alhazza et al. reported that selenium nanoparticles alleviated diabetic nephropathy symptoms by reducing oxidative stress and improving renal function, showing promise for use during pregnancy (Alhazza et al., 2022). Venkatesan et al. demonstrated that p-Coumaric acid nanoparticles effectively managed nephrotoxicity by regulating key kidney injury markers and

glucose transport (Venkatesan et al., 2022). Chen et al. highlighted the effectiveness of polyethyleneglycol- polycaprolactone- polyethylenimine (PEG-PCL-PEI) nanoparticles in enhancing the solubility, bioavailability, and kidney distribution of rhein, significantly improving diabetic nephropathy symptoms in a mouse model (Chen et al., 2018). Abd El-Hameed found that polydatin-loaded chitosan nanoparticles outperformed free polydatin in reducing oxidative stress, inflammation, and improving renal function, indicating a more effective delivery system (Abd El-Hameed, 2020). Yang showed that crocetin-loaded PLGA nanoparticles effectively reduced renal damage in diabetic rats by lowering inflammatory biomarkers and fibrotic factors (Yang, 2019). Alomari et al. also noted the benefits of zinc oxide nanoparticles in improving renal function and reducing fibrosis, oxidative stress, inflammation, and abnormal angiogenesis in diabetic nephropathy (Alomari et al., 2021). Wardani et al. demonstrated that fucoidan nanoparticles decreased oxidative stress, protected kidney structure, and reduced necrosis in diabetic rats, highlighting their nephroprotective effects (Wardani et al., 2022).

#### **2.4. Polymeric nanoparticles**

Biodegradable polymeric nanoparticles are widely studied for drug delivery due to their excellent biodegradability and biocompatibility. Natural polymers, including chitosan, shellac, gelatin, sodium alginate, and albumin, are valued for their natural breakdown and compatibility with the body, but their use can be limited by batch-to-batch variability. Synthetic polymers such as polylactides (PLA), polyglycolides (PGA), and poly(lactide-co-glycolides) (PLGA) offer controlled chemical compositions, which address some of these issues. However, synthetic polymers can also present challenges, including potential long-term biocompatibility concerns and higher production costs (Liu et al., 2020; Crucho and Barros, 2017; Nagavarma et al., 2012)

### 2.4.1. Shellac

Shellac, a natural polymer derived from the lac insect, *Kerria lacca*, offers a sustainable and biodegradable alternative to synthetic nanoparticulate carriers (Figure 2.2). While synthetic polymers have been extensively studied (Krongrawa et al., 2024), shellac's potential remains relatively unexplored despite its unique properties and environmental benefits. Primarily cultivated in India, China, and Thailand, shellac is a purified resin known for its non-toxicity and biocompatibility, earning its approval as a food additive (E904) (Yuan et al., 2021b). In recent years, researchers have delved into shellac-based delivery systems, demonstrating their promising applications in medicine and food (Yuan et al., 2021a).

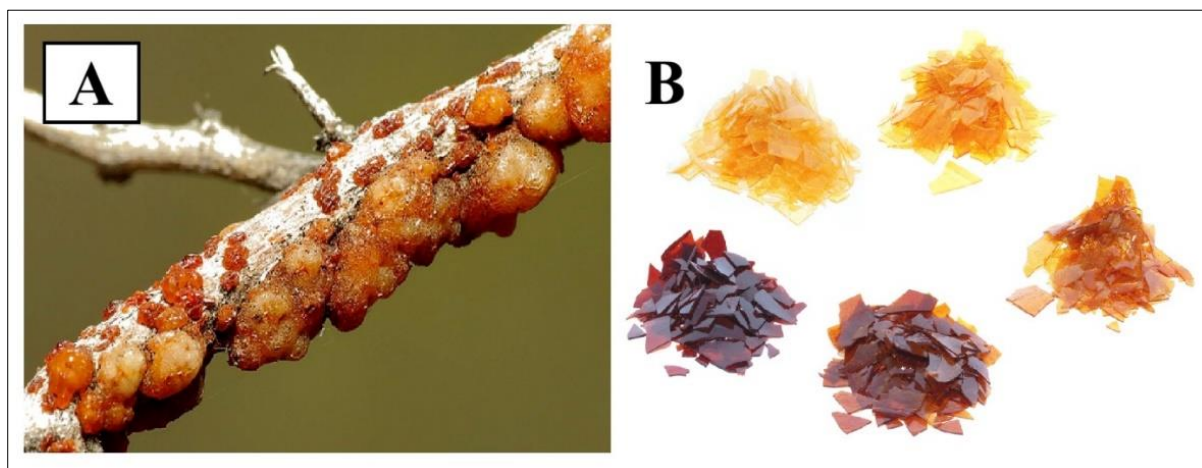


**Figure 2. 2:** (A) Lac tubes produced by *Kerria lacca* and (B) shellac in different colours

Shellac, is composed of aleuritic acid and cyclic terpene acids, linked together by ester bonds. These components create a unique structure with hydrophobic and hydrophilic properties (Luo et al., 2016). The cyclic terpene acid moiety in shellac can be classified into different types based on their R and R' groups, including jalaric, laccijalaric, shellolic, laccilaksholic, laksholic, and laccishellolic acid (Sutherland and Del Río, 2014). As illustrated in Figure 2.3, a typical shellac unit contains five hydroxyl groups, three ester groups, a free carboxyl group, a double bond, and a partially hidden aldehyde group (Thombare et al., 2022).

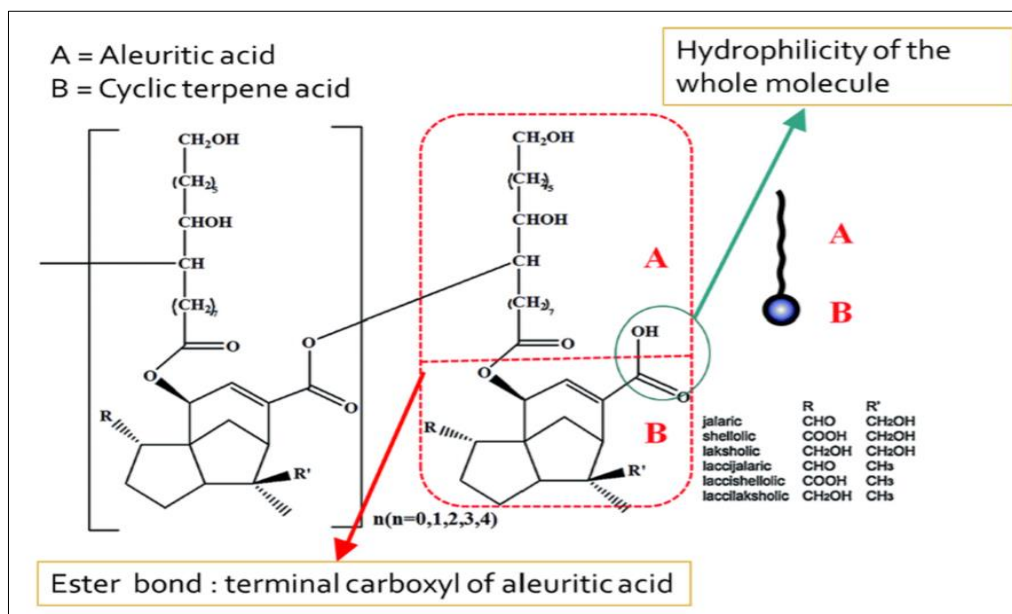


**Figure 2. 3:** Chemical composition of a typical structural unit of shellac

Researchers have explored the potential of shellac as a versatile material for drug delivery. Shiromani et al. created nanocomplexes of sodium caseinate and shellac to encapsulate quercetin, thereby improving its stability and bioavailability (Shiromani et al., 2023). Al-Obaidy et al. developed nanocarriers made of shellac nanoparticles stabilized with steric barriers to deliver chlorhexidine more effectively and stably (Al-Obaidy et al., 2021). Yuan et al. encapsulated curcumin within a shellac matrix to enhance its stability, bioaccessibility, and solubility (Yuan et al., 2022). Furthermore, Doost et al. demonstrated that quercetin-loaded almond gum/shellac nanoparticles exhibit superior uptake compared to free quercetin (Doost et al., 2019). Shellac's recognized safety, film-forming properties, chemical reactivity, unique solubility characteristics, pH sensitivity in the colon, and amphiphilicity make it an attractive candidate for developing drug delivery systems (Yuan et al., 2021a). Despite its acid resistance, shellac faces challenges in oral drug delivery due to severe aggregation at pH 1.2. To address this limitation, researchers have explored the use of natural polymers as stabilizers. Doost et al. incorporated almond gum into shellac nanoparticles loaded with quercetin to prevent aggregation (Doost et al., 2018). Similarly, Muhammad et al. employed xanthan gum as a

stabilizer for shellac nanoparticles encapsulating cinnamon bark extract (Muhammad et al., 2020). These studies demonstrate the potential of natural polymers to enhance the stability of shellac-based drug delivery systems under acidic conditions.

#### 2.4.2. Locust bean gum

Locust bean gum (LBG) is a natural polysaccharide derived from the endosperm of the carob tree. *Cerotonia siliqua* L. seeds (illustrated in Figure 2.4), is a high-molecular-weight galactomannan. Renowned for its non-toxicity, biocompatibility, and biodegradability, LBG is a versatile material with a wide range of potential applications (Giuliani et al., 2022).



**Figure 2. 4:** Locust bean gum derived from carob fruit

LBG is a galactomannan composed of two sugar units: galactose and mannose. Its structure comprises a linear backbone of (1→4)-linked  $\beta$ -D-mannopyranosyl units with (1→6)-linked  $\alpha$ -D-galactopyranosyl residues branching off (Figure 2.5) (Matar and Andac, 2021). The galactose-to-mannose ratio in LBG typically falls within the range of 1:3.1 to 1:3.9, with mannose constituting 77-78% and galactose accounting for 21-23% of its total composition (Barak and Mudgil, 2014). This distinctive structural arrangement positions LBG as a promising candidate for facilitating nanoparticle uptake by M cells. These specialized epithelial

cells in the gut are known to preferentially interact with mannose residues. Consequently, LBG's high mannose content may enhance nanoparticle uptake through these privileged sites (Braz et al., 2017).

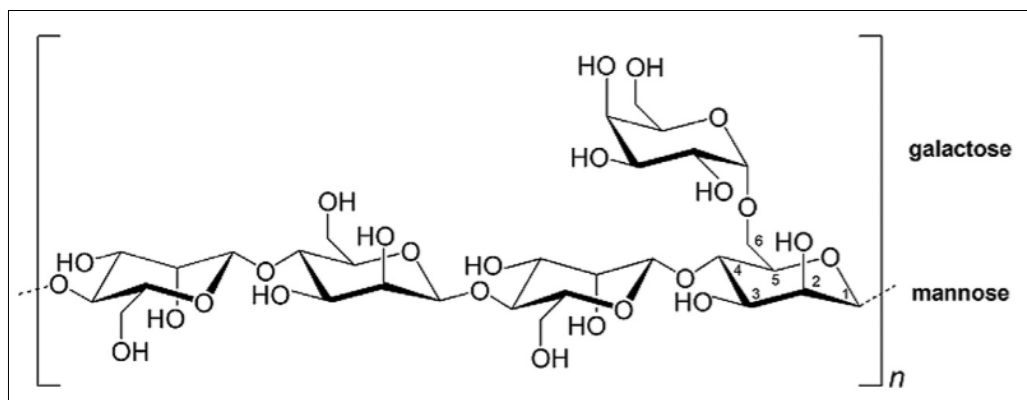


**Figure 2. 5:** Molecular composition of locust bean gum

LBG, a natural gum derived from carob tree seeds, distinguishes itself from synthetic polymers through its accessibility, low toxicity, and affordability (Barak and Mudgil, 2014). Recognized as safe by the FDA (GRAS status), LBG has found widespread applications in the food industry as an emulsifier, stabilizer, thickener, and gelling agent (E410). Moreover, its versatility extends to the pharmaceutical industry, where it serves as an excipient in drug formulations, and the biomedical field (Braz et al., 2018).

Sharma et al. successfully encapsulated zirconium-based nanoparticles using LBG (Sharma et al., 2023). Braz et al. developed nanoparticles composed of LBG and chitosan for oral vaccination, aiming to enhance immune responses (Braz et al., 2017). Jana et al. formulated interpenetrating polymeric network nanocomposites of aceclofenac using chitosan and LBG, cross-linked with glutaraldehyde (Jana and Sen, 2017). These studies highlight the potential of LBG as a versatile and promising material in diverse fields.

### 2.4.3. Ascorbyl palmitate

Ascorbyl palmitate (AP), a fat-soluble derivative of vitamin C, offers superior chemical stability compared to its parent compound (Üner et al., 2005). Known by various names, including L-ascorbic acid 6-hexadecanoate, 6-O-palmitoyl-L-ascorbic acid, palmitoyl L-ascorbic acid, ascorbic acid palmitate, or vitamin C palmitate. AP is synthesized through a chemical reaction involving palmitic acid and ascorbic acid. Its molecular structure, consisting of a 16-carbon saturated fatty acid (palmitic acid) bonded to ascorbic acid, is depicted in Figure 2.6 (Younes et al., 2020).

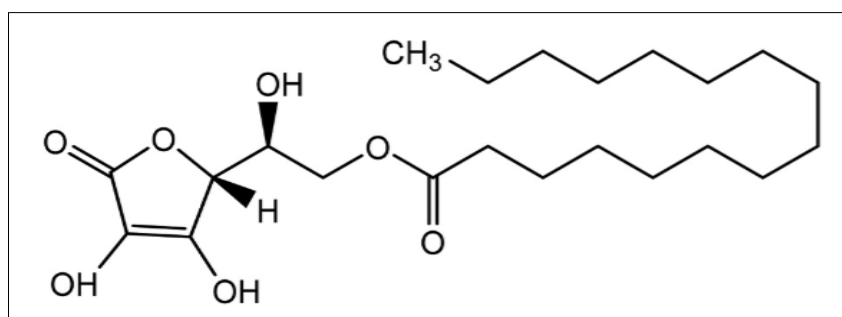


**Figure 2. 6:** Molecular structure of ascorbyl palmitate

AP stands out from other vitamin C derivatives due to its enhanced solubility. AP exhibits amphipathic properties, possessing both hydrophilic and lipophilic characteristics. This dual nature allows AP to dissolve in both aqueous and lipid solutions, with its lipophilic nature predominating (Imran et al., 2024). AP's greater stability compared to ascorbic acid makes it a suitable candidate for incorporation into nanocarriers, addressing challenges such as low bioavailability, poor water solubility, and the need for frequent dosing without compromising therapeutic efficacy (El-Far et al., 2022).

Li et al. demonstrated that incorporating AP into soy phosphatidylcholine liposomes improved their physical stability and core retention ratio by increasing repulsive forces (Li et al., 2021). Amiri-Rigi et al. focused on developing hemp seed oil-in-water nanoemulsions loaded with

ascorbyl palmitate. Their findings revealed that AP significantly enhanced the bioavailability and oxidative stability of the hemp seed oil (Amiri-Rigi et al., 2023).

#### 2.4.4. Hydroxypropyl methylcellulose

Hydroxypropyl methylcellulose (HPMC), a naturally derived biopolymer from cellulose, is classified as non-toxic and safe by the US Food and Drug Administration (FDA) (Chen and Doyle, 2022). As shown in Figure 2.7, HPMC is a propylene glycol ether of methylcellulose. The substituent R in its structure can be a hydrogen atom,  $-\text{CH}_3$ , or  $-\text{CH}_2\text{CH}(\text{CH}_3)\text{OH}$  group. The physical and chemical properties of HPMC are greatly influenced by the amount of methoxy groups, hydroxypropoxy groups, and its molecular weight. (Siepmann and Peppas, 2012).

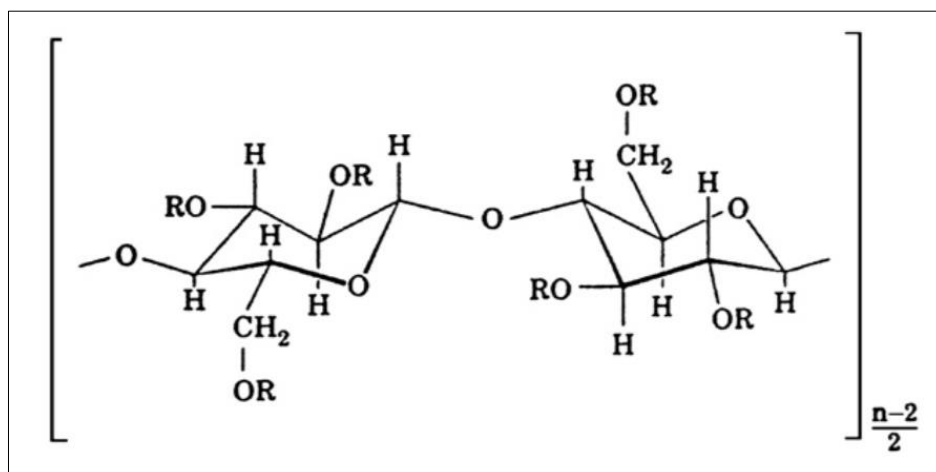


**Figure 2. 7:** Molecular structure of hydroxypropyl methylcellulose

HPMC, a widely used hydrophilic additive, finds applications in diverse fields such as drug delivery, food and pharmaceutical industry as a stabilizer, thickener, and emulsifier. Its water solubility, rheological properties, biocompatibility, and transparency contribute to its versatility (Tundisi et al., 2021; Jayaramudu et al., 2021). Its ability to swell and form a gel layer, controlling drug release rates in matrix systems, makes it a valuable component in controlled-release drug delivery systems. Formulating pH-sensitive nanoparticles, particularly

those incorporating HPMC, is crucial for boosting bioavailability and enhancing oral drug delivery (Mašková et al., 2020).

Yonashiro et al. prepared amorphous glibenclamide nanoparticles using an antisolvent method, with HPMC serving as a stabilizer for dispersion in water (Yonashiro et al., 2018). Tiwari et al. demonstrated that HPMC significantly contributed to the stabilization of zinc sulfide nanoparticles in their formulation. HPMC's role as a green chemical agent facilitated the synthesis of nanoparticles within a polymer-associated matrix, ensuring stability, consistent particle size, and enhanced potential as luminescent markers (Tiwari et al., 2014).

#### 2.4.5. Transcutol®

Transcutol® is a purified form of diethylene glycol monoethyl ether (DEGEE), which is a derivative of ethylene oxide. Transcutol®, known for its low toxicity and ability to dissolve other substances, has a long history of safe use as a solvent in various products, such as , pharmaceuticals, cosmetics, and food (Sullivan et al., 2014). Its molecular formula is  $C_6H_{14}O_3$  and its chemical name is 2-(2-ethoxyethoxy) ethanol (Javadzadeh et al., 2015). Figure 2.8 depicts the chemical structure of Transcutol®.

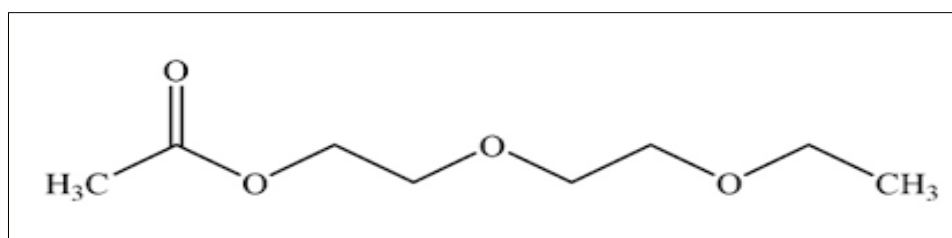


**Figure 2. 8:** Chemical structure of Transcutol®

Transcutol®, a slightly viscous liquid, is miscible with a wide range of co-solvents, surfactants, and oils in liquid form. Its ability to improve the solubility of poorly water-soluble drugs through its surfactant and co-surfactant properties makes it a valuable excipient (Hashemzadeh and Jouyban, 2022). Transcutol®'s, compatibility with both polar and nonpolar solvents,

coupled with its high solubilization power, allows it to dissolve various hydrophilic and lipophilic active substances (Ha et al., 2020). Numerous studies have explored the applications of Transcutol® in drug delivery systems.

Alghananim et al. developed a solid self-nanoemulsifying carrier for deferasirox, incorporating Peceol, Kolliphor EL, and Transcutol® as excipients to enhance solubility. The resulting formulation demonstrated improved solubility and oral bioavailability of deferasirox (Alghananim et al., 2020). Shradha et al. reported that a porous silica-based lipid-solid formulation using Labrasol® and Transcutol® as surfactants in silica lipid hybrid particles enhanced the solubility and dissolution rate of nateglinide (Shradha et al., 2020). Raghuveer and Prameela investigated a self-nanoemulsifying drug delivery system (SNEDDS) for candesartan cilexetil, incorporating Transcutol® as a co-surfactant. Optimized formulations containing 64%w/w Transcutol® exhibited an enhanced dissolution profile compared to the pure drug (Raghuveer and Prameela, 2020).

#### **2.4.6. Aerosil 200**

Aerosil 200, also known as fumed silica, is a commercially available form of colloidal silicon dioxide (SiO<sub>2</sub>) synthesized through a high-temperature reaction involving silicon tetrachloride and oxygen gas (Albertini et al., 2004). As illustrated in Figure 2.9, its chemical structure is characterized by a unique arrangement of silicon and oxygen atoms. While liquid nanoformulations often present challenges such as drug precipitation and degradation, solidification offers a viable solution. By combining the benefits of enhanced solubility and bioavailability from liquid formulations with the advantages of solid dosage forms, including lower production costs, improved stability, precise dosing, and ease of handling, solidified nanoformulations address the limitations of conventional liquid formulations (Chavan et al., 2015). Aerosil 200 has been extensively utilized as a solid carrier in the solidification of various liquid nanoformulations. Bhagwat et al. demonstrated the effective adsorption of liquid self-

microemulsifying drug delivery systems (SMEDDS) by Aerosil 200, leading to successful conversion into a solid form. This adsorption process not only enhances the physical properties of the solid-state SMEDDS but also improves drug release and intestinal permeability, ultimately resulting in enhanced bioavailability (Bhagwat and D'Souza, 2012). Similarly, Sharma et al. reported that solid-state self-nanoemulsifying drug delivery systems (SNEDDS) prepared with Aerosil 200 exhibited superior in vitro dissolution properties and improved pharmacokinetic parameters in rats compared to the marketed formulation (Sharma et al., 2018).

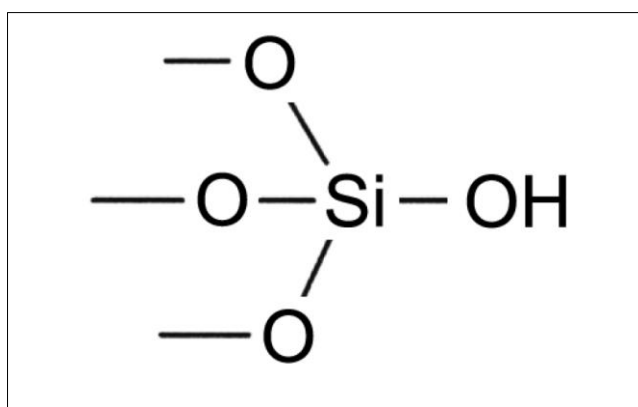


**Figure 2. 9:** Chemical structure of Aerosil 200

## 2.4.7. Curcumin

### 2.4.7.1. Source and physical appearance

Curcumin (CUR), a bioactive polyphenol belonging to the curcuminoid group, is extracted from the rhizomes of *Curcuma longa*, commonly known as turmeric (Figure 2.10A). Turmeric, a member of the Zingiberaceae family, thrives in tropical regions, particularly on the Indian subcontinent and in South Asia (Hussain et al., 2022). Curcuminoids, the active compounds of turmeric, consist of curcumin, demethoxycurcumin, and bisdemethoxycurcumin. Curcumin, the most extensively studied curcuminoid, is an orange-yellow crystalline powder, as depicted in Figure 2.10B (Villegas et al., 2008).

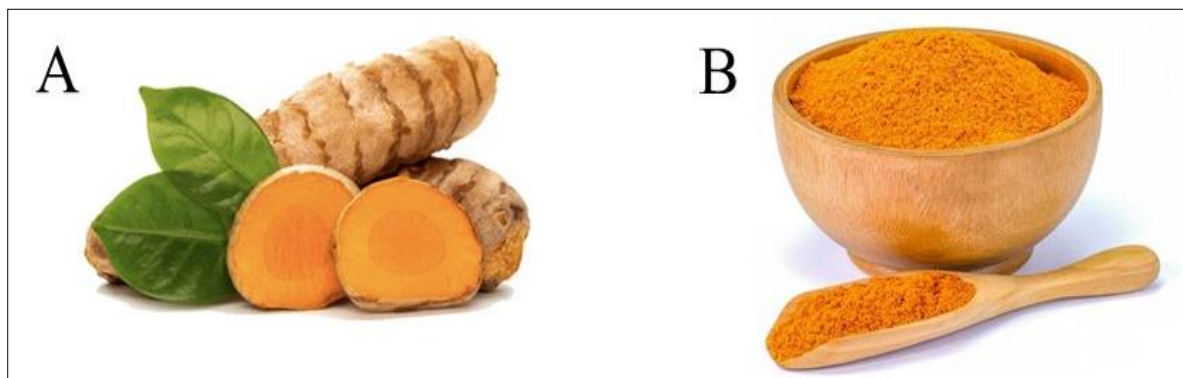


**Figure 2. 10:** (A) Rhizomes of turmeric (*Curcuma longa*) and (B) turmeric powder containing curcumin

#### 2.4.7.2. Structural characteristics of curcumin

Curcumin, a symmetrical molecule also known as diferuloyl methane, possesses a unique structure. The IUPAC name of curcumin is (1E,6E)-1,7-bis(4-hydroxy-3-methoxyphenyl)-1,6-heptadiene-3,5-dione. Its molecular weight is 368.38 grams per mole and its chemical formula is  $C_{21}H_{20}O_6$  (Figure 2.11). The molecule is composed of three distinct components: two aromatic rings containing o-methoxy phenolic groups, joined together by a 7-carbon chain with an  $\alpha$ ,  $\beta$ -unsaturated  $\beta$ -diketone group (Priyadarsini, 2014).

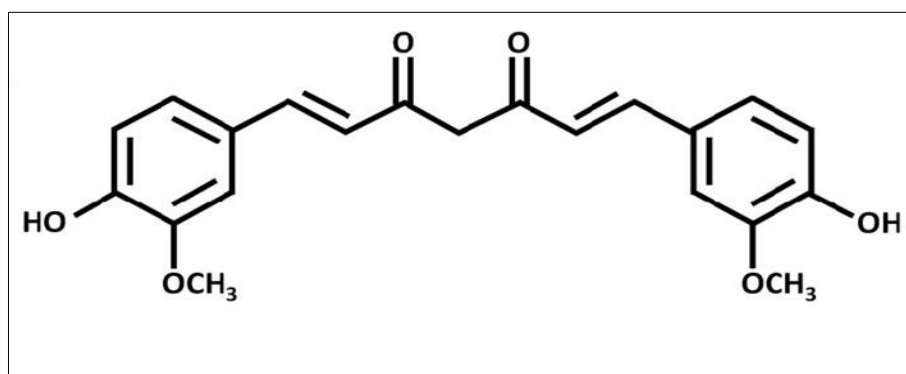


**Figure 2. 11:** Chemical structure of curcumin

#### 2.4.7.3. Solubility of curcumin

Curcumin exhibits poor water solubility, with a reported value of 0.6  $\mu\text{g}/\text{mL}$ , which translates to low bioavailability in the serum (up to 60 nM). However, curcumin demonstrates significant

solubility in organic solvents such as ethanol, dimethyl sulfoxide (DMSO), methanol, acetone, Transcutol®, and chloroform (Górnicka et al., 2023; Ucisik et al., 2013).

#### **2.4.7.4. Biological activities of curcumin**

Curcumin exhibits a wide range of pharmacological properties, including anticarcinogenic, antioxidant, antimicrobial, and anti-inflammatory activities. Furthermore, curcumin has shown antithrombotic, cardioprotective, nephroprotective, antirheumatic, hypoglycemic, and hepatoprotective properties (Ucisik et al., 2013).

Researchers have investigated the therapeutic potential of curcumin-loaded nanoparticles. Joshi et al. formulated self-nanoemulsifying drug delivery systems (SNEDDS) containing curcumin, demonstrating neuroprotective effects in diabetic rats by reducing inflammatory markers such as NF- $\kappa$ B, TNF- $\alpha$ , and IL-6, and improving nerve function (Joshi et al., 2013). Kumari et al. developed nanoparticles composed of polyglycerol-malic acid-dodecanedioic acid and curcumin, exhibiting anticancer activity against breast cancer cells through apoptosis (Kumari et al., 2021). Bhawana et al. prepared nanocurcumin, which demonstrated enhanced water dispersibility and stronger antimicrobial activity compared to free curcumin, particularly against Gram-positive bacteria. TEM analysis revealed the nanoparticle's ability to disrupt bacterial cell walls, leading to cell death (Bhawana et al., 2011). Pontes-Quero et al. reported that curcumin nanoparticles (CUR-NPs) reduced toxicity, improved solubility, and provided sustained release. They exhibited antioxidant and anti-inflammatory properties by reducing reactive oxygen species (ROS) and proinflammatory factors. In vivo biocompatibility studies confirmed their potential for treating oxidative stress and inflammation-related diseases (Pontes-Quero et al., 2021). Abdulmalek et al. found that CUR-NPs significantly restored AKT pathway activity and reduced hepatic inflammation in type 2 diabetes rats. They alleviated oxidative stress and inflammation in hepatic and pancreatic tissues, suggesting their potential as a low-toxicity therapeutic agent for managing T2DM complications (Abdulmalek et al.,

2021). Abdel-Mageid et al. demonstrated that nanocurcumin reduced serum triglycerides, AST, CK-MB, and LDH levels in diabetic rats, indicating its effectiveness in lowering myocardial enzyme activities. Additionally, it increased manganese-superoxide dismutase (Mn-SOD) levels, highlighting its role in mitigating oxidative stress in diabetic heart tissue (Abdel-Mageid et al., 2018). Ganugula et al. reported that CUR-NPs effectively mitigated diabetic nephropathy by improving kidney histopathology and normalizing plasma biomarkers. In combination with insulin, curcumin nanoparticles demonstrated enhanced efficacy in reducing inflammation and hyperglycemia compared to curcumin alone, suggesting their potential for improving DN treatment (Ganugula et al., 2023). Jia et al. found that nanoparticle-encapsulated curcumin reduced diabetic neuropathic pain by decreasing P2Y<sub>12</sub> receptor upregulation on satellite glial cells (SGCs), lowering IL-1 $\beta$  and connexin43 levels, and alleviating mechanical and thermal hyperalgesia in diabetic rats (Jia et al., 2018).

#### **2.4.7.5. Safety and toxicity of curcumin**

Numerous studies have investigated the safety of turmeric and curcumin, encompassing cell culture, animal models, and human subjects. These studies consistently demonstrate the safety of standardized turmeric powder and curcumin extract for human consumption, even at high doses. For instance, oral administration of curcumin at a dosage of 6 grams per day for 4-7 weeks has been deemed safe in humans (Soleimani et al., 2018).

#### **2.4.8. Epigallocatechin-3-gallate**

##### **2.4.8.1. Source and physical appearance**

Tea, made from the leaves and buds of the *Camellia sinensis* plant (Figure 2.12A), is the world's second most popular beverage, after water (Zhong and Shahidi, 2011). It is a rich source of bioactive flavonoids, known for their numerous functional and physiological benefits (Zhong et al., 2012). Catechins, the primary flavonoids found in green tea, constitute 30-40% of its solid components. The major catechins in tea are (-)-epicatechin-3-gallate (ECG), (-)-

epigallocatechin-3-gallate (EGCG), (-)-epicatechin (EC), and (-)-epigallocatechin (EGC). Among these compounds, EGCG is the most prevalent, comprising approximately 59% of the total catechins, while EC 6.4%, ECG 13.6%, and EGC constitutes 19% (Chakrawarti et al., 2016). EGCG in its pure state typically manifests as a white, or cream-colored powder or crystals with no distinct odor. Its precise appearance may vary slightly based on its source and purity, as shown in Figure 2.12B (Bartosikova and Necas, 2018).

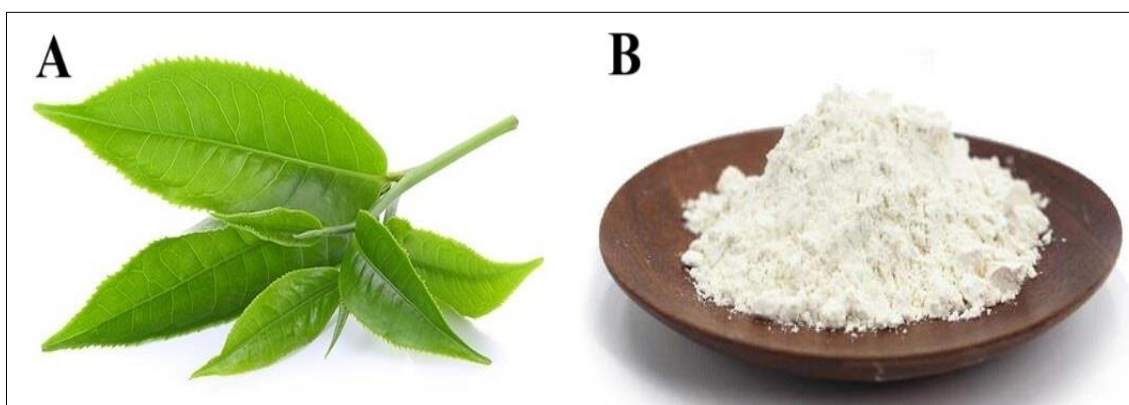


**Figure 2. 12:** (A) Leaves of *Camellia sinensis* and (B) EGCG in powder form

#### 2.4.8.2. Structural characteristics of EGCG

Epigallocatechin-3-gallate, depicted in Figure 2.13, is an ester formed by the combination of epigallocatechin and gallic acid. Its IUPAC nomenclature is (2R,3R)-5,7-dihydroxy-2-(3,4,5-trihydroxyphenyl)-3,4-dihydro-2H-1-benzopyran-3-yl-3,4,5-trihydroxybenzoate, with a chemical formula of  $C_{22}H_{18}O_{11}$  and a molecular weight of 458.37 g/mol (Aree and Jongrungruangchok, 2016). EGCG's structure features three heterocyclic rings, labeled A, B, and C. The trihydroxyl group on ring B and the gallate moiety at the 3' position on ring C are responsible for EGCG's potent antioxidant properties (Davinelli et al., 2012).

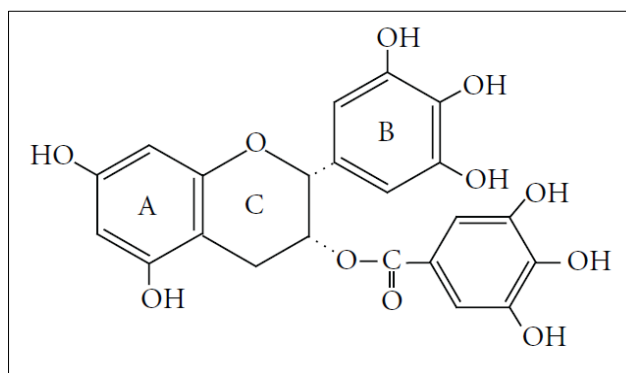


**Figure 2. 13:** Chemical structure of epigallocatechin gallate

#### 2.4.8.3. Solubility of EGCG

EGCG dissolves in water, forming a clear, colorless solution at a concentration of 5 mg/ml. Additionally, it is soluble in methanol, pyridine, ethanol, tetrahydrofuran, and acetone (Mehmood et al., 2022).

#### 2.4.8.4. Biological activities of EGCG

Numerous preclinical and clinical studies have demonstrated the diverse biological and pharmacological properties of epigallocatechin-3-gallate (EGCG), including antidiabetic, anti-inflammatory, antioxidant, nephroprotective, cardiovascular, antimicrobial, anti-allergic, immunomodulatory, and anticarcinogenic effects (Mehmood et al., 2022).

Jeon et al. reported EGCG's effectiveness against antibiotic-resistant strains, particularly those causing skin infections due to gram-negative bacteria like *Pseudomonas aeruginosa* and *Escherichia coli* (Jeon et al., 2014). Zhang et al. investigated the neuroprotective effects of EGCG in an animal model of glaucoma, finding that EGCG consumption reduces retinal ganglion cell degradation by lowering intraocular pressure (Zhang et al., 2021). Xie et al. reported that EGCG can neutralize free radical ions and increase the activity of antioxidant enzymes. Their research showed that EGCG can reduce inflammatory cytokines by influencing notch-1 signaling pathways and the production of reactive oxygen species in human umbilical vein endothelial cells exposed to uric acid (Xie et al., 2015). Gao et al. found that EGCG

protected kidneys in patients with contrast-induced nephropathy by improving kidney function, reducing kidney damage, and decreasing cell death, oxidative stress, and inflammation. (Gao et al., 2016).

Despite these promising effects, the application of EGCG faces limitations, including poor bioavailability, rapid metabolism by liver enzymes, and non-targeting effects on intimal macrophages. Nanotechnology offers a potential solution to overcome these challenges, enhancing EGCG's stability, bioavailability, target specificity, and bioactivities (Zhang et al., 2016). Rolim et al. formulated EGCG nanoparticles using green tea extract, demonstrating significant antibacterial activity against *Salmonella enterica* while exhibiting low cytotoxicity to human keratinocyte cells (Rolim et al., 2019). Similarly, Wu et al. developed  $\beta$ -lactoglobulin and EGCG nanoparticles (E $\beta$ -NPs), enhancing EGCG's chemopreventive effects. E $\beta$ -NPs showed superior inhibition of melanoma and esophageal carcinoma cell proliferation compared to free EGCG (Wu et al., 2017). Es-haghi et al. formulated EGCG/tyrosol-loaded chitosan/lecithin nanoparticles, demonstrating significant therapeutic potential in STZ-induced diabetic mice by reducing fasting blood sugar, oxidative stress, and inflammation, while enhancing liver glutathione levels (Es-haghi et al., 2024). Shariare et al. introduced a novel EGCG and egg phospholipid nanophytosome with enhanced drug loading, physical stability, and anti-inflammatory properties. These nanoparticles, averaging 100-250 nm in size and achieving up to 90% drug loading, demonstrated significant anti-inflammatory activity in a rat model, outperforming both green tea extract and pure EGCG (Shariare et al., 2020).

#### **2.4.8.5. Safety and toxicity of EGCG**

The safety and toxicity of EGCG preparations have been thoroughly assessed through various studies, including dermal, acute, and short-term toxicity evaluations. Research into dermal toxicity has confirmed that EGCG does not irritate the skin. Acute toxicity tests conducted on rats have established an LD50 of 2000 mg/kg, indicating that EGCG has low acute toxicity.

Additionally, short-term toxicity studies have found no significant adverse effects, suggesting that EGCG is safe for consumption at standard dietary levels (Isbrucker et al., 2006).

## **2.4.9. Methods for preparation of biopolymer nanoparticles**

### **2.4.9.1. Emulsification**

Several methods for formulating nanoparticles utilize nano-emulsion templates. Gulotta et al. developed nanoemulsions using polyunsaturated ( $\omega$ -3) oils through a spontaneous emulsification technique. Their study explored how variations in the surfactant-to-oil ratio, oil composition, and co-solvent composition affect the stability and formation of these nanoemulsions. Their findings reveal that fine-tuning these parameters can yield clear and stable nanoemulsions, demonstrating the method's promise for applications in food, personal care, and pharmaceutical industries (Gulotta et al., 2014). In a different approach, Negi et al. employed the hot self-nano-emulsification technique to prepare solid lipid nanoparticles (SLNs) of lopinavir, a drug with poor bioavailability. This method achieved SLNs with optimized particle size and entrapment efficiency, significantly improving lopinavir's oral bioavailability. Their results highlight the effectiveness of the hot self-nano-emulsification technique in enhancing drug delivery (Negi et al., 2013).

### **2.4.9.2. Anti-solvent precipitation**

Anti-solvent precipitation is a flexible method for creating nanoparticles from both polysaccharides and proteins. Kakran et al. successfully fabricated quercetin nanoparticles using anti-solvent precipitation, significantly improving the dissolution rate of this poorly water-soluble drug (Kakran et al., 2012a). Dong et al. demonstrated a similar enhancement in the dissolution rate of spironolactone, a poorly water-soluble diuretic, by preparing nanoparticles through anti-solvent precipitation. The resulting nanoparticles exhibited reduced crystallinity and dissolved 2.59 times faster than the free drug in 0.1 M HCl, significantly improving dissolution rates (Kakran et al., 2012a). Hu and McClements fabricated zein

nanoparticles using a pH-modulated anti-solvent precipitation method, incorporating Tween 80 as a stabilizer. The nanoparticles, featuring a zein core of approximately 78 nm and a 4 nm surfactant shell, exhibited variable surface charges depending on pH. Notably, they remained stable across a broad pH range except between pH 5 and 6.5. However, they were susceptible to aggregation at high ionic strengths and upon heating (Hu and McClements, 2014).

#### **2.4.9.3. Coacervation**

Coacervation involves mixing an aqueous protein solution with an organic solvent, such as acetone or ethanol, to form tiny coacervates. Chirio et al. utilized this technique to develop curcumin-loaded nanoparticles aimed at improving bioavailability. Their method produced nanoparticles under 500 nm in size, with encapsulation efficiencies ranging from 28% to 81%, depending on the specific fatty acid and polymer used. The incorporation of chitosan improved bioadhesion, and preliminary findings suggested promising anticancer effects against colon cancer cells (Chirio et al., 2011). Similarly, Talarico et al. enhanced quercetin bioavailability by creating quercetin-loaded solid lipid nanoparticles (SLNs) using a coacervation method combined with stearic acid and arabic gum. They characterized these SLNs for size, charge, and stability, noting high encapsulation efficiency and controlled release properties, which indicate their potential as an effective quercetin delivery system (Talarico et al., 2021). In another study, Hedayati et al. developed nanoparticles for drug delivery using Bovine Serum Albumin (BSA) and Gum Arabic. They optimized critical parameters such as pH, temperature, and ionic strength, resulting in nanoparticles with a minimum size of 108 nm. Their research identified heating as the most effective stabilization method. The nanoparticles were analyzed using techniques such as PCS, SEM, FTIR, and DSC, demonstrating their potential as effective nanocarriers (Hedayati et al., 2012).

#### **2.4.9.4. Electrospray drying**

Electrospray drying, a versatile technique conducted under ambient conditions, offers advantages such as high yield, single-step processing, cost-effectiveness and high reproducibility. Luo et al. introduced electrospray nanoprecipitation, a novel method combining electrospray with agitated solvent displacement, enabling the production of polymeric nanoparticles with diameters below 100 nm and near-monodispersity. This technique demonstrated significantly smaller particle sizes compared to traditional methods (Luo et al., 2015). Songsurang et al. fabricated doxorubicin-loaded chitosan nanoparticles using electrospray ionization, incorporating tripolyphosphate as a stabilizer. The optimized process resulted in nanoparticles with diameters ranging from 300 to 870 nm and achieved high encapsulation efficiency (63.4–67.9%). These nanoparticles demonstrated a sustained release of doxorubicin over seven hours, underscoring the technique's potential for controlled drug delivery (Songsurang et al., 2011).

In addition to the methods mentioned above, other techniques for preparing biopolymer nanoparticles include inclusion complexation, fluid gel formation, and extrusion (Joye and McClements, 2014).

#### **2.5. Nanostructured lipid carriers**

Nanostructured lipid carriers (NLCs) represent a promising drug delivery system characterized by enhanced stability, drug loading capacity, and the ability to form concentrated dispersions. Pharmaceutical manufacturers have successfully scaled up the production of NLCs through industrial processes. However, the physicochemical properties of NLCs, including solubility, phase transition, bioavailability, particle shape, and size, are significantly influenced by various factors such as excipients, preparation methods, surfactants, and lipid composition. To ensure consistent NLC production, strict adherence to standardized protocols for stirring, melting, mixing, and homogenization is essential (Sharma and Baldi, 2018). The versatility of NLCs is

evident in their successful application across diverse administration routes, including dermal, pulmonary, oral, and ocular.

Patel et al. pioneered the development of a topical NLC-based gel containing aceclofenac for the treatment of inflammation. Employing a combination of stearic acid, pluronic F68, oleic acid, and phospholipon 90G, the researchers fabricated NLCs using a melt-emulsification process followed by low-temperature solidification and high-speed homogenization. The resulting NLC gel exhibited remarkable anti-inflammatory efficacy, characterized by a rapid onset and sustained duration of action, surpassing the performance of commercially available aceclofenac gels (Patel et al., 2012). Cirri et al. found that NLCs significantly improved the oral absorption of drugs, including hydrochlorothiazide, by enhancing their bioavailability, solubility, and stability. Oral formulations based on NLCs demonstrated increased drug encapsulation and sustained drug release, leading to improved therapeutic outcomes in animal studies (Cirri et al., 2018). Patlolla et al. encapsulated celecoxib (Cxb) in NLCs and assessed their pulmonary distribution after nebulization in Balb/c mice. Nebulization of Cxb-NLCs resulted in a fourfold increase in lung tissue concentration compared to free Cxb solution, with slower systemic clearance. The Cxb-NLC formulation exhibited stability and enhanced pulmonary bioavailability, potentially leading to improved patient adherence with reduced dosing frequency (Patlolla et al., 2010). Varela-Fernandez et al. developed lactoferrin-loaded NLCs as a novel therapeutic approach for keratoconus. The NLCs exhibited a particle size of 119.45 nm, PDI of 0.151, and a surface charge of  $-17.50$  mV. Additionally, they demonstrated high entrapment efficiency and loading capacity (up to 75%), controlled release of lactoferrin, stability, non-toxicity, and mucoadhesive properties, suggesting their potential as a controlled-release drug delivery system for keratoconus treatment (Varela-Fernández et al., 2022).

### 2.5.1. Compritol 888 ATO

Compritol 888 ATO, known as glyceryl dibehenate, is a fine, free-flowing powder that appears white or off-white and has a mild odor. This tasteless substance is chemically inert, meaning it does not react with other components in formulations. As a non-swelling wax material, it is frequently used as a lubricant and has the chemical formula  $C_{25}H_{50}O_4$  (Devi and Agarwal, 2019). This waxy, hydrophobic material is a blend of glycerol behenates, comprising 12–18% mono-behenates, 45–54% di-behenates, and 28–32% tri-behenates by weight. It has a melting point ranging from 69 to 74 °C and a hydrophilic-lipophilic-balance (HLB) of 2. Compritol 888 ATO is produced by combining glycerol with behenic acid, a 22-carbon fatty acid, through a chemical reaction called esterification that doesn't require any catalysts (Aburahma and Badr-Eldin, 2014). The molecular structures of glyceryl monobehenate, dibehenate, and tribehenate are illustrated in Figure 2.14.

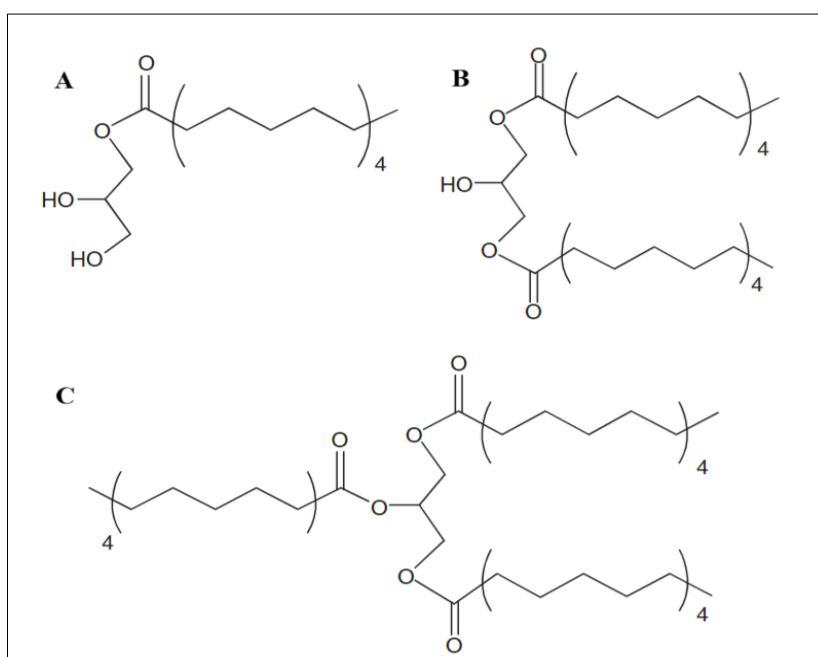


**Figure 2. 14:** Diagrams illustrating the structures of (A) glyceryl monobehenate, (B) glyceryl dibehenate, and (C) glyceryl tribehenate

In the last decade, researchers have explored various methods for utilizing Compritol 888 ATO, in formulation of lipid nanoparticles, hot melt coating, direct compression, melt granulation, controlled release applications, and pelletization (Devi and Agarwal, 2019). Barthelemy et al. investigated the coating capabilities of Compritol® 888 on drug-loaded sugar beads and lactose granules, using theophylline as a tracer to assess prolonged drug release. Their study demonstrated that the hot-melt fluid-bed coating process achieved uniform and consistent coatings, with the amount of Compritol 888 ATO applied directly affecting the drug release rate (Barthelemy et al., 1999). Shah et al. developed oral nanosuspensions of simvastatin, selecting Compritol 888 ATO as the lipid carrier due to its non-polarity and low cytotoxicity. They found that Compritol 888 ATO facilitated high drug entrapment efficiency. The high content of mono-, di-, and triglycerides in Compritol 888 ATO allowed for effective drug solubilization within the lipid matrix, while the less-defined acylglycerol mixture created additional space for drug molecules to be trapped (Shah et al., 2011). Elmowafy et al. formulated thymoquinone (TQ)-loaded NLCs to enhance oral bioavailability, incorporating Compritol 888 ATO and Pluronic F127. Although Compritol 888 ATO contributed to larger particle sizes and reduced stability, it significantly improved TQ's bioavailability by up to 3.97-fold, demonstrating considerable hepatoprotective and antioxidant effects (Elmowafy et al., 2016).

### **2.5.2. Triolein**

Triolein, also referred to as glyceryl trioleate, is a key ingredient in Lorenzo's oil. This symmetrical triglyceride consists of glycerol and three molecules of oleic acid, an unsaturated fatty acid (Figure 2.15). With the chemical formula  $C_{57}H_{104}O_6$ , triolein constitutes between 4% and 30% of olive oil (Thomas, 2000). It is an excellent vehicle for delivering drugs topically in both pharmaceutical and cosmetic formulations, due to its compatibility with biological systems and its ability to maintain the efficacy of products (Shiadeh et al., 2022). In

pharmaceuticals, it finds applications as an antifoaming agent, stabilizing agent, emulsifiable paste, suppository component, lotion ingredient, lubricating agent, emulsifier in aerosol formulations, and an ointment base (Naseri et al., 2015). Triolein has proven to be an effective liquid lipid in numerous NLCs for drug delivery. Zhang et al. demonstrated that triolein notably increased the transfection efficiency of polycation- NLC, matching the performance of Lipofectamine™ 2000. By enhancing the stability and efficacy of the PNLC, triolein plays a vital role in optimizing gene transfer vectors (Zhang et al., 2008). Houacine et al. showed that triolein markedly improved the stability and quality of NLCs by resulting in smaller particle sizes and higher melting points compared to less lipophilic lipids. NLCs incorporating triolein exhibited excellent storage stability, preserving particle size and distribution over time. This underscores triolein's importance as a key lipid for optimizing NLC formulations (Houacine et al., 2020). Kar et al. developed cedrol-loaded NLCs using triolein to boost the antileishmanial activity of cedrol against *Leishmania donovani*. Their formulation of cedrol-loaded NLCs demonstrated enhanced antileishmanial efficacy and selectivity compared to free cedrol. The NLCs showed significant improvements in activity and bioavailability, benefiting both wild-type and drug-resistant strains (Kar et al., 2017).

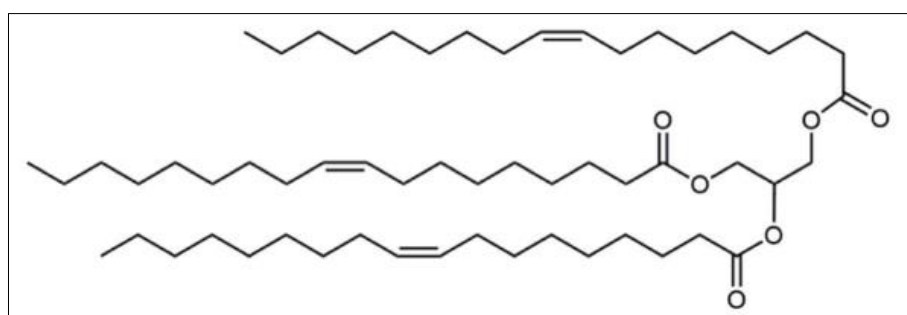


**Figure 2. 15:** Chemical structure of triolein

### 2.5.3. Soybean lecithin

Soybean lecithin is a by-product of soybean oil extraction. It comprises of various phospholipids, including phosphatidic acid, phosphatidylcholine, phosphatidylinositol, and

phosphatidylethanolamine, which impart its distinctive surface-active properties with both hydrophobic and hydrophilic characteristics. With a molecular formula of  $C_{42}H_{80}NO_8P$  and a molecular weight of 758 g/mol, soybean lecithin plays a crucial role in many applications (Ugandar et al., 2015). Figure 2.16 illustrates the chemical structure of soybean lecithin. In the pharmaceutical industry, formulations containing phospholipids offer multiple benefits. They enhance the bioavailability of drugs that have low aqueous solubility or poor membrane penetration. These formulations can also improve or modify drug uptake and release, protect sensitive active ingredients from degradation in the gastrointestinal (GI) tract, reduce GI side effects associated with non-steroidal anti-inflammatory drugs (NSAIDs), and even mask the bitter taste of orally administered medications (Fricker et al., 2010). Ahmaditabar et al. employed soybean lecithin as a lipid monolayer in the formulation of N-acetyl cysteine-loaded hybrid PLGA/lecithin nanoparticles (NPs) using the nanoprecipitation technique (Ahmaditabar et al., 2017). Chan et al. formulated a biodegradable core-shell nanoparticle system that merges the advantages of liposomal and PNPs for controlled drug delivery. They found that incorporating soybean lecithin improved the system's biocompatibility and biodegradability, positioning it as a promising option for scalable drug delivery applications (Chan et al., 2009).

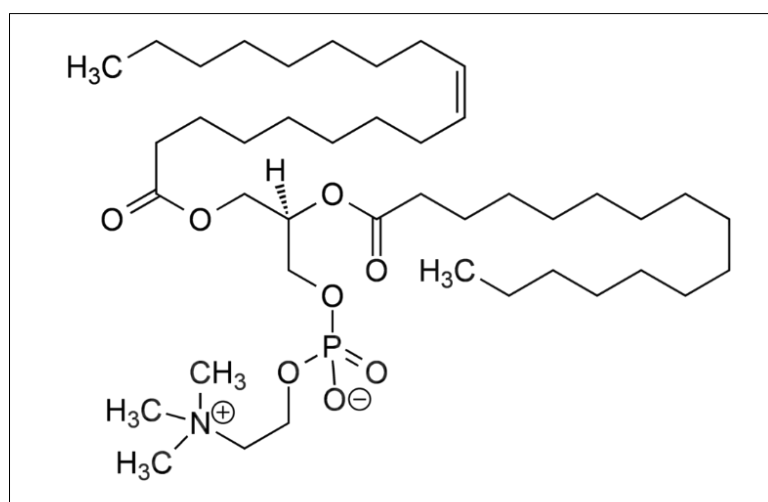


**Figure 2. 16:** Chemical structure of soybean lecithin

#### **2.5.4. Sodium deoxycholate**

Sodium deoxycholate (NaDC) is a bile acid salt synthesized in the human liver from cholesterol. These bile salts play a crucial biological role as emulsifiers for various compounds in the body, including fat-soluble vitamins in the intestine, bilirubin, cholesterol, and lecithin (Kamel et al., 2020). Unlike conventional surfactants, which have a polar head and an alkyl chain, NaDC features a unique steroid structure, as shown in Figure 2.17. This distinctive structure allows NaDC to form crystalline and gel-like coordination complexes (Moheman et al., 2011). Due to its enhanced bioavailability, non-toxic nature, and significant permeation-enhancing abilities, NaDC is highly favored in pharmaceutical research (Abdel-moneum and Abdel-Rashid, 2023). Gagliardi et al. demonstrated the use of NaDC-loaded zein NPs to create a stable colloidal drug delivery system. NaDC significantly contributes to stabilizing the zein NPs, improving their physical properties, and boosting their effectiveness as drug delivery systems (Gagliardi et al., 2018). Cadete et al. created chitosan nanoparticles that incorporated NaDC for use as gene delivery carriers in mucosal administration. NaDC enhanced the stability of the nanoparticles, improved DNA encapsulation, and potentially increased interaction with cell membranes, thereby contributing to greater transfection efficiency (Cadete et al., 2012). Bhattacharjee et al. developed anionic mixed micelles using Tween 80 and NaDC to deliver doxorubicin hydrochloride. NaDC played a vital role in forming these mixed micelles, affecting their structure and properties, and aiding in the binding and delivery of doxorubicin. The anionic nature of NaDC likely improved drug delivery and enhanced anticancer activity (Bhattacharjee et al., 2010).

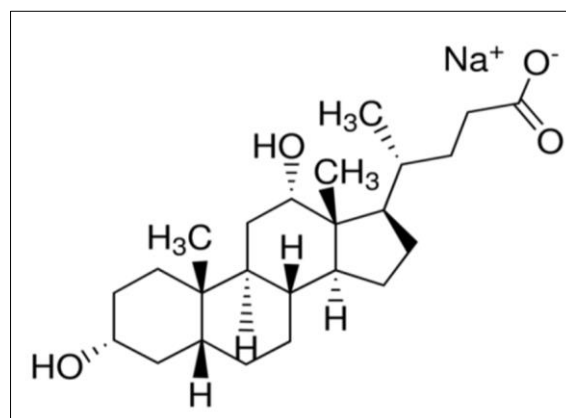


**Figure 2. 17:** Chemical structure of sodium deoxycholate

### 2.5.5. Cetyltrimethylammonium bromide

Cetyltrimethylammonium bromide (CTAB) is a quaternary ammonium surfactant with a positively charged quaternary amine group. This group can be attached to one or two long alkyl chains. The cationic head of CTAB, which is electrostatically paired with a counter anion ( $\text{Br}^-$ ), connects to a hydrophobic alkyl chain consisting of 16 carbon atoms (Carvalho et al., 2022). It has a chemical formula of  $\text{C}_{19}\text{H}_{42}\text{BrN}$  and a molecular weight of 364.45 g/mol. Its chemical structure is shown in Figure 2.18. The widespread use of CTAB is due to its advantageous properties, such as its effective ability to prevent particle aggregation and its affordability as a surfactant (Carvalho et al., 2022). CTAB serves as a cationic surfactant and stabilizer in the preparation of various novel nanoparticles. Liu et al. developed a new cetyltrimethylammonium silver bromide (CTASB) complex for potential nanoformulation applications by reacting silver nitrate with CTAB in an aqueous solution at room temperature (Liu et al., 2007). Cheng et al. successfully created CTAB-coated gold nanoparticles using a two-phase system of toluene and water, where CTAB acted as a phase-transfer stabilizer and catalyst. The CTAB layers on the nanoparticles influenced their interactions, allowing for controlled assembly and spacing (Cheng et al., 2003). Bao et al. examined how CTAB affects chitosan nanoparticles cross-linked with pentasodium triphosphate. They found that adding CTAB reduced the size of the nanoparticles and increased their zeta potential in salt solutions.

The critical micelle concentration of CTAB played a role in the formation of polyelectrolyte-surfactant complexes, which in turn influenced the properties of the nanoparticles. These observations were confirmed by TEM analysis (Bao et al., 2008).

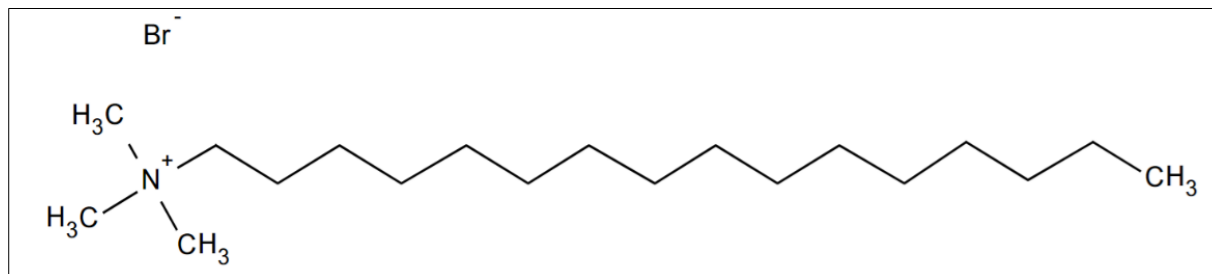


**Figure 2. 18:** Chemical structure of cetyltrimethylammonium bromide

### 2.5.6. *Pueraria tuberosa*

*Pueraria tuberosa* (Roxb. ex Willd.) DC. (Fabaceae), also called Vidarikand or Indian kudzu, is a perennial woody vine belonging to the Fabaceae family. This plant is highly esteemed in both traditional Chinese medicine and Ayurveda. It is characterized by its coiling, climbing, and trailing growth pattern, along with a tuberculated, woody stem, and substantial tuberous roots, as shown in Figure 2.20 (Malviya et al., 2016). *Pueraria tuberosa* thrives in humid climates, monsoon forests, and coastal areas. It is widely distributed throughout India, from the western Himalayas to Sikkim, and can grow at altitudes of up to 4,000 feet in Kumaon. Additionally, it is indigenous to the tropical and subtropical areas of Nepal and Pakistan (Maji et al., 2014b).

#### 2.5.6.1. Scientific classification of *Pueraria tuberosa*

*Pueraria tuberosa*, belongs to the kingdom Plantae and the subkingdom Trachebionta. It is classified under the class Magnoliopsida and the subclass Rosidae. This species falls within the order Fabales and is a member of the Fabaceae family. The genus *Pueraria* DC encompasses this species, which is scientifically recognized as *Pueraria tuberosa* (Bharti et al., 2021).

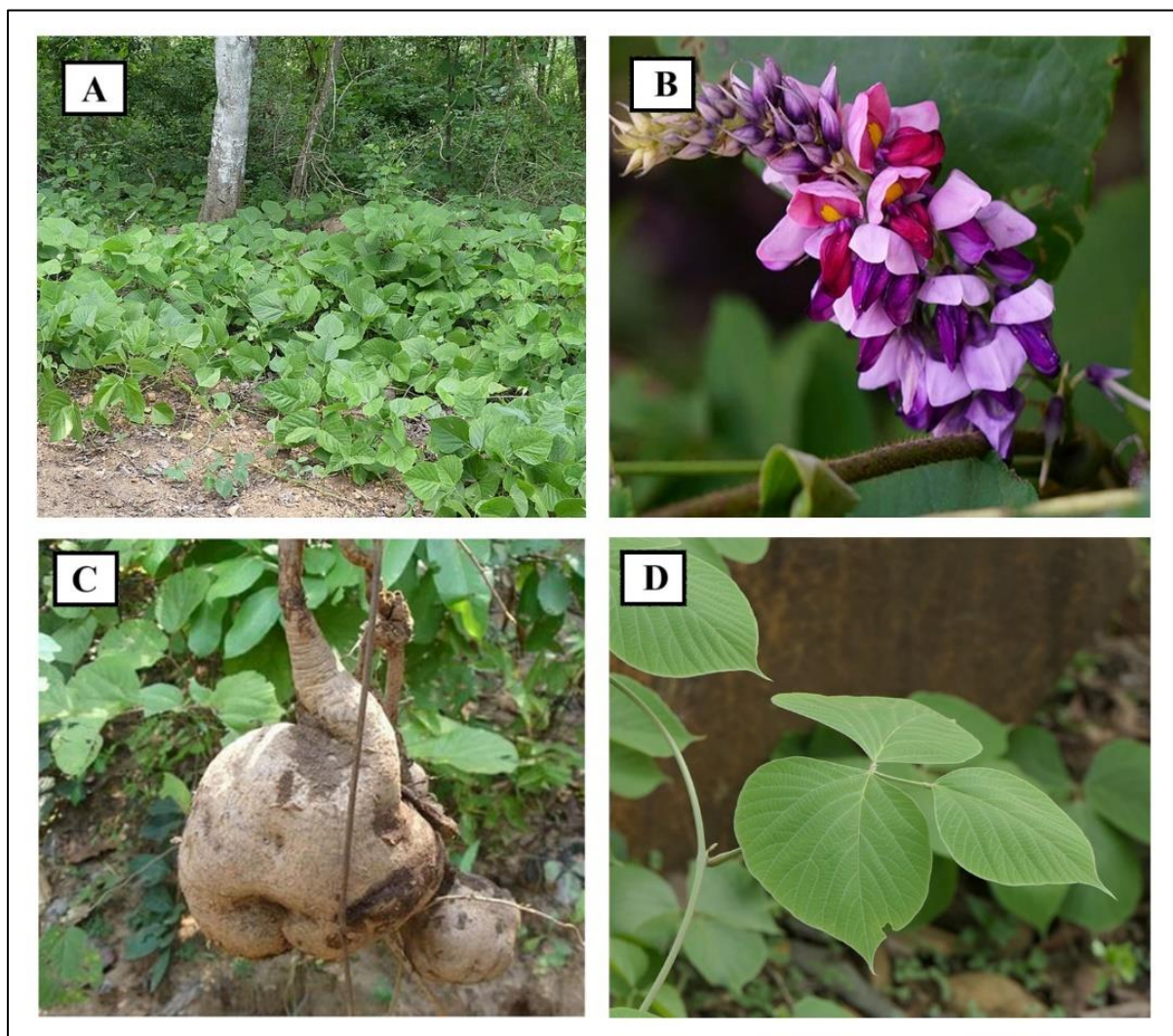


**Figure 2. 19:** *Pueraria tuberosa*: (A) whole plant, (B) flower, (C) tubers, and (D) leaves

#### 2.5.6.2. Phytochemistry of *Pueraria tuberosa* extract

The crude extract of *Pueraria tuberosa* tubers (PTE) (Figure 2.21A) is rich in various bioactive compounds. It contains flavonoids, anthracene, terpenoids, anthocyanidins, carbohydrates, alkaloids, catecholic compounds, glycosides, steroids, hexose sugars, anthraquinone, saponins, coumarins, and volatile oils (Maji et al., 2014a; Bharti et al., 2021). The recent RP-HPLC analysis of the tuber extract identified several flavonoids, including puerarin (8.3%), daidzein (1.7%), and genistein (1.3%) (Maji et al., 2014a). This analysis highlights puerarin (Figure 2.21B) as a major bioactive component derived from the tubers of *Pueraria tuberosa*. The tuber also includes various flavonoid compounds such as quercetin, puerarone, daidzin, biochanin A

and B, genistin, irisolidone, 4-methoxypuerarin, tuberosin, hydroxytuberosone, tectoridin, robinin, and 6-diacetylpuerarin (Scott, 2010; Chauhan et al., 2011; Sawale et al., 2013). Additionally, it contains coumestan, pterocarpanoids, 3-O-methylanhydrotuberosin, and puetuberosanol (Pandey and Tripathi, 2010).

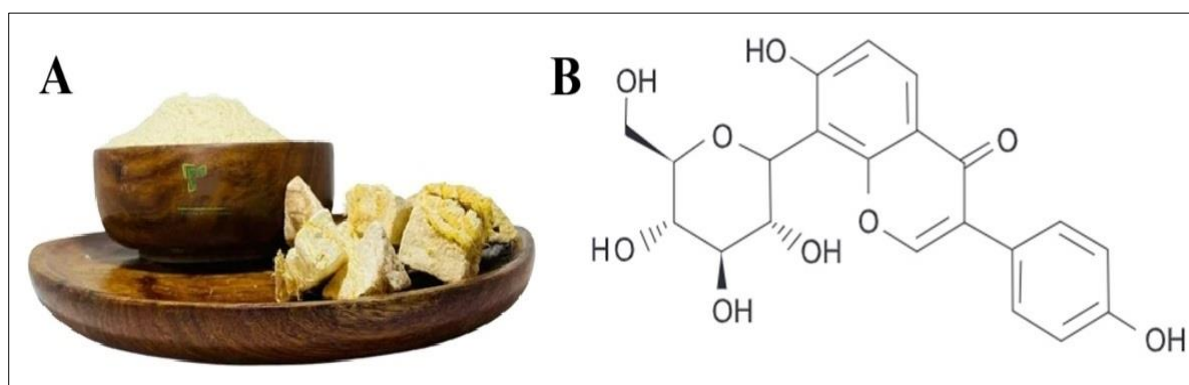


**Figure 2. 20:** (A) *Pueraria tuberosa* extract and (B) chemical structure of puerarin

### 2.5.6.3. Biological activities of *Pueraria tuberosa* extract

*Pueraria tuberosa* extract (PTE) demonstrates significant medicinal value, particularly as a fertility-controlling agent with cardiotoxic, aphrodisiac, galactagogue, and diuretic properties. Experimental studies have shown that PTE exhibits antioxidant, anti-inflammatory, antihyperglycemic, and anti-hyperlipidemic effects. Additionally, it has been found to possess *in vivo* immunomodulatory activities, anti-implantation, hepatoprotective, and anti-fertility effects in male rats (Aruna et al., 2016; Anilkumar et al., 2017).

Numerous studies have highlighted the pharmacological activities of PTE. Nagwani and Tripathi found that administering methanolic PTE orally alleviated cisplatin-induced nephrotoxicity. They observed significant reductions in blood urea nitrogen, serum creatinine, glutathione, and superoxide dismutase (SOD) levels. Additionally, PTE controlled, catalase activity, DNA damage, cellular necrosis, prevented protein coagulation, and tubular swelling compared to the control group. They attributed the nephroprotective effect of the tuber extract to its free radical scavenging activity (Nagwani and Tripathi, 2010). Shukla et al. investigated

the effects of PTE on STZ-induced kidney damage caused by diabetic nephropathy, focusing on hypoxia-related factors. Their findings indicated that PTE treatment significantly reversed these changes in a dose-dependent manner (Shukla et al., 2017). Pandey et al. observed that PTE significantly reduced blood glucose levels and improved liver function in a diabetic rat model induced by alloxan. Additionally, they found that PTE restored the normal structure of liver tissue and suppressed the expression of VEGF and MMP9, suggesting its potential to prevent inflammation and cell death. These findings indicate that PTE may be a promising therapeutic agent for liver diseases (Pandey et al., 2019b). Furthermore, Srivastava et al. investigated the protective effects of PTE on islet stress in diabetic rats induced by STZ. A 10-day treatment with PTE significantly decreased the expression of pro-inflammatory, apoptotic, and hypoxic markers, including TNF- $\alpha$ , MMP-9, HIF-1 $\alpha$ , VEGF, and Caspase-3. Concurrently, PTE increased the levels of antioxidant markers such as SOD and nephrin. These findings suggest that PTE possesses antioxidant, anti-apoptotic, anti-hypoxic, and anti-inflammatory properties, making it a promising candidate for the management of diabetes mellitus (Srivastava et al., 2019). Yadav et al. explored the protective effects of methanolic extract from *Pueraria tuberosa* in rats with alloxan-induced diabetic nephropathy. The extract notably lowered serum urea and creatinine levels, improved kidney function, and boosted antioxidant levels in diabetic rats. Histopathological studies further validated its protective role, indicating that *Pueraria tuberosa* may help prevent renal damage in DN due to its antioxidant properties (Yadav et al., 2019). Satpathy et al. synthesized silver nanoparticles (AgNPs) using PTE, producing spherical particles with notable antioxidant and anticancer properties. These AgNPs demonstrated strong activity against various cancer cell lines, underscoring their potential for cancer therapy (Satpathy et al., 2018).

#### 2.5.6.4. Safety and toxicity of *Pueraria tuberosa* extract

Pandey et al. evaluated the toxicity of *Pueraria tuberosa* water extract (PTWE) in rats. Acute toxicity testing revealed no harmful effects at single doses of 2000 and 5000 mg/kg body weight. However, in repeated dose toxicity studies, mild symptoms appeared at doses of 500 and 1000 mg/kg, while mortality was observed at 2000 mg/kg, with 17% occurring by day 7, 50% by day 14, and 100% by day 21. PTWE showed hepatotoxicity at 500 mg/kg after 14 days, although no kidney toxicity was detected at 1000 mg/kg over 28 days. The LD50 was determined to be greater than 5000 mg/kg, suggesting that lower doses are generally safe (Pandey et al., 2018).

#### 2.5.7. *Pterocarpus santalinus* extract

*Pterocarpus santalinus* L., also known as red sanders or red sandalwood, is a deciduous tree of small to medium size belonging to the Fabaceae family. This species thrives in tropical regions such as India, Taiwan, Sri Lanka, and China (Bulle et al., 2016). In India, it is primarily found in the southern Eastern Ghats, flourishing in dry, rocky terrains at elevations ranging from 150 to 900 meters. Native to the hills of Andhra Pradesh, it also grows in parts of Karnataka and Tamil Nadu, with additional cultivation occurring in West Bengal, Maharashtra, and Odisha (Azamthulla et al., 2015a). *Pterocarpus santalinus*, is considered globally endangered due to excessive exploitation and illegal harvesting, leading to a significant decline in its natural populations. This tree (Figure 2.22) is characterized by its exceptionally hard, dark purple heartwood with a bitter taste. Its bark is blackish brown, measuring 1-1.5 cm in thickness, and deeply furrowed into rectangular plates by vertical and horizontal cracks (Arunakumara et al., 2011).

##### 2.5.7.1. Scientific classification of *Pterocarpus santalinus*

*Pterocarpus santalinus* L., belongs to the kingdom Plantae and the subkingdom Tracheobionta. It is classified under the class Magnoliopsida and the subclass Rosidae. This species falls within

the order Fabales and is a member of the Fabaceae family. The genus *Pterocarpus* Jacq. encompasses this species, which is scientifically recognized as *Pterocarpus santalinus* L.

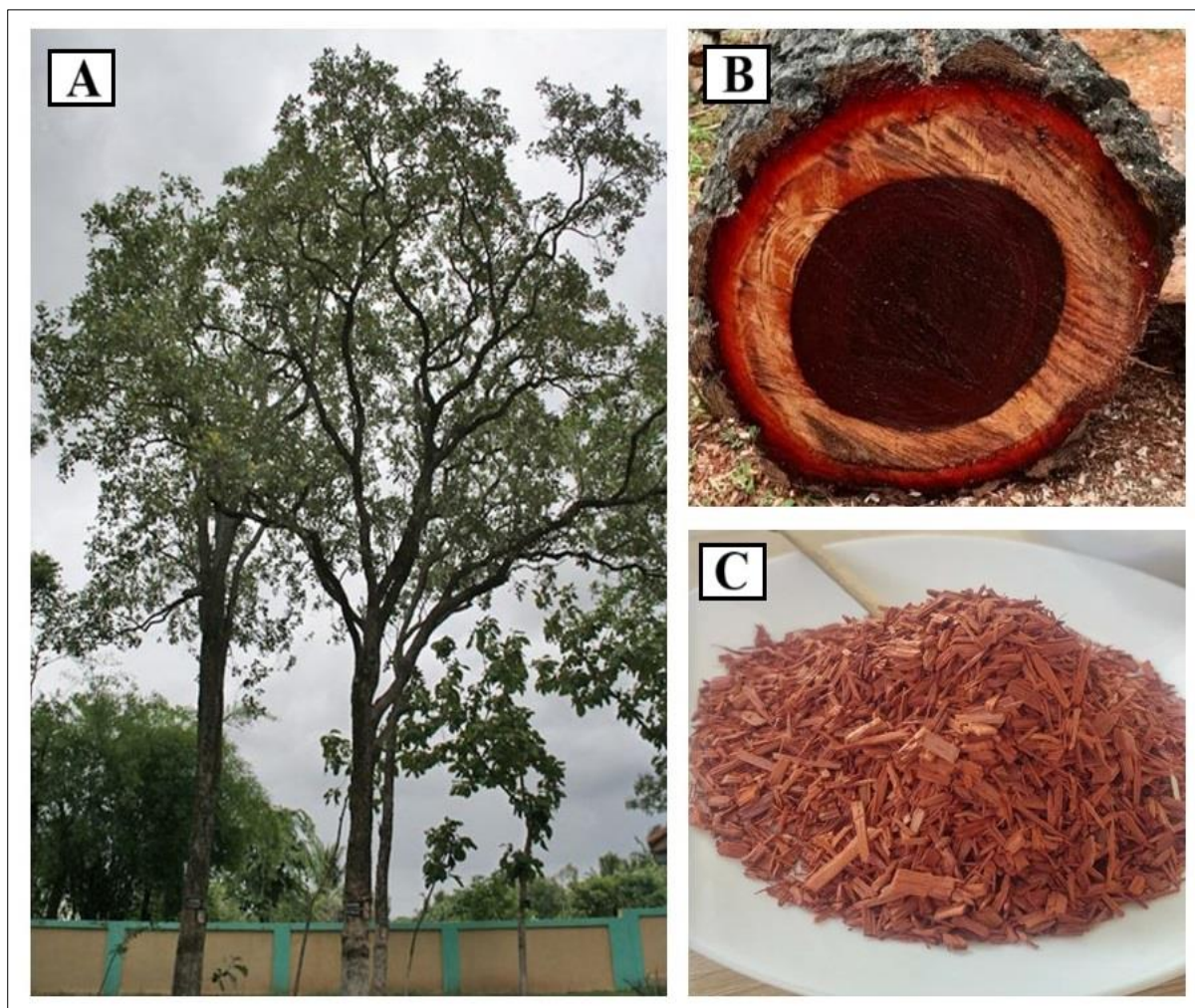


**Figure 2. 21:** *Pterocarpus santalinus*: (A) tree, (B) heartwood, and (C) heartwood chips

#### 2.5.7.2. Phytochemistry of *Pterocarpus santalinus* extract

The phytochemical analysis of *Pterocarpus santalinus* extract (PSE) (Figure 2.23A) revealed the presence of several bioactive compounds, including flavonoids, glycerides, tannins, carbohydrates, anthocyanins, glycosides, phenols, steroids, saponins, and triterpenoids (Azamthulla et al., 2015a). Additionally, the literature has identified several specific components in the heartwood powder, including santalins A and B,  $\beta$ -eudeslols, pterocarpol, cryptomeridol, pterocarptriol, pterocarpodiolones, and ispterocarpolone (Arunakumara et al.,

2011). The presence of various nonspecific compounds has also been reported, including triterpenes, isoflavones, sesquiterpenes, isoflavonoid glucosides, and related phenolic compounds such as lupeol,  $\beta$ -sitosterol, lignans, epicatechin, and pterostilbenes. Pterostilbene, a structural analog of resveratrol, is noted for its greater stability compared to resveratrol (Bulle et al., 2016). Its chemical structure is depicted in Figure 2.23B.

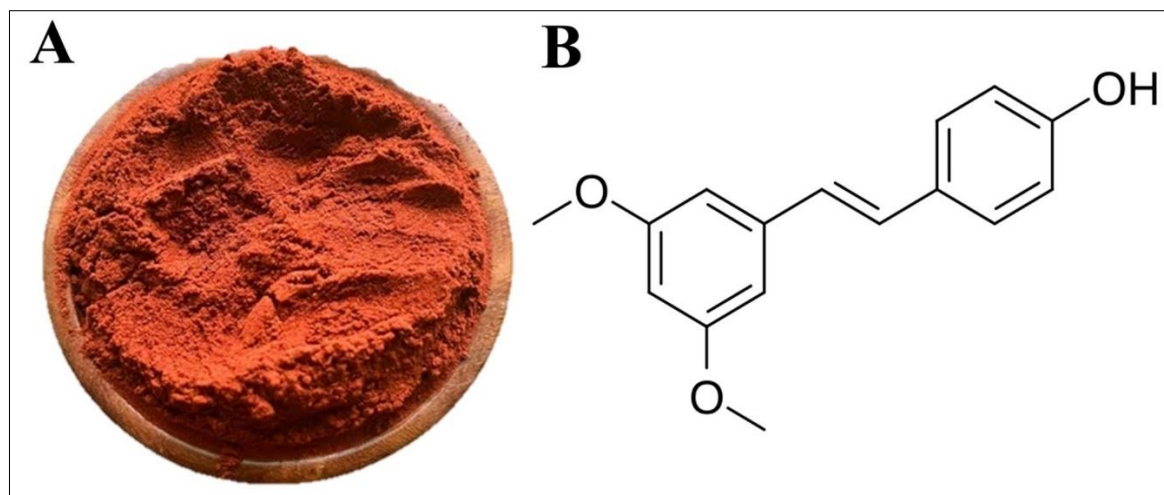


**Figure 2. 22:** (A) *Pterocarpus santalinus* extract and (B) chemical structure of pterostilbene

### 2.5.7.3. Biological activities of *Pterocarpus santalinus* extract

PSE demonstrates a broad spectrum of biological activities. Traditionally, it has been utilized to treat common ailments such as headache, fever, and malaria. Additionally, it has been effective in managing chronic inflammatory conditions like cystitis and bronchitis (Narayan et al., 2005). The wood paste has been utilized for its aphrodisiac, antipyretic, alexiteric, and anthelmintic properties. It has also been employed in treating various conditions, including mental disorders, ulcers, biliousness, and diabetes (Rao et al., 2001).

Halim and Misra investigated the antioxidant, hypoglycemic, hypolipidemic, and nephroprotective effects of *Pterocarpus santalinus* extract (PSE), both alone and in combination with vitamin E, in STZ-induced diabetic rats. PSE demonstrated significant reductions in blood glucose levels, improved glucose tolerance, and decreased lipid

peroxidation, accompanied by increased antioxidant enzyme activity. Furthermore, serum creatinine and urine albumin levels returned to normal, and histological analysis revealed regression of diabetic nephropathy, suggesting the therapeutic potential of PSE for managing diabetic complications (Halim and Misra, 2011). Kondeti et al. investigated the antidiabetic properties of *Pterocarpus santalinus* bark in STZ-induced diabetic rats. Their treatment notably lowered blood glucose levels, enhanced insulin levels, and corrected hyperlipidemia by promoting glycolysis and reducing gluconeogenesis, underscoring its potential for diabetes management (Kondeti et al., 2010). Sri et al. reported the free radical scavenging activity of the ethanolic extract of *Pterocarpus santalinus* (Sri et al., 2021). Stella et al. observed that the methanolic extract of *Pterocarpus santalinus* exhibited antibacterial properties and the ability to scavenge free radicals. The extract was notably effective against *Bacillus subtilis*, with a minimum inhibitory concentration (MIC) of 0.312 mg/ml. Additionally, it showed a concentration-dependent free radical scavenging activity in DPPH, nitric oxide, and total antioxidant assays (Stella et al., 2011). The research assessed the liver-protective properties of *Pterocarpus santalinus* stem bark extracts in rats with CCl<sub>4</sub>-induced liver damage. Both aqueous and ethanol extracts lowered serum markers of liver injury and enhanced total protein levels. The ethanol extract, in particular, provided superior protection according to histological analysis (Manjunatha, 2006). Kwon et al. investigated the cytotoxic and apoptotic effects of PSE on human cervical cancer cells (HeLa). They found that PSE inhibited cell proliferation and triggered apoptosis by promoting the release of mitochondrial cytochrome C and activating caspases (Kwon et al., 2006). Vaishnavi et al. synthesized silver nanoparticles (AgNPs) using an extract from the leaves of *Pterocarpus santalinus*. These spherical AgNPs, ranging in size from 5 to 15 nm, exhibited notable antibacterial and antioxidant properties, suggesting their potential applications in nanomedicine and the enhancement of polymer composites (Vaishnavi et al., 2020). Similarly, Kitture et al. explored the anti-diabetic potential of combining PSE

with ZnO nanoparticles. The resulting conjugate demonstrated a 61.93% inhibition of  $\alpha$ -amylase and  $\alpha$ -glucosidase, significantly surpassing the effectiveness of the individual components. This suggests its promising application in managing diabetes (Rohini et al., 2015).

#### **2.5.7.4. Safety and toxicity of *Pterocarpus santalinus* extract**

Azamthulla et al. assessed the safety of ethanol and chloroform extracts of *Pterocarpus santalinus* heartwood through acute (50-2000 mg/kg) and sub-acute (100, 400, 750 mg/kg) toxicity tests in rats. Both extracts were well tolerated up to 2000 mg/kg in acute tests, showing no significant toxicity or mortality. Sub-acute studies also indicated no adverse effects, confirming that these extracts are safe for both single and long-term therapeutic use (Azamthulla et al., 2013).

### **2.5.8. Methods for preparation of nanostructured lipid carriers**

#### **2.5.8.1. High-pressure homogenization method**

The high-pressure homogenization (HPH) technique is the most widely used method for producing nanoparticles, primarily because of its ease of scale-up, avoidance of organic solvents, and relatively short production time compared to other methods (Lüdtke et al., 2022). Multiple studies have utilized HPH to synthesize NLCs. Souto and Muller successfully incorporated clotrimazole into tripalmitin-based SLNs and NLCs using the HPH technique, resulting in stable, spherical particles with a mean diameter below 200 nm. The HPH method played a crucial role in achieving uniform particle size and long-term stability (Souto and Müller, 2006). Sadiyah et al. conducted a study on the preparation of NLCs loaded with Red Ginger (RG) extract using the HPH method. The findings revealed that the RG-NLCs had particle sizes between 131 and 154 nm, a stable zeta potential ranging from -33.00 to -46.53 mV, and an entrapment efficiency exceeding 98% (Sadiyah et al., 2017). Duong et al. developed NLCs for the sustained-release delivery of ondansetron hydrochloride using a modified cold HPH method. The study achieved an entrapment efficiency of around 90% and demonstrated

prolonged drug release for up to 96 hours in rats. This enhanced systemic exposure and therapeutic effect, making it effective for managing emesis induced by chemotherapy and radiotherapy (Duong et al., 2019).

#### **2.5.8.2. High-shear homogenization and ultrasonication method**

High-shear homogenization (HSH) and ultrasonication are dispersion techniques that do not require organic solvents, excessive amounts of surfactants, or additives (Üner, 2006). Ajiboye et al. investigated the effects of HSH and ultrasonication on the properties of blank and olanzapine-loaded NLCs, focusing on drug loading capacity and release profiles. The optimized NLCs, with particle sizes ranging from 112 to 191 nm, effectively encapsulated olanzapine and achieved 89% drug release within 24 hours at pH 7.4 (Ajiboye et al., 2021). Rosli et al. formulated NLC) encapsulating *Zingiber zerumbet* oil using ultrasonication. The ZZ-NLC formulation had an average particle size of 97 nm, PDI of 0.19, zeta potential of -39.9 mV, and an encapsulation efficiency (EE) of 90% (Rosli et al., 2015). Ma et al. developed NLCs encapsulating lemongrass oil using ultrasonication to protect its aroma under high-temperature conditions. The Lemongrass-NLC formulation exhibited an average particle size of 44 nm, PDI of 0.28, zeta potential of -43 mV, and EE of 82% (Ma et al., 2021).

#### **2.5.8.3. Solvent emulsification evaporation technique**

This method enables the creation of extremely small particle sizes with a low lipid content (5%) compared to the organic solvent. Moreover, it prevents thermal stress, making it suitable for incorporating highly heat-sensitive drugs (Parhi and Suresh, 2012). Jia et al. successfully developed silybin-loaded NLCs using emulsion evaporation and solidification techniques. Differential scanning calorimetry (DSC) and X-ray diffraction (XRD) analyses revealed that liquid lipids disrupt the crystallization of solid lipids. This disruption allows for the control of the release rate by adjusting the liquid lipid content (Jia et al., 2010). Shirazi et al. developed NLCs containing SN38, an active metabolite of irinotecan, with a mean size of 140 nm and

81% entrapment effectiveness. The NLCs dramatically improved cytotoxicity against U87MG glioma cells compared to free SN38 and displayed efficient cellular penetration, indicating their potential as a new glioblastoma therapy (Shirazi et al., 2021). Khan et al. created stable NLCs for tacrolimus to solve issues with its low solubility and first-pass metabolism. Optimized NLCs with particle sizes of around 70 nm and high drug entrapment efficiency (87-94%) demonstrated considerably improved and prolonged drug release compared to oral suspension (Khan et al., 2016).

#### **2.5.8.4. Microemulsion method**

Gasco et al. originally developed and optimized the microemulsion technique for producing SLN, a method that has since been adapted and modified by various research groups (Gasco, 1993). Lin et al. incorporated liquid oil into a solid lipid matrix using an oil-in-water microemulsion technique to compare SLNs and NLCs. They observed that NLCs had a broader size range (approximately 25 to 120 nm) compared to SLNs (around 42 nm) and exhibited imperfect crystallization. This finding suggests that the microemulsion method effectively produces NLCs with enhanced encapsulation capacity (Lin et al., 2007). Joshi and Patravale formulated a NLC-based topical gel for delivering celecoxib to treat inflammation. Using the microemulsion template technique, they prepared and characterized the NLCs for size and morphology. In both pharmacodynamic and skin permeation studies, the NLC gel exhibited higher drug encapsulation efficiency, a faster onset of action, and prolonged activity compared to a micellar gel (Joshi and Patravale, 2008). In another study, Joshi and Patravale developed a valdecoxib-loaded NLC gel aimed at achieving rapid onset and sustained release. Prepared using similar microemulsion techniques, the gel demonstrated high encapsulation efficiency and desirable properties, delivering extended activity for up to 24 hours in pharmacodynamic evaluations (Joshi and Patravale, 2006).

## 2.6. Streptozotocin

STZ-induced diabetes serves as a valuable model for examining the development of diabetes and its related complications in experimental animals, as it closely mimics the biochemical, structural, and functional changes observed in human diabetes (Eleazu et al., 2013). The diabetogenic effects of STZ are dose-dependent, with appropriate doses varying across species. Lower doses may fail to induce diabetes, while higher doses can lead to animal mortality. Optimizing STZ dosage based on body weight is essential to achieve satisfactory diabetes induction with minimal mortality (Goyal et al., 2016). Akbarzadeh et al. reported that intravenous administration of STZ at 60 mg/kg body weight effectively induced diabetes in rats within three days by selectively targeting and destroying  $\beta$  cells (Akbarzadeh et al., 2007). STZ administration results in hyperglycemia, polyuria, macroproteinuria, and a decrease in glomerular filtration rate (GFR), making STZ-induced diabetic rat models widely used for simulating human diabetic nephropathy (Osicka et al., 2000). Fernandes et al. found that a single intraperitoneal injection of STZ at 65 mg/kg body weight effectively produced diabetic nephropathy in animals (Fernandes et al., 2016). Additionally, Hongmei et al. demonstrated that STZ-induced diabetes leads to renal and vascular dysfunctions, with significant effects on signaling mechanisms in the later stages of the disease (Chen et al., 2005).

## 2.7. Glibenclamide

Glibenclamide (GLI), also known as glyburide, is a widely prescribed oral antidiabetic medication. It is a sulfonylurea compound with IUPAC name 5-chloro-N-[2-[4-[[[(cyclohexylamino)carbonyl]-amino]-sulfonyl]-phenyl]-ethyl]-2-methoxybenzamide, and its chemical structure is illustrated in Figure 2.19. GLI primarily functions by stimulating insulin release from pancreatic beta cells, thereby lowering blood sugar levels in hyperglycemic conditions (Pandarekandy et al., 2017). Beyond its antidiabetic properties, GLI has exhibits

platelet aggregation inhibitor, anti-nociceptive, and anti-tumor activity. Additionally, GLI is known to induce the release of nitric oxide, which is associated with its stimulatory effect on endothelial Ca<sup>2+</sup> levels and subsequent endothelium-dependent relaxation. Antioxidant studies suggest that GLI may counteract oxidative stress mediated by reactive oxygen species (Rabbani et al., 2010). The prevalence of GLI as a standard drug can be attributed to its proven effectiveness in managing diabetes, its well-characterized mechanism of action, and its suitability for comparative research. Ahmadi et al. examined the impact of ginger on oxidative stress markers in diabetic rats induced with STZ, utilizing GLI as a standard drug at a dosage of 1 mg/kg for 30 days (Ahmadi et al., 2013). Gutiérrez et al. similarly assessed the antidiabetic activity of selenium nanoparticles, synthesized from a combination of luteolin and diosmin, on STZ-induced diabetes in mice, employing GLI as a standard drug at a dosage of 5 mg/kg (Gutiérrez et al., 2022). Guo et al. likewise utilized GLI as a standard drug (0.1 mg/kg) to evaluate the antidiabetic effects of *Fritillaria cirrhosa* gold nanoparticles on STZ-induced diabetic rats for 28 days (Guo et al., 2020).

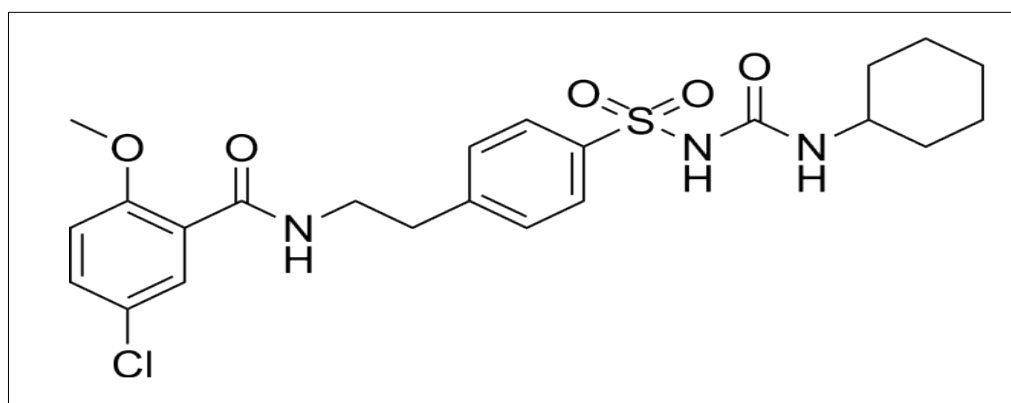


**Figure 2. 23:** Chemical structure of glibenclamide

# **Chapter III**

## **Objectives & Plan of Study**

### 3. OBJECTIVES AND PLAN OF STUDY

#### 3.1. Objectives

The objectives of the research were:

- 1) To formulate a nanoformulation utilizing a carbohydrate polymer coacervation system that incorporates curcumin (CUR) and epigallocatechin gallate (EGCG), alongside a nanostructured lipid carrier system containing *Pueraria tuberosa* extract (PTE) and *Pterocarpus santalinus* extract (PSE), and to conduct their physical characterization.
- 2) To establish a diabetic and nephropathic animal model using streptozotocin (STZ) and confirm the induction of these conditions through histopathological examination of pancreatic and kidney tissues.
- 3) To administer both free and nanoformulated drugs to nephropathic animals over a 60-day period, subsequently assessing therapeutic efficacy by measuring fasting blood glucose, serum creatinine, albumin, and blood urea nitrogen levels.

#### 3.2. Plan of study for curcumin and epigallocatechin gallate coacervated nanoparticles

- Preparation of nanoparticles using the anti-solvent precipitation method, including shellac and locust bean gum coacervated combined drugs (CUR+EGCG) nanoparticles (CESL-NP), as well as single drug nanoparticles for curcumin (CUR) only (CSL-NP) and epigallocatechin gallate (EGCG) only (ESL-NP)
- Development of an RP-HPLC method for the simultaneous quantification of CUR and EGCG in CESL-NP.
- Determination of drug loading (%) and entrapment efficiency (%) of CSL-NP, ESL-NP, and CESL-NP.
- Morphological characterization of CESL-NP utilizing dynamic light scattering (DLS), atomic force microscopy (AFM), field emission scanning electron microscopy (FESEM), and transmission electron microscopy (TEM) analysis.

- Examination of interactions between the drug and other excipients used in the formulation by fourier transform infrared spectroscopy (FTIR).
- Physicochemical characterization of CESL-NP using x-ray diffraction (XRD) and differential scanning calorimetry (DSC) techniques.
- Evaluation of the solubility of free CUR and CESL-NP through solubility studies.
- *In vitro* drug release study of CESL-NP in different release media, including simulated gastric fluid (SGF, pH 1.2), which mimics the acidic environment of the stomach, and simulated intestinal fluid (SIF, pH 7.4), which represents the slightly alkaline pH of the small intestine.
- Assessment of CESL-NP particle size, zeta potential and polydispersity index during stability study after 90 days of storage.

#### ***In-vivo studies***

- Development of a diabetic and nephritic animal model through a single dose of STZ injection.
- Evaluation of the antidiabetic potential of free drugs (CUR and EGCG) and nanoformulated drugs (CSL-NP, ESL-NP and CESL-NP) by measuring fasting blood glucose levels and calculating the percentage inhibition of blood glucose.
- Assessment of the nephroprotective potential of free drugs (CUR and EGCG) and nanoformulated drugs (CSL-NP, ESL-NP, and CESL-NP) by analyzing kidney size, kidney weight, kidney hypertrophy index, serum creatinine, albumin, and blood urea nitrogen levels.
- Histological examination of thin sections of pancreatic and kidney tissues from untreated mice, as well as those treated with free drugs (CUR and EGCG) and nanoformulated drugs (CSL-NP, ESL-NP, and CESL-NP).

### Statistical analysis

- To analyze the data statistically, a one-way analysis of variance (ANOVA) was employed. This statistical method is used to compare the means of multiple groups. Following the ANOVA, Dunnett's t-test was conducted to identify specific differences between the experimental groups and the control group.

### 3.3. Plan of study for *Pueraria tuberosa* and *Pterocarpus santalinus* extracts co-encapsulated nanoparticles

- Preparation of nanostructured lipid carriers (NLCs) containing combined plant extracts (PTE+PSE-NLC) and single plant extracts (PTE-NLC and PSE-NLC) using the hot high-pressure homogenization method.
- Development of an RP-HPLC method for the simultaneous estimation of PTE and PSE in the formulated (PTE+PSE)-NLC.
- Determination of drug loading (%) and entrapment efficiency (%) of PTE-NLC, PSE-NLC, and (PTE+PSE)-NLC.
- Morphological characterization of (PTE+PSE)-NLC using DLS, AFM, FESEM, and TEM analysis.
- Examination of interactions between plant extracts and other excipients used in the formulation by FTIR.
- Physicochemical characterization of (PTE+PSE)-NLC using XRD and DSC techniques.
- *In vitro* drug release study of (PTE+PSE)-NLC in different release media, including simulated gastric fluid (SGF, pH 1.2), which mimics the acidic environment of the stomach, and simulated intestinal fluid (SIF, pH 7.4), which represents the slightly alkaline pH of the small intestine.

- Assessment of (PTE+PSE)-NLC particle size, zeta potential and polydispersity index during stability study after 90 days of storage.

#### ***In-vivo studies***

- Development of a diabetic and nephritic animal model through a single dose of STZ injection.
- Evaluation of the antidiabetic potential of plant extracts in free form (PTE and PSE) and nanostructured lipid carriers (PTE-NLC, PSE-NLC, and PTE+PSE-NLC) by measuring fasting blood glucose levels and calculating the percentage inhibition of blood glucose.
- Assessment of the nephroprotective potential of plant extracts in free form (PTE and PSE) and nanostructured lipid carriers (PTE-NLC, PSE-NLC, and PTE+PSE-NLC) by analyzing kidney size, kidney weight, kidney hypertrophy index, serum creatinine, albumin, and blood urea nitrogen levels.
- Histological examination of thin sections of pancreatic and kidney tissues from untreated mice, as well as those treated with free plant extracts (PTE and PSE) and nanostructured lipid carriers (PTE-NLC, PSE-NLC, and PTE+PSE-NLC).

#### **Statistical analysis**

- To analyze the data statistically, a one-way analysis of variance (ANOVA) was employed. This statistical method is used to compare the means of multiple groups. Following the ANOVA, Dunnett's t-test was conducted to identify specific differences between the experimental groups and the control group.

# **Chapter IV**

## **Studies on curcumin and epigallocatechin gallate- loaded nanoparticles**

## 4. STUDIES ON CURCUMIN AND EPIGALLOCATECHIN GALLATE-LOADED NANOPARTICLES

### 4.A. MATERIALS AND METHODS

#### 4.A.1. Materials

##### 4.A.1.1. Chemicals and reagents used for the study

**Table 4. 1:** List of chemicals with their respective sources used in the study

Sl. No.	Chemical name	Source
1)	Acetonitrile	Merck Life Science, Bengaluru, India
2)	Aerosil 200	Sisco Research Laboratories, India
3)	Ammonia	Merck Life Science, Bengaluru, India
4)	Ascorbyl palmitate	Sigma-Aldrich Co, St Louis, MO, USA
5)	Citric acid	Merck Life Science, Bengaluru, India
6)	Curcumin	Sigma-Aldrich Co, St Louis, MO, USA
7)	Transcutol®	Loba Chemie, Mumbai, India
8)	Epigallocatechin gallate	Sigma-Aldrich Co, St Louis, MO, USA
9)	Ethanol	Merck Life Science, Bengaluru, India
10)	Ethyl acetate	Merck Life Science, Bengaluru, India
11)	Glibenclamide	HiMedia Laboratories, Mumbai, India
12)	Hydrochloric acid	Merck Life Science, Bengaluru, India
13)	Hydroxypropyl methylcellulose	Loba Chemie, Mumbai, India
14)	Locust bean gum	Sigma-Aldrich Co, St Louis, MO, USA
15)	Methanol	Merck Life Science, Bengaluru, India
16)	Orthophosphoric acid	HiMedia Laboratories, Mumbai, India
17)	Potassium dihydrogen orthophosphate	Merck Life Science, Bengaluru, India

18)	Potassium dihydrogen phosphate	Merck Life Science, Bengaluru, India
19)	Shellac	Sigma-Aldrich Co, St Louis, MO, USA
20)	Sodium chloride	HiMedia Laboratories, Mumbai, India
21)	Sodium citrate dihydrate	Merck Life Science, Bengaluru, India
22)	Sodium hydroxide	HiMedia Laboratories, Mumbai, India
23)	Streptozotocin	Sigma-Aldrich Co, St Louis, MO, USA
24)	Sulphuric acid	HiMedia Laboratories, Mumbai, India

#### 4.A.1.2. Instruments used for the study

**Table 4. 2:** List of all the equipment and instruments used in the study

Sl. No.	Instrument name	Source
1)	0.45 $\mu\text{m}$ syringe filter	Millipore, Merck, Germany
2)	Atomic force microscope	Bruker Dimension Icon Innova AFM, USA
3)	Bath sonicator	Trans-O-Sonic, Mumbai, India
4)	Blood glucometer	Accuchek Guide, Roche Diagnostics, Germany
5)	BOD incubator shaker	BOD-INC-1S, Incon, India
6)	Cold centrifuge	Rota 4R-V/FM, Plastocrafts, India
7)	Disposable syringe	Hindustan Syringes and Medical Devices, Ltd., Haryana, India
8)	Differential scanning calorimeter	DSC Q2000, TA Instruments, USA
9)	Digital pH meter	DBK instruments, Mumbai, India
10)	Electronic weighing balance	Sartorius Corporate Administration, Otto-Brenner-Straße 20, Goettingen, Germany
11)	Field emission scanning electron microscopy	Quanta 250 FEG-SEM, FEI, Hillsboro, USA
12)	Freezer (-80 °C)	New Brunswick Scientific, Eppendorf House, Arlington Business Park, Stevenage, UK
13)	FTIR spectrometer	IR Affinity 1, Shimadzu, Japan

14)	High performance liquid chromatography (HPLC)	Agilent 1260 series, Agilent, USA
15)	High speed homogenizer	IKA Laboratory Equipment, Model T10B Ultras-Turrax, Staufen, Germany
16)	Light microscope	Zeiss Axio Imager 2, Germany
17)	Magnetic stirrer	Remi Sales & Engineering Ltd, Kolkata, India
18)	Particle size and zetasizer	Zetasizer nano ZS 90, Malvern Zetasizer Limited, Malvern, UK
19)	Transmission electron microscope	Tecnai G2 TF20-ST, FEI, Hillsboro, USA
20)	UV visible spectrometer	Shimadzu UV-1800, Shimadzu, Japan
21)	Vacuum oven	Thermo Fisher Scientific, Waltham, MA, USA
22)	Vortex machine	CM101 cyclomixer, Remi, India
23)	Water bath	Remi, India
24)	X-ray diffractometer	X'Pert Pro, PANalytical, Almelo, Neitherlands

#### 4.A.2. Methods

##### 4.A.2.1. Preparation procedures for buffers and reagents used in the study

###### 4.A.2.1.1. Preparation of enzyme-free simulated gastric fluid buffer at pH 1.2

Simulated gastric fluid (SGF) buffer was prepared following the United States Pharmacopoeia (USP) (Volume 1) guidelines. SGF buffer was prepared by dissolving 2 grams of NaCl and 7 mL of conc. HCl in 800 mL of Milli-Q water. The mixture was then stirred using a magnetic stirrer until all components were completely dissolved. Next, the pH of the solution was adjusted to 1.2 using either sodium hydroxide or hydrochloric acid, as needed. Finally, Milli-Q water was added to bring the final volume up to 1000 mL.

###### 4.A.2.1.2. Preparation of enzyme-free simulated intestinal fluid buffer at pH 7.4

Simulated intestinal fluid (SIF) buffer was prepared following the USP (Volume 1) guidelines. To make 1000 mL of SIF buffer, 6.8 g of potassium dihydrogen orthophosphate were dissolved

in 800 mL of Milli-Q water. The mixture was then stirred using a magnetic stirrer until the potassium dihydrogen orthophosphate was completely dissolved. Next, the pH of the solution was adjusted to 6.8 using either sodium hydroxide or orthophosphoric acid. Finally, Milli-Q water was added to bring the final volume up to 1000 mL.

#### **4.A.2.1.3. Preparation of citrate buffer at pH 4.5**

To prepare 100 mL of citrate buffer, 1.204 grams of sodium citrate dehydrate and 1.134 grams of citric acid were weighed and transferred into a 100 mL volumetric flask. The chemicals were then dissolved completely in 50 mL of double distilled water. More double distilled water was added to the flask until the final volume reached 100 mL. Finally, the pH of the solution was adjusted to 4.5 using a pH meter.

#### **4.A.2.2. Synthesis of ammonium salt of hydrolyzed shellac**

A 2% (w/v) sodium hydroxide solution was used to partially hydrolyze shellac at 30 °C for one hour. The hydrolysis reaction was then stopped by neutralizing the mixture with 2 N sulphuric acid. This caused the hydrolyzed product to precipitate, which was then washed thoroughly with water and dried under vacuum at 30 °C. The hydrolyzed shellac was subsequently mixed with a 28% (w/v) ammonia solution and dried at 50 °C (Limmatvapirat et al., 2005).

#### **4.A.2.3. Synthesis of colloidal complex coacervate nanoparticles (CSL, ESL, and CESL)**

Colloidal CSL, ESL, and CESL complex coacervate nanoparticles were fabricated using a modified anti-solvent precipitation technique inspired by the methodologies of Patel et al. and Doost et al. (Patel et al., 2011; Doost et al., 2019). Three different nanoformulations—CSL-NP, ESL-NP, and CESL-NP—were synthesized, each containing 250 mg of CUR, 250 mg of EGCG, and a combination of 125 mg CUR and 125 mg EGCG, respectively. The lipid phase was prepared by dissolving CUR, EGCG, the CUR+EGCG mixture, and ascorbyl palmitate (AP) in a 1:1 (v/v) mixture of transcutool®-ethanol. This mixture was gently stirred magnetically

at 40°C until a uniform solution was obtained. For the aqueous phase, 63 mg of hydrolyzed shellac, 375 mg of locust bean gum (LBG), and 25 mg of hydroxypropyl methylcellulose (HPMC) were dissolved in Milli-Q water at 70°C until fully swollen and dissolved, forming a uniform solution. Lipid phase was then slowly added to the aqueous phase using a syringe at a 1:3 (w/w) ratio to achieve a homogenous mixture. The mixture was homogenized at a high speed of 20,000 rpm while keeping it at a constant temperature of 50°C for a duration of 15 min.

#### **4.A.2.4. Solidification of CSL, ESL, and CESL colloidal nanoparticles**

The obtained colloidal CSL, ESL, and CESL nanoparticles were solidified using a surface adsorption method. Each homogenized nanoparticle suspension was individually mixed with 600 mg of Aerosil 200 and triturated for 15 minutes at ambient temperature. The resulting solid nanoparticles were then subjected to vacuum drying at 45°C and stored at 4°C for further analysis. Figure 4.1 illustrates the preparation process of CESL-NP. Figure 4.1 represent the schematic diagram for the preparation of CESL-NP.

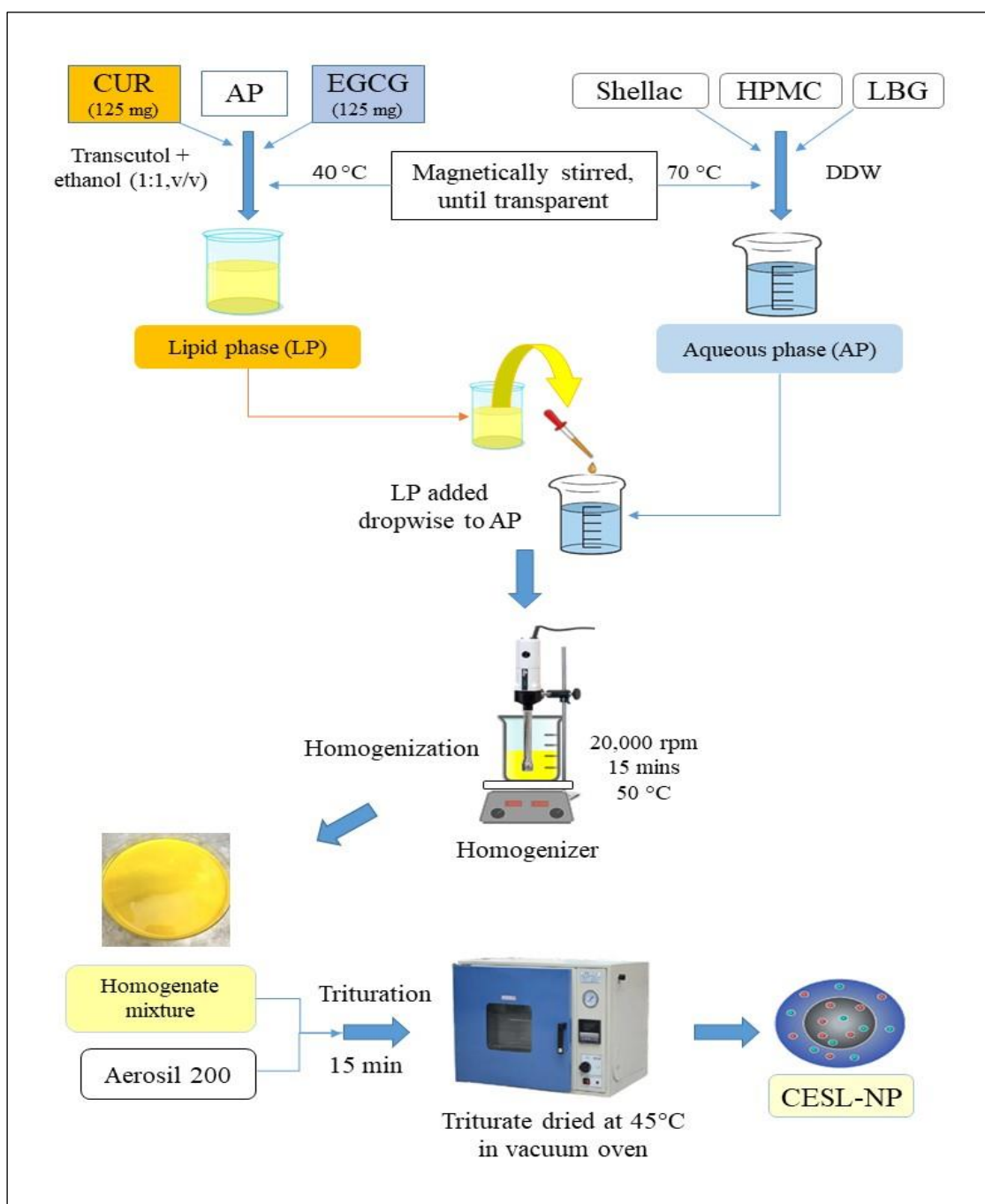


**Figure 4. 1:** Schematic diagram for preparation of CESL-NP coacervate by anti-solvent precipitation method

#### 4.A.2.5. RP-HPLC analytical method for estimation of curcumin and epigallocatechin gallate

A new validated reverse-phase high-performance liquid chromatography (RP-HPLC) method was established to simultaneously quantify the levels of curcumin (CUR) and epigallocatechin gallate (EGCG) within a novel nanoformulation (CESL-NP). The method adhered to

International Council for Harmonisation (ICH) guidelines for system suitability criteria and demonstrated acceptable performance (ICH, 2005).

#### 4.A.2.5.1. Selection of UV wavelength for HPLC analysis

To determine the optimal wavelength for UV detection, CUR and EGCG were individually dissolved in methanol and scanned within the 200-400 nm range using a UV-visible spectrophotometer. EGCG exhibited a maximum absorbance at 275 nm, while CUR's peak was observed at 262 nm. The spectra intersected at 268 nm, indicating an isosbestic point. Therefore, 268 nm was selected as the detection wavelength for simultaneous quantification. Figure 4.2 illustrates the overlapping UV spectra of CUR and EGCG.

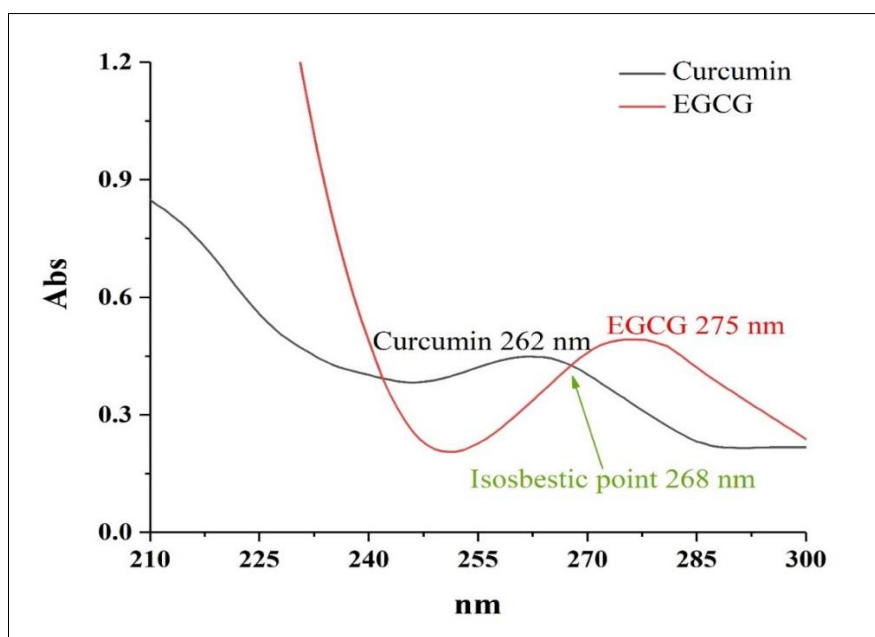


**Figure 4. 2:** Overlay of UV spectra for curcumin and epigallocatechin gallate

#### 4.A.2.5.2. Instrumentation and chromatographic conditions for HPLC analysis

An Agilent 1260 series HPLC system, equipped with a quaternary pump, an autosampler, column oven compartment, and diode array detector (DAD), was used to perform HPLC analyses. UV spectra were recorded using a Shimadzu UV 1800 UV-visible spectrophotometer with UV probe software. Chromatographic separation was performed using gradient elution

with a Thermo Scientific Hypersil BDS C18 column. The mobile phase consisted of (A) 0.025 M potassium dihydrogen phosphate buffer (pH 4.0) and (B) acetonitrile. The flow rate was maintained at 1.5 mL/min, and the column temperature was set at 35°C. A gradient was employed, starting with a mixture of 80% A and 20% B for 5 min, followed by a gradual transition to 40% A and 60 % B over the next 5-13 min. Finally, the composition returned to 80% A and 20% B for the remaining 13-16 min. A 20 µL injection volume was used, and UV detection was performed at 268 nm (Bhutia et al., 2022). UV data was captured and analyzed using UV probe software from Shimadzu. All HPLC data was acquired and processed with EZ Chrome Elite software (Agilent). Statistical calculations were carried out using Origin software and Table 4.3 represents the optimized chromatographic parameters of the HPLC method.

**Table 4.3:** Optimized chromatographic parameters of the validated RP-HPLC method

Sl. No.	Parameters	Conditions
1)	Column	Thermo Scientific Hypersil BDS, C18 column (250 mm × 4.6 mm, 5 µm)
2)	Column oven temperature	35 °C
3)	Detection wavelength	268 nm
4)	Diluent	Mobile phase
5)	Flow rate	1.5 ml/min
6)	Injection volume	20 µL
7)	Mobile phase	Buffer (0.025 M KH <sub>2</sub> PO <sub>4</sub> , pH 4.0) and acetonitrile; Gradient programming
8)	Run Time	16 min

#### 4.A.2.5.3. Preparation of stock standards and sample solutions

A standard solution containing CUR and EGCG, each at a concentration of 500 µg/mL, was prepared in methanol. Subsequent dilution of this stock solution yielded the final standard solution. To evaluate entrapment efficiency, drug loading, and cumulative *in vitro* drug release,

appropriate amounts of nanoformulations were dissolved in methanol followed by dilution with a suitable diluent (Aswathy et al., 2022).

#### **4.A.2.5.4. Method validation**

##### **4.A.2.5.4.1. Specificity**

To assess method specificity, HPLC analyses were performed on blank nanoparticle solutions and stress degradation solutions. The absence of interfering peaks, other than those attributed to curcumin and epigallocatechin gallate, confirmed the method's ability to accurately differentiate the target analytes from potential impurities or degradation products.

##### **4.A.2.5.4.2. Linearity**

To evaluate linearity, a standard stock solution containing curcumin and EGCG at a concentration of 500 µg/mL was prepared. From this stock solution, calibration standards were prepared at various concentrations: 12.5, 25, 50, 75, and 100 µg/mL for CUR, and 25, 50, 100, 150, and 175 µg/mL for EGCG. Calibration curves were constructed by plotting the peak area (Y-axis) against the concentration (X-axis).

##### **4.A.2.5.4.3. Accuracy**

To assess accuracy, known quantities of EGCG and curcumin were added to the nanoformulation at 75%, 100%, and 125% of the expected concentration. The percent recovery of these added standards was then calculated for each level.

##### **4.A.2.5.4.4. Precision**

To evaluate precision, three distinct concentration levels were prepared from each standard stock solution. Percent relative standard deviation (RSD) was calculated to assess precision. Low, medium, and high concentrations were selected: 12.5, 50, and 100 µg/mL for CUR, and 25, 100, and 175 µg/mL for EGCG. For intraday precision, each solution was injected in triplicate on the same day (n=3). To assess interday precision, each solution was stored in a

freezer and then injected in triplicate on a different day under identical chromatographic conditions.

#### **4.A.2.5.4.5. Sensitivity**

To evaluate the sensitivity of the analytical method, the minimum detectable concentration (limit of detection, LOD) and the minimum quantifiable concentration (limit of quantification, LOQ) were determined. The limit of detection represents the smallest amount of the analyte that can be reliably distinguished from the background noise of the analytical system, while the limit of quantification is the lowest concentration that can be measured.

#### **4.A.2.5.4.6. Robustness**

The method's robustness was assessed by evaluating its sensitivity to small, deliberate alterations in chromatographic conditions. The impact of these variations on the analytical results was then analyzed to determine the method's overall reliability and reproducibility

#### **4.A.2.5.5. System suitability**

A mixed standard solution containing curcumin at 50 µg/mL and EGCG at 100 µg/mL was prepared. A 20 µg/mL aliquot of this solution was injected into the HPLC system under optimized chromatographic conditions. System suitability parameters, including theoretical plates, tailing factor, retention time, resolution, and others, were evaluated (Sesharao and Madhavarao, 2018).

#### **4.A.2.5.6. Forced degradation studies**

To evaluate forced degradation, 5 mL aliquots of CUR and EGCG standard stock solutions (500 µg/mL each) were subjected to various stress conditions including basic, thermal, peroxide, UV light exposure, photolytic, and acidic. The solutions were diluted to concentrations of 50 µg/mL for curcumin and 100 µg/mL for epigallocatechin gallate. These diluted solutions were then quantified using known standards of the same concentrations.

(Sesharao and Madhavarao, 2018). Table 4.4 summarizes the different forced degradation conditions employed for CUR and EGCG.

**Table 4. 4:** Optimized parameters for CUR and EGCG forced degradation study

Sl. No.	Stress type	Stress condition
1)	Acid	Hydrochloric acid (0.1 M, 5 mL) was used for 5 h at 80°C
2)	Base	Sodium hydroxide (0.1 M, 5 mL) was used for 5 h at 80°C
3)	Heat	Maintained at a temperature of 80 °C for 5 h
4)	Peroxide	Hydrogen peroxide (10 % v/v, 5 mL) was used for 5 h at 80°C
5)	Photo light	Subjected to daylight for 5 h
6)	UV light	Exposed to ultraviolet light with a wavelength of 254 nm for 5 h

#### 4.A.2.5.7 Assessment of drug loading and entrapment efficiency

To assess drug loading (DL) and entrapment efficiency (EE) of the prepared CSL-NP, ESL-NP, and CESL-NP, a specified amount of nanoparticle samples was dissolved in methanol. The solution was then centrifuged at 5000 rpm for 15 minutes, and the supernatant was subsequently diluted. A 20 µL aliquot of the solution was filtered through a 0.45 µm syringe filter and then injected into the high-performance liquid chromatography system. DL and EE were calculated using the following equations (Xu et al., 2013):

$$DL (\%) = (\text{Amount of the drug contained in the nanoparticles} / \text{overall weight of the nanoparticles}) \times 100$$

$$EE (\%) = (\text{Amount of drug within nanoparticles} / \text{overall weight of drug utilized in nanoparticle preparation}) \times 100$$

#### 4.A.2.6. Characterization of the formulated nanoparticles

##### 4.A.2.6.1. DLS analysis

To evaluate nanoparticle properties, CSL-NP, ESL-NP, and CESL-NP (10 mg each) were dispersed in 10 mL of Milli-Q water and sonicated for 15 minutes. Dynamic light scattering (DLS) study was conducted using a Zetasizer Nano ZS90 instrument (Malvern Instruments,

UK) featuring Data Transfer Assistance (DTA) software to determine mean particle size, zeta potential, and polydispersity index (PDI). Measurements were performed at a temperature of 25°C (Cho and Hackley, 2010).

#### **4.A.2.6.2. FTIR analysis**

Fourier transform infrared spectroscopy (FTIR) was employed to detect the presence of pure CUR and EGCG within CESL-NP and to explore potential interactions between the drugs and the other excipients used in the formulation. FTIR spectra were obtained for pure CUR, pure EGCG, a physical mixture containing all excipients including CUR and EGCG, a blank mixture comprising all excipients without the pure drugs, and CESL-NP, using an FTIR Spectrometer (IR Affinity 1, Shimadzu, Japan) over the spectral range of 4000-500 cm<sup>-1</sup> (Sarmiento et al., 2006). The collected spectra were analyzed using IRsolution version 1.60 software.

#### **4.A.2.6.3. DSC analysis**

Differential scanning calorimetry (DSC) was employed to characterize the thermal behavior of pure CUR, EGCG, a blank mixture, a physical mixture, and CESL-NP. Thermograms were acquired using a DSC Q2000 (TA Instruments, USA). Approximately 5-6 mg of each sample was hermetically sealed in an aluminum pan. The heating rate was maintained at 10°C per minute, and the temperature range was set from 0 to 500°C (Castelli et al., 2005).

#### **4.A.2.6.4. XRD analysis**

X-ray diffraction (XRD) was employed to characterize the structural properties of CESL-NP, pure CUR, pure EGCG, a blank mixture, and a physical mixture. Structural analyses were conducted using an X'Pert Pro X-ray Diffractometer (PANalytical, Almelo, Netherlands) operating at 40 mA and 45 kV, utilizing CuK $\infty$  radiation with a wavelength of 1.54 Å. Diffraction data were collected within the 2 $\theta$  range of 10 to 80 ° (Dung et al., 2009).

#### **4.A.2.6.5. AFM analysis**

Atomic force microscopy (AFM) was employed to verify the size of the prepared CUR and EGCG-loaded nanoparticles. CESL-NP samples were diluted 1:50 in Milli-Q water, filtered, deposited onto glass slides, and allowed to air-dry (Garg and Garg, 2018). AFM analysis was conducted using a Bruker Dimension Icon Innova AFM (USA). NanoDrive V8 real-time control software and NanoScope Analysis data processing software was employed to analyze the acquired images.

#### **4.A.2.6.6. HRTEM analysis**

High-resolution transmission electron microscopy (HRTEM) micrographs of the formulated CESL-NP were obtained using a Tecnai G2 TF20-ST microscope (FEI, Hillsboro, USA) operating at an accelerating voltage of 200 kV. Initially, the nanoparticle powder was diluted 1:100 in Milli-Q water and filtered using 0.45  $\mu\text{m}$  syringe filter. A drop of the filtered solution was then pipetted onto a carbon-supported 3 mm copper grid and allowed to air-dry at room temperature (Sathiyabama et al., 2020).

#### **4.A.2.6.7. FESEM analysis**

Field emission scanning electron microscopy (FESEM) was utilized to examine the morphology of the prepared CESL-NP. The sample was diluted 1:100 in Milli-Q water, filtered through a 0.45  $\mu\text{m}$  syringe filter, and then spread as a thin layer on a glass coverslip and air dried. A thin layer of gold was sputtered on the top surface prior to imaging (Ayubi et al., 2019). FESEM analysis was conducted using a Quanta 250 FEG-SEM (FEI, Hillsboro, USA).

#### **4.A.2.7. Solubility study of CESL-NP**

The solubility of CESL-NP and free CUR was compared through solubility study conducted in water. A total of 20 mg of free CUR and an equivalent amount of CESL-NP were each added to 2 ml of Milli-Q water. The mixtures were subjected to vortexing, sonication, and

centrifugation for 10 minutes each. The resulting supernatants were filtered through a 0.45  $\mu\text{m}$  syringe filter and mixed with ethyl acetate in a 1:1 ratio to extract free curcumin. The resulting samples were analyzed using high-performance liquid chromatography (HPLC) at 420 nm (Kim et al., 2011).

#### **4.A.2.8. Stability study of CESL-NP**

Storage stability was evaluated by preparing CESL-NP samples and sealing them in vials, adhering to ICH guidelines. These vials were then carefully stored in a refrigerator at 4°C. After 90 days, the CESL-NP samples were analyzed for particle size, polydispersity index, zeta potential, and drug loading (Kim et al., 2011).

#### **4.A.2.9. *In vitro* release of CESL-NP**

CESL-NP (200 mg) was subjected to sonication for 15 minutes in 20 mL of Milli-Q water. Following a previously described method with minor modifications (De and Bera, 2021), the solution was divided into two separate dialysis bags (10 mL each). Each dialysis bag was then immersed in a 250 mL conical flask containing 200 mL of a specific dissolution medium. To assess drug release, the nanoformulation was exposed to simulated gastric fluid (SGF, pH 1.2) and simulated intestinal fluid (SIF, pH 7.4). The dissolution media were housed in a temperature-controlled shaking incubator (INCON, BOD-INC-1S) maintained at  $37 \pm 0.5$  °C and a constant shaking speed of 100 rpm. Periodically, 2 mL aliquots of the dissolution medium were withdrawn and replenished with an equivalent volume of fresh medium. The drug content of the collected samples was then quantified using HPLC.

#### **4.A.2.10. *In vitro* drug release kinetic models**

To elucidate the drug release kinetics, the data collected were evaluated using several models, including zero-order, first-order, Korsmeyer-Peppas, Higuchi, and Hixon-Crowell. The model with the highest  $R^2$  value was chosen to best represent the drug release profile in the various

media. The equations corresponding to these models are outlined below (Singhvi and Singh, 2011; Rudra et al., 2010):

- **Zero-Order:**  $[D]_t = [D]_0 + Kt$

Where,  $D_t$  = quantity of drug released at time  $t$ ,  $D_0$  = initial quantity of drug,  $K_0$  = zero-order rate constant, and  $t$  = time. This model suggests that the drug release rate is constant over time. (% cumulative drug release vs. time)

- **First-Order:**  $\text{Log } [D]_t = \text{Log } [D]_0 - Kt / 2.303$

This model suggests that the drug release rate is proportional to the concentration of the drug remaining (log % amount of drug released vs. time).

- **Higuchi model:**  $[D]_t = k_H (t)^{0.5}$

Where,  $K_H$  = Higuchi rate constant. This model proposes that drug release is a diffusion-controlled process, often applicable to matrix systems, adhering to Fick's law (% cumulative drug release vs. square root of time).

- **Hixson-Crowell model:**  $[D]_0^{1/3} - [D]_t^{1/3} = K_{HC} t$

Where,  $K_{HC}$  = Hixson-Crowell rate constant. This model considers changes in the surface area and diameter of particles during the dissolution process (Cube root of % amount of drug released vs. time).

- **Korsmeyer-peppas model:**  $M_t/M_\infty = Kt^n$

Where,  $M_t/M_\infty$  = drug release fraction at time  $t$ ,  $K$  = Korsmeyer release rate constant, and  $n$  = drug release exponent, indicates the mechanism of release (log % cumulative drug release vs. log  $t$ ).

#### **4.A.2.11. *In vivo* antidiabetic and antinephritic studies**

##### **4.A.2.11.1. Experimental animals**

Animal studies adhered to CPCSEA guidelines, with the study protocol approved by the Institutional Animal Ethics Committee (IAEC) at Jadavpur University, Kolkata, India (Ref no. JU/IAEC-22/02). The animals were housed in polycarbonate cages in a room maintained at a constant temperature of  $23 \pm 3.0$  °C, with a relative humidity of 44-52% and a 12-hour day and night cycle. Prior to the experiment, all animals were allowed to adapt to the laboratory environment for a period of ten days, with unrestricted access to food and water.

##### **4.A.2.11.2. Induction of diabetes**

Swiss albino mice were subjected to overnight fasting before being administered streptozotocin (STZ) via intraperitoneal injection at a dosage of 80 mg/kg of body weight. A freshly prepared 0.1 M citrate buffer with a pH of 4.5 was used to dissolve STZ. To prevent hypoglycemia and death caused by rapid and excessive beta-cell necrosis, the mice were administered a 5% glucose solution 6 hours after the STZ injection. Hyperglycemia was confirmed 1 week after STZ injection by measuring the fasting blood glucose level (FBGL) using an ACCU-CHEK active glucometer, following the protocol described by Kifle et al. and employed by Adugna et al. (Kifle et al., 2020; Adugna et al., 2022). Mice exhibiting a FBGL above 200 mg/dL were diagnosed as diabetic and included in the study.

##### **4.A.2.11.3. Experimental design and animal treatment**

To assess the antidiabetic effects, 35 male mice were divided into seven groups, each consisting of five mice. Male mice were chosen because female mice are less prone to developing diabetes after STZ administration (Sisay et al., 2022). Two weeks post-STZ injection, treatments with various formulations commenced. The groups were organized as follows:

- Group 1 (normal control): Received saline and a regular diet.

- Group 2 (disease control): Induced with STZ but received no treatment.
- Group 3 (standard drug): Received glibenclamide (1 mg/kg b.w.) (Sarkodie et al., 2013).
- Group 4 (free drug): Received curcumin (CUR) and epigallocatechin gallate (EGCG) in free form (100 mg/kg b.w.).
- Group 5 (co-encapsulated nanoparticle): Received CUR and EGCG-loaded nanoparticles (CESL-NP) (20 mg/kg b.w.).
- Group 6 (single drug nanoparticle - CUR): Received CUR-only nanoparticles (CSL-NP) (20 mg/kg b.w.).
- Group 7 (single drug nanoparticle - EGCG): Received EGCG-only nanoparticles (ESL-NP) (20 mg/kg b.w.).

Each group received their respective doses daily by oral gavage for 60 days at a fixed time. Every seventh day, FBGL were measured using an ACCU-CHEK Guide glucometer on tail-prick blood. Throughout the experiment, the mice had unrestricted access to standard food and water. Their behavior and general health were closely monitored daily.

#### **4.A.2.11.4. Collection of serum and tissue samples**

Upon completion of the study, the animals were weighed, and blood samples were collected through cardiac puncture under mild isoflurane anesthesia. The blood samples were subjected to centrifugation to extract the serum, which was subsequently stored at a temperature of -20 °C for analysis of various biochemical parameters, including serum albumin (Alb), serum creatinine (Scr), and blood urea nitrogen (BUN). Following blood collection, the animals were euthanized, and their pancreas and kidneys were promptly removed and washed in ice-cold saline. Morphological changes in the right kidney were compared, and the kidney weight (KW) was recorded, with an electronic weighing balance. The kidney hypertrophy index (KHI) was

calculated using the formula  $KHI = \text{kidney weight} / \text{body weight}$  (Wu et al., 2018). The pancreas and kidneys were preserved in 10% formalin for histopathological examination.

#### **4.A.2.11.5. Histopathological analysis**

The pancreas and kidneys, once dehydrated, were first cleaned with xylene and ethanol. They were then embedded in paraffin wax and sliced into 5  $\mu\text{m}$  sections using a microtome. Following staining with hematoxylin and eosin (H&E), the sections were analyzed under a light microscope for histopathological evaluation (Asgary et al., 2014).

#### **4.A.2.11.6. Statistical analysis**

The results are reported as mean  $\pm$  SEM for five mice per group. Statistical analysis was performed using one-way analysis of variance (ANOVA), a statistical method used to compare the means of multiple groups, followed by Dunnett's t-tests to identify significant differences between the groups. A p value of  $\leq 0.05$  was considered statistically significant,  $**p \leq 0.01$  was deemed moderately significant, and  $***p \leq 0.001$  was regarded as highly significant.

## 4.B. RESULTS

### 4.B.1. Preformulation study of CESL-NP

In this study, we successfully formulated a novel, stable nanoformulation utilizing exclusively Generally Recognized as Safe (GRAS) ingredients. The formulation incorporated shellac as a biopolymer, locust bean gum as a natural polysaccharide, Transcutol® as a penetration enhancer, ascorbyl palmitate and hydroxypropyl methylcellulose as excipients, and aerosil 200 as a solidifying agent (Table 4.5).

**Table 4. 5:** Ingredients of CUR and EGCG-loaded nanoparticles

Sl. No.	Ingredients	Role in formulation
1)	Aerosil 200	Mechanical properties enhancer, stabilizer, anti-caking agent
2)	Ascorbyl palmitate	Stabilizer, emulsifier, lipid component
3)	Curcumin	Active constituent
4)	Epigallocatechin gallate	Active constituent
5)	HPMC	Viscosity enhancer, binding and thickening agent
6)	LBG	Natural polysaccharide, binding and gelling agent
7)	Shellac	Biopolymer matrix, stabilizer
8)	Transcutol®	Co-surfactant, solubility and stability enhancer

Note: HPMC-hydroxypropyl methylcellulose; LBG- locust bean gum

### 4.B.2. RP-HPLC analytical method for estimation of CUR and EGCG

#### 4.B.2.1. Method development

Method optimization for HPLC analysis involved adjusting various chromatographic parameters. Different columns, including cyano, phenyl, and others, were evaluated. The mobile phase composition, flow rate, and pH were modified in gradient elution mode. An isobestic wavelength of 268 nm was selected for UV detection. The method was optimized

for quantifying EGCG and curcumin, which eluted at 3.9 and 10.7 minutes, respectively. All system suitability parameters were found to be within acceptable limits. Figures 4.3A, 4.3B, and 4.3C depict the HPLC chromatograms of standard CUR, standard EGCG, and a mixed standard of CUR and EGCG.

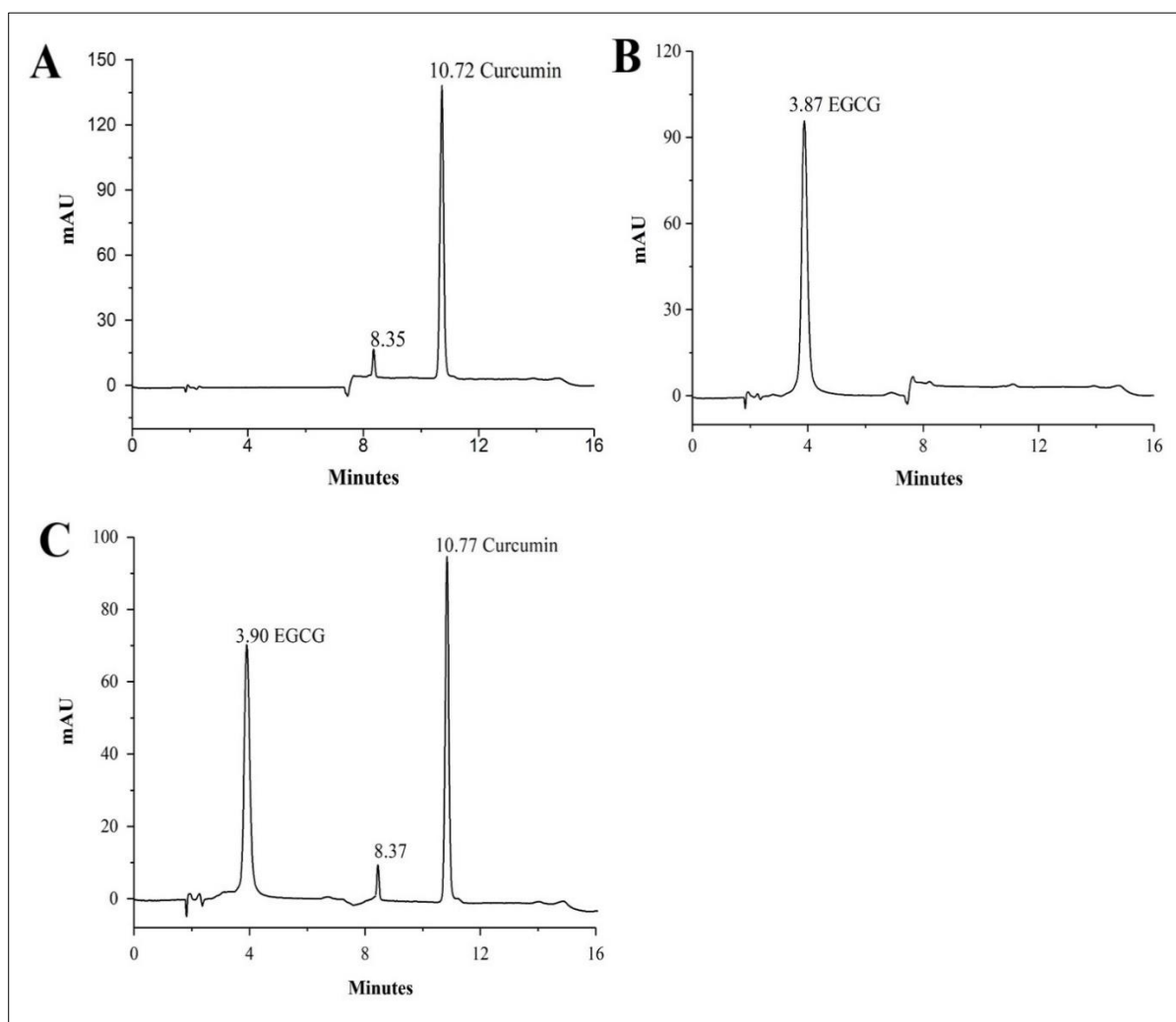


**Figure 4. 3:** HPLC chromatograms of (A) standard curcumin, (B) standard epigallocatechin gallate, and (C) optimized chromatogram of a mixture of curcumin and epigallocatechin gallate

#### 4.B.2.2. Method validation

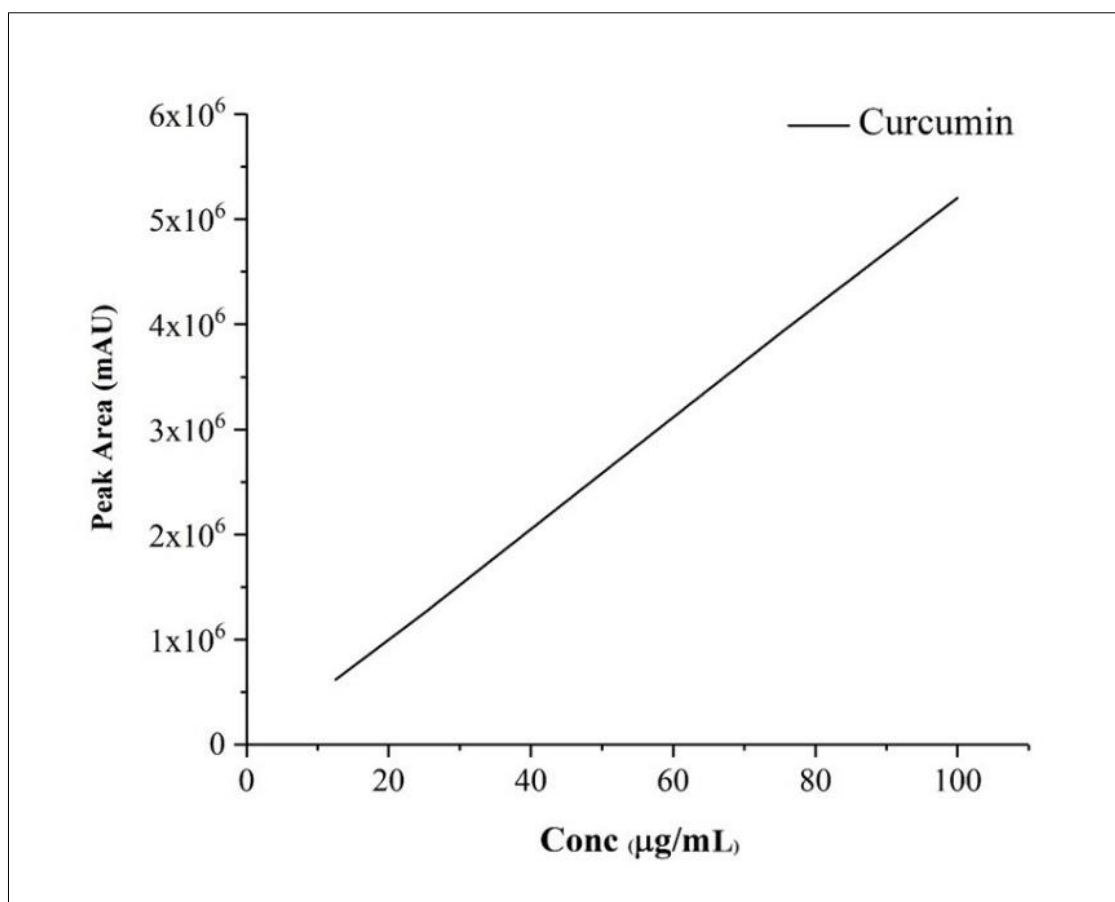
##### 4.B.2.2.1. Specificity

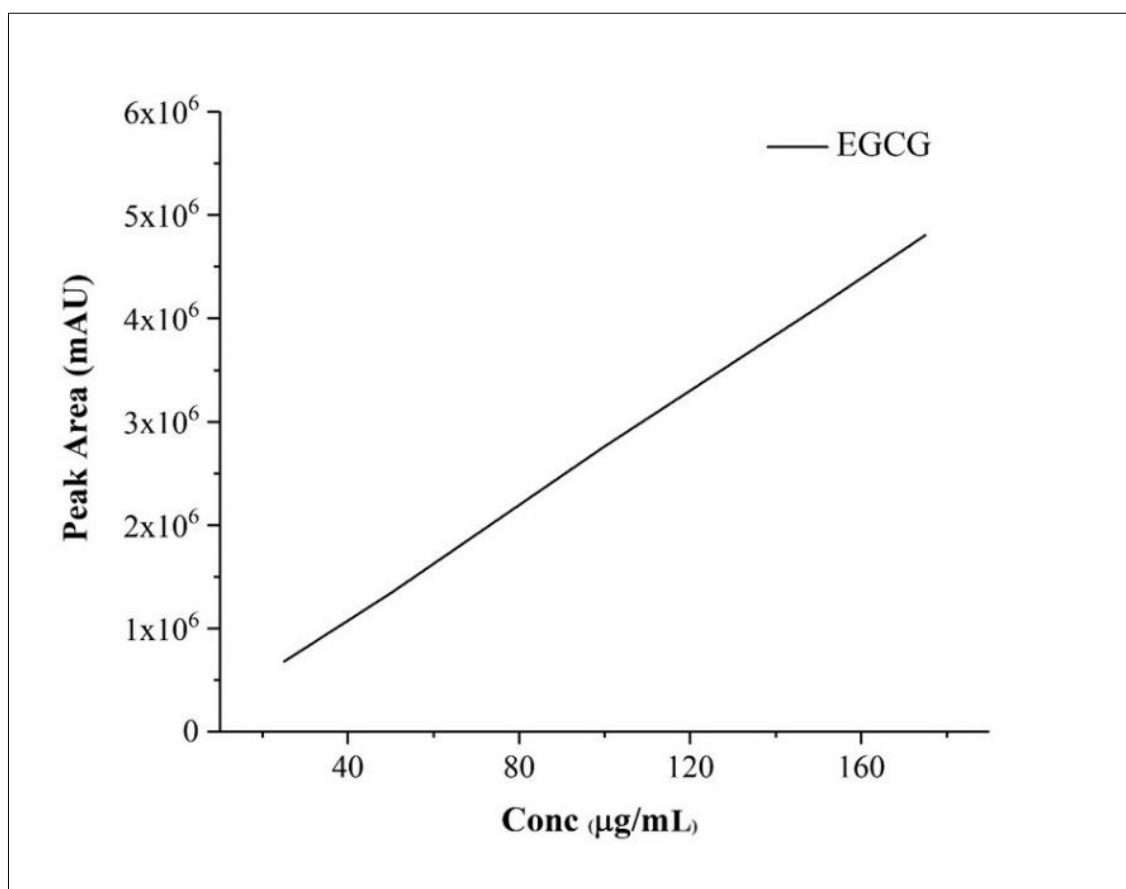
The HPLC chromatogram of the CESL-NP revealed distinct peaks corresponding to CUR and EGCG, eluting at retention times of 10.7 minutes and 3.9 minutes, respectively. The absence

of overlapping peaks in the chromatogram highlights the specificity of the analytical method. Moreover, forced degradation studies successfully separated the CUR and EGCG peaks from any degradation products, further confirming the method's selectivity (De and Bera, 2021).

#### 4.B.2.2.2. Linearity

CUR exhibited a linear response between 12.5 and 100  $\mu\text{g/mL}$ , with a regression equation of  $y = 51643x - 17550$  and a correlation coefficient of 0.999. Similarly, EGCG demonstrated linearity between 25 and 175  $\mu\text{g/mL}$ , following the equation  $y = 46092x + 20019$  and exhibiting a correlation coefficient of 0.991. These high correlation coefficients indicate the reliability and accuracy of the developed method for quantifying both compounds (Pal and Pal, 2020). The calibration curves for curcumin and EGCG are illustrated in Figures 4.4 and 4.5, respectively.



**Figure 4. 4:** Calibration curve of standard curcumin**Figure 4. 5:** Calibration curve of standard EGCG

#### 4.B.2.2.3. Accuracy

The mixed standard contained CUR (50  $\mu\text{g/mL}$ ) and EGCG (100  $\mu\text{g/mL}$ ). The developed method exhibited excellent accuracy for quantifying both compounds, with average recoveries of 98.63% and 97.90% for CUR and EGCG, respectively. These recovery values fall well within the acceptable range, demonstrating the method's accuracy (Mishra et al., 2022). Accuracy data are presented in Table 4.6.

**Table 4. 6:** Accuracy findings by the validated HPLC method

Drugs	Spiked level (%)	Spiked amount (mg)	Recovered amount (mg)	Recovery (%)	RSD (%)
EGCG	75	7.52 ± 0.16	7.39 ± 0.12	98.27	0.67
	100	11.92 ± 0.35	11.67 ± 0.35	97.90	0.58
	125	16.13 ± 0.28	15.91 ± 0.21	98.63	0.54
CUR	75	7.46 ± 0.25	7.31 ± 0.17	97.98	0.52
	100	12.13 ± 0.19	11.92 ± 0.38	98.27	0.37
	125	15.93 ± 0.33	15.69 ± 0.25	98.49	0.45

Note: RSD- Relative Standard Deviation; All values are presented as mean ± standard deviation (SD), with n representing the sample size of 3.

#### 4.B.2.2.4. Precision

CUR exhibited intraday and interday relative standard deviation (RSD) values ranging from 0.129% to 0.421%, while EGCG displayed slightly lower RSD values of 0.068% to 0.321% (Tables 4.7 and 4.8). These results are well within the acceptable range of 2% (Rayudu et al., 2022), confirming the method's high precision.

**Table 4. 7:** Intraday precision findings by the validated HPLC method

Drugs	Nominal concentration (µg/ml)	Recovered concentration (µg/ml)	Recovery (%)	Precision (% RSD)
EGCG	50	49.31 ± 0.56	98.62 ± 1.21	0.210
	100	99.22 ± 0.35	99.22 ± 0.68	0.068
	150	149.29 ± 0.89	99.52 ± 0.56	0.071
CUR	25	24.33 ± 0.55	97.32 ± 0.71	0.421
	50	49.41 ± 0.62	98.82 ± 0.36	0.318
	75	74.34 ± 0.48	99.12 ± 0.65	0.212

Note: All values are presented as mean ± standard deviation (SD), with n representing the sample size of 3.

**Table 4. 8:** Interday precision findings by the validated HPLC method

Drugs	Nominal concentration (µg/ml)	Recovered concentration (µg/ml)	Recovery (%)	Precision % RSD
EGCG	50	48.73 ± 0.63	97.46 ± 0.58	0.321
	100	98.31 ± 0.41	98.31 ± 1.32	0.225
	150	147.87 ± 0.58	98.58 ± 0.87	0.105
CUR	25	24.18 ± 0.81	96.72 ± 0.72	0.412
	50	48.54 ± 0.72	97.08 ± 0.53	0.129
	75	73.76 ± 0.54	98.34 ± 0.25	0.165

Note: All values are presented as mean ± standard deviation (SD), with n representing the sample size of 3.

#### 4.B.2.2.5. Sensitivity

Curcumin exhibited a low limit of detection (LOD) of 1.02 µg/mL and a limit of quantification (LOQ) of 3.05 µg/mL, while EGCG displayed slightly higher LOD and LOQ values of 2.51 µg/mL and 7.53 µg/mL, respectively. These results confirm the method's sensitivity to accurately quantify both compounds even at low concentrations (Sura et al., 2022).

#### 4.B.2.2.6. Robustness

To evaluate the method's robustness, its sensitivity to intentional variations in chromatographic parameters was assessed, including column temperature, buffer pH, flow rate, and UV detection wavelength. The robustness study yielded RSD values, confirming the method's resilience to minor variations in these parameters (Devi and Rambabu, 2022). The robustness data for both CUR and EGCG are summarized in Table 4.9.

**Table 4. 9:** Robustness parameter of the validated method

Parameters	CUR area (%RSD)	EGCG area (%RSD)
A. Change in buffer pH of mobile phase		
3.4	0.083	0.061
3.5	0.673	0.081
3.6	0.731	0.072
B. Change in UV detector wavelength (nm)		
266	0.157	0.131
268	0.235	0.152
270	0.321	0.126
C. Change in flow rate (ml/min) of mobile phase		
1.4	0.053	0.089
1.5	0.139	0.132
1.6	0.158	0.087
D. Change in column oven temp( °C ) of mobile phase		
29	0.105	0.113
30	0.162	0.136
31	0.087	0.083

Note: All values are presented as mean  $\pm$  standard deviation (SD), with n representing the sample size of 3

#### 4.B.2.3. System suitability

The resolution between CUR and EGCG peaks was an impressive  $22.9 \pm 0.03$ , indicating complete separation of the two compounds. The peak asymmetry values for CUR and EGCG were  $1.08 \pm 0.03$  and  $1.04 \pm 0.06$ , respectively, demonstrating symmetrical peak shapes. Additionally, the theoretical plate numbers for CUR and EGCG were calculated to be  $44128 \pm 121$  and  $3414 \pm 131$ , respectively. The detailed system suitability data are presented in Table 4.10.

**Table 4. 10:** System suitability parameters of the validated HPLC method

Parameters	CUR (mean $\pm$ SD)	EGCG (mean $\pm$ SD)
Injection precision	0.05 $\pm$ 0.030	0.0730 $\pm$ 0.020
Resolution	17.860 $\pm$ 0.050	-
Retention time	10.77 $\pm$ 0.040	3.90 $\pm$ 0.030
Tailing factor	1.29 $\pm$ 0.040	1.360 $\pm$ 0.030
Theoretical plates/meter	44128 $\pm$ 121	3414 $\pm$ 131

Note: SD- Standard Deviation; All values are presented as mean  $\pm$  standard deviation (SD), with n representing the sample size of 6

#### 4.B.2.4. Forced degradation studies

When exposed to alkaline (0.1 M NaOH), peroxide (10% H<sub>2</sub>O<sub>2</sub>), and acidic (0.1 M HCl) conditions, CUR demonstrated varying degrees of degradation. The recovered amounts were significantly lower under alkaline (20.48%) and peroxide (30.75%) conditions compared to acidic conditions (55.88%). Similarly, EGCG was susceptible to degradation under these conditions, with recovery rates of 24.32%, 49.42%, and 84.97% for alkaline, peroxide, and acidic environments, respectively.

Regarding degradation product formation, CUR produced four degradation products under alkaline conditions, one under peroxide conditions, and no degradation products under thermal, photolytic, or UV exposure. In contrast, EGCG produced one degradation product under alkaline, peroxide, and acidic conditions, but no degradation products under thermal, photolytic, or UV exposure.

The degradation data are summarized in Table 4.11, and the corresponding HPLC chromatograms are shown in Figures 4.6-4.17. These results provide valuable insights into the

stability of the compounds and aid in developing appropriate storage and handling conditions to prevent degradation (Reddy and Rao, 2021).

**Table 4. 11:** Percentage recovery and degradation of CUR and EGCG following stress conditions

Stress conditions	% Recovery*		% Degradation*	
	CUR	EGCG	CUR	EGCG
Acidic	55.88 ± 1.32	84.97 ± 0.87	44.12 ± 0.27	15.03 ± 1.83
Alkali	20.48 ± 0.57	24.32 ± 0.68	79.52 ± 1.13	75.68 ± 0.87
Peroxide	30.75 ± 1.21	49.42 ± 0.58	69.25 ± 0.78	50.58 ± 1.75
Photolytic	100.18 ± 0.59	100.13 ± 0.39	0 ± 0.36	0 ± 0.38
Thermal	89.25 ± 0.53	99.95 ± 0.28	10.75 ± 0.83	0.05 ± 0.23
UV light	99.53 ± 0.37	100.21 ± 0.49	0.47 ± 0.63	0 ± 0.53

Note: \*All values are presented as mean ± standard deviation (SD), with n representing the sample size of 3

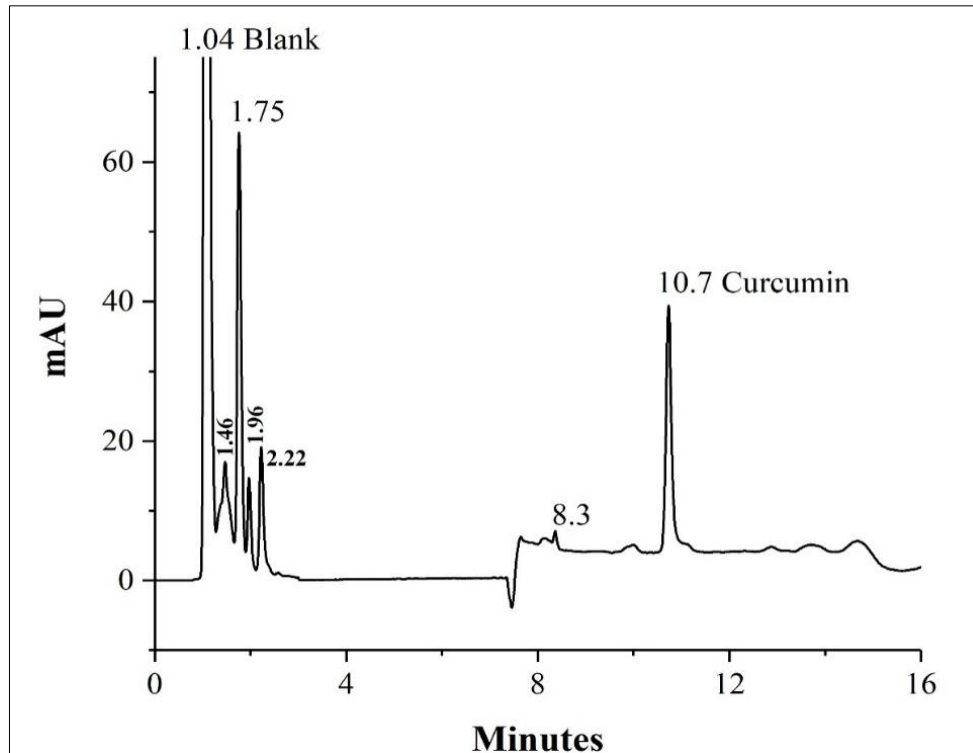


**Figure 4. 6:** Standard CUR degradation profile in 0.1 M NaOH under forced conditions

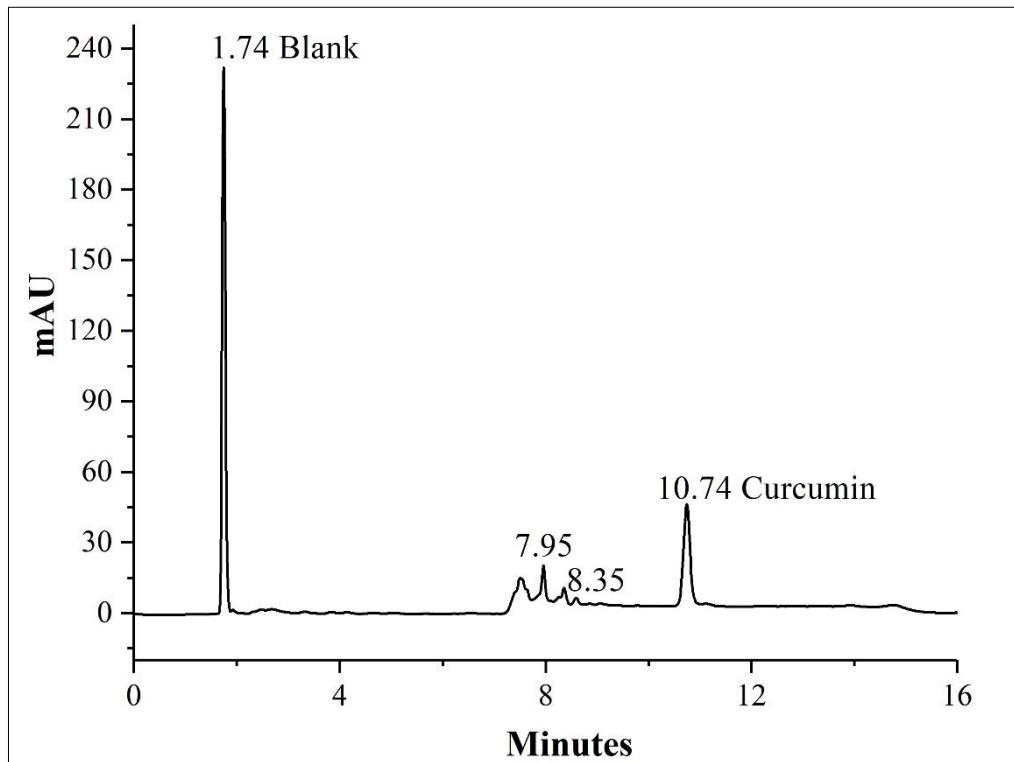


**Figure 4. 7:** Standard CUR degradation profile in 10% (v/v) H<sub>2</sub>O<sub>2</sub> under forced conditions

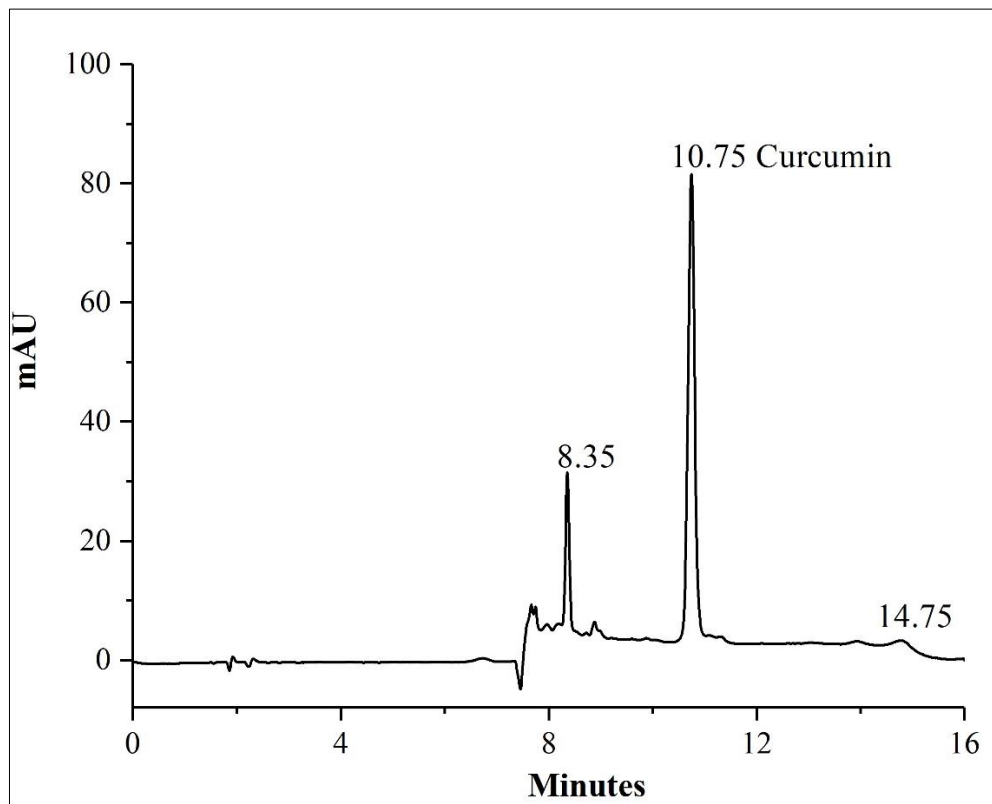


**Figure 4. 8:** Standard CUR degradation profile in 0.1 M HCl under forced conditions

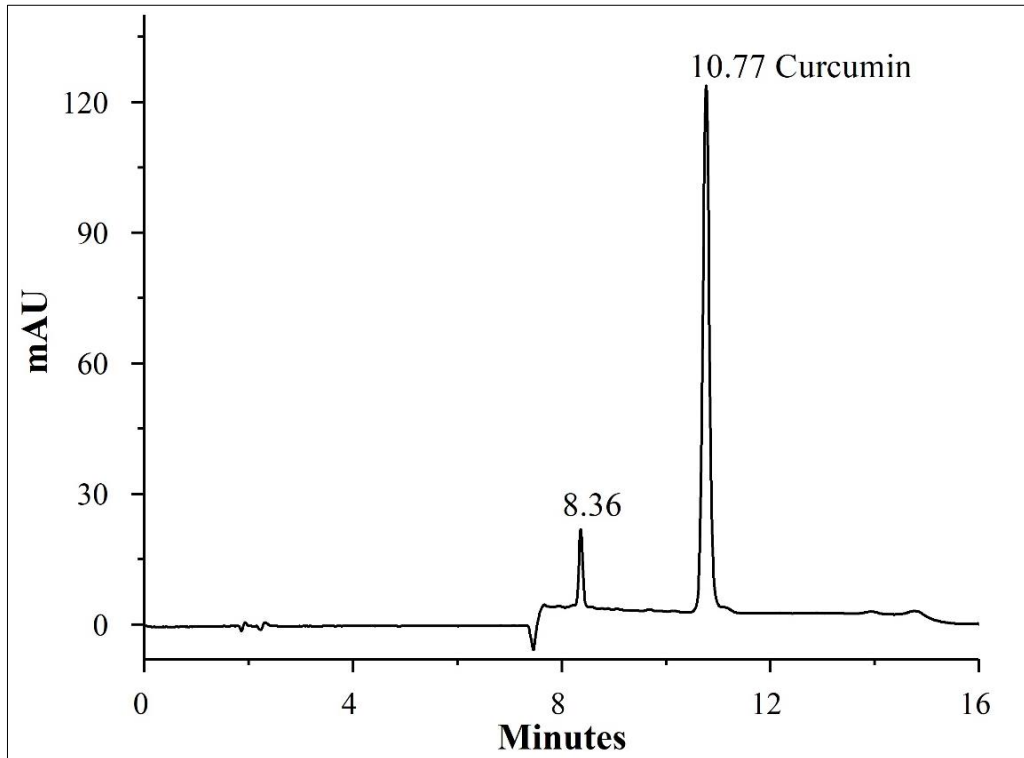


Figure 4. 9: Standard CUR degradation profile under heat stress conditions

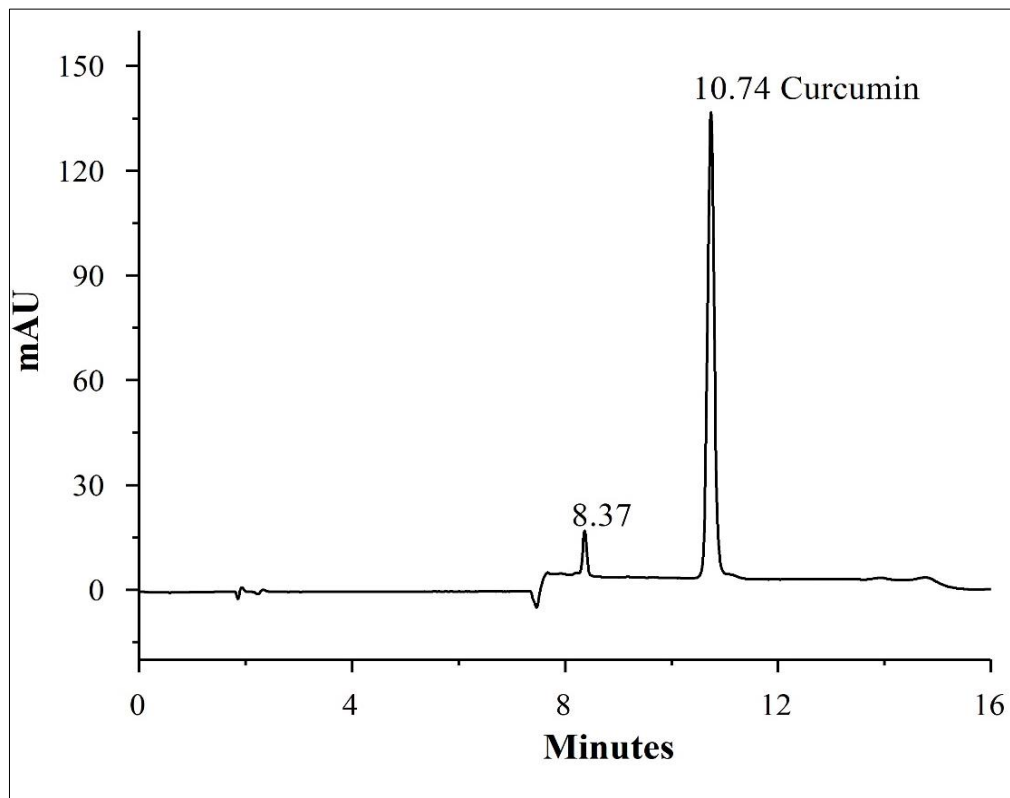


Figure 4. 10: Standard CUR degradation profile under photolytic stress conditions

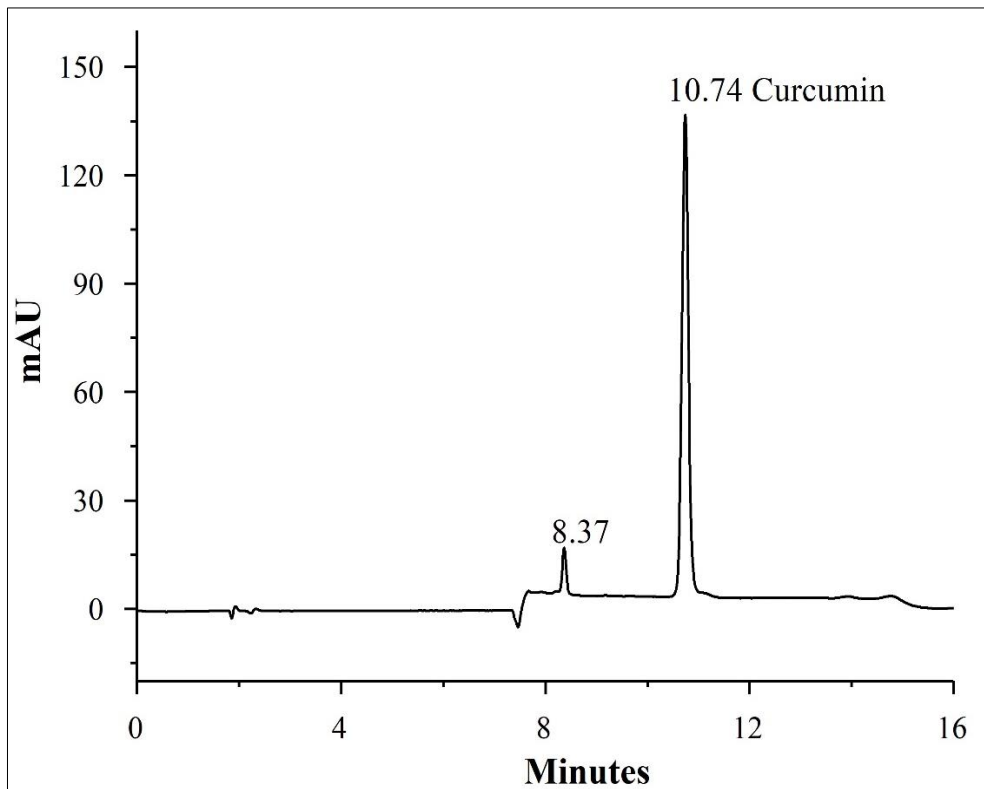
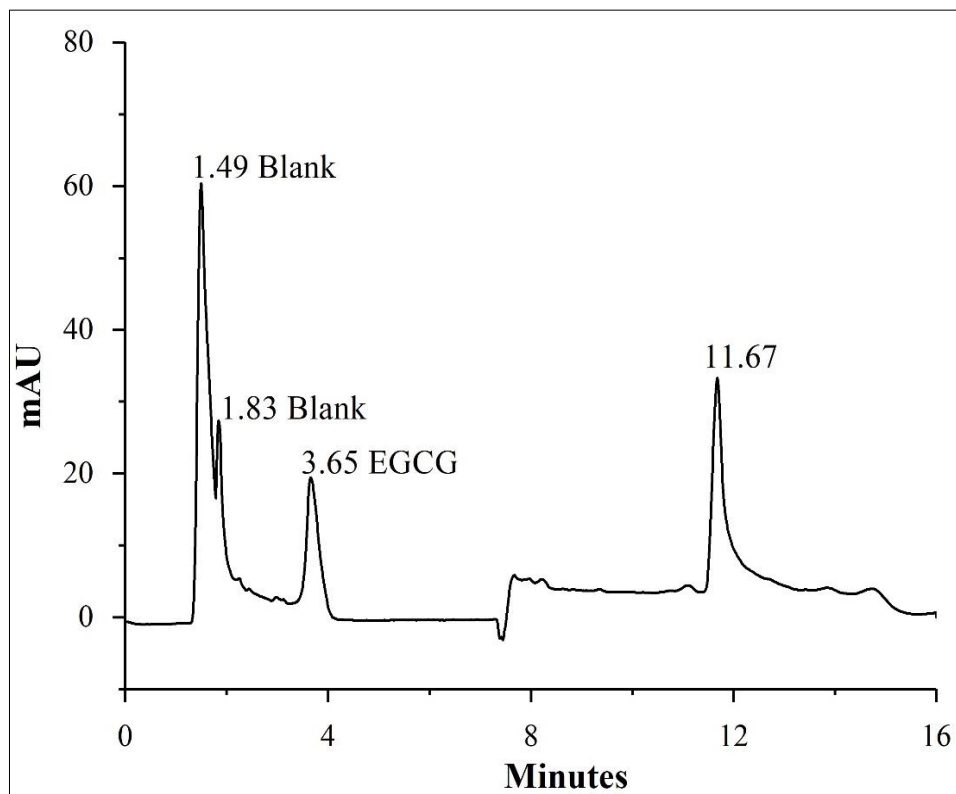
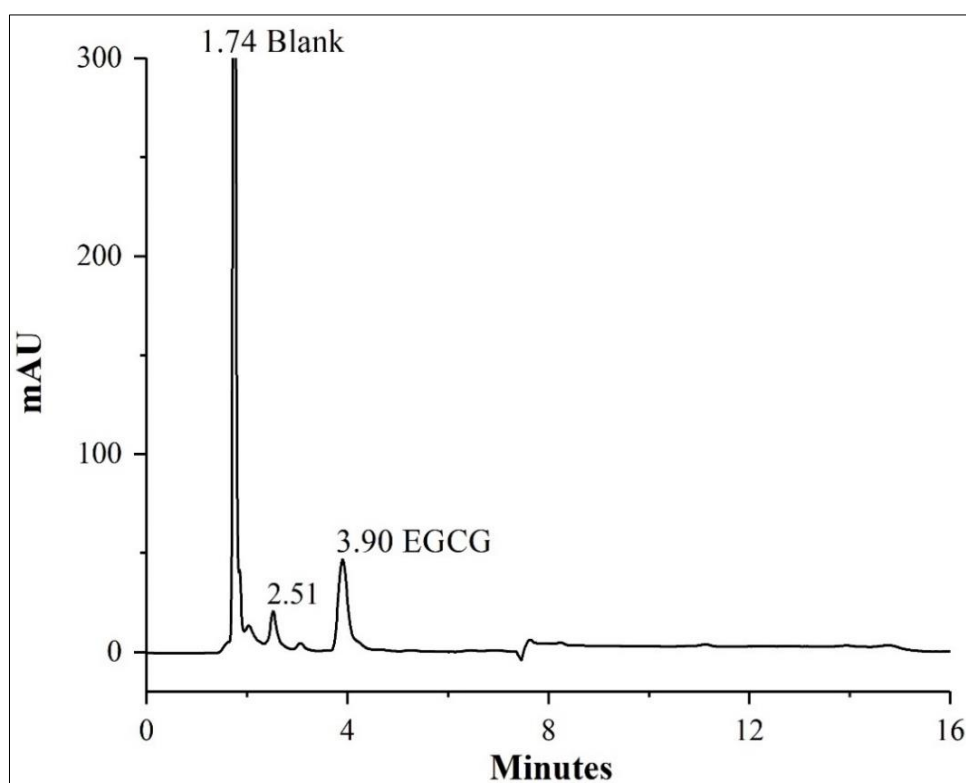
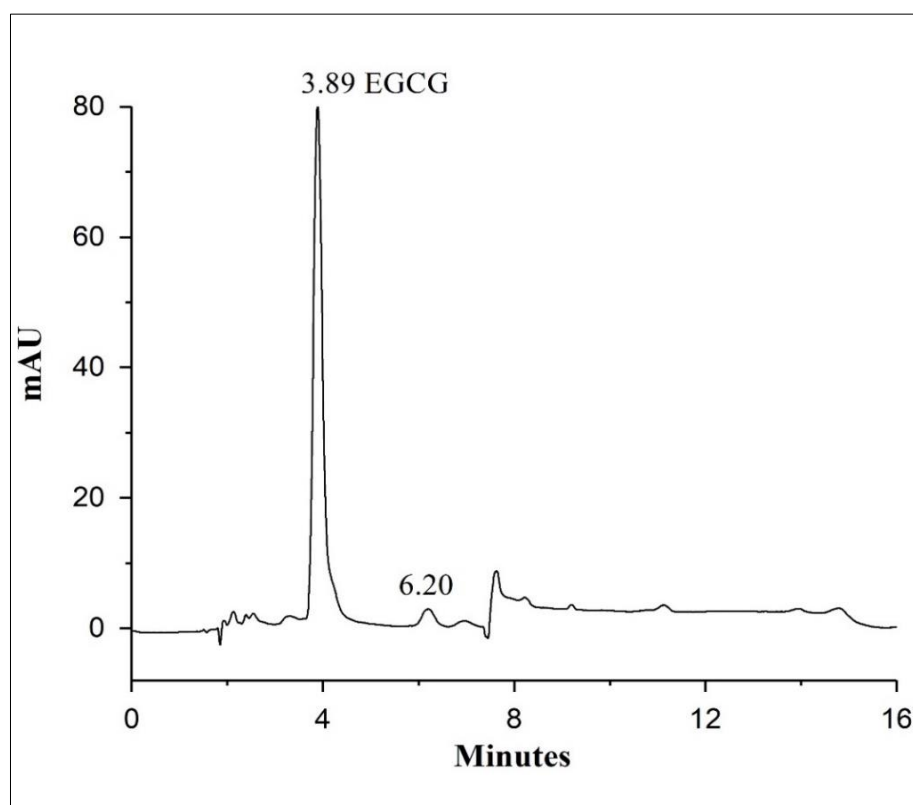
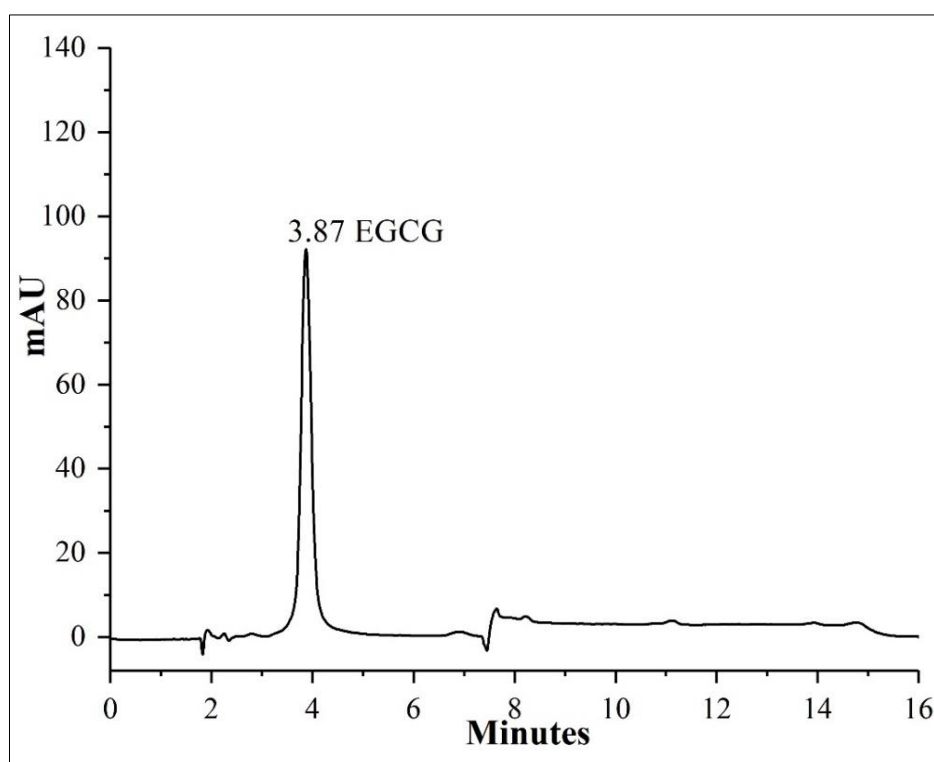


Figure 4. 11: Standard CUR degradation profile under UV light exposure



**Figure 4. 12:** Standard EGCG degradation profile in 0.1 M NaOH under forced conditions**Figure 4. 13:** Standard EGCG degradation profile in 10% (v/v) H<sub>2</sub>O<sub>2</sub> under forced conditions

**Figure 4. 14:** Standard EGCG degradation profile in 0.1 M HCl under forced conditions



**Figure 4. 15:** Standard EGCG degradation profile under heat stress conditions

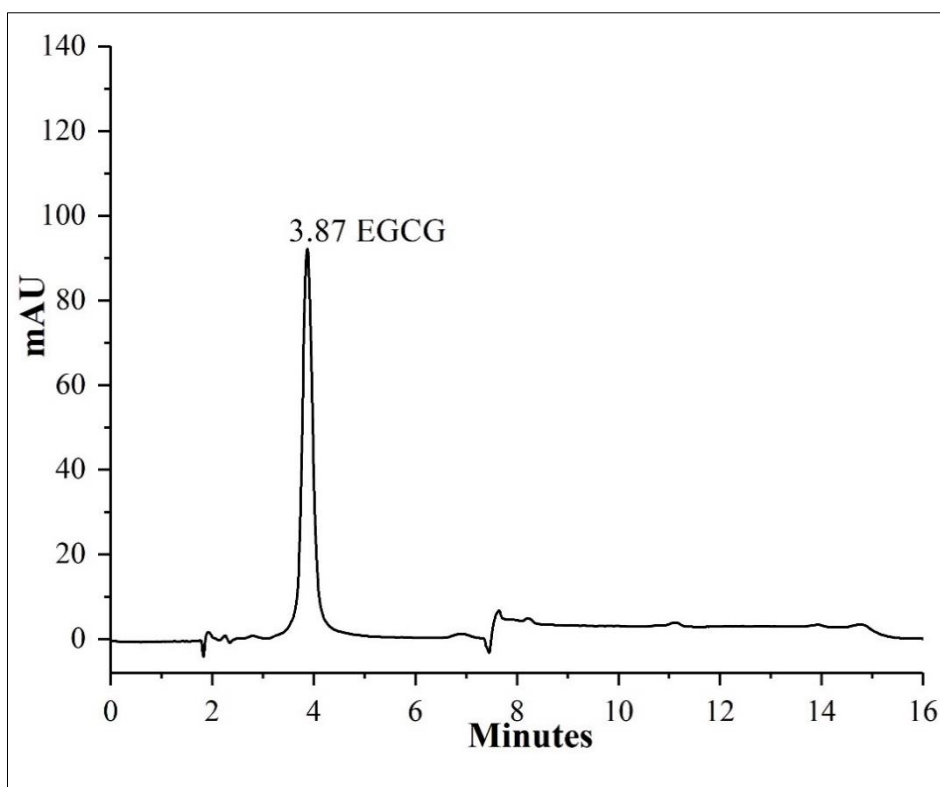


**Figure 4. 16:** Standard EGCG degradation profile under photolytic stress conditions

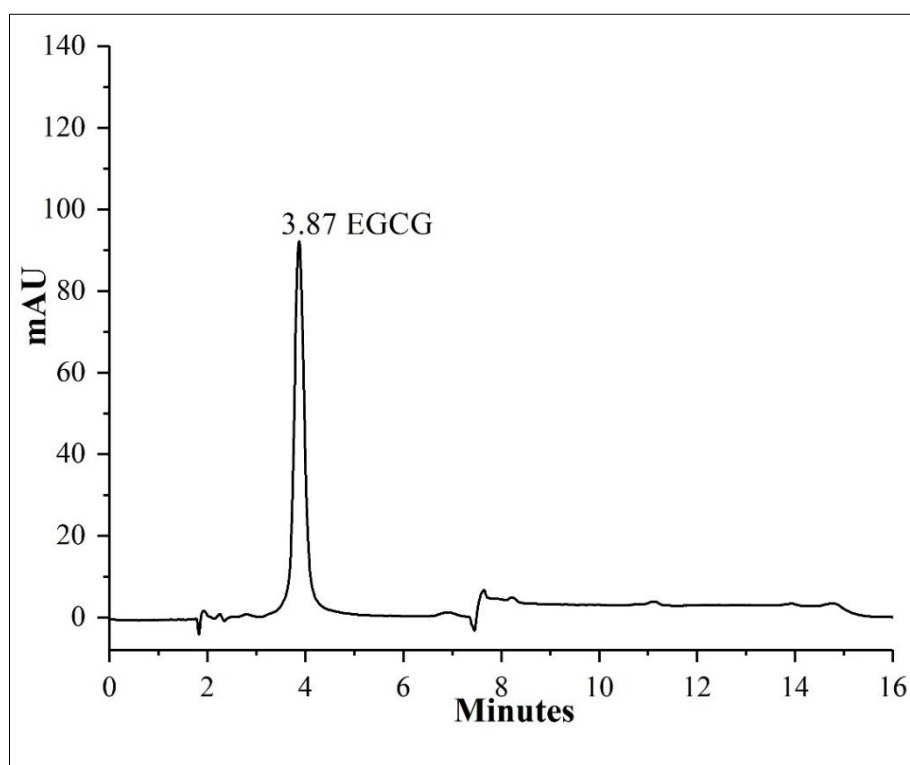


**Figure 4. 17:** Standard EGCG degradation profile under UV light exposure

#### 4.B.2.5. Drug loading and entrapment efficiency of formulated nanoparticles

Drug loading (DL) and entrapment efficiency (EE) are crucial for assessing drug delivery systems (Zhang and Feng, 2006). The DL values for CUR in CSL-NP, EGCG in ESL-NP, and both CUR and EGCG in CESL-NP were 33.12%, 32.11%, and 34.25%, respectively. The EE of CUR in CSL-NP and CESL-NP was 93.66% and 95.12%, while the EE of EGCG in ESL-NP and CESL-NP was 92.34% and 94.35%. CESL-NP showed the highest DL values, with CUR at  $16.69 \pm 0.68\%$  and EGCG at  $17.56 \pm 0.83\%$ , indicating their respective contents in the matrix. To evaluate the synergistic activity of CUR and EGCG in CESL-NP, we employed characterization techniques such as DLS, FTIR, DSC, XRD, AFM, FESEM, and TEM. Detailed DL and EE values are depicted in Table 4.12, and HPLC chromatograms of CUR and EGCG-loaded nanoparticles are shown in Figure 4.18.

**Table 4. 12:** Drug loading and entrapment efficiency of formulated nanoparticles

Formulation	Drug loading (%)		Entrapment efficiency (%)	
	CUR	EGCG	CUR	EGCG
CSL-NP	33.12 ± 0.4	-	93.66 ± 2.3	-
ESL-NP	-	32.11 ± 0.6	-	92.37 ± 1.9
CESL-NP	16.69 ± 0.6	17.56 ± 0.8	95.12 ± 1.8	94.35 ± 2.6

Note: Data expressed as mean ± SEM (n = 3)

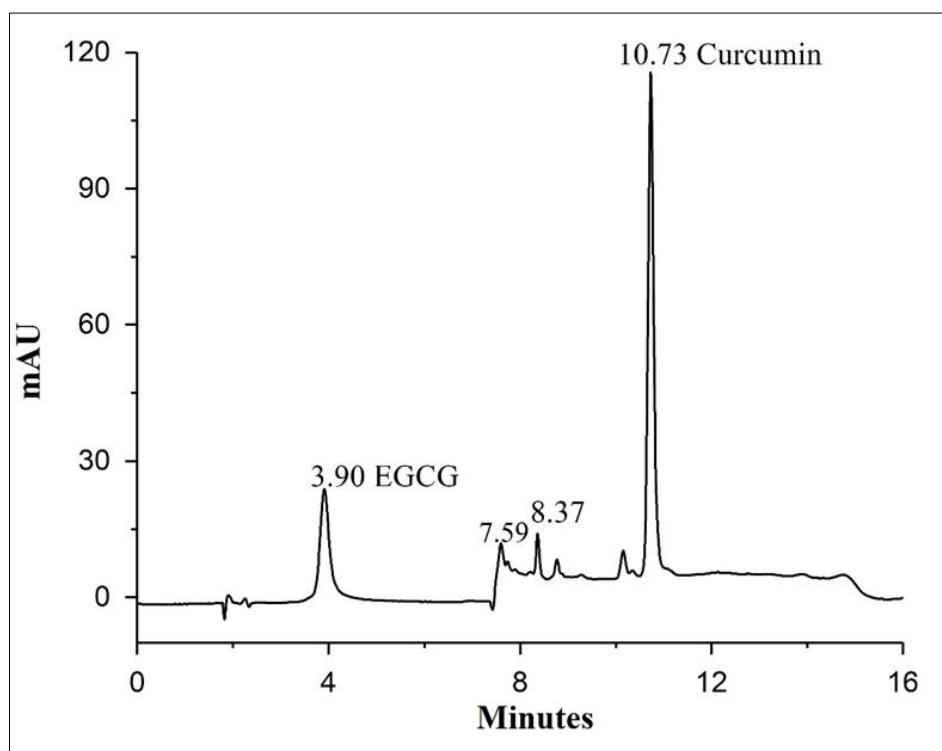


**Figure 4. 18:** HPLC chromatogram of CUR and EGCG in drug-loaded nanoparticles

### 4.B.3. Characterization of formulated nanoparticles

#### 4.B.3.1. DLS analysis

Dynamic light scattering (DLS) was employed to characterize the hydrodynamic diameter of the formulated nanoparticles. The mean hydrodynamic diameter of CSL-NP, ESL-NP, and CESL-NP was determined to be  $145.5 \pm 3.6$  nm,  $128.2 \pm 1.3$  nm, and  $104 \pm 2.4$  nm, respectively. Smaller particle sizes often correlate with enhanced drug release due to increased surface area, facilitating diffusion and penetration through physiological barriers (Zhang and Feng, 2006). Additionally, the polydispersity index (PDI) values for these nanoparticles were

measured as 0.28, 0.32, and 0.21, respectively. A PDI value below 0.3 generally indicates a narrow size distribution, while values above 0.3 suggest a wider range of particle sizes (Yen et al., 2010). Zeta potential reflects the surface charge that affects particle stability through electrostatic repulsion. The zeta potentials of CSL-NP, ESL-NP, and CESL-NP were  $-12.70 \pm 1.8$  mV,  $-13.10 \pm 1.6$ , and  $-08.75 \pm 2.2$ , respectively. These data are summarized in Table 4.13, and the particle size distribution graph of CESL-NP is depicted in Figure 4.19.

**Table 4. 13:** Mean particle size, polydispersity index, and zeta potential of formulated nanoparticles

Formulation	Mean particle size (nm)	PDI*	Zeta potential (mV)
CSL-NP	$145.5 \pm 3.6$	0.28	$-12.70 \pm 1.8$
ESL-NP	$128.2 \pm 1.3$	0.32	$-13.10 \pm 1.6$
CESL-NP	$104 \pm 2.4$	0.21	$-08.75 \pm 2.2$

\*PDI- Polydispersity index; Data expressed as mean  $\pm$  SEM (n = 3)

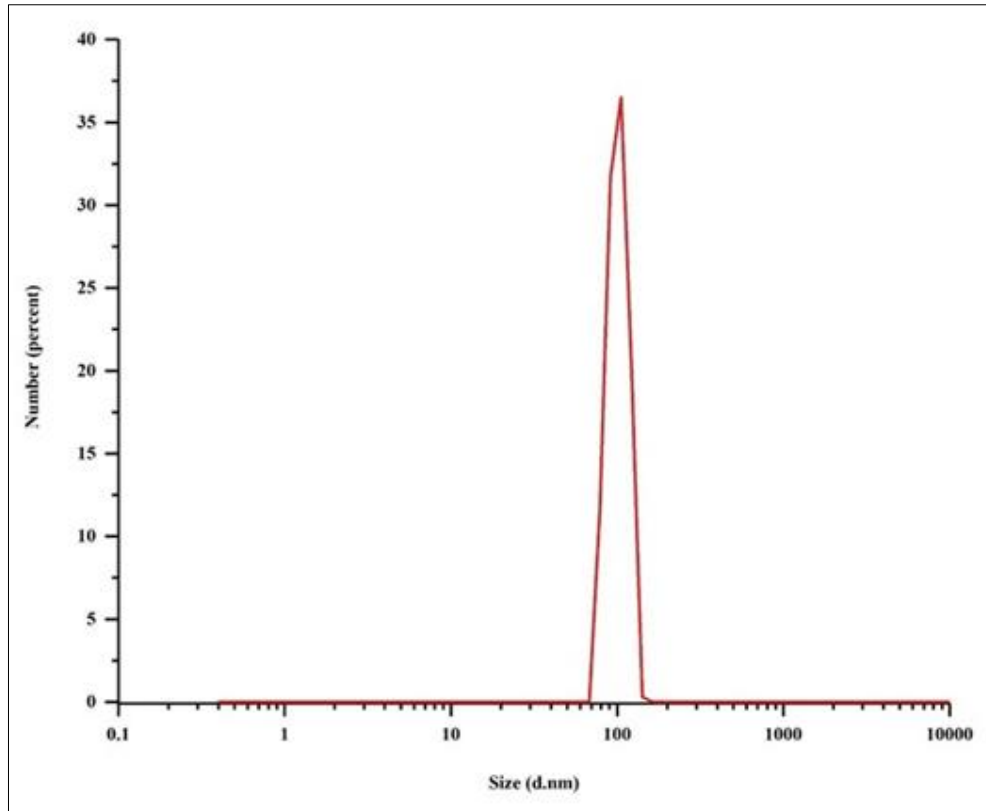


**Figure 4. 19:** Particle size distribution of formulated CESL-NP

#### **4.B.3.2. FTIR analysis**

FTIR analysis was employed to confirm the presence of CUR and EGCG within the CESL-NP formulation and to investigate potential interactions between the pure drugs and the excipients of the nanoformulation. The FTIR spectra of pure CUR, EGCG, physical mixture, blank sample, and CESL-NP are presented in Figure 4.20. The primary peaks for CUR were observed at  $3501\text{ cm}^{-1}$  and  $2945\text{ cm}^{-1}$ , corresponding to the stretching of -OH and the vibration of C-H bonds, respectively (Yen et al., 2010; Nair et al., 2019). Additional peaks associated with CUR were detected at  $1608\text{ cm}^{-1}$  (C=O and C=C),  $1277\text{ cm}^{-1}$  (C-O),  $1426\text{ cm}^{-1}$  (C-H),  $1020\text{ cm}^{-1}$  (C-O-C),  $1159$  and  $801\text{ cm}^{-1}$  (C-H),  $958\text{ cm}^{-1}$  (C=O), and  $714\text{ cm}^{-1}$  (aromatic ring cis vibration) (Yen et al., 2010). Notably, the absence of bands in the carbonyl region ( $1800\text{-}1650\text{ cm}^{-1}$ ) suggests that CUR exists in its biologically active keto-enol tautomer (Hu et al., 2015). The FTIR spectrum of EGCG revealed a prominent peak at  $3385\text{ cm}^{-1}$  and  $3351\text{ cm}^{-1}$ , indicating the stretching vibration of the phenolic hydroxyl group (Xie et al., 2021). Furthermore, a distinct peak at  $1695\text{ cm}^{-1}$  was observed due to the stretching vibration of the C=O group (Li et al., 2022). Other prominent bands in the  $1000\text{-}1500\text{ cm}^{-1}$  range correspond to stretching vibrations of C-O, C-OH, and C-H (Huang et al., 2020). In the CESL-NP spectra, the characteristic absorption peaks of both CUR and EGCG were no longer evident, suggesting a potential interaction between the pure drugs and the nanoparticle matrix.

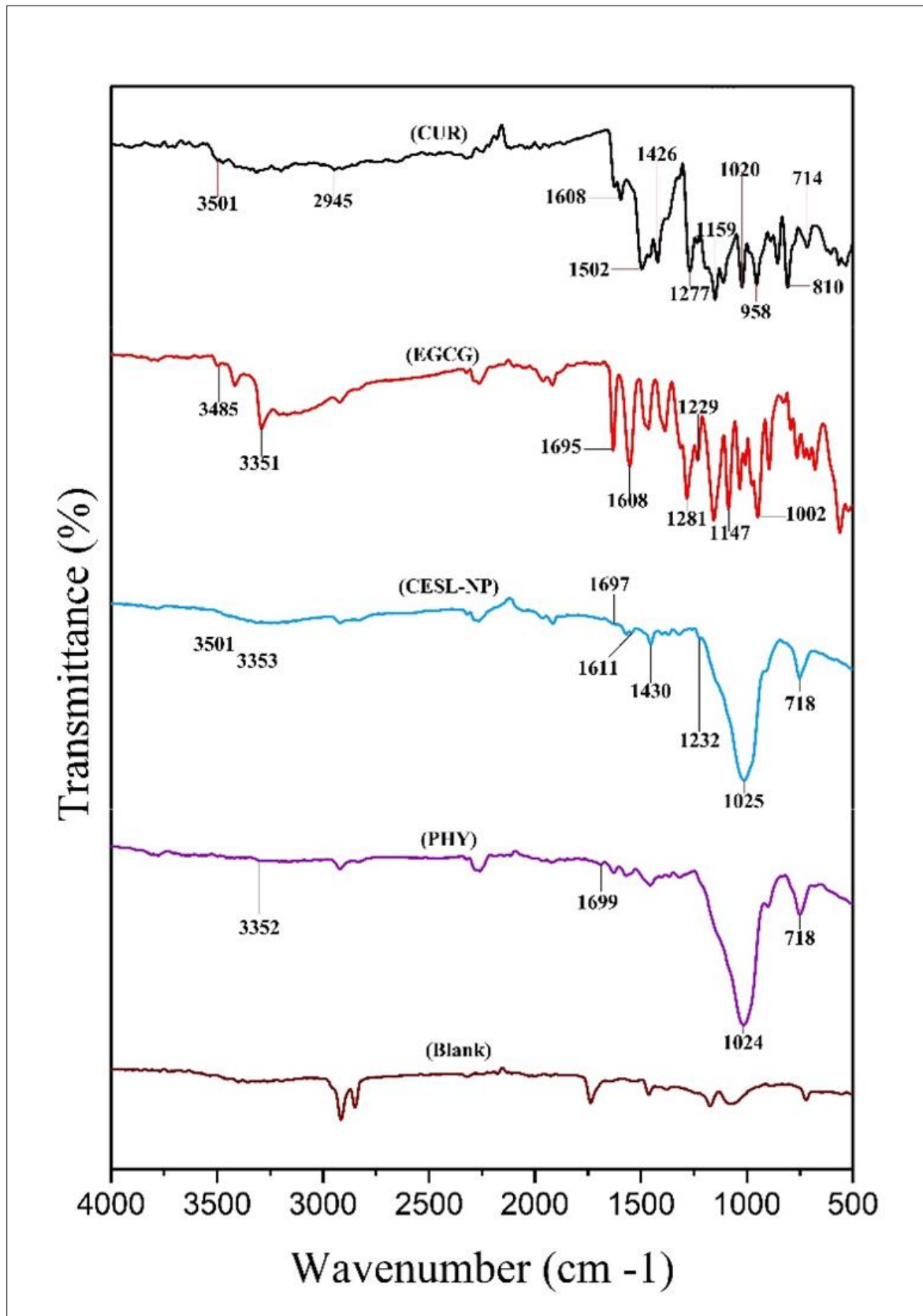


**Figure 4. 20:** FTIR spectra of curcumin, epigallocatechin gallate, CESL-NP, physical mixture, and blank

#### 4.B.3.3. DSC analysis

DSC analysis revealed distinct thermal profiles for the pure compounds, physical mixture, and nanoparticle formulations as depicted in Figure 4.21. CUR exhibited a single endothermic peak at 183.81°C, indicative of its melting point in crystalline form. EGCG, on the other hand, displayed a more complex thermal behavior with an initial endothermic peak at 149.67°C attributed to water loss, followed by two sharp endothermic and exothermic peaks at 236.56°C and 243.43°C, respectively. The exothermic peaks likely result from dehydration reactions within the EGCG structure (Sarmiento et al., 2006). When incorporated into CESL-NP, the thermal behavior of both CUR and EGCG was significantly altered. The characteristic melting peaks observed in the pure compounds were markedly reduced or absent in the nanoparticle formulation. This suggests a potential transformation from a crystalline to an amorphous state upon encapsulation, which could contribute to enhanced solubility compared to the pure drugs (Dora et al., 2010).

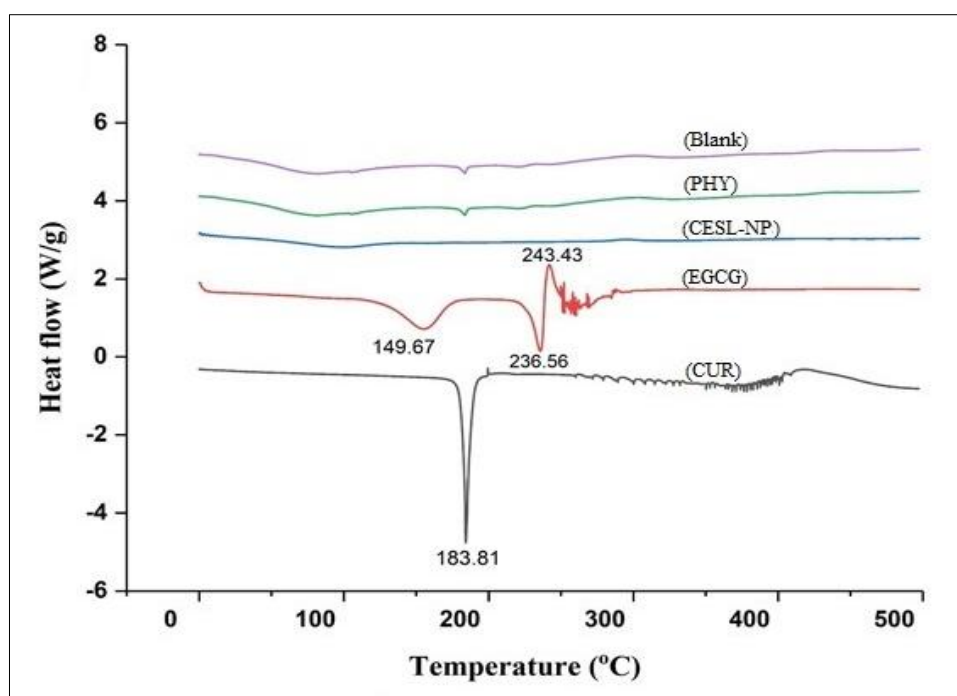


**Figure 4. 21:** DSC thermograms of curcumin, epigallocatechin gallate, CESL-NP, physical mixture, and blank

#### **4.B.3.4. XRD analysis**

XRD analysis was conducted to investigate the crystalline nature of the pure compounds, physical mixture, and nanoparticle formulations, as depicted in Figure 4.22. CUR powder exhibited a highly crystalline structure, as evidenced by its multiple sharp and intense peaks in the XRD pattern. The most prominent peak was observed at 17.25°, with additional peaks at 12.27°, 14.53°, 15.83°, 18.15°, 21.13°, 23.28°, and 24.69°. Similarly, EGCG powder displayed a high degree of crystallinity with intense peaks at 12.08°, 15.37°, 16.88°, 20.55°, 21.36°, 24.36°, and 25.76°. In contrast, the XRD pattern of CESL-NP revealed a significant disappearance of the characteristic peaks associated with CUR and EGCG. This suggests a potential transformation from a crystalline to an amorphous state upon encapsulation within the shellac-LBG polymer matrix (Shaikh et al., 2009). XRD pattern of the physical mixture displayed a combination of peaks from CUR and EGCG, albeit with reduced intensity, suggesting the persistence of crystalline structures. The blank mixture exhibited no discernible peaks, indicating an amorphous nature. Similar behavior has been reported for quercetin dispersed in poly lactic-co-glycolic acid (PLGA) nanoparticles, where the drug was found to exist in an amorphous state (Giannouli et al., 2018).

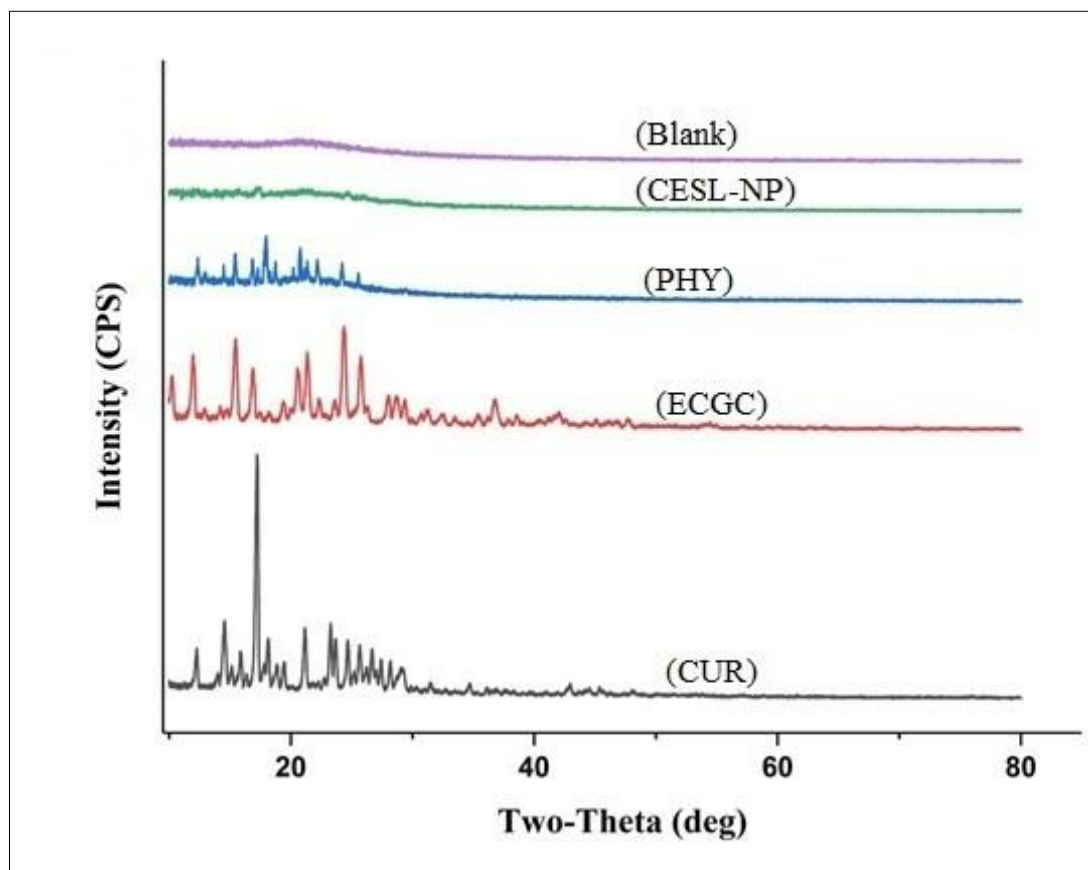


**Figure 4. 22:** XRD patterns of curcumin, epigallocatechin gallate, physical mixture, CESL-NP, and blank

#### 4.B.3.5. AFM analysis

AFM analysis revealed spherical CESL-NPs with no evidence of aggregation, indicating their uniformity and stability at the nanoscale, as depicted in Figure 4.23A. The AFM measurements suggest an average particle size of 65 nm, slightly smaller than the hydrodynamic diameter determined by DLS. This discrepancy can be attributed to the collapsed state of the micelles observed by AFM after water evaporation (Danafar et al., 2014). Figure 3A provides a 3D image of CESL-NPs, further illustrating their well-defined spherical morphology.

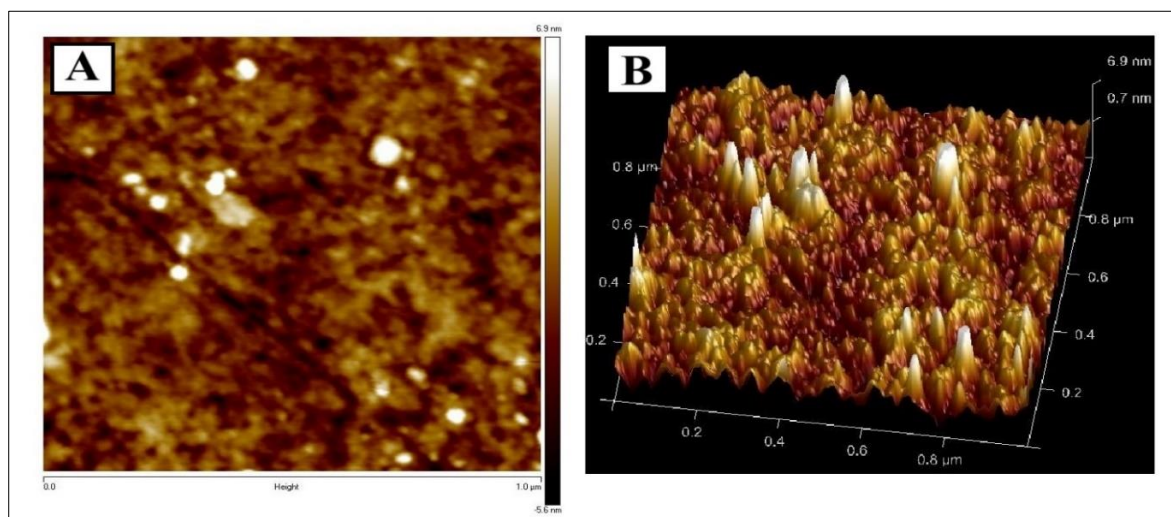


**Figure 4. 23:** Atomic force microscopy images of CESL-NP: (A) Top-down view and (B) 3D topography

#### 4.B.3.6. HRTEM analysis

The HRTEM analysis was used to examine the morphology of the synthesized CESL-NP. It was identified as spherical, with sizes ranging from 60 to 80 nm, as represented in Figure 4.24. The scale bar represents 50 nm.

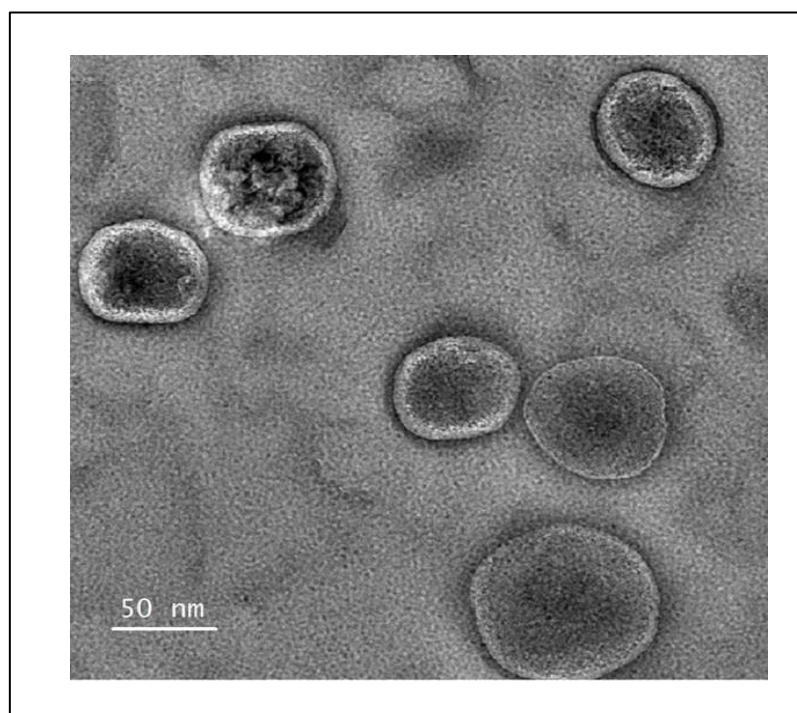


**Figure 4. 24:** TEM image of CESL-NP at the scale 50 nm

#### 4.B.3.7. FESEM analysis

FESEM analysis confirmed the spherical morphology and size of the CESL-NP as observed in DLS, AFM, and HRTEM studies. The prepared nanoparticles exhibited a spherical shape, with clusters of 60-80 nm shellac nanoparticles bound together by the LBG polymer, as shown in the inset of Figure 4.25B. The scale bar represents 1  $\mu\text{m}$  and 500 nm for Figures 4.25A and 4.25B, respectively.

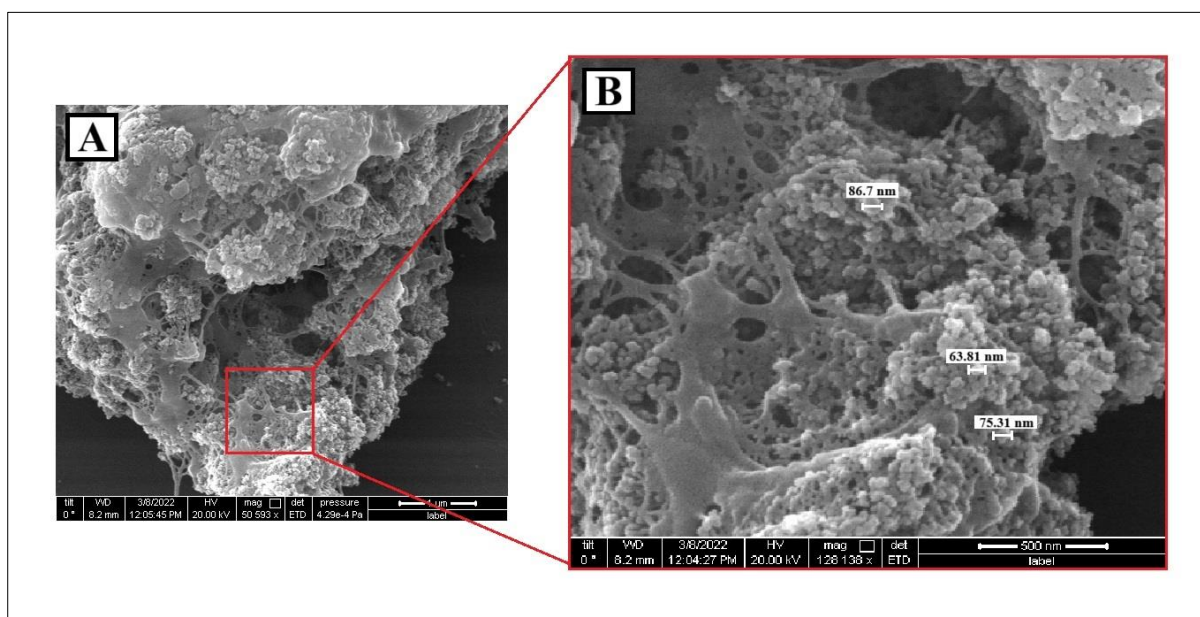


**Figure 4. 25:** FESEM image of CESL-NP at the scale of: (A) 1  $\mu\text{m}$  and (B) 500 nm

#### 4.B.4. Solubility study of CESL-NP

The solubility of free CUR and CUR-loaded CESL-NP was evaluated in water. Notably, free CUR exhibited poor water solubility, forming visible particles and flakes in the solution (tube A in Figure 4.26A). In contrast, CESL-NP demonstrated significantly improved water solubility, dispersing evenly in the solution (tube B in Figure 4.26A). This enhanced dispersion is indicative of successful curcumin encapsulation within the nanoparticles. Furthermore, HPLC analysis revealed a remarkable 70-fold increase in the water solubility of curcumin when encapsulated in CESL-NPs compared to free curcumin. The specific solubility values were determined to be  $75.833 \pm 1.896 \mu\text{g/ml}$  for CESL-NPs and  $1.268 \pm 0.120 \mu\text{g/ml}$  for free CUR,

as depicted in Figure 4.26B. The enhanced solubility CUR in CESL-NP can be attributed to several factors. Encapsulation within the nanoparticles protects CUR from aggregation, while the small particle size increases the surface area available for dissolution (Zhang et al., 2010). Additionally, the transformation of CUR from a crystalline to an amorphous state within the nanoparticles may further contribute to increased solubility and dissolution rate (Kakran et al., 2012b).

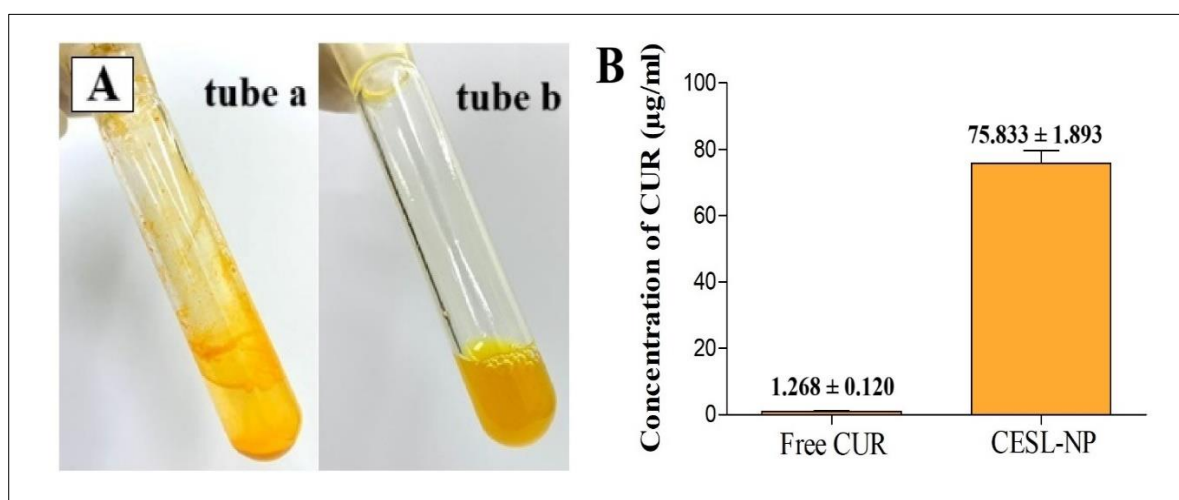


**Figure 4. 26:** Solubility assessment of free CUR and CESL-NP: (A) Image illustrating the lack of solubility of free CUR in water (tube a) versus the solubility of CESL-NP in water (tube b) at a concentration of 10 mg/mL. (B) Water solubility of free CUR and CESL-NP quantified by HPLC (n = 3) and expressed as mean  $\pm$  SEM

#### 4.B.5. Stability study of CESL-NP

The stability of the CUR and EGCG-loaded nanoparticles was assessed over 90 days at 2-8°C by monitoring changes in mean particle size, polydispersity index (PDI), zeta potential, and drug loading (DL), as summarized in Table 4.14. During storage, a slight increase in mean particle size and PDI was observed, accompanied by a slight decrease in zeta potential and DL.

**Table 4. 14:** Characterization of CESL-NP after 90 days: mean particle size, polydispersity index, zeta potential, and drug loading

Sample	Particle size (nm)		Polydispersity index		Zeta potential (mV)		Drug loading (%)			
	Before	After	Before	After	Before	After	CUR		EGCG	
							Before	After	Before	After
CESL-NP	104.0 ±2.4	105.1 ±1.2	0.21	0.23	-08.75 ± 2.2	-07.98 ± 1.5	16.69 ±0.6	16.93 ±0.2	17.51 ±0.8	17.88 ±0.3

Note: All values represent mean  $\pm$  SD, n=3

#### 4.B.6. *In vitro* drug release study of CESL-NP

The *in vitro* drug release behavior of CESL-NP was assessed in SGF (pH 1.2) and SIF (pH 7.4), as illustrated in Figure 4.27. The nanoparticles released the drug in two phases: a rapid burst over 12 hours, followed by a slower, steady release for 7 days. This pattern is likely due to loosely attached drug molecules on the nanoparticle's surface (R.S et al., 2020). Notably, CUR and EGCG were released more rapidly in SIF (pH 7.4) than in SGF (pH 1.2). This pH-dependent release is likely due to shellac's higher dissolution pH of approximately 7.3, making it a suitable carrier for colon-targeted drug delivery (Frag and Leopold, 2011; Thombare et al., 2022).

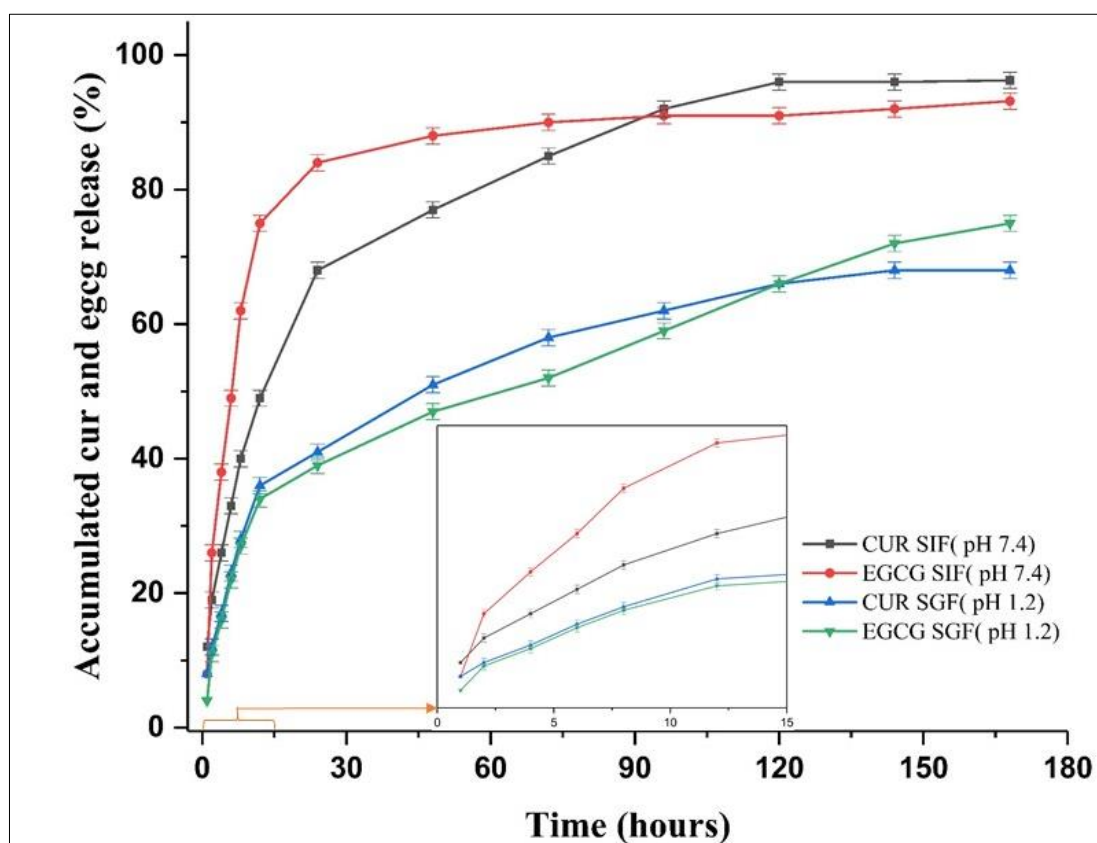


**Figure 4. 27:** Cumulative release comparison of CUR and EGCG from CESL-NP at pH 1.2 and 7.4.

#### 4.B.7. Drug release kinetics of CESL-NP

To elucidate the drug release mechanism, the release kinetics of CUR and EGCG from nanoparticle matrices were investigated by fitting their release data to various kinetic models. Based on the results in Table 4.15, the first-order model best describes the release of CUR in simulated gastric fluid (SGF, pH 1.2), while the Korsmeyer-Peppas model provides the best fit for CUR release in simulated intestinal fluid (SIF, pH 7.4), as evidenced by higher correlation coefficients ( $R^2$ ) of 0.972 and 0.965, respectively. Conversely, the Higuchi model demonstrated superior linearity for EGCG release in both media, with  $R^2$  values of 0.956 and 0.818. Furthermore, the release exponent ( $n$ ) values, derived from the Korsmeyer-Peppas model, provided valuable insights into the release mechanisms. For CUR, the  $n$  values were consistently below 0.43, indicating Fickian diffusion, a mechanism characterized by diffusion-

controlled release. In contrast, the  $n$  values for EGCG fell within the range of 0.43 to 0.85, suggesting non-Fickian diffusion. This intermediate  $n$  value range implies that both diffusion and other factors, such as matrix erosion or swelling, contribute to the release of EGCG from the nanoparticles (Maji et al., 2015).

**Table 4. 15:** In vitro drug release kinetics of CUR and EGCG: Fitted models,  $R^2$  values, and release exponents ( $n$ ) from CESL-NP

Drugs	Different Kinetics model	Equations and $R^2$ value of corresponding release kinetics model	
		Release in SGF (pH 1.2)	Release in SIF (pH 7.4)
CUR	Zero order	$Y = 0.785X + 28.58$ $R^2 = 0.941$	$Y = 0.732X + 28.58$ $R^2 = 0.935$
	First order	$Y = -0.018X + 1.852$ $R^2 = 0.972$	$Y = -0.021X + 1.275$ $R^2 = 0.881$
	Higuchi	$Y = 7.019X + 15.53$ $R^2 = 0.918$	$Y = 7.575X + 17.85$ $R^2 = 0.842$
	Hixon–Crowell	$Y = -0.018X + 3.852$ $R^2 = 0.962$	$Y = -0.028X + 3.13$ $R^2 = 0.891$
	Korsmeyer–Peppas	$Y = 0.278X + 1.213$ $R^2 = 0.932$	$Y = 0.259X + 1.320$ $R^2 = 0.965$
	Release exponent value	$n = 0.36$	$n = 0.39$
EGCG	Zero order	$Y = 1.610X + 15.15$ $R^2 = 0.905$	$Y = 1.15X + 23.46$ $R^2 = 0.625$
	First order	$Y = -0.013X + 1.525$ $R^2 = 0.798$	$Y = -0.014X + 1.451$ $R^2 = 0.632$
	Higuchi	$Y = 10.58X - 1.325$ $R^2 = 0.956$	$Y = 9.38X + 5.685$ $R^2 = 0.818$
	Hixon–Crowell	$Y = -0.027X + 3.85$ $R^2 = 0.855$	$Y = -0.053X + 3.152$ $R^2 = 0.685$
	Korsmeyer–Peppas	$Y = 0.571X + 0.721$ $R^2 = 0.921$	$Y = 0.612X + 0.785$ $R^2 = 0.787$
	Release exponent value	$n = 0.58$	$n = 0.51$

#### **4.B.8. *In vivo* antidiabetic and antinephritic studies**

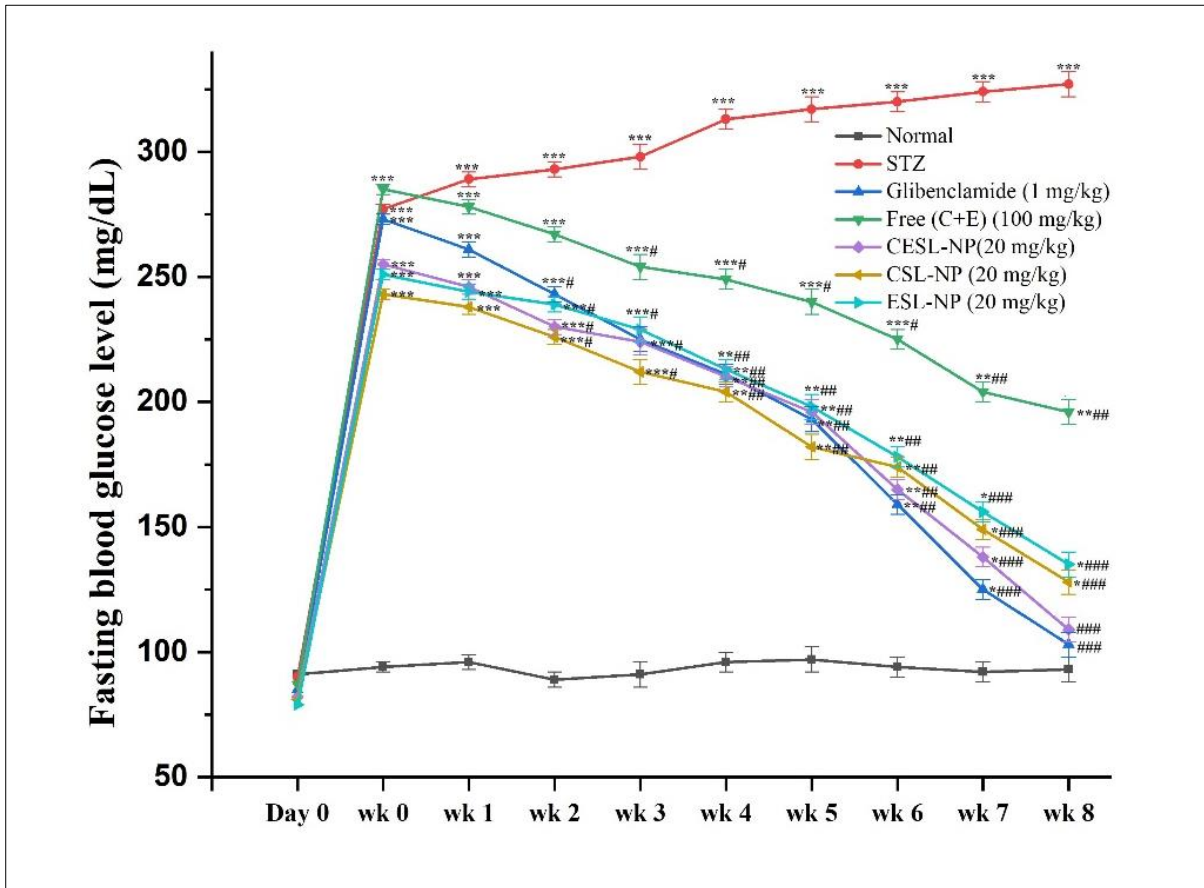
##### **4.B.8.1. Effects of CESL-NP on glycemic control in STZ-induced diabetic mice**

Table 4.16 and Figure 4.28 illustrates the fasting blood glucose (FBGL) levels of mice during the study period, while Figure 4.29 depicts the percentage inhibition of FBGL. The normal control group maintained FBGL levels within the range of  $94.2 \pm 5.6$  mg/dL to  $98.5 \pm 6.3$  mg/dL. In contrast, STZ-induced diabetic mice exhibited a significant elevation in FBGL, with a percentage increase ranging from 203.75% to 227.58%. Eight weeks of treatment with glibenclamide (1 mg/kg b.w.) effectively reduced FBGL by 98.24%. Similarly, CESL-NP (20 mg/kg b.w.) demonstrated a significant reduction in FBGL of 95.61%. The free drug combination (CUR+EGCG) at 100 mg/kg b.w. resulted in a 36.14% decrease in FBGL. Furthermore, single drug treatments with CSL-NP (20 mg/kg b.w.) and ESL-NP (20 mg/kg b.w.) led to reductions of 81.28% and 78.10%, respectively. These findings suggest a synergistic effect between CUR and EGCG when combined in CESL-NP. At a concentration of 10 mg/kg for each drug, CESL-NP exhibited a 38.68-fold greater inhibition of blood glucose elevation compared to the free drug combination.

**Table 4. 16:** Antidiabetic activity of glibenclamide, free (C+E), CESL-NP, CSL-NP, and ESL-NP on STZ-induced diabetic mice

Time period	Normal group (mg/dL)	STZ group (mg/dL)	STD group (mg/dL)	Free (C+E) (100 mg/kg) (mg/dL)	CESL-NP (20 mg/kg) (mg/dL)	CSL-NP (20 mg/kg) (mg/dL)	ESL-NP (20 mg/kg) (mg/dL)
<b>Before STZ</b>	91 ± 1.23	90 ± 0.99	85 ± 0.36	87 ± 1.11	82 ± 2.36	81 ± 2.33	79 ± 3.26
<b>After STZ</b>	94 ± 0.91	277 ± 3.51 <sup>c</sup>	273 ± 2.66 <sup>c</sup>	285 ± 1.89 <sup>c</sup>	255 ± 2.01 <sup>c</sup>	243 ± 1.55 <sup>c</sup>	251 ± 2.16 <sup>c</sup>
<b>Week 1</b>	96 ± 0.73	289 ± 2.36 <sup>c</sup>	261 ± 2.54 <sup>c</sup>	278 ± 1.66 <sup>c</sup>	246 ± 1.86 <sup>c</sup>	238 ± 1.89 <sup>c</sup>	244 ± 1.56 <sup>c</sup>
<b>Week 2</b>	89 ± 1.30	293 ± 2.75 <sup>c</sup>	243 ± 2.42 <sup>c,d</sup>	267 ± 2.12 <sup>c</sup>	230 ± 1.63 <sup>c,d</sup>	226 ± 2.45 <sup>c,d</sup>	239 ± 2.36 <sup>c,d</sup>
<b>Week 3</b>	91 ± 1.21	298 ± 2.63 <sup>c</sup>	225 ± 1.96 <sup>c,d</sup>	254 ± 2.03 <sup>c,d</sup>	224 ± 1.22 <sup>c,d</sup>	212 ± 2.36 <sup>c,d</sup>	229 ± 2.14 <sup>c,d</sup>
<b>Week 4</b>	96 ± 0.91	313 ± 1.96 <sup>c</sup>	211 ± 1.56 <sup>b,e</sup>	249 ± 1.84 <sup>c,d</sup>	210 ± 1.87 <sup>b,e</sup>	204 ± 2.06 <sup>b,e</sup>	213 ± 1.96 <sup>b,e</sup>
<b>Week 5</b>	97 ± 0.23	317 ± 2.78 <sup>c</sup>	193 ± 1.86 <sup>b,e</sup>	240 ± 1.69 <sup>c,d</sup>	196 ± 2.36 <sup>b,e</sup>	182 ± 1.86 <sup>b,e</sup>	198 ± 1.56 <sup>b,e</sup>
<b>Week 6</b>	94 ± 0.65	320 ± 2.93 <sup>c</sup>	159 ± 1.43 <sup>b,e</sup>	225 ± 1.22 <sup>c,d</sup>	165 ± 1.64 <sup>b,e</sup>	174 ± 1.33 <sup>b,e</sup>	178 ± 1.23 <sup>b,e</sup>
<b>Week 7</b>	92 ± 0.98	324 ± 3.66 <sup>c</sup>	125 ± 1.57 <sup>a,f</sup>	204 ± 2.01 <sup>b,e</sup>	138 ± 1.98 <sup>a,f</sup>	149 ± 1.49 <sup>a,f</sup>	156 ± 1.36 <sup>a,f</sup>
<b>Week 8</b>	93 ± 1.25	327 ± 2.36 <sup>c</sup>	103 ± 1.45 <sup>f</sup>	196 ± 1.36 <sup>b,e</sup>	109 ± 1.36 <sup>f</sup>	128 ± 1.65 <sup>a,f</sup>	135 ± 1.57 <sup>a,f</sup>

Note: All values represent mean ± SD, n=5; <sup>a</sup>p ≤ 0.05 considered significant, <sup>b</sup>p ≤ 0.01 moderately significant, <sup>c</sup>p ≤ 0.001 highly significant vs. the normal group; <sup>d</sup>p ≤ 0.05 considered significant, <sup>e</sup>p ≤ 0.01 moderately significant, <sup>f</sup>p ≤ 0.001 highly significant vs. the STZ group.



**Figure 4. 28:** Effects of glibenclamide, free (C+E), CESL-NP, CSL-NP, and ESL-NP on blood glucose in STZ-diabetic mice. Data are presented as mean  $\pm$  SEM based on five readings. Statistical significance was determined using a p-value of less than or equal to 0.05 (\*), 0.01 (\*\*), or 0.001 (\*\*\*) compared to the normal group. Similarly, significance was assessed against the STZ group using p-values of less than or equal to 0.05 (#), 0.01 (##), or 0.001 (###).

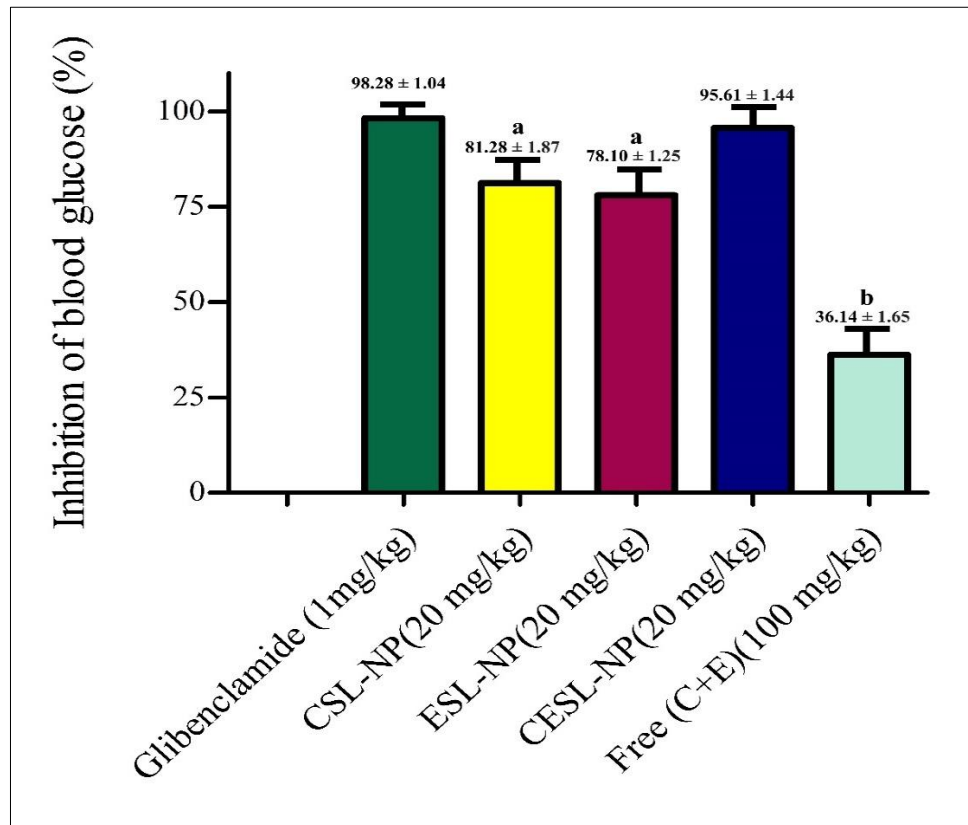


**Figure 4. 29:** Effects of glibenclamide, free (C+E), CESL-NP, CSL-NP, and ESL-NP on fasting blood glucose inhibition in STZ-diabetic mice. Glibenclamide (1 mg/kg) for 8 weeks reduced fasting blood glucose to ~100 mg/dL. The percentage inhibition was calculated by comparing the eighth-week fasting blood glucose values to those of the glibenclamide group. Data are presented as mean  $\pm$  SEM (n = 5); <sup>a</sup>p  $\leq$  0.05 considered significant, <sup>b</sup>p  $\leq$  0.01 moderately significant vs. the standard group

#### 4.B.8.2. Effects of CESL-NP on renal parameters in mice with early diabetic nephropathy

After 8 weeks of treatment, the kidney shape and weight in mice treated with glibenclamide, the free drugs (CUR+EGCG), and CESL-NP remained within normal ranges, as illustrated in Figure 4.30. In contrast, the untreated group exhibited significant kidney swelling and excessive weight gain, as witnessed in the early stages of diabetic nephropathy (Pourghasem et al., 2015). The renal shape and kidney weight of the treated mice improved remarkably compared to the STZ-induced diabetic group. Diabetic mice showed a marked increase in the kidney hypertrophy index (KHI), which represents the ratio of kidney weight to body weight

(Table 4.17). Mice treated with glibenclamide experienced a considerable gain in body weight and a significant decrease in kidney weight and KHI compared to the diabetic group. Those treated with free drugs (CUR+EGCG) exhibited a slight decrease in kidney weight and KHI, along with a slight increase in body weight. Treatment with CESL-NP not only reduced kidney weight but also prevented weight loss compared to untreated diabetic mice. Notably, CESL-NP administration led to a significant decrease in KHI, a critical marker for the onset of diabetic nephropathy. Thus, CESL-NP demonstrated efficacy in maintaining kidney weight, body weight, and KHI values within normal ranges.

**Table 4. 17:** Antinephritic effects of glibenclamide, free (C+E) and CESL-NP on renal parameters in mice with early diabetic nephropathy

Groups	Kidney weight (g)	Body weight (g)	KHI* X 100
Normal group	0.202 ± 0.004	28.52 ± 0.633	0.708
STZ group	0.271 ± 0.005 <sup>a</sup>	19.94 ± 0.668 <sup>a</sup>	1.359 <sup>a</sup>
STD group (1 mg/kg)	0.210 ± 0.005 <sup>b</sup>	29.22 ± 0.780 <sup>b</sup>	0.718 <sup>b</sup>
Free drug (C+E) (100 mg/kg)	0.238 ± 0.007 <sup>c,d</sup>	24.76 ± 0.727 <sup>c,d</sup>	0.961 <sup>c,d</sup>
CESL-NP (20 mg/kg)	0.220 ± 0.004 <sup>b</sup>	28.28 ± 0.746 <sup>b</sup>	0.777 <sup>b</sup>

\*KHI- Kidney hypertrophy index; Data are presented as mean ± SEM (n = 5); a indicates p < 0.001 compared to the normal group; b indicates p < 0.001 compared to the STZ group; c indicates p < 0.05 compared to the normal group; d indicates p < 0.01 compared to the STZ group.

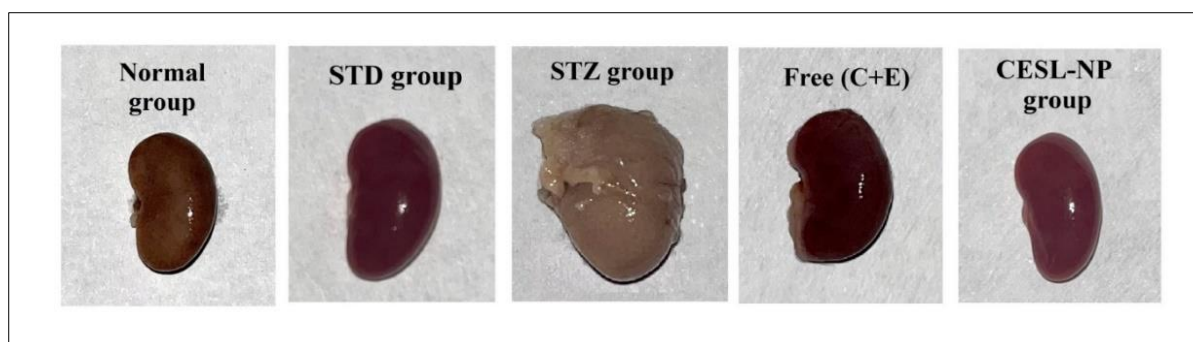


**Figure 4. 30:** Impact of different treatments on kidney structure: glibenclamide (1mg/kg), free (C+E) (100 mg/kg), and CESL-NP (20 mg/kg)

#### 4.B.8.3. Effects of CESL-NP on renal biomarkers in early diabetic nephropathy in mice

The therapeutic effects of CESL-NP on serum albumin (Alb), serum creatinine (Scr), and blood urea nitrogen (BUN) were assessed in diabetic mice. Compared to the normal control group, untreated diabetic mice showed a significant decrease in Alb levels and a marked increase in Scr and BUN levels, indicating the onset of diabetic nephropathy (Gil et al., 2012). Treatment with the free drug combination (CUR+EGCG) resulted in slight improvements in Alb levels and reductions in Scr and BUN levels compared to the diabetic control group. However, CESL-NP exhibited a more pronounced effect, significantly lowering Scr levels and reducing BUN levels. These findings suggest that CESL-NP may offer protective effects against diabetic nephropathy. Additionally, CESL-NP maintained biochemical parameters closer to those of the normal control group, further supporting their potential therapeutic benefits in managing diabetic nephropathy. Table 4.18 and Figures 4.31(A-C) illustrates the antinephritic effects of various treatment groups on serum albumin, serum creatinine, and blood urea nitrogen levels in mice with early diabetic nephropathy.

**Table 4. 18:** Effect of glibenclamide, free (C+E) and CESL-NP on serum albumin, serum creatinine, and blood urea nitrogen (BUN) of diabetic mice

Groups	Albumin (g/dL)	Creatinine (mg/dL)	BUN (mg/dL)
Normal group	2.836 ± 0.065	0.292 ± 0.006	31.366 ± 0.608
STZ group	1.380 ± 0.109 <sup>a</sup>	0.452 ± 0.014 <sup>a</sup>	48.762 ± 1.955 <sup>a</sup>
STD group (1 mg/kg)	2.628 ± 0.089 <sup>b</sup>	0.302 ± 0.009 <sup>b</sup>	34.156 ± 0.714 <sup>b</sup>
Free (C+E) (100 mg/kg)	2.212 ± 0.077 <sup>c,d</sup>	0.358 ± 0.015 <sup>c,d</sup>	39.514 ± 1.317 <sup>c,d</sup>
CESL-NP (20 mg/kg)	2.636 ± 0.081 <sup>b</sup>	0.314 ± 0.013 <sup>b</sup>	34.900 ± 1.314 <sup>b</sup>

Note: Data are presented as mean ± SEM (n = 5); a indicates p < 0.001 compared to the normal group; b indicates p < 0.001 compared to the STZ group; c indicates p < 0.05 compared to the normal group; d indicates p < 0.01 compared to the STZ group.

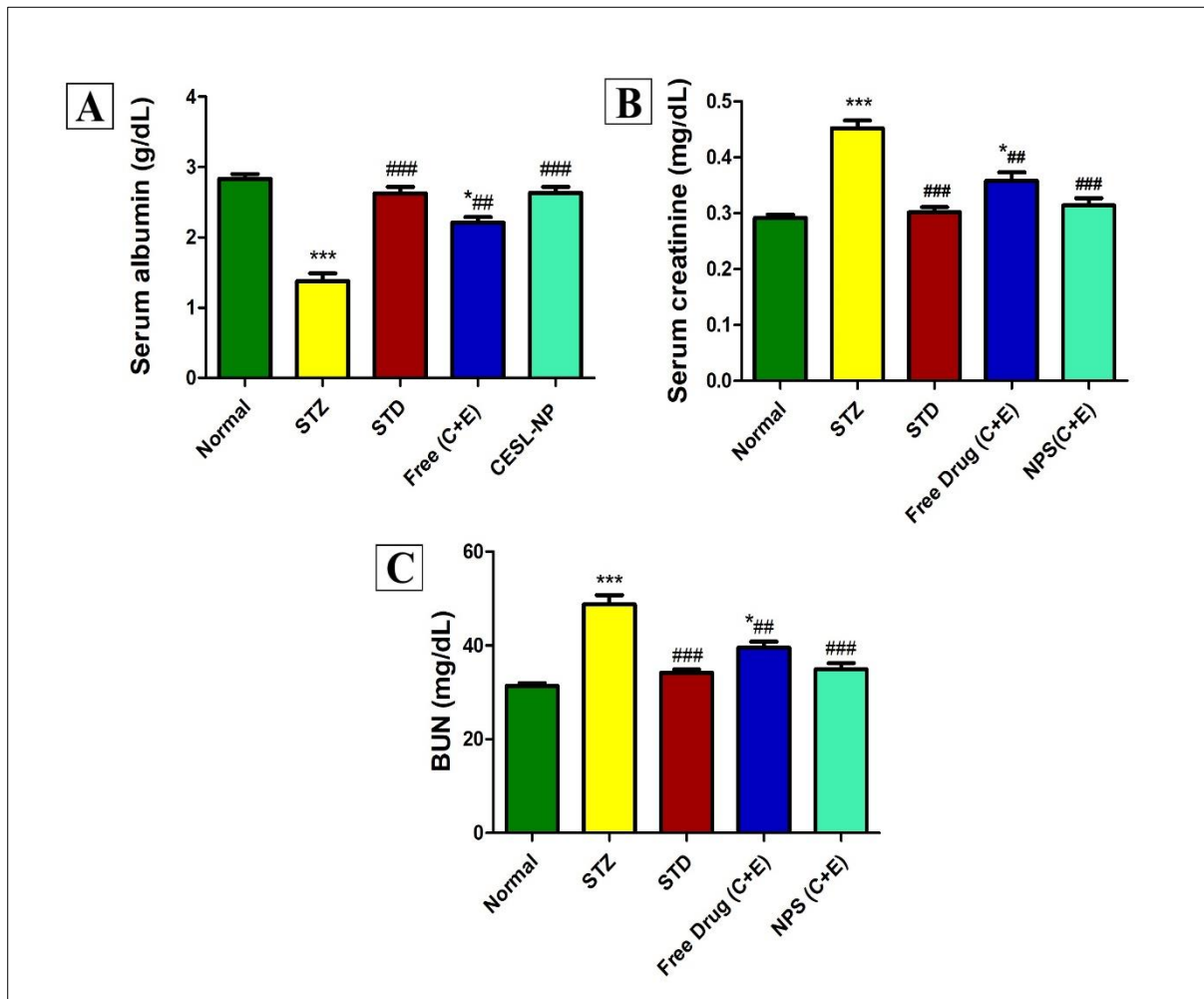


**Figure 4. 31:** Antinephritic effects of glibenclamide, free (C+E), and CESL-NP on: (A) serum albumin, (B) serum creatinine, and (C) blood urea nitrogen levels in mice with early diabetic nephropathy. Data are presented as mean  $\pm$  SEM (n = 5); level of significance: \* $p \leq 0.05$ , \*\* $p \leq 0.01$ , \*\*\* $p \leq 0.001$  vs. normal group; # $p \leq 0.05$ , ## $p \leq 0.01$ , ### $p \leq 0.001$  vs. STZ group

#### 4.B.8.4. Effects of CESL-NP on pancreatic and renal tissue in mice with early diabetic nephropathy

Figures 4.32 (A-E) illustrates the effects of glibenclamide, free (CUR+EGCG), and CESL-NP on pancreatic tissues using H&E staining at 100x magnification. Figure 4.32B, we observe a significant reduction in beta cells within the islet regions of STZ-induced diabetic mice. Diabetic mice also show a markedly lower number of pancreatic islets compared to healthy controls. Figures 4.32C and 4.32E demonstrate that 8 weeks of treatment with glibenclamide (1 mg/kg) and CESL-NP (20 mg/kg), respectively, substantially repaired islet damage and

improved the structural integrity of pancreatic islet beta-cells and tissues. Our histopathological analyses indicate that STZ disrupts and causes atrophy of pancreatic islet structures in diabetic mice. However, CESL-NP treatment significantly repairs pancreatic damage and enhances the architectural robustness of islet cells. These findings suggest that CESL-NP protects pancreatic tissues in diabetic mice, effectively shielding them against oxidative stress.

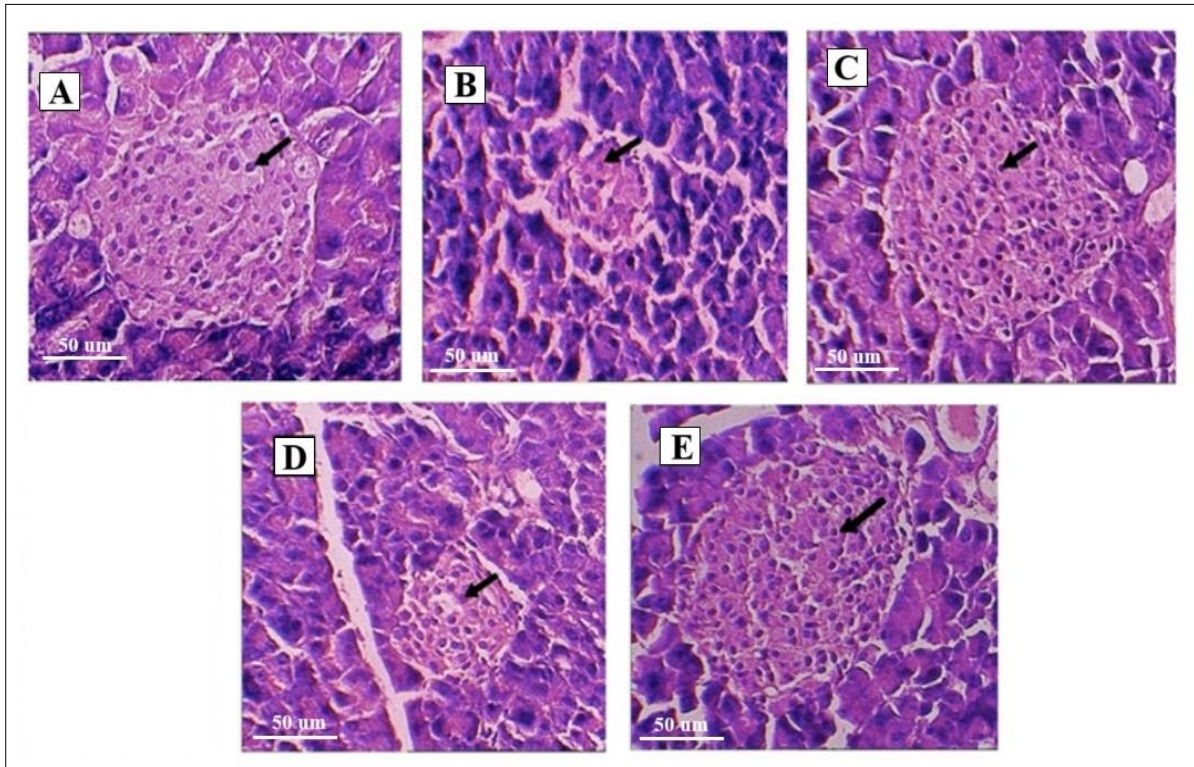


**Figure 4. 32:** Histopathological photomicrographs of pancreatic islet sections (H&E stain, 100x; scale bar: 50  $\mu\text{m}$ ). (A) Control: normal pancreatic islets and  $\beta$ -cells (arrow). (B) STZ-induced diabetes: shrinkage of islet volume and reduced  $\beta$ -cell count. (C) Glibenclamide treated (1 mg/kg): restored normal architecture. (D) Free (C + E) treated (100 mg/kg): partial recovery of islet volume and  $\beta$ -cell numbers. (E) CESL-NP treated (20 mg/kg): complete recovery of islet volume and  $\beta$ -cell numbers. (Arrow:  $\beta$ -cells)

The renal histopathology was examined, focusing on the glomeruli structures in both treated and untreated mice, as shown in Figure 4.33(A-E). In the normal group, we observed well-organized and undamaged Bowman's capsules, glomeruli, and tubular structures (Figure 4.33A). Conversely, the untreated diabetic group displayed irregular renal tissue arrangements,

as seen in Figure 4.33B. This included expanded urine spaces, constricted capillary loops, atrophied tubular structures, and increased vacuolization of tubular epithelial cells. However, treatments with glibenclamide (1 mg/kg) and CESL-NP (20 mg/kg) significantly improved these abnormal histological features, as illustrated in Figures 4.33C and 4.33E. The histopathological findings indicate that CESL-NP significantly mitigates diabetic damage in renal tissues. It enhances the structural integrity of glomeruli and tubules, reduces pathological changes, and demonstrates potential as a therapeutic agent for diabetes-induced renal damage.

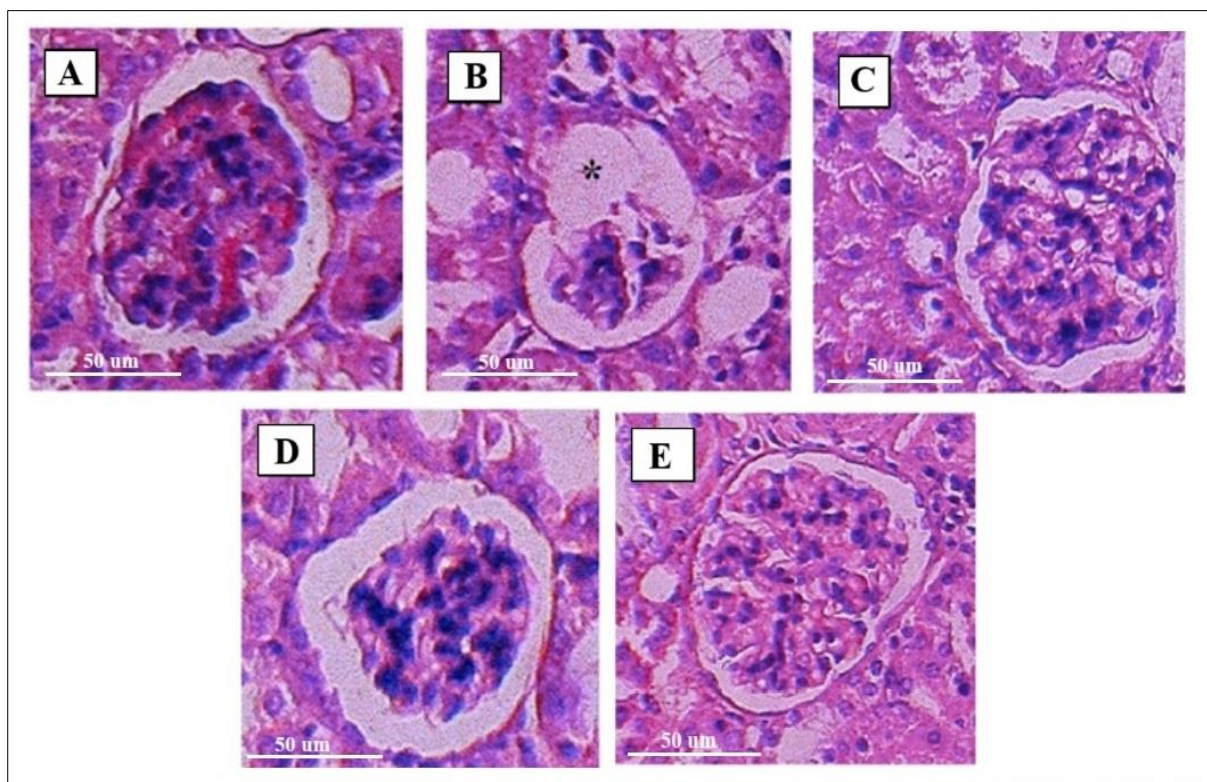


**Figure 4. 33:** Histopathological photomicrographs of kidney sections (H&E stain, 100x; scale bar: 50 μm). (A) Control: normal glomeruli and tubules. (B) STZ-induced diabetes: epithelial denudation and tubular necrosis. (C) Glibenclamide treated: restored normal architecture. (D) Free (C+E) treated: partial recovery of glomerular and tubular structures. (E) CESL-NP treated: near-normal architecture. (Asterisk: expansion in urinary space)

#### 4.C. DISCUSSION

Recent trends show that combining multiple medications is becoming a popular strategy for managing diabetes. This approach aims to lower blood sugar levels and slow the progression of diabetic nephropathy (DN), more effectively than using a single drug (Selby and Taal, 2020). Curcumin (CUR) and epigallocatechin gallate (EGCG) are two natural compounds with demonstrated anti-oxidant, hypoglycemic, anti-inflammatory, and immunomodulatory properties (Soetikno et al., 2013; Huang et al., 2013; Mohan et al., 2017; Yoon et al., 2014). These characteristics suggest their potential to ameliorate DN through various molecular pathways. However, their poor aqueous solubility and bioavailability limit their therapeutic effectiveness when administered directly (Ching et al., 2019; Li et al., 2020).

This study aimed to address these limitations by developing a novel nanocomposite carrier system (CESL-NP) based on shellac and locust bean gum for co-delivery of CUR and EGCG. M cells in the Peyer's patches of the intestine are known to have a particular affinity for mannose residues (Davitt and Lavelle, 2015; Alonso-Sande et al., 2009; Tomizawa et al., 1993). Locust bean gum, a galactomannan polysaccharide, provides mannose moieties on the surface of CESL-NP, facilitating its preferential uptake by M cells. This targeted delivery approach offers the potential for synergistic effects of the combined drugs.

To quantify CUR and EGCG content in CESL-NP, a simple and reliable reverse-phase HPLC method was established. This method enabled assessments such as drug loading, entrapment efficiency, solubility, stability, and *in vitro* release studies. Using a single isosbestic UV wavelength with a DAD detector, we identified CUR and EGCG absorption maxima at 262 nm and 275 nm, respectively. Both spectra crossed at 268 nm, the isosbestic wavelength, chosen for HPLC detection. CUR and EGCG were eluted at 10.7 and 3.9 minutes, respectively. The method underwent successful validation for specificity, accuracy, precision, linearity, robustness, and sensitivity, aligning with ICH Q2R1 guidelines (Sai et al., 2021; Madriwala

and Jays, 2022). Forced degradation studies assessed the method's suitability for analyzing degradation products and identifying potential stability issues during formulation (Rayudu et al., 2022; Devi and Rambabu, 2022). Aerosil 200 was subsequently employed to solidify the liquid CESL-NP formulation. Solidified CESL-NP exhibited excellent drug loading and entrapment efficiency, as shown in Table 4.12.

DLS measurements confirmed the successful encapsulation of CUR and EGCG in the shellac and locust bean gum matrix, indicated by nanometric size, a relatively narrow size distribution, and a high negative surface charge. Further morphological analyses using AFM, FESEM, and TEM showed spherical nanoparticles with no aggregation, suggesting uniformity and nanoscale stability.

FTIR, DSC, and XRD analyses provided insights into the physicochemical interactions between drugs and excipients within CESL-NP. The formation of new peaks or disappearance of characteristic peaks of pure drugs suggested interactions such as weak hydrogen bonds, van der Waals forces, and dipole-dipole interactions. Additionally, encapsulation transformed the crystalline nature of pure drugs into an amorphous state within the nanoparticle matrix.

Solubility studies demonstrated a significant improvement in the water solubility of CUR encapsulated within CESL-NP, with a 70-fold increase compared to free CUR. This enhancement can be attributed to the protection from aggregation offered by the nanoparticle matrix and the increased surface area available for dissolution due to the small particle size (Zhang et al., 2010). Furthermore, the transformation of CUR from a crystalline to an amorphous state likely contributes to its faster dissolution rate (Kakran et al., 2012b). *In vitro* release studies revealed an initial burst release of CUR and EGCG from CESL-NP within the first 12 hours, followed by a sustained release pattern for up to seven days in simulated gastric fluid (SGF) and simulated intestinal fluid (SIF) media. This biphasic release profile suggests a promising approach for maintaining therapeutic drug levels over an extended period.

The antidiabetic efficacy of CESL-NP was compared with independent drug-loaded nanoparticles (CSL-NP and ESL-NP), free drug (CUR+EGCG), and the standard drug glibenclamide in an eight-week *in vivo* study. Notably, our formulation (CESL-NP) demonstrated a superior ability to reduce fasting blood glucose levels to near normal ranges compared to glibenclamide. Histological analysis of pancreatic tissues revealed evidence of beta-cell regeneration and increased pancreatic islet volume in the CESL-NP treated group. These findings highlight the improved efficacy of CESL-NP in managing diabetes.

Additionally, the antinephritic activity of CESL-NP demonstrated significant reductions in kidney weight, kidney hypertrophy index, and maintained body weight within normal ranges. Furthermore, CESL-NP was able to preserve normal serum albumin levels and significantly reduce serum creatinine and BUN levels. Histological analysis of kidney tissues revealed restoration of kidney architecture and alleviation of podocyte injury, suggesting the potential of CESL-NP in mitigating the progression of diabetic nephropathy.

These observations emphasized the fact that CUR and EGCG encapsulated in CESL-NP have better bioavailability and effectiveness as antidiabetic and antinephritic agents compared to the free drugs, which are poorly water-soluble and may degrade in intestinal pH ranges. Our experimental findings revealed improved efficacy and the benefit of significantly lower dose frequency for the treatment of diabetic nephropathy.

#### **4.D. CONCLUSION**

This study demonstrates the significant potential of shellac and locust bean gum-based nanocomposites (CESL-NP) as effective carriers for the simultaneous delivery of curcumin (CUR) and epigallocatechin gallate (EGCG) in the treatment of diabetic nephropathy. The developed nanocomposite effectively addressed the challenges associated with the poor aqueous solubility and bioavailability of these drugs, offering a promising approach for improving their therapeutic efficacy. CESL-NP exhibited enhanced drug loading and entrapment efficiency, ensuring efficient encapsulation and controlled release of CUR and EGCG. The sustained release profiles observed *in vitro* suggest the potential for prolonged therapeutic action, minimizing the need for frequent dosing.

Furthermore, the nanocomposite demonstrated promising antidiabetic and antinephritic activities *in vivo*. CESL-NP effectively reduced blood glucose levels, improved pancreatic function, and mitigated kidney damage, highlighting its potential to address the key complications of diabetic nephropathy. The results of this study provide compelling evidence that CESL-NP is a promising approach for the treatment of diabetic nephropathy, offering a more effective and efficient delivery system for CUR and EGCG. By overcoming the limitations of traditional drug delivery methods, CESL-NP has the potential to improve patient outcomes and enhance the management of diabetic nephropathy.

# Chapter V

## Studies on *Pueraria tuberosa* and *Pterocarpus santalinus* extracts-loaded nanoparticles

## 5. STUDIES ON *PUERARIA TUBEROSA* AND *PTEROCARPUS SANTALINUS* EXTRACTS-LOADED NANOPARTICLES

### 5.A. MATERIALS AND METHODS

#### 5.A.1. Materials

##### 5.A.1.1. Chemicals and reagents used in the study

**Table 5. 1:** List of chemicals with their respective sources used in the study

Sl. No.	Chemical name	Source
1.	Acetonitrile	Merck Life Science, Bengaluru, India
2.	Aerosil 200	Sisco Research Laboratories, Mumbai, India
3.	Ammonia	Merck Life Science, Bengaluru, India
4.	Ascorbyl palmitate	Sigma-Aldrich Co, St Louis, MO, USA
5.	Cetyltrimethylammonium bromide	Sisco Research Laboratories, Mumbai, India
6.	Citric acid	Merck Life Science, Bengaluru, India
7.	Compritol 888 ATO	Gattefossé India Pvt. Ltd., Mumbai, India
8.	Diethylene glycol monoethyl ether	Loba Chemie, Mumbai, India
9.	Ethanol	Merck Life Science, Bengaluru, India
10.	Ethyl acetate	Merck Life Science, Bengaluru, India
11.	Glibenclamide	HiMedia Laboratories, Mumbai, India
12.	Hydrochloric acid	Merck Life Science, Bengaluru, India
13.	Methanol	Merck Life Science, Bengaluru, India
14.	Orthophosphoric acid	HiMedia Laboratories, Mumbai, India
15.	Potassium dihydrogen orthophosphate	Merck Life Science, Bengaluru, India
16.	Potassium dihydrogen phosphate	Merck Life Science, Bengaluru, India
17.	<i>Pterocarpus santalinus</i> extract	Vital herbs Pvt. Ltd., New Delhi, India

18.	Pterostilbene	Tokyo Chemical Industry, Hyderabad, India
19.	<i>Pueraria tuberosa</i> extract	Vital herbs Pvt. Ltd., New Delhi, India
20.	Puerarin	Tokyo Chemical Industry, Hyderabad, India
21.	Sodium chloride	HiMedia Laboratories, Mumbai, India
22.	Sodium citrate dihydrate	Merck Life Science, Bengaluru, India
23.	Sodium deoxycholate	Loba Chemie, Mumbai, India
24.	Sodium hydroxide	HiMedia Laboratories, Mumbai, India
25.	Soybean lecithin	Sigma-Aldrich Co, St Louis, MO, USA
26.	Streptozotocin	Sigma-Aldrich Co, St Louis, MO, USA
27.	Sulphuric acid	HiMedia Laboratories, Mumbai, India
28.	Triolein	Sigma-Aldrich Co, St Louis, MO, USA

### 5.A.1.2. Instruments used in the study

**Table 5. 2:** List of all the equipment and instruments used in the study

Sl. No.	Instrument name	Source
1.	0.45 µm syringe filter	Millipore, Merck, Germany
2.	Atomic force microscope	Bruker Dimension Icon Innova AFM, USA
3.	Bath sonicator	Trans-O-Sonic, Mumbai, India
4.	Blood glucometer	Accuchek Guide, Roche Diagnostics, Germany
5.	BOD incubator shaker	BOD-INC-1S, Incon, India
6.	Cold centrifuge	Rota 4R-V/FM, Plastocrafts, India
7.	Disposable syringe	Hindustan Syringes and Medical Devices, Ltd., Haryana, India
8.	Differential scanning calorimeter	DSC Q2000, TA Instruments, USA
9.	Digital pH meter	DBK instruments, Mumbai, India
10.	Electronic weighing balance	Sartorius Corporate Administration, Otto-Brenner-Straße 20, Goettingen, Germany

11.	Field emission scanning electron microscopy	Quanta 250 FEG-SEM, FEI, Hillsboro, USA
12.	Freezer (-80 °C)	New Brunswick Scientific, Eppendorf House, Arlington Business Park, Stevenage, UK
13.	FTIR spectrometer	IR Affinity 1, Shimadzu, Japan
14.	High performance liquid chromatography (HPLC)	Agilent 1260 series, Agilent, USA
15.	High speed homogenizer	IKA Laboratory Equipment, Model T10B Ultras-Turrax, Staufen, Germany
16.	Light microscope	Zeiss Axio Imager 2, Germany
17.	Magnetic stirrer	Remi Sales & Engineering Ltd, Kolkata, India
18.	Particle size and zetasizer	Zetasizer nano ZS 90, Malvern Zetasizer Limited, Malvern, UK
19.	Transmission electron microscope	Tecnai G2 TF20-ST, FEI, Hillsboro, USA
20.	UV visible spectrometer	Shimadzu UV-1800, Shimadzu, Japan
21.	Vacuum oven	Thermo Fisher Scientific, Waltham, MA, USA
22.	Vortex machine	CM101 cyclomixer, Remi, India
23.	Water bath	Remi, India
24.	X-ray diffractometer	X'Pert Pro, PANalytical, Almelo, Neitherlands

## **5.A.2. Methods**

### **5.A.2.1. Preparation procedures for buffers and reagents used in the study**

#### **5.A.2.1.1. Preparation of enzyme-free simulated gastric fluid buffer at pH 1.2**

Simulated gastric fluid (SGF) buffer was prepared following the United States Pharmacopoeia (USP) (Volume 1) guidelines. SGF buffer was prepared by dissolving 2 grams of NaCl and 7 mL of conc. HCl in 800 mL of Milli-Q water. The mixture was then stirred using a magnetic stirrer until all components were completely dissolved. Next, the pH of the solution was adjusted to 1.2 using either sodium hydroxide or hydrochloric acid, as needed. Finally, Milli-Q water was added to bring the final volume up to 1000 mL.

#### **5.A.2.1.2. Preparation of enzyme-free simulated intestinal fluid buffer at pH 7.4**

Simulated intestinal fluid (SIF) buffer was prepared following the USP (Volume 1) guidelines. To make 1000 mL of SIF buffer, 6.8 g of potassium dihydrogen orthophosphate were dissolved in 800 mL of Milli-Q water. The mixture was then stirred using a magnetic stirrer until the potassium dihydrogen orthophosphate was completely dissolved. Next, the pH of the solution was adjusted to 6.8 using either sodium hydroxide or orthophosphoric acid. Finally, Milli-Q water was added to bring the final volume up to 1000 mL.

#### **5.A.2.1.3. Preparation of citrate buffer at pH 4.5**

To prepare 100 mL of citrate buffer, 1.204 grams of sodium citrate dehydrate and 1.134 grams of citric acid were weighed and transferred into a 100 mL volumetric flask. The chemicals were then dissolved completely in 50 mL of double distilled water. More double distilled water was added to the flask until the final volume reached 100 mL. Finally, the pH of the solution was adjusted to 4.5 using a pH meter.

#### **5.A.2.2. Preparation of *Pueraria tuberosa* and *Pterocarpus santalinus* extracts**

Tubers of *Pueraria tuberosa* and heartwood of *Pterocarpus santalinus* were thoroughly rinsed and chopped into small pieces, then dried in the shade at room temperature. After drying, they were ground into powder using a plant grinder. The extracts were prepared through a hydroalcoholic extraction process using a solvent mixture of ethanol and water in a ratio of 3:7. The crude drug powders of *Pueraria tuberosa* and *Pterocarpus santalinus* were individually boiled in the solvent mixture for 3 hours at 80 °C, followed by filtration through a 180-mesh filter. The resulting hydroalcoholic solutions of *Pueraria tuberosa* extract (PTE) and *Pterocarpus santalinus* (PSE) were then concentrated using a continuous vacuum evaporator and dried under vacuum at 720 mmHg. The obtained powders were stored at 4 °C until use. This procedure was followed by Vital Herbs in preparing the herbal extracts.

### 5.A.2.3. Preparation of NLCs loaded with *Pueraria tuberosa* extract, *Pterocarpus santalinus* extract, and their combination

*Pueraria tuberosa* extract (PTE) and *Pterocarpus santalinus* extract (PSE)-loaded nanostructured lipid carriers (NLCs) were prepared using a modified hot homogenization method (Pimentel-Moral et al., 2019). Three distinct NLC formulations were developed: *Pueraria tuberosa* extract-loaded NLC (PTE-NLC), *Pterocarpus santalinus* extract-loaded NLC (PSE-NLC), and a combination of both extracts-loaded NLC (PTE+PSE-NLC). Each formulation contained the specified amounts of PTE (260 mg), PSE (260 mg), and a combination of both extracts (130 mg each). The lipid phase was composed of Compritol 888 ATO and triolein, dissolved in Transcutol®, using magnetic stirrer at 70 °C. The aqueous phase consisted of two separate mixtures: the first mixture contained sodium deoxycholate (10 mg), soybean lecithin (160 mg), cetyltrimethylammonium bromide (CTAB) (50 mg), and ascorbyl palmitate (25 mg), dissolved in Milli-Q water at 50 °C; the second mixture involved dissolving PTE, PSE, or a combination of both (PTE+PSE) in a Transcutol-Milli-Q water solution (50%, v/v) with gentle magnetic stirring at 50 °C. The lipid phase was introduced into the aqueous phase gradually using a syringe, maintaining a 1:3 weight-to-weight ratio to ensure uniform mixing. The resulting mixture was subjected to hot homogenization at 20,000 rpm and  $75 \pm 5$  °C for 10 minutes, resulting in the formation of the liquid-nanostructured lipid carriers.

### 5.A.2.4. Solidification of the formulated liquid nanostructured lipid carriers

The homogenized formulations, including PTE-NLC, PSE-NLC, and (PTE+PSE)-NLC, were solidified using the surface adsorption technique. Each formulation was mixed with 1.415 grams of Aerosil 200 and triturated at room temperature for 10 minutes. The resulting viscous complexes were then vacuum-dried at 45 °C and stored at 4 °C for subsequent analysis.

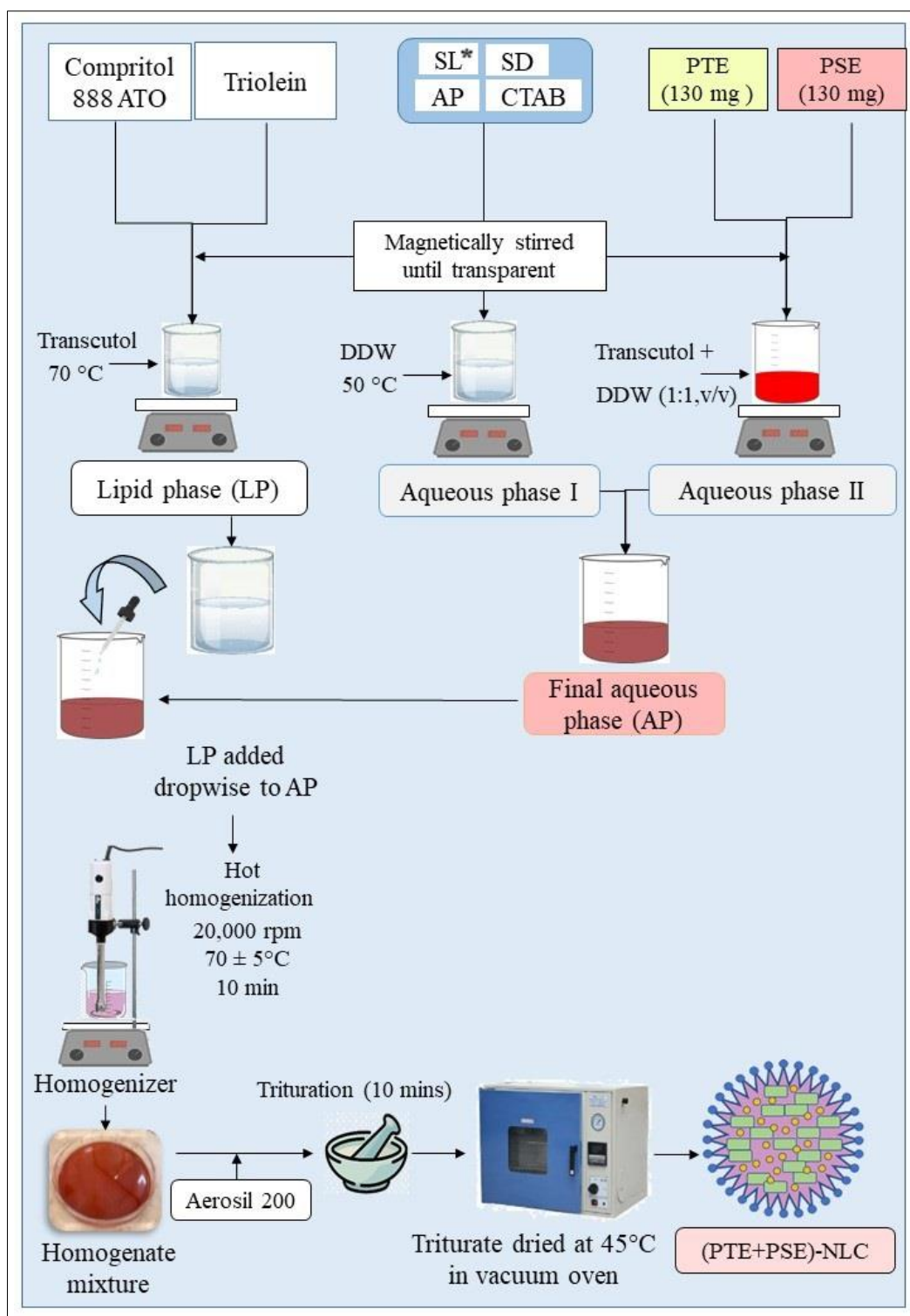


**Figure 5. 1:** Schematic diagram for preparation of Pueraria tuberosa and Pterocarpus santalinus extracts-loaded NLC by hot homogenization method; \*SL- soybean lecithin, SD- sodium deoxycholate, AP- ascorbyl palmitate, CTAB- cetyltrimethyl ammonium bromide

### 5.A.2.5. RP-HPLC analytical method for estimation of puerarin and pterostilbene

A new validated RP-HPLC method was established to simultaneously quantify puerarin and pterostilbene within combined plant extracts encapsulated in NLCs. The method was thoroughly validated in accordance with the International Council for Harmonisation (ICH) guidelines for system suitability criteria, demonstrating acceptable performance (ICH, 2005).

#### 5.A.2.5.1. Determination of UV wavelength for HPLC analysis

Standard solutions of puerarin and pterostilbene were prepared by dissolving each compound in methanol. These solutions were then analyzed using a UV-Vis spectrophotometer within the spectral range of 200 to 400 nm. The peak absorbance was observed at 282 nm for puerarin and 280 nm for pterostilbene. Notably, the spectra of these compounds intersected at 284 nm, a wavelength known as the isosbestic point, as illustrated in Figure 5.2. Consequently, UV detection of puerarin and pterostilbene was conducted at 284 nm to ensure accurate and simultaneous quantification of both compounds.

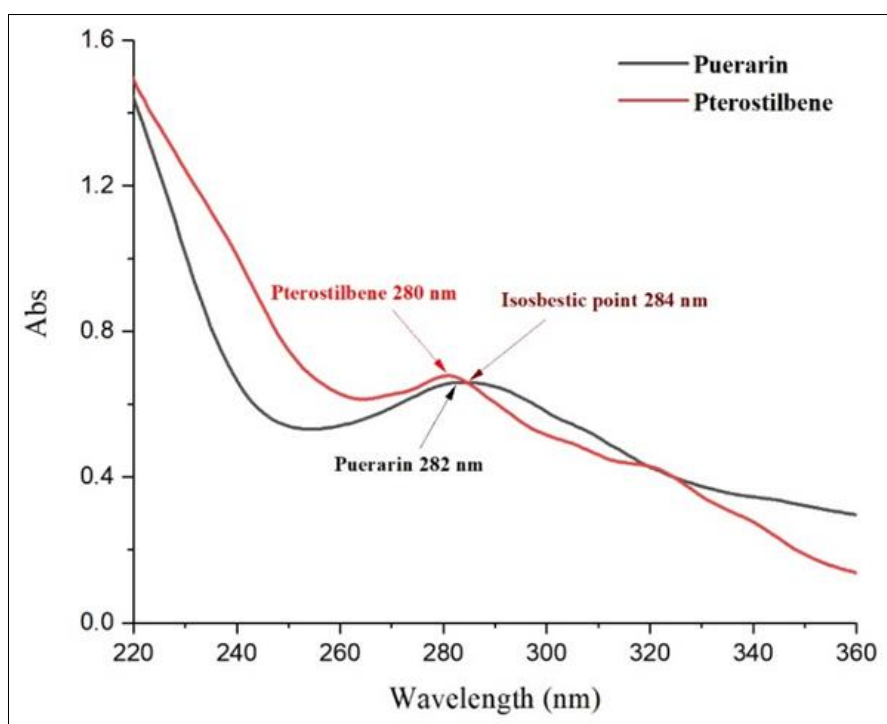


**Figure 5. 2:** UV overlay spectrum of puerarin and pterostilbene

#### **5.A.2.5.2. Instrumentation and chromatographic conditions**

To quantify the concentrations of puerarin and pterostilbene, the active compounds in PTE, PSE, and (PTE+PSE)-NLC, HPLC analysis was conducted. An Agilent HPLC system (Agilent 1260 series) was used, featuring a column oven compartment, a diode array detector (DAD), an autosampler, and a quaternary pump to ensure precise and reliable measurements. Chromatographic separation was achieved using a Thermo Scientific Hypersil BDS C18 column (5  $\mu\text{m}$ , 4.6 x 250 mm) under gradient elution mode. The mobile phase consisted of two components: (A) a buffer solution of 20 mM potassium dihydrogen orthophosphate ( $\text{KH}_2\text{PO}_4$ ) at pH 3.5, and (B) acetonitrile. Both components were degassed and filtered before being introduced into the system to maintain column integrity and ensure accurate separation. The gradient program was meticulously designed, starting with 80% of component A and 20% of component B for the first 10 minutes. This was followed by a change to 20% A and 80% B from 10.1 to 25 minutes, and concluded with a return to 80% A and 20% B from 25.1 to 27 minutes. Operating conditions were carefully controlled, with a flow rate set at 1.5 mL/min, an injection volume of 20  $\mu\text{L}$ , and a column oven temperature maintained at 35  $^\circ\text{C}$  to optimize the separation and detection of the analytes. These parameters were selected to achieve high resolution and reproducibility in the analysis. The specific chromatographic conditions employed are detailed in Table 5.3. Peak identification was confirmed by comparing the retention times (RT) of puerarin and pterostilbene in the reference standards to those in the PTE, PSE, and (PTE+PSE)-NLC samples. This comparison validated the presence of these compounds within the nanoparticle formulations, ensuring the accuracy of the analysis.

The UV data was recorded and processed using Shimadzu's UV Probe software. In contrast, EZ Chrome Elite software from Agilent was employed for the collection and processing of all HPLC data, ensuring accurate and efficient handling of the chromatographic information. To

prepare the HPLC chromatograms, OriginPro 2017 (V 9.4) software was utilized, providing detailed visual representation and analysis.

**Table 5. 3:** Validated RP-HPLC method: optimized conditions

Sl. No.	Parameters	Conditions
1)	Column	Thermo Scientific Hypersil BDS, C18 column (250 mm × 4.6 mm, 5 μm)
2)	Column oven temperature	35 °C
3)	Detection wavelength	284 nm
4)	Diluent	Mobile phase
5)	Flow rate	1.5 ml/min
6)	Injection volume	20 μL
7)	Mobile phase	Buffer (0.020 M KH <sub>2</sub> PO <sub>4</sub> , pH 3.5) and acetonitrile; Gradient programming
8)	Run Time	27 min

#### 5.A.2.5.3. Preparation of standard stock and sample solutions

#### 5.A.2.5.4. Validation of the developed RP-HPLC analytical method

The developed RP-HPLC method was validated in accordance with the International Conference on Harmonization (ICH) guidelines for validating analytical procedures. This validation process involved evaluating several key parameters, including accuracy, linearity, sensitivity, robustness, precision, and system suitability, to ensure the method's reliability and reproducibility (ICH, 2005).

##### 5.A.2.5.4.1. Accuracy

The accuracy of the method was evaluated by spiking the pre-quantified nanoformulation with known concentrations of puerarin and pterostilbene standards at 80%, 100%, and 120% levels. The percentage recovery of these standards was subsequently calculated for each concentration to assess the method's accuracy in quantifying the analytes.

#### **5.A.2.5.4.2. Linearity**

Linearity studies were performed using standard stock solutions of puerarin and pterostilbene at a concentration of 500 µg/mL. Serial dilutions of the stock solutions were prepared to achieve concentrations of 15, 30, 45, 60, and 90 µg/mL for both puerarin and pterostilbene. A calibration curve was constructed by plotting these concentrations on the X-axis against their corresponding peak areas on the Y-axis, allowing for the assessment of the method's linear response.

#### **5.A.2.5.4.3. Precision**

To assess precision, three concentration levels were prepared from each standard stock solution of puerarin and pterostilbene, specifically at 25, 50, and 75 µg/mL for both compounds. Intraday precision was evaluated by performing triplicate injections (n=3) of each concentration on the same day. To assess interday precision, injections were conducted on different days while ensuring that chromatographic conditions remained consistent throughout the study.

#### **5.A.2.5.4.4. Sensitivity**

The LOD represents the lowest amount of substance that can be detected by the method, while the LOQ denotes the lowest concentration that can be reliably quantified within acceptable system suitability criteria. These parameters were established to ensure the method's capability to detect and measure trace amounts of the analytes accurately.

#### **5.A.2.5.4.5. Robustness**

Robustness was evaluated by deliberately varying key chromatographic conditions, including flow rate, buffer pH, column oven temperature, and UV detection wavelength. This assessment aimed to determine the method's reliability and consistency for analyzing puerarin and

pterostilbene under altered conditions, ensuring that the method remains accurate and reliable despite these variations.

#### **5.A.2.5.4.6. Selectivity**

Selectivity assesses the developed method's ability to distinguish the primary peaks of the active constituents from potential impurities or interferences from excipients in the formulation. A suitable amount of (PTE+PSE)-NLC was diluted in methanol, then centrifuged and filtered to assess its selectivity. The resulting filtrate was then analyzed using the validated HPLC method to confirm the method's capacity to selectively identify the active ingredients amidst any potential contaminants.

#### **5.A.2.5.5. System suitability**

System suitability was checked by analyzing a standard solution containing both puerarin and pterostilbene under the optimized chromatographic conditions. The evaluation focused on key parameters including retention time, resolution, injection precision, tailing factor, and theoretical plates. These parameters were analyzed to ensure that the system performs consistently and meets the required criteria for reliable and accurate analysis.

#### **5.A.2.5.6. Estimation of loading capacity and entrapment efficiency**

To assess the loading capacity and entrapment efficiency, a specified quantity of PTE-NLC, PSE-NLC, and (PTE+PSE)-NLC was first dissolved in methanol. This solution was then subjected to centrifugation at 10,000 rpm for 10 minutes to separate the nanocarriers from the supernatant. The supernatant was filtered using a 0.45  $\mu\text{m}$  filter to remove impurities. A 20 $\mu\text{L}$  aliquot of the filtered solution was analyzed using HPLC (De and Bera, 2021).

The loading capacity (LC) was determined by measuring the amount of plant extract present in the nanocarriers relative to the total weight of the nanocarriers and entrapment efficiency (EE) was calculated to determine the percentage of the plant extract that was successfully

incorporated into the nanocarriers compared to the total amount used in the formulation. LC and EE were determined using the following equations (Azmi et al., 2020):

$$\text{LC (\%)} = (\text{Weight of the plant extract in the NLC} / \text{Total weight of NLC}) \times 100$$

$$\text{EE (\%)} = (\text{Actual weight of plant extract incorporated into NLC} / \text{Overall weight of plant extract used to prepare NLC}) \times 100$$

### **5.A.2.6 Characterization of the prepared nanostructured lipid carriers**

#### **5.A.2.6.1. Dynamic Light Scattering analysis**

DLS was employed to evaluate the zeta potential, mean particle size, and polydispersity index (PDI) of the nanostructured lipid carriers: PTE-NLC, PSE-NLC, and (PTE+PSE)-NLC. The measurements were performed using a Zetasizer Nano ZS90 instrument (Malvern Instruments, UK). For each measurement, the experimental procedure was conducted in triplicate to ensure reliability. Prior to analysis, the samples were dispersed in Milli-Q water at a concentration of 1 mg/mL, subjected to ultrasonic agitation to ensure uniform dispersion, and then filtered through a 0.45  $\mu\text{m}$  syringe filter to remove any particulates. This preparation ensured accurate and consistent measurements of the nanocarriers' size and stability characteristics (Anandalakshmi et al., 2016).

#### **5.A.2.6.2. Fourier transform infrared analysis**

FTIR spectroscopy was employed to confirm the incorporation of PTE and PSE into the formulated (PTE+PSE)-NLC. FTIR spectra were recorded for several samples: PTE, PSE, a physical mixture of all excipients including PTE and PSE, a blank mixture of all excipients excluding the plant extracts, and the final (PTE+PSE)-NLC formulation. The measurements were conducted using a FTIR Spectrometer (IR Affinity 1, Shimadzu, Japan), covering a frequency range from 500 to 4000  $\text{cm}^{-1}$ . This range provided comprehensive information on the functional groups and molecular interactions within the samples, enabling the identification

of any changes or interactions due to the incorporation of PTE and PSE into the nanocarrier system (Kharat and Mendhulkar, 2016).

#### **5.A.2.6.3. Differential scanning calorimeter analysis**

The DSC Q2000 (TA Instruments, USA) was used to study the thermal behavior of PTE, PSE, (PTE+PSE)-NLC, the blank formulation, and the physical mixture. This analysis aimed to observe changes in the crystalline structure of the lipid core. Each sample, weighing approximately 6-8 mg, was placed in standard alumina pans, with an empty pan used as the reference. The temperature was gradually increased at a rate of 10 °C per minute, from 10 to 500 °C. This procedure allowed for a detailed examination of the thermal properties and stability of the formulations (Marquele-Oliveira et al., 2016).

#### **5.A.2.6.4. X-ray diffraction analysis**

XRD analysis was performed using an X'Pert Pro X-Ray Diffractometer (PANalytical, Almelo, Neitherlands), to evaluate the crystalline or amorphous characteristics of the solidified nanostructured lipid carriers. The analysis was conducted with an operating current of 40 mA and a voltage of 45 kV, employing a Cu K $\alpha$  X-ray source with a wavelength of 1.5406 Å. Data were collected over a range of 10° to 80° (2 $\theta$ ). The XRD analysis encompassed samples of PTE, PSE, the blank formulation, the physical mixture, and the (PTE+PSE)-NLC (Logeswari et al., 2015).

#### **5.A.2.6.5. Atomic force microscopy analysis**

AFM was employed to examine the morphology and confirm the size of the (PTE+PSE)-NLCs. The sample was air-dried on a glass slide before analysis. The measurements were conducted using a Bruker Dimension Icon Innova AFM (USA), equipped with NanoScope analysis software and NanoDrive v8 real-time control. This approach provided detailed insights into the surface characteristics and dimensions of the nanoparticles (Santhoshkumar et al., 2017).

#### **5.A.2.6.6. High-resolution transmission electron microscopy analysis**

HRTEM was utilized to examine the surface morphology of the prepared (PTE+PSE)-NLC formulation, using a Tecnai G2 TF20-ST microscope (FEI, Hillsboro, USA). The NLCs were diluted in Milli-Q water at a 1:100 dilution ratio, subsequently applied to 3 mm carbon-supported copper grids, and allowed to air-dry. The analysis was conducted with an accelerating voltage of 200 kV to reveal detailed structural information about the nanoparticles (Santhosh et al., 2015).

#### **5.A.2.6.7. Field emission scanning electron microscopy analysis**

FESEM was employed to characterize the surface morphology and shape of the samples. Quanta 250 FEG-SEM (FEI, Hillsboro, USA) operating at an accelerating voltage of 30 kV was utilized for this purpose. A diluted (PTE+PSE)-NLC solution (1:100) was evenly distributed on a glass coverslip and allowed to air-dry. Prior to imaging, the sample was subjected to gold coating using ion sputtering (Rajakumar et al., 2012).

#### **5.A.2.7. Stability study of (PTE+PSE)-NLC**

To assess storage stability, (PTE+PSE)-NLC samples were prepared and sealed in vials according to International Council for Harmonisation (ICH) guidelines. These vials were subsequently stored in a refrigerator at 4°C. After a storage period of 90 days, the (PTE+PSE)-NLC samples were subjected to analysis to evaluate their physical and chemical stability. Specifically, particle size, polydispersity index, zeta potential, and drug loading were determined (Kim et al., 2011).

#### **5.A.2.8. *In vitro* release of (PTE+PSE)-NLC**

An *in vitro* drug release study was conducted using the dialysis bag technique, (De and Bera, 2021), to evaluate the release of PTE and PSE from the formulated NLCs. The dissolution was evaluated in simulated gastric and intestinal fluids with pH values of 1.2 and 7.4, respectively.

First, 20 mg of (PTE+PSE)-NLC was dissolved in 20 mL of Milli-Q water and subjected to sonication for 15 minutes to ensure complete dispersion. This NLC dispersion was then transferred into two dialysis bags, which were securely sealed at both ends to prevent leakage. The bags were placed in 200 mL of the respective dissolution media. The study was conducted under controlled conditions using a BOD incubator shaker (INCON, BOD-INC-1S), maintained at  $37 \pm 0.5$  °C and continuously stirred at 100 rpm. To maintain sink conditions throughout the experiment, fresh dissolution medium was added to replace the aliquots withdrawn for analysis. Samples were collected at various time intervals, specifically 0.5 h, 1 h, 2 h, 4 h, 6 h, 8 h, 12 h, 24 h, 48 h, 72 h, 96 h, 120 h, 144 h, and 168 h. The samples were filtered and analyzed using RP-HPLC to determine how much PTE and PSE were released from the NLCs.

#### 5.A.2.9. *In vitro* drug release kinetic models

The drug release data was subjected to various kinetic models to determine the pattern of drug release from the formulated NLCs. These models included zero-order, first-order, Higuchi, Korsmeyer-Peppas, and Hixson-Crowell models. The model with the strongest correlation to the data was selected to represent the most appropriate kinetic pattern for drug release in the different media. The equations for these models are as follows (Singhvi and Singh, 2011; Rudra et al., 2010):

- **Zero-Order:**  $[D]_t = [D]_0 + Kt$
- **First-Order:**  $\text{Log } [D]_t = \text{Log } [D]_0 - Kt / 2.303$
- **Higuchi model:**  $[D]_t = K_H (t)^{0.5}$
- **Hixson-Crowell model:**  $[D]_0^{1/3} - [D]_t^{1/3} = K_{HC} t$
- **Korsmeyer-peppas model:**  $M_t/M_\infty = Kt^n$

#### **5.A.2.10. *In vivo* antidiabetic and antinephritic studies**

##### **5.A.2.10.1. Experimental animals**

The animal studies complied with CPCSEA guidelines, and the Institutional Animal Ethics Committee (IAEC) at Jadavpur University, Kolkata, India, approved the study protocol (Ref no. JU/IAEC-22/02). The animals were housed in polycarbonate cages within a room maintained at a constant temperature of  $22 \pm 3.0$  °C, relative humidity of 44-52%, and day and night cycle. Prior to the experiment, the animals underwent a ten-day acclimatization period in the laboratory environment, during which they had unrestricted access to water and a standard pellet diet.

##### **5.A.2.10.2. Induction of diabetes**

To induce diabetes in the mice, they were fasted overnight after a ten-day acclimatization period. Streptozotocin (STZ) was administered intraperitoneally at a dose of 80 mg/kg, after being dissolved in ice-cold citrate buffer (0.1 M, pH 4.5). The use of cold citrate buffer ensured the stability of STZ, which is prone to degradation in aqueous solutions. Control mice received an equal volume of citrate buffer alone. Six hours after the STZ injection, the mice were provided with a 5% glucose solution to prevent hypoglycemia, a common side effect of STZ administration (BarathManiKanth et al., 2010). Blood glucose levels were monitored every three days using an Accu-Chek Guide blood glucose meter. Mice exhibiting blood glucose levels consistently above 250 mg/dL for fifteen days post-STZ injection were classified as diabetic and nephritic. These mice were then selected for further experiments, as indicated in previous studies (Dkhil et al., 2016).

##### **5.A.2.10.3. Experimental design and animal treatment**

To evaluate antidiabetic activity, the study divided STZ-induced diabetic mice into seven groups, each containing five mice. Treatments began two weeks after STZ administration. The groups were as follows:

- Group 1 (normal control): Served as the control, receiving oral doses of double-distilled water for 60 consecutive days.
- Group 2 (disease control): Received no further treatment after the STZ injection.
- Group 3 (standard drug): Administered glibenclamide orally at a dose of 1 mg/kg body weight (Sarkodie et al., 2013).
- Group 4 (extracts in free form): Received an oral dose of the plant extracts mixture (PTE+PSE) at 1000 mg/kg body weight.
- Group 5 (combined plant extracts-loaded NLCs): Treated with (PTE+PSE)-NLC at a dose of 200 mg/kg body weight.
- Group 6 (single plant extract-loaded NLC): Given PTE-NLC at a dose of 200 mg/kg body weight.
- Group 7 (single plant extract-loaded NLC): Received PSE-NLC at a dose of 200 mg/kg body weight.

The treatments were continued for 60 consecutive days. Fasting blood glucose levels (FBGL) and body weight were measured at the beginning of the study and weekly thereafter for a period of 60 days. Blood samples were collected aseptically from the tail tips of each animal, and FBGL was determined using an ACCU-CHEK Guide glucometer. Throughout the study, the mice had unrestricted access to regular food and water.

#### **5.A.2.10.4. Serum collection and tissue preparation**

Following the completion of the experimental procedures, blood samples ranging from 0.5 to 1.0 mL were carefully collected through cardiac puncture while the animals were under mild isoflurane anesthesia. These samples were placed into labeled vials without anticoagulants, then centrifuged to separate the serum. The resulting serum was immediately stored at -20 °C for subsequent analysis. Serum analysis included the evaluation of various biochemical markers, such as blood urea nitrogen (BUN), serum albumin (Alb), and serum creatinine (Scr).

After blood collection, the animals were euthanized using a high dose of isoflurane. The kidneys and pancreas were promptly removed to preserve tissue integrity and rinsed with a saline solution. The kidneys were weighed using an electronic scale, and morphological alterations in the right kidneys were assessed. The kidney hypertrophy index (KHI) was calculated using the formula  $KHI = \text{kidney weight (KW)} / \text{body weight}$  (Li et al., 2021). Both the kidneys and pancreas were preserved in 10% formaldehyde for histopathological examination.

#### **5.A.2.10.5. Histopathological analysis for pancreas and kidney tissues**

The pancreas and kidney specimens, previously preserved in formalin, underwent a series of histological processing steps. These steps included xylene cleaning, dehydration with ethanol, paraffin embedding, and sectioning into 5  $\mu\text{m}$ -thick slices. After staining with hematoxylin and eosin (H&E), the sections were examined microscopically (El-Far et al., 2016).

#### **5.A.2.10.6. Statistical analysis**

The data for each group of mice (n=5) are expressed as mean  $\pm$  standard error. Statistical analysis was conducted using one-way ANOVA, followed by Dunnett's t-tests. A \*p-value of  $\leq 0.05$  was considered statistically significant.

## 5.B. RESULTS

### 5.B.1. Preformulation study of (PTE+PSE)-NLC

In this study, we developed nanostructured lipid carriers (NLCs) loaded with *Pueraria tuberosa* and *Pterocarpus santalinus* extracts using Generally Recognized as Safe (GRAS) ingredients to ensure safety and biocompatibility. The formulation featured Compritol 888 ATO as a solid lipid to provide a stable and biocompatible matrix for drug encapsulation. Triolein was included as a liquid lipid to enhance fluidity and flexibility. Transcutol® was added as a penetration enhancer to improve the permeation of the encapsulated extracts across biological barriers. Aerosil 200 served as a solidifying agent to increase the physical stability of the NLCs. Additionally, ascorbyl palmitate, soybean lecithin, CTAB, and sodium deoxycholate were incorporated as surfactants and co-surfactants to optimize the formation, stability, and efficiency of the NLCs, ensuring effective drug encapsulation and release.

**Table 5. 4:** Composition of PTE and PSE-loaded NLC

Sl. No.	Ingredients	Role in formulation
1)	Aerosil 200	Mechanical properties enhancer, stabilizer,
2)	Ascorbyl palmitate	Stabilizer, emulsifier, lipid component
3)	CTAB*	Surfactant and co-surfactant, stabilizer
4)	Compritol 888 ATO	Solid lipid matrix, targeted drug release
5)	<i>Pterocarpus santalinus</i> extract	Active constituent
6)	<i>Pueraria tuberosa</i> extract	Active constituent
7)	Sodium deoxycholate	Co-surfactant, encapsulation enhancer
8)	Soybean lecithin	Surfactant, stabilizer, drug encapsulation enhancer
9)	Transcutol®	Co-surfactant, solubility and stability enhancer
10)	Triolein	Liquid lipid matrix, control drug release

\*CTAB: cetyltrimethylammonium bromide

## 5.B.2. RP-HPLC analytical method for estimation of puerarin and pterostilbene

### 5.B.2.1. Validation of method

#### 5.B.2.1.1. Accuracy

The mixed standard solutions were prepared with concentrations of 25 µg/mL for puerarin and 20 µg/mL for pterostilbene. The method demonstrated high accuracy, with average recovery rates for puerarin and pterostilbene ranging from 97.22% to 98.77%. These recovery rates fall within the acceptable range, confirming the method's precision and reliability for quantifying these compounds (Arayne et al., 2006). Detailed accuracy data are presented in Table 5.5.

**Table 5. 5:** Accuracy assessment of the validated HPLC method

Active compound	Spiked level (%)	Spiked amount (mg)	Recovered amount (mg)	Recovery (%)	RSD* (%)
Puerarin	80	08.56 ± 0.18	08.45 ± 0.16	98.71	0.75
	100	12.26 ± 0.30	11.92 ± 0.35	97.22	0.62
	120	16.23 ± 0.23	16.12 ± 0.23	98.77	0.53
Pterostilbene	80	08.23 ± 0.22	08.11 ± 0.17	98.54	0.64
	100	12.35 ± 0.15	12.05 ± 0.38	97.57	0.56
	120	16.56 ± 0.36	16.13 ± 0.25	97.34	0.72

\*RSD –Relative Standard Deviation; All values are presented as mean ± standard deviation (SD), with n representing the sample size of 3

#### 5.B.2.1.2. Linearity

To evaluate the linearity of the RP-HPLC method, standard solutions of puerarin and pterostilbene were analyzed over a concentration range of 15-90 µg/mL. The resulting calibration curves exhibited strong linearity, with correlation coefficients of 0.995 and 0.998 for puerarin and pterostilbene, respectively. These values demonstrate a robust linear relationship between the peak area and concentration of each compound, ensuring accurate and precise quantification within the specified range (Debata et al., 2017). The regression equations

for puerarin and pterostilbene were derived as  $y = 2061x - 181.8$  and  $y = 750.7x - 233.9$ , respectively, further confirming the linearity of the method. Figures 5.3 and 5.4 illustrate the calibration curves for both compounds.

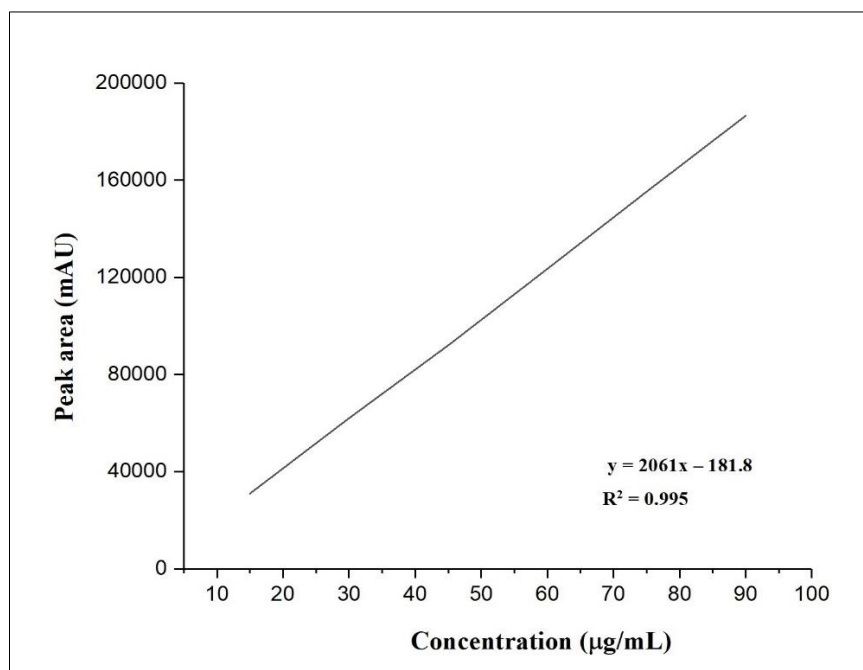


**Figure 5. 3:** Linearity curve of puerarin of the analytical HPLC method

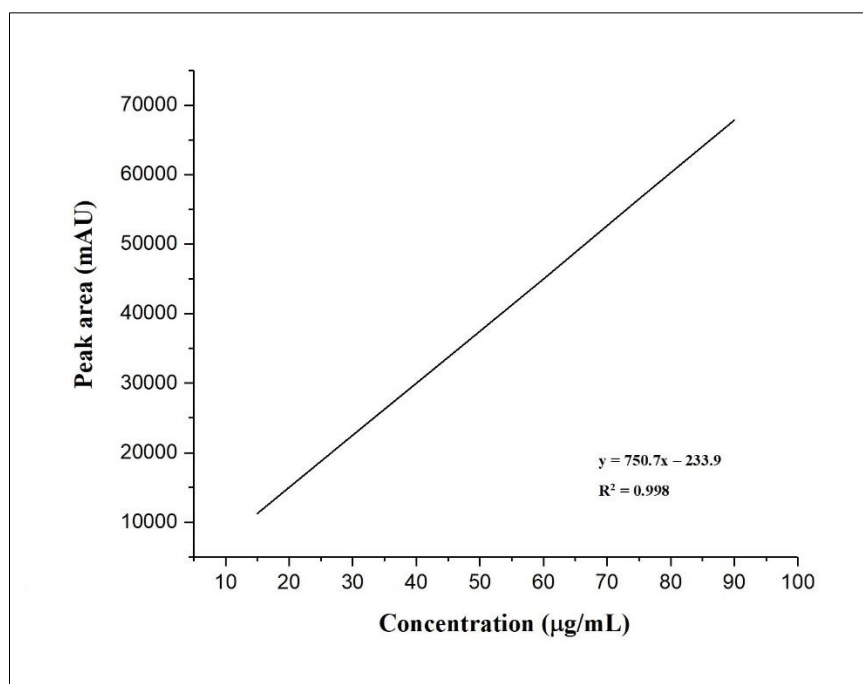


**Figure 5. 4:** Linearity curve of pterostilbene of the analytical HPLC method

### 5.B.2.1.3. Precision

The RSD % values for puerarin ranged from 0.092% to 0.316%, while for pterostilbene, ranged from 0.185% to 0.452% (Tables 5.6 and 5.7). These results consistently fall well below the acceptable limit of 2%, indicating high precision for the quantification of both compounds (Burin et al., 2011).

**Table 5. 6:** Intraday precision data of the analytical method

Active compound	Nominal concentration ( $\mu\text{g/mL}$ )	Recovered concentration ( $\mu\text{g/mL}$ )	Recovery (%)	RSD* (%)
Puerarin	25	24.86 $\pm$ 0.53	99.44 $\pm$ 0.65	0.123
	50	49.85 $\pm$ 0.31	99.70 $\pm$ 0.61	0.261
	75	74.56 $\pm$ 0.86	99.41 $\pm$ 0.58	0.092
Pterostilbene	25	24.16 $\pm$ 0.54	96.64 $\pm$ 0.86	0.312
	50	49.23 $\pm$ 0.67	98.46 $\pm$ 0.45	0.256
	75	74.14 $\pm$ 0.63	98.85 $\pm$ 0.65	0.185

\*RSD –Relative Standard Deviation; All values are presented as mean  $\pm$  standard deviation (SD), with n representing the sample size of 3

**Table 5. 7:** Interday precision data of the analytical method

Active compound	Nominal concentration ( $\mu\text{g/mL}$ )	Recovered concentration ( $\mu\text{g/mL}$ )	Recovery (%)	RSD* (%)
Puerarin	25	24.56 $\pm$ 0.60	98.24 $\pm$ 0.51	0.316
	50	49.61 $\pm$ 0.46	99.22 $\pm$ 0.32	0.129
	75	74.17 $\pm$ 0.51	98.89 $\pm$ 0.56	0.210
Pterostilbene	25	24.19 $\pm$ 0.86	96.76 $\pm$ 0.19	0.452
	50	48.53 $\pm$ 0.74	97.06 $\pm$ 0.55	0.212
	75	74.31 $\pm$ 0.58	99.08 $\pm$ 0.45	0.258

\*RSD –Relative Standard Deviation; All values are presented as mean  $\pm$  standard deviation (SD), with n representing the sample size of 3

#### 5.B.2.1.4. Sensitivity

The LOD for puerarin was found to be 3.16 µg/mL, while the LOQ was 9.48 µg/mL. For pterostilbene, the LOD was 2.82 µg/mL, and the LOQ was 8.46 µg/mL. These results collectively demonstrate the high sensitivity of the developed method in quantifying both puerarin and pterostilbene (Çelebier et al., 2013). The low LOD and LOQ values demonstrate the method's ability to accurately detect trace amounts of the compounds, making it suitable for diverse analytical applications.

#### 5.B.2.1.5. Robustness

The observed RSD values for these variations were consistently low, typically less than 2%, indicating the stability and reliability of the method (Kardani et al., 2013). Robustness data for puerarin and pterostilbene is provided in Table 5.8. These results collectively demonstrate the robustness of the developed method, ensuring its applicability and accuracy in various analytical settings.

**Table 5. 8:** Robustness parameters of the validated HPLC method

Parameters	Puerarin area RSD* (%)	Pterostilbene area RSD (%)
A. Change in buffer pH of mobile phase		
3.4	0.052	0.125
3.5	0.063	0.216
3.6	0.082	0.281
B. Change in UV detector wavelength (nm)		
282	0.139	0.172
284	0.162	0.183
286	0.135	0.216
C. Change in flow rate (mL/min) of mobile phase		
0.9	0.115	0.081
1.0	0.162	0.136
1.1	0.213	0.212
D. Change in column oven temp (°C) of mobile phase		
34	0.121	0.115
35	0.132	0.165
36	0.215	0.205

\*RSD –Relative Standard Deviation; All values are presented as mean ± standard deviation (SD), with n representing the sample size of 3

### 5.B.2.1.6. Selectivity

The HPLC chromatogram of the (PTE+PSE)-NLC exhibited distinct peaks representing puerarin and pterostilbene at retention times of 11.7 and 14.6 minutes, respectively, as shown in Figure 5.10. The absence of overlapping peaks or interference from impurities or excipients within the primary peaks highlights the selectivity of the developed RP-HPLC method (Rao et al., 2010). This selectivity is essential for the accurate and precise quantification of puerarin and pterostilbene in the presence of other components within the NLC formulation.

### 5.B.2.2. System suitability

System suitability studies were conducted to evaluate the performance of the RP-HPLC method. The resolution between the puerarin and pterostilbene peaks was determined to be  $10.81 \pm 0.04$ , indicating successful separation of the two compounds. The chromatographic peaks exhibited a symmetrical shape, with tailing factors of  $1.19 \pm 0.02$  for puerarin and  $1.21 \pm 0.05$  for pterostilbene. Additionally, the theoretical plate numbers/meter were calculated to be  $5318 \pm 152$  for puerarin and  $4853 \pm 135$  for pterostilbene. These values are well within acceptable ranges, further confirming the efficiency of the chromatographic separation (Singh et al., 2010). The results of the system suitability studies, summarized in Table 5.9.

**Table 5. 9:** System suitability parameters of the analytical HPLC method

Parameters	Puerarin *	Pterostilbene*
Injection precision	$0.052 \pm 0.02$	$0.061 \pm 0.04$
Resolution	-	$10.81 \pm 0.04$
Retention time	$11.731 \pm 0.04$	$14.673 \pm 0.05$
Tailing factor	$1.19 \pm 0.02$	$1.21 \pm 0.03$
Theoretical plates/meter	$5318 \pm 152$	$4853 \pm 135$

Note: All values are presented as mean  $\pm$  standard deviation (SD), with n representing the sample size of 3

### 5.B.2.3. Quantification of active constituents in herbal extracts and formulated NLCs using HPLC

To assess the quality of the PTE, PSE, and (PTE+PSE)-NLC formulations, HPLC analysis was conducted to quantify the concentrations of puerarin and pterostilbene. Chromatographic separation of all analytes was completed within 28 minutes. Figures 5.5-5.10 illustrates the typical chromatograms of standard puerarin, standard pterostilbene, *Pueraria tuberosa* extract (PTE), *Pterocarpus santalinus* extract (PSE), a combined standard of puerarin and pterostilbene, and (PTE+PSE)-NLC, respectively. The quantification of puerarin and pterostilbene was achieved through UV-VIS detection at a wavelength of 284 nm, with retention time serving as a key parameter for identifying and quantifying the respective peaks in the chromatogram.

In the RP-HPLC analysis, the chromatogram of *Pueraria tuberosa* extract revealed a sharp peak for puerarin at an RT of  $11.705 \pm 0.03$  minutes, closely aligning with the RT of the standard puerarin ( $11.687 \pm 0.02$  minutes), as shown in Figures 5.5 and 5.6. Similarly, the chromatogram of *Pterocarpus santalinus* extract displayed a distinct peak corresponding to pterostilbene at an RT of  $14.695 \pm 0.08$  minutes, closely matching the RT of the standard pterostilbene ( $14.613 \pm 0.05$  minutes), as presented in Figures 5.7 and 5.8. The formulated (PTE+PSE)-NLC chromatogram indicated a clear peak for puerarin at an RT of  $11.731 \pm 0.06$  minutes, closely resembling the RT of the standard puerarin ( $11.687 \pm 0.02$  minutes). Additionally, the same chromatogram displayed a distinct peak for pterostilbene at an RT of  $14.673 \pm 0.09$  minutes, in close agreement with the RT of the standard pterostilbene ( $14.613 \pm 0.05$  minutes), as depicted in Figures 5.9 and 5.10. The concentrations of puerarin and pterostilbene in the various formulations were determined using the optimized chromatographic conditions. Puerarin was found to be present at a concentration of  $51.3 \pm 0.07$  mg/g in PTE, while pterostilbene was quantified at  $65.2 \pm 0.02$  mg/g in PSE. In the (PTE+PSE)-

NLC formulation, the concentrations of puerarin and pterostilbene were measured to be  $16.3 \pm 0.05$  mg/g and  $17.3 \pm 0.01$  mg/g, respectively.

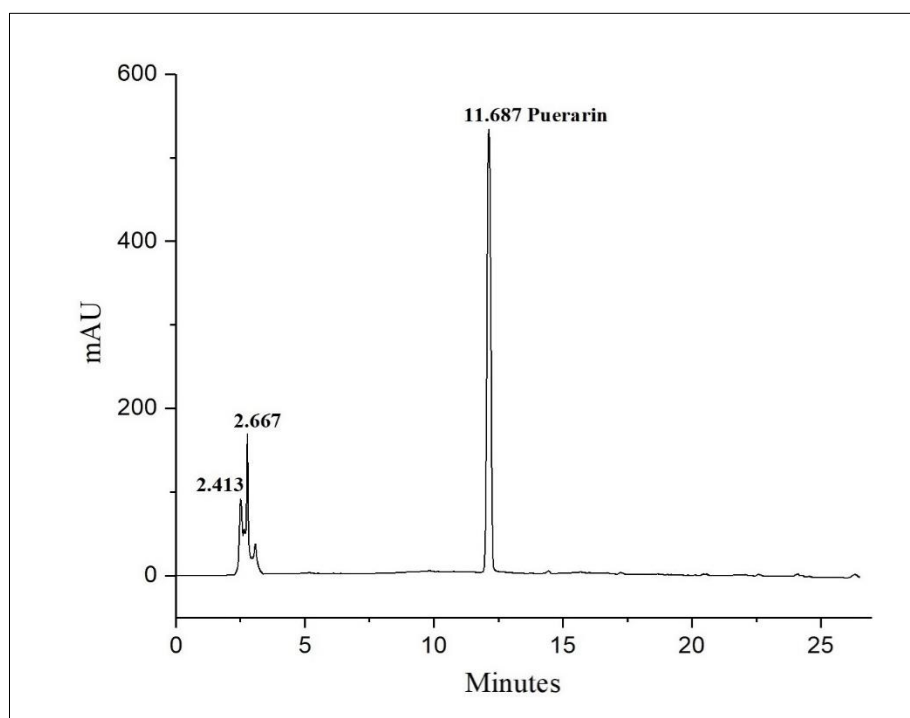


**Figure 5. 5:** HPLC chromatogram of standard puerarin

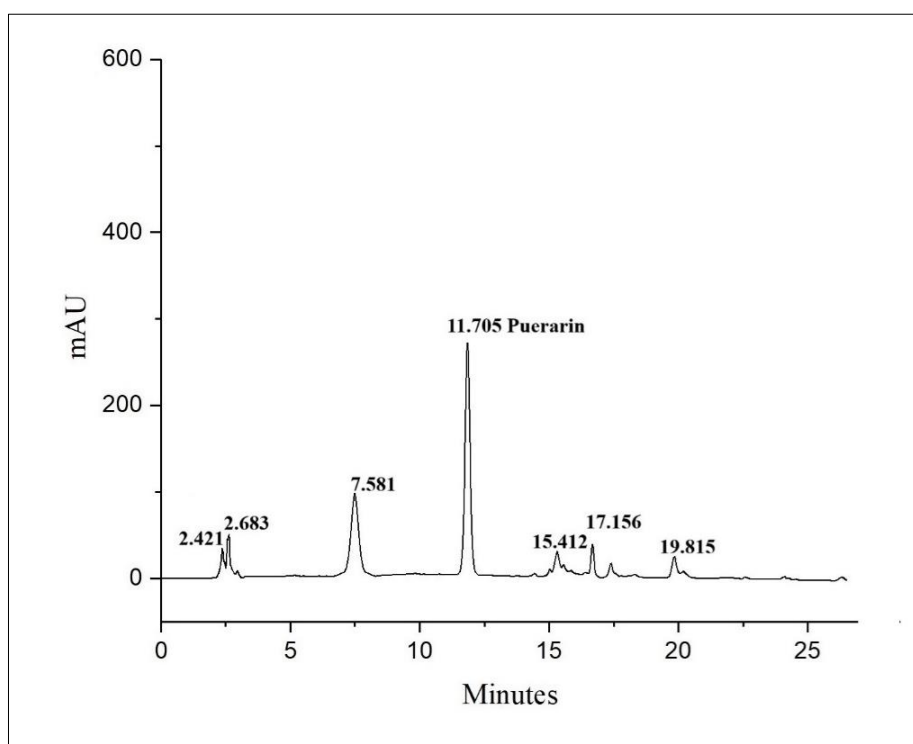


**Figure 5. 6:** HPLC chromatogram of *Pueraria tuberosa* extract

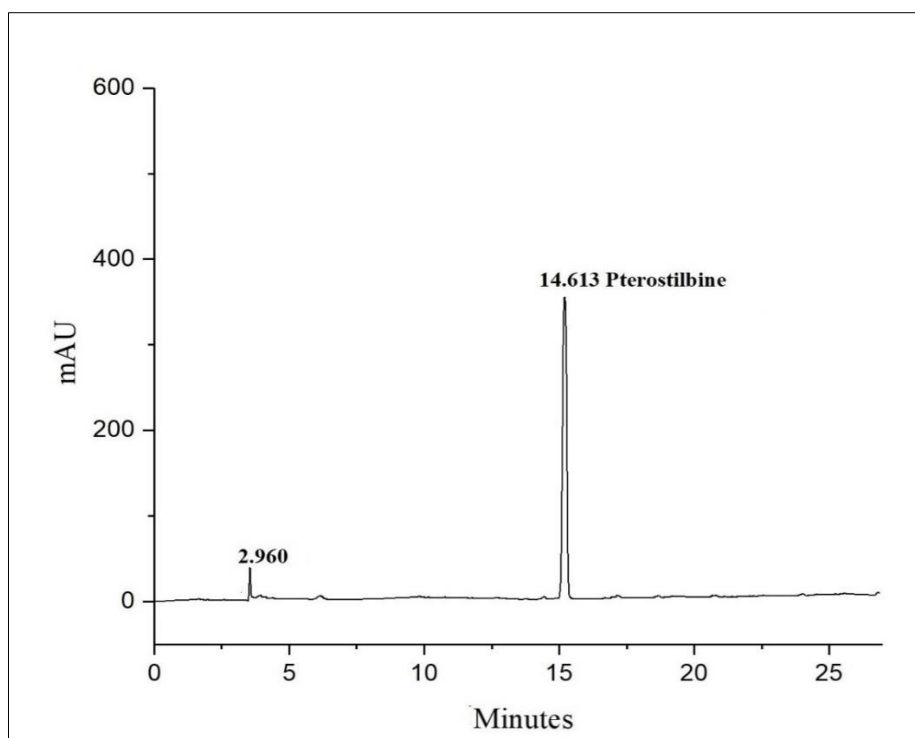


**Figure 5. 7:** HPLC chromatogram of standard pterostilbene

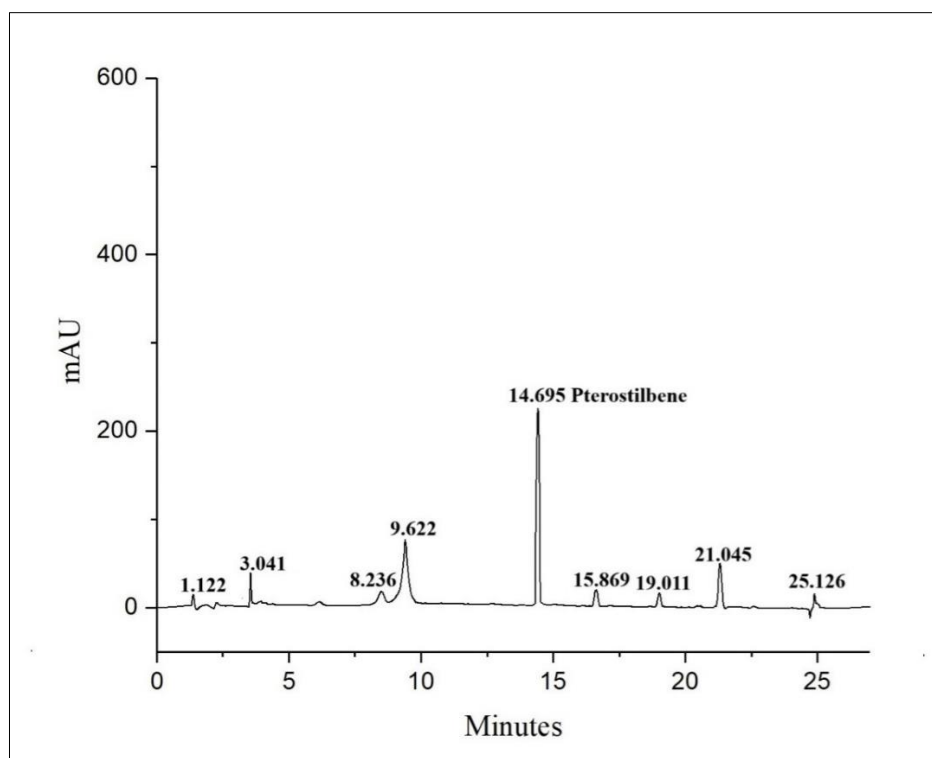


**Figure 5. 8:** HPLC chromatogram of *Pterocarpus santalinus* extract

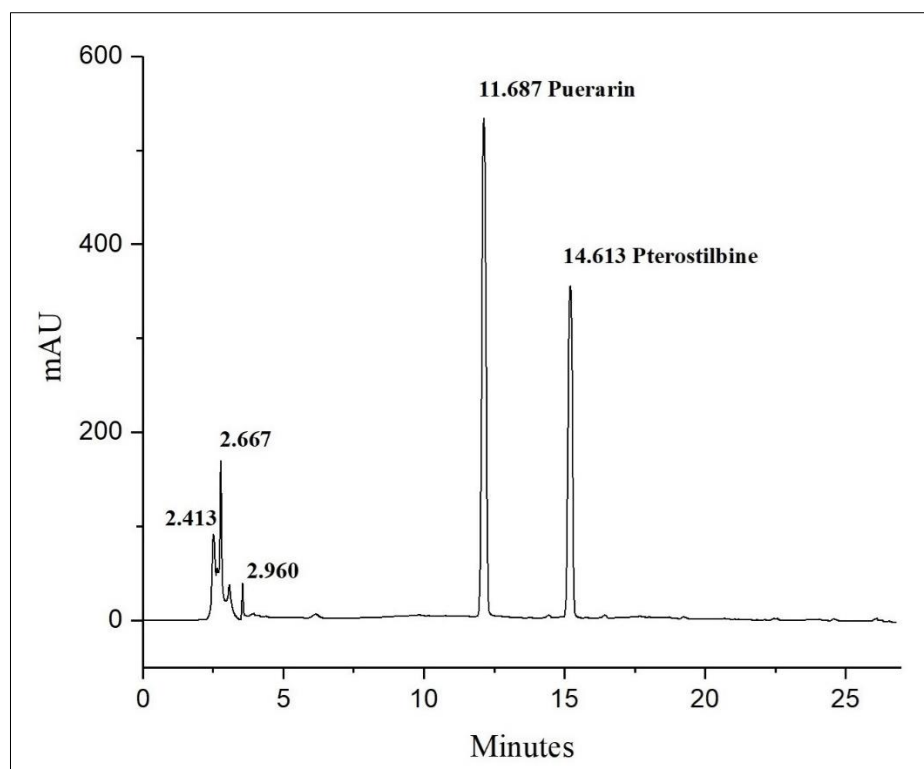


**Figure 5. 9:** HPLC chromatogram of puerarin and pterostilbene in mixed standard

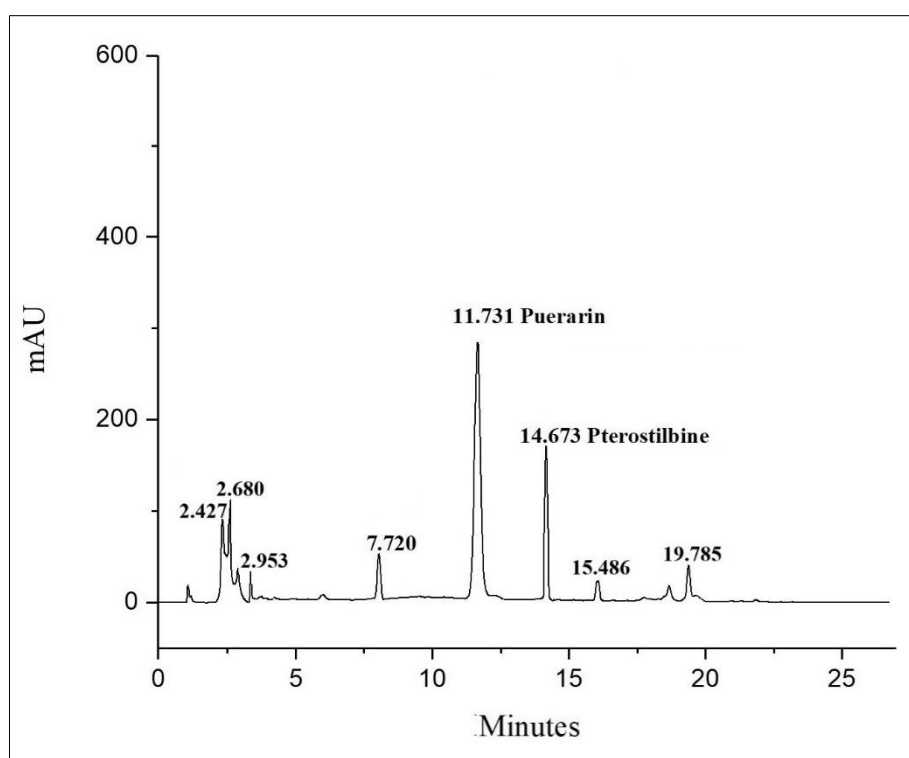


**Figure 5. 10:** HPLC chromatogram of formulated (PTE+PSE)-NLC depicting distinct peaks of puerarin and pterostilbene by the detection at 284 nm

#### 5.B.2.4. Loading capacity and entrapment efficiency

To assess the loading capacity (LC) and entrapment efficiency (EE) of the formulated NLCs, the concentrations of puerarin and pterostilbene in the extracts before and after nanoencapsulation were compared. The experiment was run in triplicate for each formulation. The calculated LC (%) and EE (%) values for the NLCs are presented in Table 5.10. Among the formulated NLCs, (PTE+PSE)-NLC exhibited the highest loading capacities, with  $10.10 \pm 0.78\%$  for PTE and  $9.92 \pm 0.95\%$  for PSE. These values indicate that in the (PTE+PSE)-NLC formulation, approximately 10.10% of the matrix weight consists of PTE, while 9.92% is composed of PSE. Furthermore, (PTE+PSE)-NLC demonstrated excellent entrapment efficiencies, with  $91.74 \pm 2.4\%$  for PTE and  $92.47 \pm 3.6\%$  for PSE. These results suggest that a significant portion of the encapsulated drugs was retained within the NLCs, highlighting their potential for controlled and sustained drug delivery. Given the objective of evaluating the potential synergistic effects between PTE and PSE, the (PTE+PSE)-NLC formulation was selected for detailed characterization through a range of analytical techniques.

**Table 5. 10:** Loading capacity and entrapment efficiency of the formulated NLCs

Formulation	Loading capacity (%)		Entrapment efficiency (%)	
	PTE*	PSE	PTE	PSE
PTE-NLC	$18.5 \pm 0.62$	-	$89.25 \pm 1.8$	-
PSE-NLC	-	$17.02 \pm 0.81$	-	$88.95 \pm 2.3$
(PTE+PSE)-NLC	$10.10 \pm 0.78$	$9.92 \pm 0.95$	$91.74 \pm 2.4$	$92.47 \pm 3.6$

\*PTE- *Pueraria tuberosa* extract; PSE- *Pterocarpus santalinus* extract; Data expressed as mean  $\pm$  SEM, n = 3

#### 5.B.3. Characterization of formulated NLCs

##### 5.B.3.1. DLS analysis

Particle size distribution plays a crucial role in assessing the stability of colloidal systems (Lasoń et al., 2013). The z-average diameter, or mean hydrodynamic diameter, is a key

parameter for determining the size of nanoformulations. In this study, the mean particle sizes of PTE-NLC, PSE-NLC, and (PTE+PSE)-NLC were found to be  $133.6 \pm 3.3$  nm,  $142.2 \pm 2.1$  nm, and  $121.4 \pm 4.3$  nm, respectively (Table 5.11, Fig. 5.11). Previous research indicates that particles within the 100-1000 nm range can traverse endothelial gaps, potentially extending circulation time as free compounds, while particles between 100-300 nm are suitable for crossing the blood-brain barrier (Elmowafy et al., 2015). The polydispersity index (PDI) values for these NLCs were 0.27, 0.33, and 0.24, respectively. A PDI above 0.3 indicates significant size variability, while values below 0.2 suggest homogeneity (Mehta et al., 2005). Zeta potential measurements revealed values of  $-29.2 \pm 0.5$  mV,  $-30.8 \pm 1.2$  mV, and  $-31.3 \pm 0.8$  mV for PTE-NLC, PSE-NLC, and (PTE+PSE)-NLC, respectively. Zeta potential is commonly used to assess the stability of nanosuspensions, with stable nanoparticles typically having zeta potential values greater or less than  $\pm 25$  mV (A. Hussain et al., 2022).

**Table 5. 11:** Average particle size, polydispersity index, and zeta potential of formulated NLCs

<b>Formulation</b>	<b>Mean particle size (nm)</b>	<b>PDI*</b>	<b>Zeta potential (mV)</b>
PTE-NLC	$133.6 \pm 3.3$	0.27	$-29.2 \pm 1.8$
PSE-NLC	$142.2 \pm 2.1$	0.33	$-30.8 \pm 1.6$
(PTE+PSE)-NLC	$121.4 \pm 4.3$	0.24	$-31.3 \pm 2.2$

\*PDI- Polydispersity index; Data expressed as mean  $\pm$  SEM, n = 3

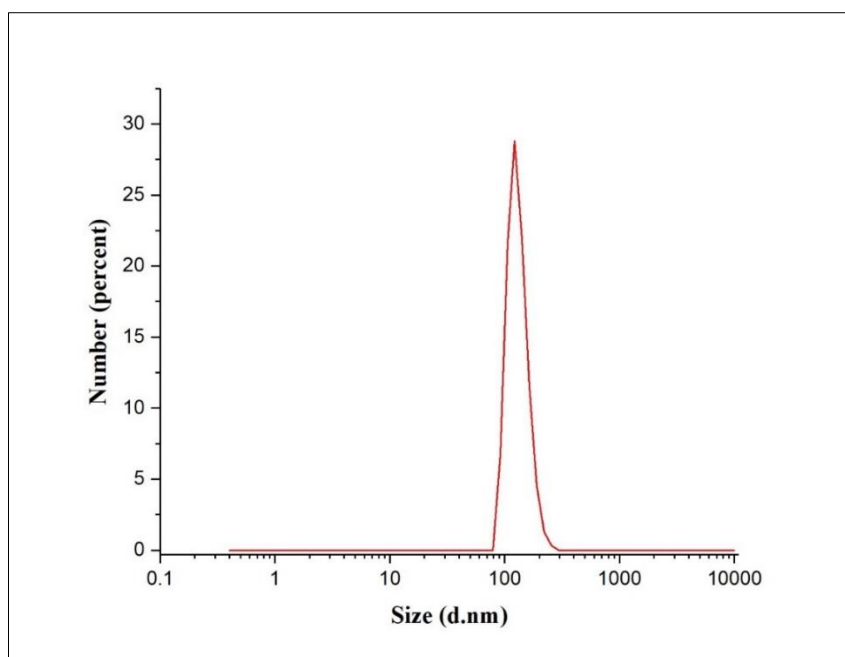


**Figure 5. 11:** Particle size distribution graph of (PTE+PSE)-NLC

### 5.B.3.2. FTIR analysis

Fourier transform infrared (FTIR) analysis was performed on PTE, PSE, their physical mixture, blank, and the (PTE+PSE)-NLC formulation, targeting the mid-infrared region (4000-500  $\text{cm}^{-1}$ ). The spectra, displayed in Figure 5.12, were analyzed to confirm the successful integration of PTE and PSE into the (PTE+PSE)-NLC matrix. The FTIR spectrum of PTE revealed a broad absorption peak at 3299  $\text{cm}^{-1}$ , indicating O–H stretching from alcoholic and phenolic groups (Satpathy et al., 2018). Peaks at 2924  $\text{cm}^{-1}$  and 1622  $\text{cm}^{-1}$  correspond to C–H and C=O stretching vibrations, respectively. Further, the peak at 1008  $\text{cm}^{-1}$  reflects C–O stretching, while the 761  $\text{cm}^{-1}$  peak suggests aliphatic C–I stretching (Ahmed et al., 2023). Similarly, the FTIR spectrum of PSE exhibited key absorption features, though with distinct differences. A prominent peak at 2928  $\text{cm}^{-1}$  corresponded to C–H stretching in methylene and methyl groups, while the characteristic peak at 1604  $\text{cm}^{-1}$  was attributed to C=O stretching vibrations (Huang et al., 2008). Intense bands at 1503  $\text{cm}^{-1}$  indicated aromatic skeletal stretching, and additional peaks at 1278  $\text{cm}^{-1}$ , 1016  $\text{cm}^{-1}$ , and 834  $\text{cm}^{-1}$  were linked to O–C–O stretching, guaiacyl ring vibrations, C–O stretching, and C–H out-of-plane bending in the

aromatic ring, respectively (Jin et al., 2022). Analysis of the FTIR spectrum of the (PTE+PSE)-NLC revealed the absence of key absorption peaks characteristic of both PTE and PSE at 3301  $\text{cm}^{-1}$ , 2912  $\text{cm}^{-1}$ , 1625  $\text{cm}^{-1}$ , 1038  $\text{cm}^{-1}$ , and 802  $\text{cm}^{-1}$ . This absence suggests that encapsulation within the lipid matrix may have masked these distinct peaks. Additionally, a new peak at 2845  $\text{cm}^{-1}$  emerged, indicating the potential formation of new chemical bonds, such as hydrogen bonds, or specific interactions between PTE, PSE, and the lipid matrix. The interaction between PTE, PSE, and the excipients in the (PTE+PSE)-NLC formulation is further supported by the disappearance of their characteristic absorption peaks.

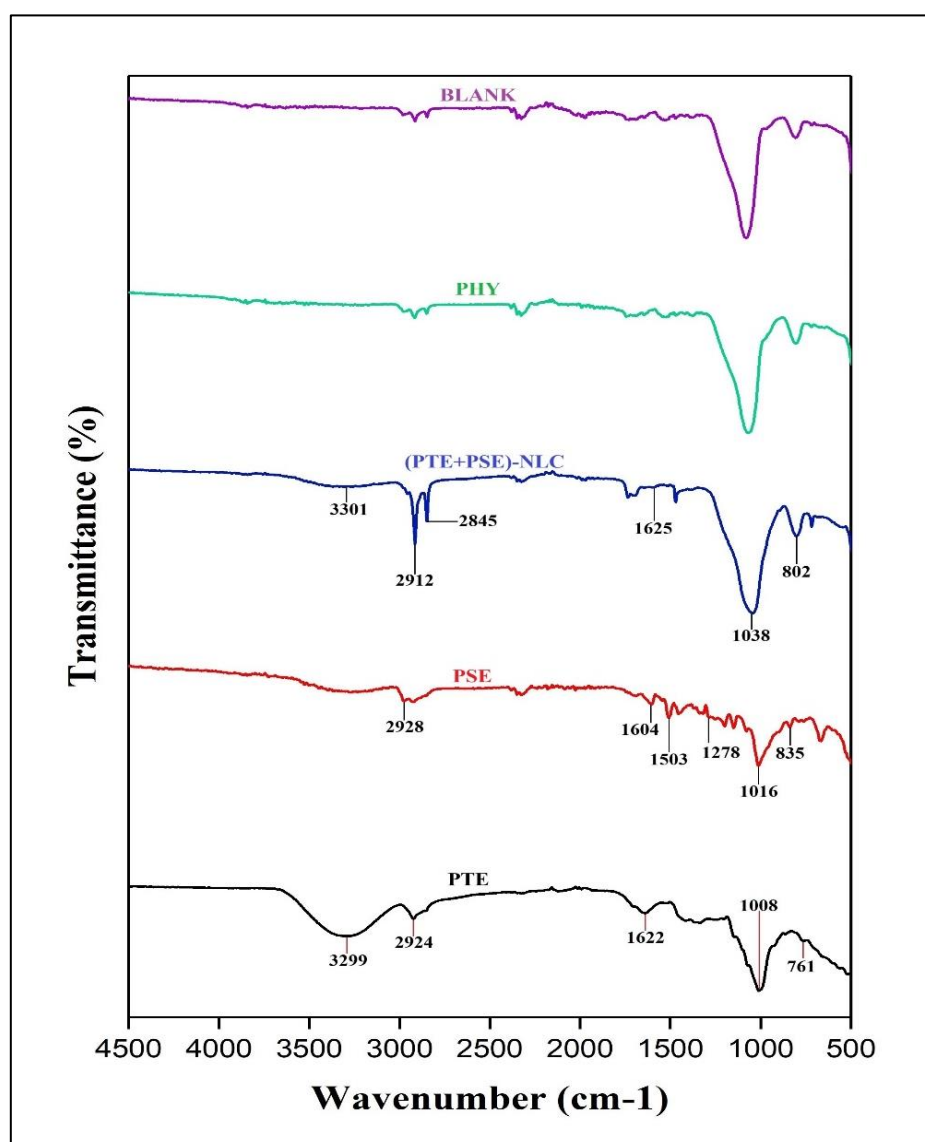


**Figure 5. 12:** Fourier transform infrared spectroscopy spectra of PTE, PSE, (PTE+PSE)-NLC, physical mixture, and blank

### **5.B.3.3. DSC analysis**

Differential Scanning Calorimetry (DSC) analysis is a widely used technique for analyzing the thermal properties of materials, particularly their melting and crystallization behaviors (Zhao et al., 2015). In this study, DSC analysis was performed using a heating rate of 10 °C per minute to investigate the decomposition and phase transitions of nanoparticles across a temperature range of 0 to 500 °C. The resulting thermograms for PTE (black), PSE (red), a physical mixture (blue), (PTE+PSE)-NLC (green), and a blank sample (purple) are displayed in Figure 5.13. The thermogram of PTE displayed a broad endothermic peak at 132.47 °C, likely indicating water loss, and a sharp peak at 187.34 °C, representing the melting transition of puerarin in its crystalline form (Wang et al., 2012). Conversely, the PSE thermogram showed an intense endothermic peak at 106.06 °C, which corresponds to the melting transition of crystalline pterostilbene (Alqarni et al., 2021). The thermogram of the physical mixture showed a small, smooth endothermic peak, suggesting a transition between amorphous and crystalline states. In contrast, the (PTE+PSE)-NLC thermogram lacked the characteristic endothermic peaks of puerarin and pterostilbene, indicating the formation of an amorphous solid dispersion. This absence suggests successful encapsulation of PTE and PSE within the lipid matrix, likely facilitated by intermolecular hydrogen bonding or van der Waals interactions (Xie et al., 2013).

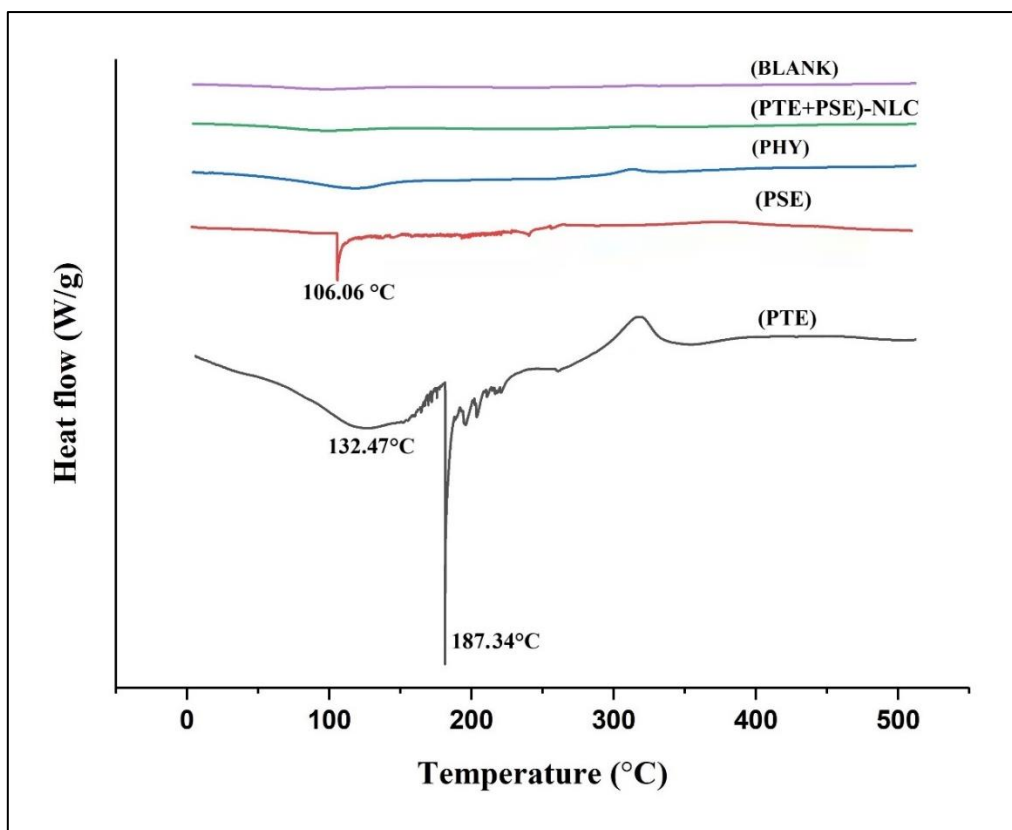


**Figure 5. 13:** Differential scanning calorimetry thermograms of PTE, PSE, physical mixture, (PTE+PSE)-NLC, and blank

#### 5.B.3.4. XRD analysis

XRD analysis was performed to examine the crystalline structure of the particles and confirm the findings from the DSC analysis. Figure 5.14 illustrates the XRD patterns for PTE, PSE, their physical mixture, the (PTE+PSE)-NLC formulation, and the blank mixture. The XRD pattern for PTE revealed sharp diffraction peaks at  $2\theta$  angles of  $14.57^\circ$ ,  $17.39^\circ$ ,  $18.89^\circ$ ,  $23.33^\circ$ ,  $28.65^\circ$ ,  $32.03^\circ$ , and  $38.66^\circ$ , indicating its crystalline nature. Similarly, PSE showed several diffraction peaks at  $2\theta$  angles of  $21.45^\circ$ ,  $28.77^\circ$ ,  $36.46^\circ$ , and  $40.74^\circ$ , with a distinct doublet at  $19.33^\circ$  and  $19.81^\circ$ , confirming its high crystallinity. In the physical mixture, the diffraction peaks' intensity significantly decreased, indicating that PTE and PSE were only minimally encapsulated within the lipid carriers. In contrast, the XRD pattern for the (PTE+PSE)-NLC lacked distinctive peaks for either PTE or PSE, implying that these compounds were molecularly dispersed within the lipid matrix in an amorphous form, likely due to

intermolecular interactions (Shaikh et al., 2009). The absence of diffraction peaks verifies the effective incorporation of PTE and PSE into the nanostructured lipid matrix. This phenomenon aligns with previous studies, which have shown that the crystalline forms of drugs like puerarin and pterostilbene are converted into an amorphous state (Tu et al., 2013; Tzeng et al., 2021). This evidence corroborates that (PTE+PSE)-NLC primarily exists in an amorphous form, consistent with the results of DSC analysis. Additionally, various studies have demonstrated that a lower degree of crystallinity can enhance both solubility and bioavailability (Zhang et al., 2016).

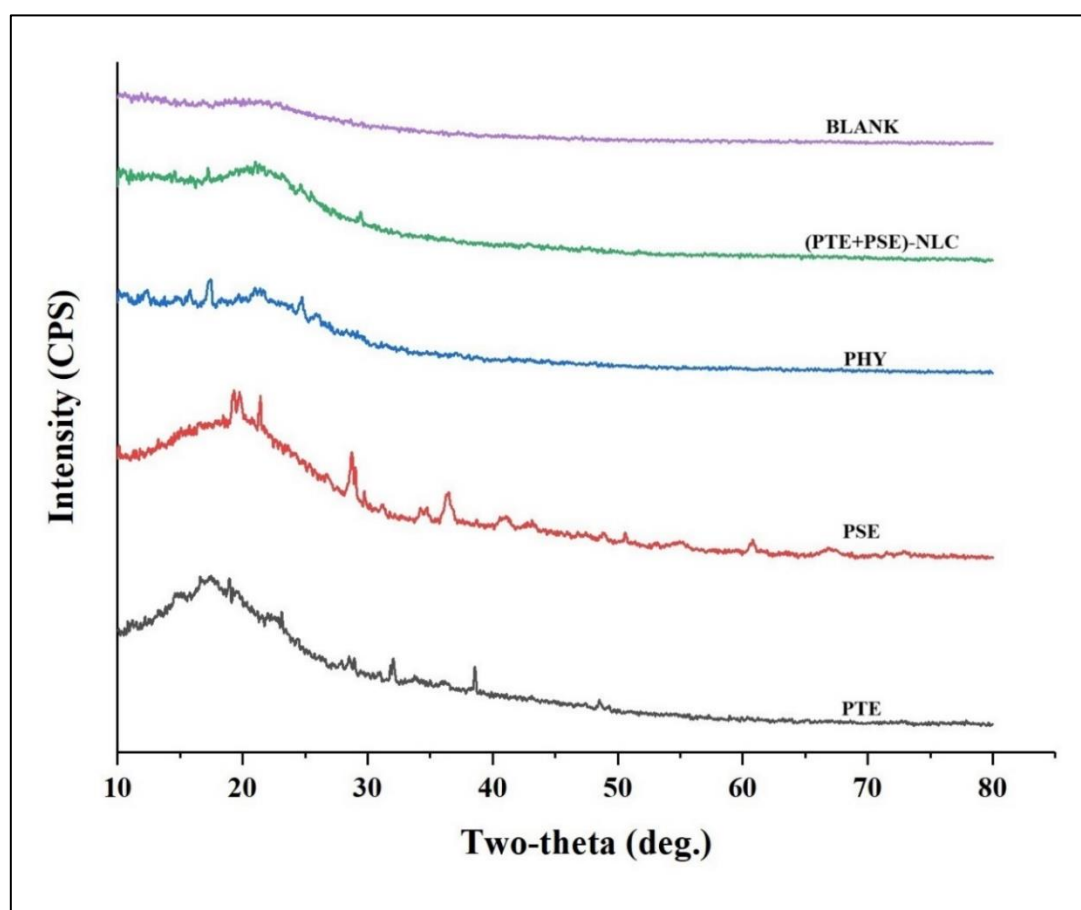


**Figure 5. 14:** X-ray diffraction patterns of PTE, PSE, physical mixture, (PTE+PSE)-NLC, and blank

### 5.B.3.5. AFM analysis

Atomic Force Microscopy (AFM) is an advanced spectroscopic method used to analyze nanoparticle morphology and surface properties (Manikandan et al., 2021). AFM analysis revealed spherical nanoparticles with an average diameter of 90 nm, which is significantly smaller than the sizes measured by DLS. This discrepancy in particle size measurements between AFM and DLS can be explained by the polydispersity index of the samples. Specifically, larger particles scatter light more significantly, affecting DLS measurements. Consequently, the average diameter determined by DLS, based on light intensity distributions, is typically larger than that measured by AFM, even with a small number of larger particles (Zanetti-Ramos et al., 2009). Figures 5.15A and 5.15B depict the two-dimensional and three-dimensional topographical representations of (PTE+PSE)-NLC. The surfaces of these particles exhibit no significant roughness.

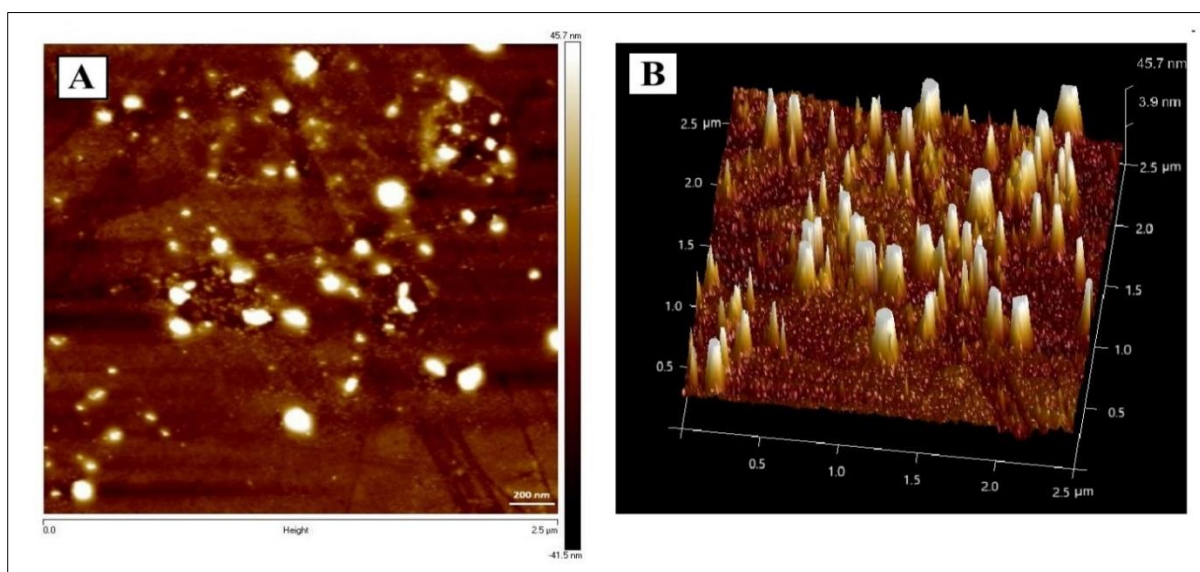


**Figure 5. 15:** Atomic force microscopy analysis of (PTE+PSE)-NLC: (A) surface topography and (B) three dimensional view

### 5.B.3.6. HRTEM analysis

The HRTEM image in Figure 5.16 reveals that (PTE+PSE)-NLC particles are nearly spherical, with an average diameter of 90-110 nm. This observation is consistent with the findings from

the FESEM image depicted in Figure 5.17B. The scale bar, measuring 50 nm, further emphasizes the nanoscale dimensions of these particles.

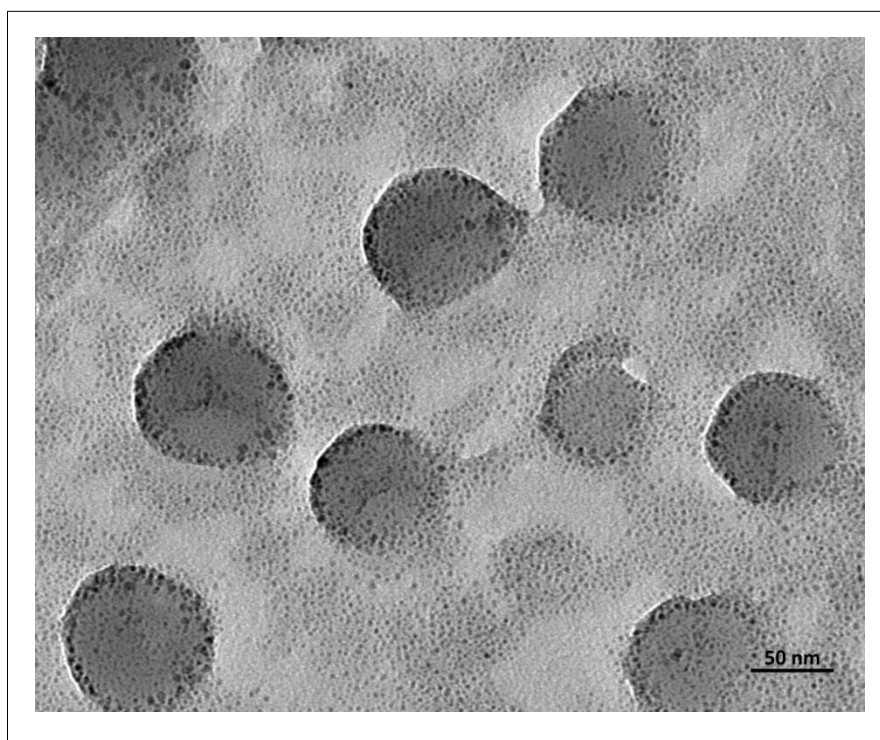


**Figure 5. 16:** Transmission electron microscopic image of (PTE+PSE)-NLC at the scale of 50 nm

#### **5.B.3.7. FESEM analysis**

FESEM analysis corroborated the morphological characteristics and size distribution of (PTE+PSE)-NLC, aligning with the findings of DLS, AFM, and TEM studies. The nanoparticles exhibited a spherical morphology with a smooth surface, as observed under the FESEM microscope. These spherical structures are advantageous for the sustained release and protection of bioactive compounds due to their increased diffusion pathways and reduced interaction with aqueous environments (Santos et al., 2019). Additionally, the observed uniformity in particle size suggests a narrow size distribution. The inset of Figure 5.17B illustrates the NLC structure, with diameters ranging from 90 to 105 nm. The scale bars for Figures 5.17A and 5.17B are 1  $\mu\text{m}$  and 500 nm, respectively.

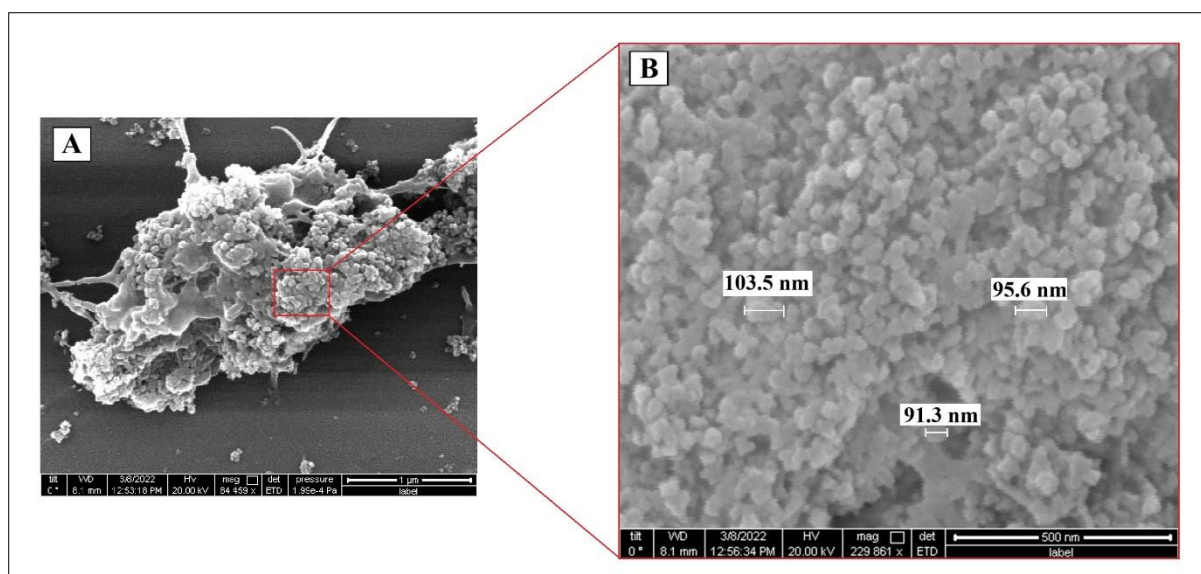


**Figure 5. 17:** Field emission scanning electron microscopy of (PTE+PSE)-NLC at different magnifications: (A) at the scale of 1 $\mu$ m and (B) at the scale of 500 nm

#### 5.B.4. Stability study of (PTE+PSE)-NLC

The stability of the (PTE+PSE)-NLC was evaluated based on average particle size, polydispersity index, zeta potential, and drug loading (Table 5.12). After storage at 4°C for 90 days, a minimal change in particle size and PDI was observed, along with a slight decrease in zeta potential and loading capacity.

**Table 5. 12:** Characterization of (PTE+PSE)-NLC at 4 °C after 90 days: mean particle size, polydispersity index, zeta potential, and drug loading

Sample	Particle size (nm)		PDI*		Zeta potential (mV)		Drug loading (%)			
	Before	After	Before	After	Before	After	PTE		PSE	
							Before	After	Before	After
(PTE+PSE)-NLC	121.4 $\pm$ 4.3	122.7 $\pm$ 1.2	0.24	0.25	-31.3 $\pm$ 2.2	-30.7 $\pm$ 1.4	10.10 $\pm$ 0.78	9.88 $\pm$ 0.88	9.92 $\pm$ 0.95	9.76 $\pm$ 0.45

\*PDI- Polydispersity index; All values represent mean  $\pm$  SD, n=3

### 5.B.5. *In vitro* drug release study of (PTE+PSE)-NLC

The dialysis method is a widely used technique for evaluating the *in vitro* release of nanoformulations. This study investigated the release patterns of PTE and PSE from (PTE+PSE)-NLC in various dissolution media, including simulated gastric and intestinal fluid with pH of 1.2 and 7.4, respectively. The release experiments were conducted at a constant temperature of  $37 \pm 0.5^\circ\text{C}$ , and the results are presented in Figure 5.18. The NLC formulations exhibited a two-stage release pattern at both pH levels, releasing PTE and PSE rapidly in the first day and then releasing them more slowly for up to seven days. The rapid initial release of the plant extracts from the lipid carriers may be attributed to the diffusion of loosely bound plant extracts within the nanostructure (Fahmy et al., 2020). Conversely, the sustained release may be a result of the plant extracts being incorporated and encapsulated together within the lipid matrix (Mahmood et al., 2022). While the release patterns of (PTE+PSE)-NLC at pH 1.2 and 7.4 exhibited similarities, the cumulative release of PTE at pH 7.4 reached 88.36%, significantly exceeding the 66.12% observed at pH 1.2 by the conclusion of the study. Likewise, the cumulative release of PSE at pH 7.4 was 85%, compared to 62.3% at pH 1.2. This pH-dependent release behavior indicates that PTE and PSE demonstrate improved solubility under alkaline conditions, likely due to alterations in their phenolic and alcohol hydroxyl groups (Ansari et al., 2019; Yu et al., 2022). The observed differences in release patterns between SGF and SIF indicate that the effective incorporation of PTE and PSE in NLCs may shield these compounds from the harsh acidic conditions of the stomach, thereby enhancing their absorption in the intestines. Additionally, the sustained release from the formulation offers a prolonged delivery of the encapsulated plant extracts, potentially allowing for better control of physiological conditions over an extended duration.

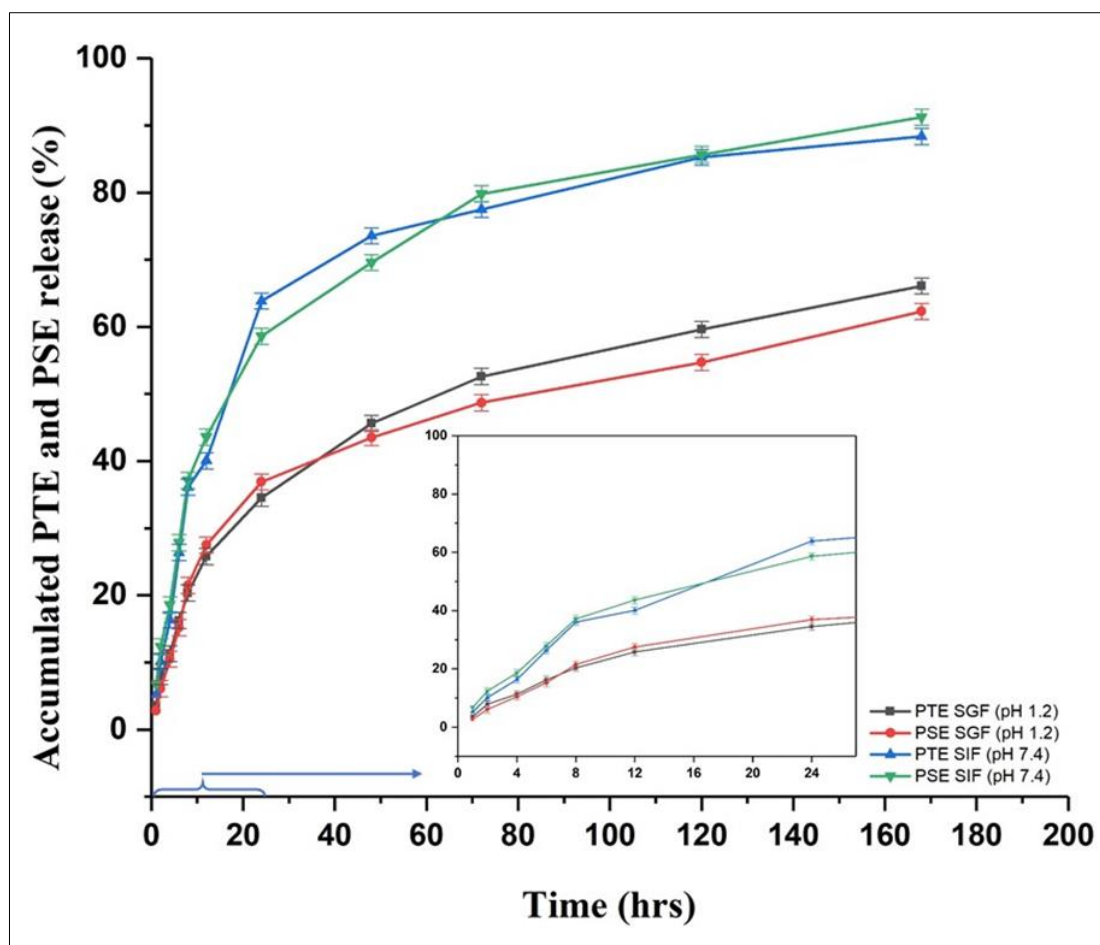


**Figure 5. 18:** In vitro cumulative drug release study of PTE and PSE from NLC formulation at pH 1.2 and 7.4

### 5.B.6. Drug release kinetic study of (PTE+PSE)-NLC

To investigate the release mechanisms of PTE and PSE, various kinetic models were employed to analyze their release kinetics. The results, summarized in Table 5.13, revealed that the Higuchi model exhibited the highest correlation coefficient ( $R^2$ ) for PTE in SGF (pH 1.2), with an  $R^2$  of 0.956. Conversely, the Korsmeyer–Peppas model demonstrated the highest  $R^2$  for PTE in SIF (pH 7.4), with an  $R^2$  of 0.824. For PSE, the Hixon–Crowell model displayed the highest  $R^2$  in SGF (pH 1.2), with an  $R^2$  of 0.952, while the Korsmeyer–Peppas model exhibited the highest  $R^2$  in SIF (pH 7.4), with an  $R^2$  of 0.972. The release exponent ( $n$ ) values for PTE ranged between 0.43 and 0.85, indicating non-Fickian diffusion. In contrast, the  $n$ -value for PSE was below 0.43, suggesting Fickian diffusion (Korsmeyer et al., 1983).

**Table 5. 13:** Correlation coefficients ( $R^2$ ) and release exponents ( $n$ ) for PTE and PSE in various release kinetic models from (PTE+PSE)-NLC

Drugs	Different Kinetics model	Equations and $R^2$ value of corresponding release kinetics model	
		Release in SGF (pH 1.2)	Release in SIF (pH 7.4)
PTE	Zero order	Y= 1.513X+13.25 $R^2=0.895$	Y= 1.23X+16.87 $R^2=0.575$
	First order	Y= -0.028X+1.485 $R^2=0.721$	Y= -0.031X+1.326 $R^2=0.515$
	Higuchi	Y= 11.31X-1.410 $R^2=0.956$	Y= 8.78X+6.215 $R^2=0.787$
	Hixon–Crowell	Y= -0.032X+3.621 $R^2=0.898$	Y= -0.063X+2.815 $R^2=0.546$
	Korsmeyer–Peppas	Y= 0.631X+0.818 $R^2=0.889$	Y= 0.558X+0.687 $R^2=0.824$
	Release exponent value	n=0.48	n=0.46
PSE	Zero order	Y= 0.683X+26.85 $R^2=0.887$	Y= 0.687X+27.82 $R^2=0.883$
	First order	Y= -0.021X+1.768 $R^2=0.928$	Y= -0.034X+1.121 $R^2=0.784$
	Higuchi	Y= 5.215X+14.28 $R^2=0.732$	Y= 6.875X+18.851 $R^2=0.785$
	Hixon–Crowell	Y= -0.028X+3.723 $R^2=0.952$	Y= -0.036X+2.89 $R^2=0.798$
	Korsmeyer–Peppas	Y= 0.321X+1.425 $R^2=0.935$	Y= 0.336X+1.483 $R^2=0.972$
	Release exponent value	n=0.42	n=0.39

### 5.B.7. *In vivo* antidiabetic and antinephritic studies

#### 5.B.7.1. Effects of (PTE+PSE)-NLC on glycemic control in STZ-induced diabetic mice

Fourteen days after STZ injection, the animals developed diabetic symptoms, as indicated by fasting blood glucose levels (FBGL) exceeding 250 mg/dL (Zangeneh et al., 2018). Table 5.14 and Figure 5.19 present the FBGL profiles of different treatment groups, while Figure 5.20 illustrates the percentage reduction in these levels. The normal control group maintained a stable

blood glucose profile, ranging from  $85 \pm 2.5$  mg/dL to  $95 \pm 1.7$  mg/dL. In contrast, STZ-treated mice exhibited significantly elevated FBGL, with increases ranging from 258.36% to 283.50% across different groups. Eight weeks of glibenclamide treatment (1 mg/kg body weight) resulted in a dramatic 99.9% reduction in FBGL. Similarly, treatment with (PTE+PSE)-NLC (200 mg/kg body weight) over the same period lowered FBGL by 96.55%. The administration of plant extracts (PTE+PSE) at a dosage of 1000 mg/kg body weight resulted in a modest reduction of 15.43% FBGL. Notably, individual plant extract-loaded NLCs demonstrated a more pronounced effect on FBGL reduction. PTE-NLC and PSE-NLC treatments, at a dosage of 200 mg/kg each, led to a significant decrease in FBGL by 82.75% and 86.66%, respectively. These findings highlight a synergistic interaction between PTE and PSE when combined within (PTE+PSE)-NLC. At a dosage of 200 mg/kg, (PTE+PSE)-NLC effectively reduced elevated blood glucose levels by a remarkable 31.28-fold compared to the combined plant extracts (PTE+PSE) at a dosage of 1000 mg/kg.

**Table 5. 14:** Antidiabetic activity of glibenclamide, plant extracts (PTE+PSE), (PTE+PSE)-NLC, PTE-NLC, PSE-NLC on STZ-induced diabetic mice

Time period	Normal group (mg/dL)*	STZ group (mg/dL)*	STD group (mg/dL)*	Plant extracts (PTE+PSE) (1000 mg/kg) (mg/dL)*	(PTE+PSE)-NLC (200 mg/kg) (mg/dL)*	PTE-NLC (200 mg/kg) (mg/dL)*	PSE-NLC (200 mg/kg) (mg/dL)*
<b>Before STZ</b>	86 ± 0.54	91 ± 1.23	87 ± 0.98	95 ± 1.45	90 ± 1.26	92 ± 1.36	95 ± 1.22
<b>After STZ</b>	88 ± 1.23	258 ± 3.60 <sup>c</sup>	283 ± 5.33 <sup>c</sup>	268 ± 4.23 <sup>c</sup>	265 ± 2.36 <sup>c</sup>	241 ± 2.36 <sup>c</sup>	267 ± 2.56 <sup>c</sup>
<b>Week 1</b>	85 ± 2.50	268 ± 3.22 <sup>c</sup>	271 ± 3.25 <sup>c</sup>	263 ± 4.12 <sup>c</sup>	255 ± 2.46 <sup>c</sup>	236 ± 1.36 <sup>c</sup>	261 ± 2.11 <sup>c</sup>
<b>Week 2</b>	93 ± 7.36	279 ± 2.35 <sup>c</sup>	249 ± 2.25 <sup>c</sup>	251 ± 3.56 <sup>c</sup>	237 ± 2.37 <sup>c</sup>	215 ± 1.25 <sup>c</sup>	250 ± 2.30 <sup>c,d</sup>
<b>Week 3</b>	87 ± 2.57	291 ± 2.65 <sup>c</sup>	225 ± 3.26 <sup>c</sup>	238 ± 3.16 <sup>c</sup>	219 ± 3.61 <sup>c,d</sup>	199 ± 2.45 <sup>c</sup>	235 ± 1.56 <sup>c,d</sup>
<b>Week 4</b>	94 ± 0.94	299 ± 2.12 <sup>c</sup>	198 ± 3.16 <sup>c,d</sup>	215 ± 3.65 <sup>c,d</sup>	195 ± 2.61 <sup>c,d</sup>	182 ± 3.25 <sup>c,d</sup>	216 ± 1.59 <sup>b,e</sup>
<b>Week 5</b>	95 ± 1.73	310 ± 1.99 <sup>c</sup>	173 ± 2.36 <sup>b,e</sup>	197 ± 2.56 <sup>b,e</sup>	176 ± 2.15 <sup>b,e</sup>	166 ± 2.69 <sup>b,e</sup>	199 ± 1.23 <sup>b,e</sup>
<b>Week 6</b>	90 ± 4.65	316 ± 2.16 <sup>c</sup>	147 ± 2.14 <sup>a,f</sup>	179 ± 2.39 <sup>b,e</sup>	155 ± 2.14 <sup>a,f</sup>	155 ± 2.12 <sup>b,e</sup>	177 ± 1.96 <sup>a,f</sup>
<b>Week 7</b>	94 ± 0.98	322 ± 1.85 <sup>c</sup>	123 ± 1.36 <sup>a,f</sup>	165 ± 2.14 <sup>b,e</sup>	131 ± 1.92 <sup>a,f</sup>	141 ± 1.84 <sup>b,e</sup>	158 ± 2.65 <sup>a,f</sup>
<b>Week 8</b>	89 ± 2.27	331 ± 1.66 <sup>c</sup>	101 ± 1.45 <sup>f</sup>	155 ± 1.66 <sup>a,f</sup>	111 ± 1.69 <sup>f</sup>	132 ± 1.46 <sup>a,f</sup>	140 ± 2.33 <sup>a,f</sup>

Note: All values represent mean ± SD, n=5; <sup>a</sup>p ≤ 0.05 considered significant, <sup>b</sup>p ≤ 0.01 moderately significant, <sup>c</sup>p ≤ 0.001 highly significant vs. the normal group; <sup>d</sup>p ≤ 0.05 considered significant, <sup>e</sup>p ≤ 0.01 moderately significant, <sup>f</sup>p ≤ 0.001 highly significant vs. the STZ group

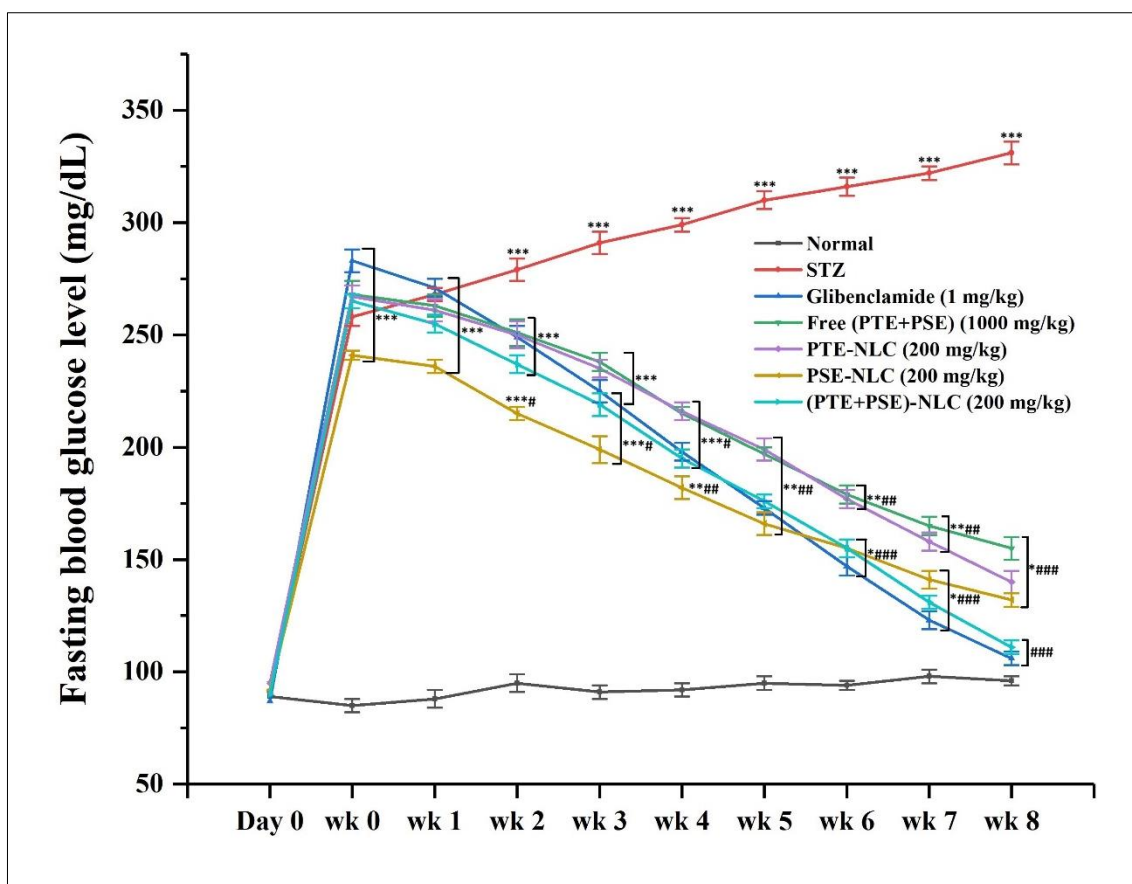


**Figure 5. 19:** Effects of glibenclamide, plant extracts (PTE+PSE), (PTE+PSE)-NLC, PTE-NLC, and PSE-NLC on blood glucose in STZ-diabetic mice. Fasting blood glucose levels were monitored weekly for eight weeks. Data are presented as mean  $\pm$  SEM based on five readings. Statistical significance was determined using a p-value of less than or equal to 0.05 (\*), 0.01 (\*\*), or 0.001 (\*\*\*) compared to the normal group. Similarly, significance was assessed against the STZ group using p-values of less than or equal to 0.05 (#), 0.01 (##), or 0.001 (###).

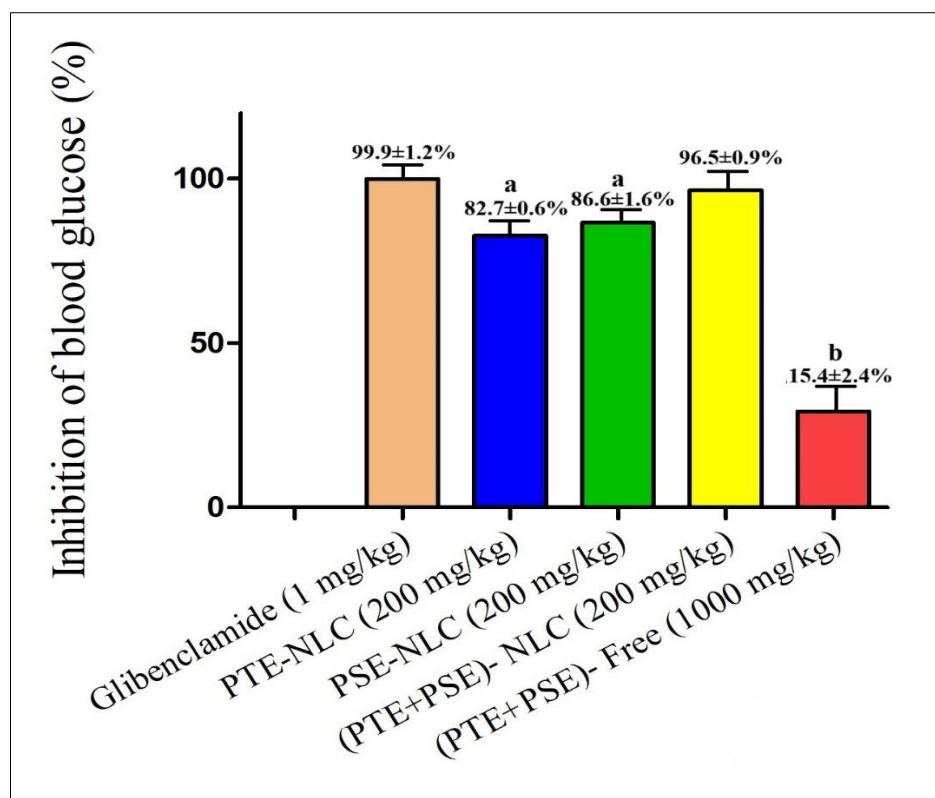


**Figure 5. 20:** Effects of glibenclamide, plant extracts (PTE+PSE), (PTE+PSE)-NLC, PTE-NLC, and PSE-NLC on the percentage inhibition of fasting blood glucose in streptozotocin-induced diabetic mice. After eight weeks of glibenclamide administration (1 mg/kg body weight), fasting blood glucose levels approached 100 mg/dL. The reduction in the difference between fasting blood glucose levels in the eighth week and those observed in the glibenclamide-treated group at the same time point is regarded as 100% inhibition. Data are presented as mean  $\pm$  SEM ( $n = 5$ ); <sup>a</sup> $p \leq 0.05$  considered significant, <sup>b</sup> $p \leq 0.01$  moderately significant vs. the standard group

#### 5.B.7.2. Effects of (PTE+PSE)-NLC on renal parameters in mice with early diabetic nephropathy

The impact of glibenclamide, plant extracts (PTE+PSE), and (PTE+PSE)-NLC treatments on kidney morphology and weight in streptozotocin-induced diabetic mice was evaluated after an 8-week treatment period. These findings are summarized in Table 5.15 and illustrated in Figure 5.21. Glibenclamide and (PTE+PSE)-NLC treatments effectively preserved both average kidney weight and renal structure in the treated groups. In contrast, the untreated diabetic

control group exhibited significant kidney enlargement and weight gain, common features in the early stages of diabetic nephropathy (Nazar, 2014). Diabetic mice also exhibited a significant reduction in body weight and a notable increase in the kidney hypertrophy index (KHI). In contrast, the glibenclamide-treated group showed a substantial increase in body weight, along with a marked reduction in both KHI and kidney weight. Treatment with plant extracts (PTE+PSE) resulted in a slight decrease in kidney weight and KHI, as well as a modest increase in body weight compared to the untreated diabetic control group. Notably, treatment with (PTE+PSE)-NLC reduced kidney weight and prevented the body weight loss seen in untreated diabetic mice. Most significantly, (PTE+PSE)-NLC treatment led to a marked reduction in KHI, underscoring its potential to delay the progression of diabetic nephropathy. These findings indicate that (PTE+PSE)-NLC effectively normalizes key renal health markers, suggesting its promise as a therapeutic option for managing diabetic kidney disease complications.

**Table 5. 15:** Antinephritic effects of glibenclamide, plant extracts (PTE+PSE) and (PTE+PSE)-NLC on renal parameters in mice with early diabetic nephropathy

Groups	Kidney weight (g)	Body weight (g)	KHI* X 100
Normal group	0.189 ± 0.003	30.21 ± 0.928	0.625
STZ group	0.299 ± 0.004 <sup>a</sup>	17.42 ± 0.711 <sup>a</sup>	1.718 <sup>a</sup>
STD group (1 mg/kg)	0.196 ± 0.004 <sup>b</sup>	30.60 ± 0.543 <sup>b</sup>	0.640 <sup>b</sup>
Plant extracts (PTE+PSE) (1000 mg/kg)	0.246 ± 0.005 <sup>c,d</sup>	20.30 ± 0.273 <sup>c,d</sup>	1.211 <sup>c,d</sup>
(PTE+PSE)-NLC (200 mg/kg)	0.205 ± 0.004 <sup>b</sup>	29.10 ± 0.299 <sup>b</sup>	0.704 <sup>b</sup>

\*KHI- Kidney hypertrophy index; Data are presented as mean ± SEM (n = 5); a indicates p < 0.001 compared to the normal group; b indicates p < 0.001 compared to the STZ group; c indicates p < 0.05 compared to the normal group; d indicates p < 0.01 compared to the STZ group.

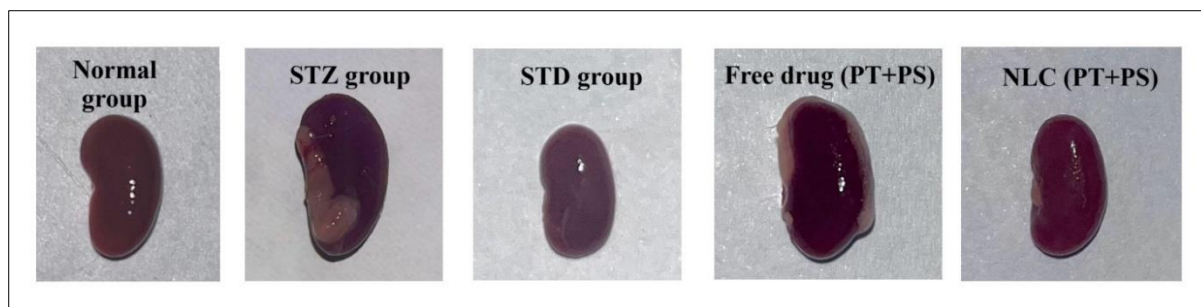


**Figure 5. 21:** Effect of various treatments on kidney structure: glibenclamide (1 mg/kg), plant extracts (PTE+PSE) (1000 mg/kg), and (PTE+PSE)-NLC (200 mg/kg)

### 5.B.7.3. Effects of (PTE+PSE)-NLC on renal biochemical markers in mice with early-stage diabetic nephropathy

The therapeutic efficacy of (PTE+PSE)-NLC on key renal function markers, like blood urea nitrogen (BUN), albumin (Alb), and serum creatinine (Scr), was comprehensively evaluated. As presented in Table 5.16, untreated animals exhibited a significant decline in Alb levels and marked elevations in both Scr and BUN concentrations compared to baseline values observed in healthy control mice over an eight-week study period. The higher levels of Scr and BUN indicate that the untreated mice developed diabetic kidney disease (Tong et al., 2017). However, mice treated with a combination of plant extracts (PTE+PSE) had slightly higher levels of Alb and lower levels of Scr and BUN. Moreover, (PTE+PSE)-NLC effectively mitigated the elevated Scr levels, characteristic of diabetic mice, suggesting its potential to ameliorate the progression of diabetic nephropathy. Additionally, (PTE+PSE)-NLC reduced BUN levels and brought Alb levels closer to normal compared to untreated diabetic mice. The potential of (PTE+PSE)-NLC to restore biochemical markers to levels comparable to those seen in healthy animals underscores its efficacy in ameliorating the pathological changes associated with diabetic nephropathy.

**Table 5. 16:** Antinephritic effects of glibenclamide, plant extracts (PTE+PSE) and (PTE+PSE)-NLC on renal parameters in mice with early diabetic nephropathy

Groups	Alb* (g/dL)	Scr (mg/dL)	BUN (mg/dL)
Normal group	2.398 ± 0.019	0.226 ± 0.011	27.270 ± 1.409
STZ group	1.346 ± 0.134 <sup>a</sup>	0.574 ± 0.017 <sup>a</sup>	50.652 ± 1.663 <sup>a</sup>
STD group (1 mg/kg)	2.496 ± 0.051 <sup>b</sup>	0.236 ± 0.013 <sup>b</sup>	33.154 ± 1.543 <sup>b</sup>
Plant extracts (PTE+PSE) (1000 mg/kg)	1.914 ± 0.024 <sup>c,d</sup>	0.304 ± 0.010 <sup>c,d</sup>	39.356 ± 1.858 <sup>c,d</sup>
(PTE+PSE)-NLC (200 mg/kg)	2.166 ± 0.049 <sup>b</sup>	0.248 ± 0.015 <sup>b</sup>	34.746 ± 1.568 <sup>b</sup>

\*Alb- albumin; Scr- serum creatinine; BUN- blood urea nitrogen; Data are presented as mean ± SEM (n = 5); a indicates p < 0.001 compared to the normal group; b indicates p < 0.001 compared to the STZ group; c indicates p < 0.05 compared to the normal group; d indicates p < 0.01 compared to the STZ group.

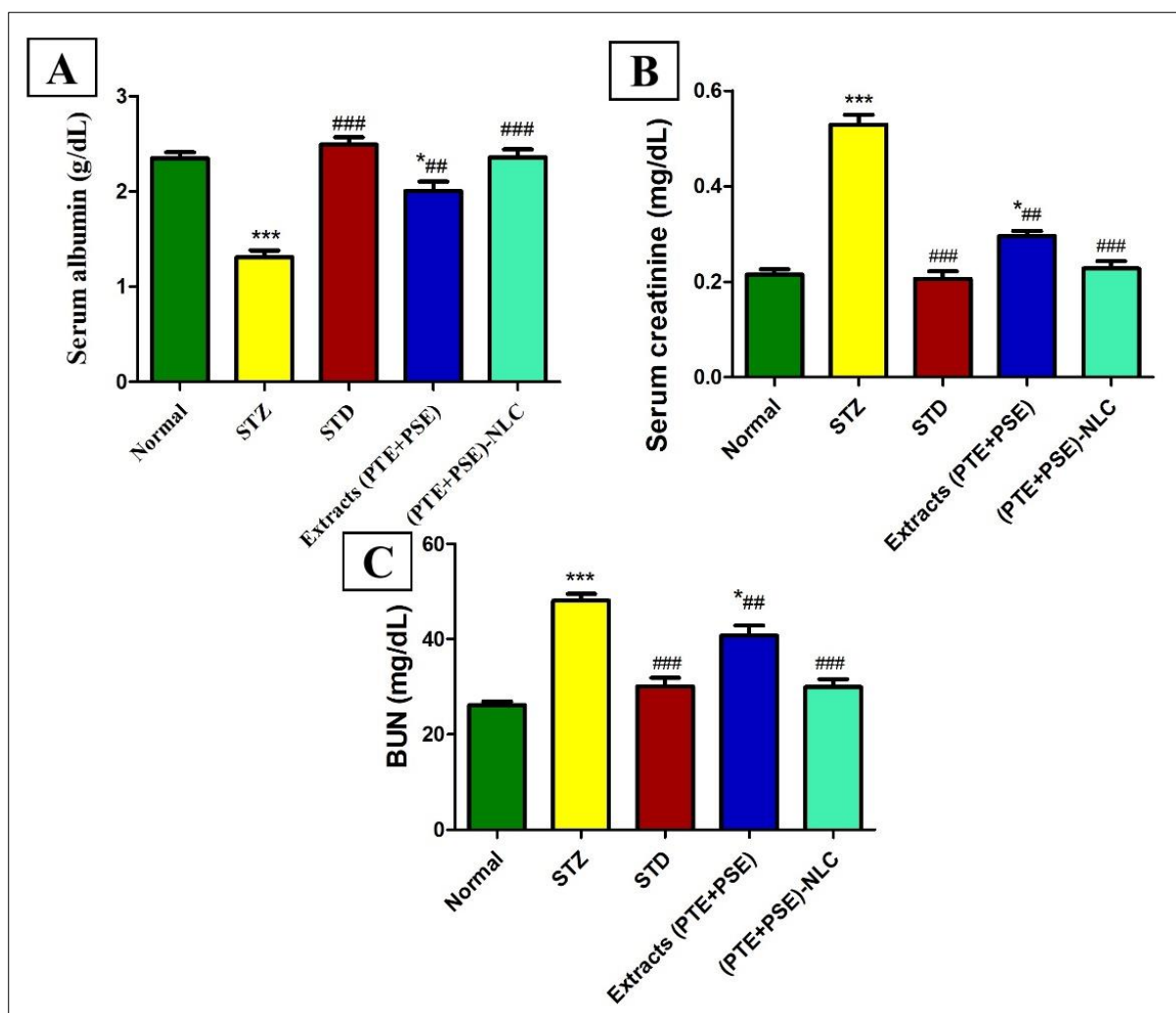


**Figure 5. 22:** Antinephritic effects of glibenclamide (1 mg/kg), plant extracts (1000 mg/kg), and (PTE+PSE)-NLC (200 mg/kg) on: (A) serum albumin, (B) serum creatinine, and (C) blood urea nitrogen levels in mice with early diabetic nephropathy. Data are presented as mean  $\pm$  SEM (n = 5); level of significance: \* $p \leq 0.05$ , \*\* $p \leq 0.01$ , \*\*\* $p \leq 0.001$  vs. normal group; # $p \leq 0.05$ , ## $p \leq 0.01$ , ### $p \leq 0.001$  vs. STZ group

#### 5.B.7.4. Effects of (PTE+PSE)-NLC on pancreatic and renal tissue in mice with early diabetic nephropathy

Histological analysis of H&E-stained sections revealed that the normal control group had well-structured pancreatic islets with uniform size and shape, and  $\beta$ -cells featuring rounded, centrally placed nuclei, as depicted in Figure 5.23A. In contrast, the STZ-induced diabetic group displayed severe islet degeneration, with fewer  $\beta$ -cells and reduced islet size, as illustrated in Figure 5.23B. Treatment with glibenclamide (1 mg/kg) and (PTE+PSE)-NLC

(200 mg/kg) for eight weeks significantly restored islet structure and  $\beta$ -cell morphology, as shown in Figures 5.23C and 5.23E. This histopathological analysis elucidates the deleterious effects of diabetes on the cellular and structural integrity of pancreatic islets in the untreated group. In contrast, treatment with (PTE+PSE)-NLC significantly mitigated pancreatic damage and restored the structural integrity of islet cells. These findings underscore the protective role of (PTE+PSE)-NLC against oxidative stress, preserving pancreatic tissue in diabetic mice and facilitating the recovery of islet architecture and function.

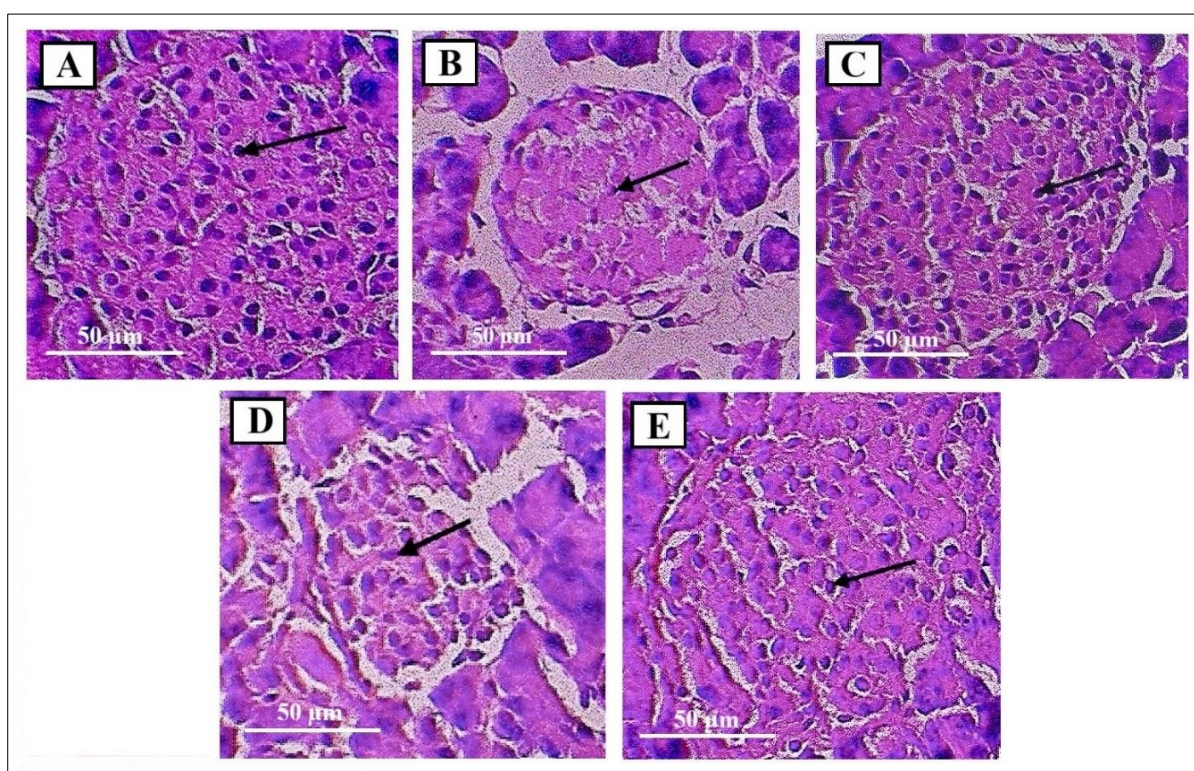


**Figure 5. 23:** Microscopic images of pancreatic tissue (H&E stain, 100x). (A) Normal control: healthy islets and  $\beta$ -cells. (B) STZ-induced diabetes: damaged islets and  $\beta$ -cells. (C) Glibenclamide treated: restored pancreatic structures. (D) PTE+PSE treated: partially recovered islets and  $\beta$ -cells. (E) (PTE+PSE)-NLC: fully restored islets and  $\beta$ -cells. (Arrow:  $\beta$  cells)

The standard histological characteristics of kidney tissues were evident in Figure 5.24A, showcasing well-preserved Bowman's capsules, tubules, and glomeruli. Conversely, kidney sections from untreated STZ-induced diabetic mice exhibited significant deviations from the

control group, as shown in Figure 5.24B. These changes included enlarged urinary spaces, glomerular shrinkage, vacuolation and lobulation of tubular epithelial cells, narrowed capillary loops, and tubular atrophy, indicating more severe damage compared to control mice. However, treatment with glibenclamide at 1 mg/kg and (PTE+PSE)-NLC at 200 mg/kg effectively reversed these pathological alterations. This is demonstrated in panels Figure 5.24C and 5.24E, where a notable restoration of cellular structures to a state resembling that of the control group was observed, particularly with respect to the appearance of urinary spaces. These findings suggest that (PTE+PSE)-NLC is a promising agent for protecting kidney tissues and structures, effectively reversing pathological changes caused by STZ-induced diabetes and restoring cellular integrity to a level comparable to that of healthy mice.

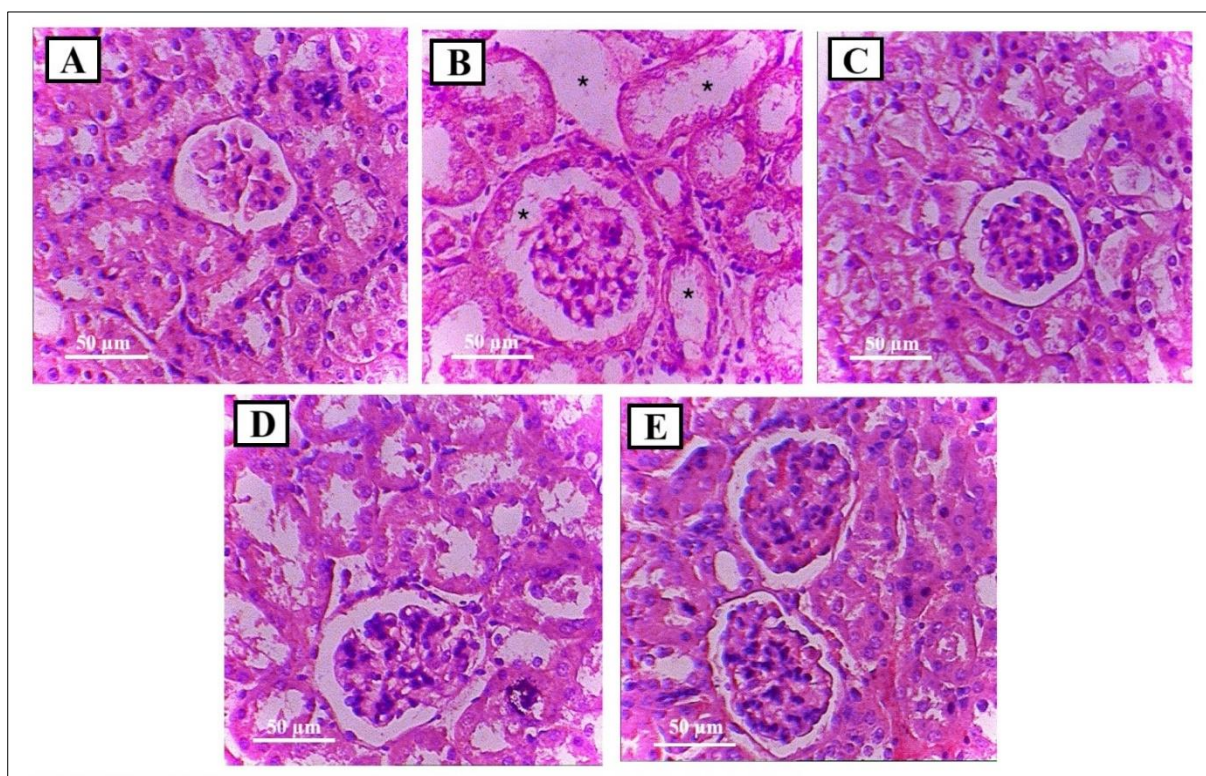


**Figure 5. 24:** Photomicrographs of kidney histological sections (H&E stain, 100x). (A) Normal control: healthy kidney appearance. (B) STZ-induced diabetes: degeneration and necrosis of tubular epithelium, expanded urinary spaces. (C) Glibenclamide treated: restored kidney structures. (D) Free (PTE+PSE) treated: partial recovery of glomerular and tubular structures. (E) (PTE+PSE)-NLC: near-normal kidney architecture. (Asterisk: expanded urinary space)

## 5.C. DISCUSSION

The International Diabetes Federation predicted a staggering 382 million people would live with diabetes by 2013, initially estimated for 2030. This alarming figure is expected to reach nearly 600 million by 2035 (Harding et al., 2019). The rising prevalence of diabetes poses a significant threat to global health, leading to increased chronic and acute diseases, straining healthcare systems, and escalating economic costs. Diabetes accounts for roughly 45% of end-stage renal disease (ESRD) cases (Satirapoj and Adler, 2015). Diabetic nephropathy development significantly elevates the kidney hypertrophy index (KHI), serum creatinine (Scr), and blood urea nitrogen (BUN) levels (Tong et al., 2017). Chronic hyperglycemia-driven metabolic and hemodynamic factors contribute to kidney damage by triggering inflammatory, oxidative, fibrotic, and ischemic pathways. These processes can lead to tubular atrophy and fibrosis, glomerular basement membrane thickening, mesangial matrix accumulation, endothelial dysfunction, renal arteriolar hyalinosis, podocyte damage (Satirapoj and Adler, 2014; Satirapoj, 2010).

Natural herbal remedies, containing a combination of phytochemicals, offer potential therapeutic benefits by activating various signaling pathways (Yang et al., 2014; Zhao et al., 2020). While crude plant extracts can be effective, they often suffer from poor oral bioavailability and difficulty in formulation (Vijayanand et al., 2018). To address these limitations, recent research has focused on developing nano-scale drug delivery systems for herbal drugs (Almasian et al., 2021). Encapsulating herbal extracts into nanoparticles can improve delivery and bioavailability, reduce the required dosage, and enable controlled, sustained release with fewer side effects (Alahmer et al., 2024).

*Pueraria tuberosa* tubers are rich in puerarin, a bioactive compound with antioxidant, anti-inflammatory, antihyperglycemic, and anti-hyperlipidemic properties. Similarly, *Pterocarpus santalinus* heartwood contains pterostilbene, an active compound known for its effectiveness

in treating diabetes, malaria, fever, and chronic inflammatory conditions (Aruna et al., 2016; Narayan et al., 2005). Despite their tremendous pharmacological activities, both compounds possess poor water solubility and bioavailability (Luo et al., 2011; Tzeng et al., 2021)

This study aimed to investigate the therapeutic efficacy of nanostructured lipid carriers (NLCs) loaded with *Pueraria tuberosa* extract (PTE) and *Pterocarpus santalinus* extract (PSE) in a streptozotocin-induced early diabetic nephropathy mouse model. We prepared and characterized NLCs encapsulating combined plant extracts [(PTE+PSE)-NLC] and conducted *in vivo* antidiabetic and antinephritic studies.

A robust and sensitive RP-HPLC method was established to quantitatively evaluate the concentrations of puerarin and pterostilbene within the prepared (PTE+PSE)-NLC formulation. The method employed a mobile phase composed of  $\text{KH}_2\text{PO}_4$  buffer (pH 3.5) and acetonitrile, with ultraviolet (UV) detection at 284 nm, the isosbestic point of the two compounds (Figure 5.2). Puerarin and pterostilbene exhibited distinct retention time (RT) of 11.7 and 14.6 minutes, respectively, allowing for their accurate separation and quantification. The method was rigorously validated according to International Conference on Harmonization (ICH) guidelines, ensuring its reliability and accuracy for subsequent analyses (ICH, 2005). This validated RP-HPLC method proved invaluable for estimating the loading capacity, entrapment efficiency, stability, and *in vitro* release profiles of the (PTE+PSE)-NLC formulation.

The (PTE+PSE)-NLC formulation demonstrated superior loading capacity and entrapment efficiency compared to NLCs containing single plant extracts (Table 5.10). Dynamic light scattering (DLS) analysis revealed the spherical morphology of the NLCs with a narrow size distribution, indicating a homogenous particle population. The high negative zeta potential values ensured excellent physicochemical stability and minimized aggregation, as strong repulsive forces reduced particle collision (Fonseca et al., 2017).

Morphological characterization confirmed the spherical shape of the NLCs, with no signs of aggregation. Physicochemical analysis revealed successful encapsulation of the extract into the NLCs, converting its crystalline structure into an amorphous form. This crystalline-to-amorphous conversion has been reported to enhance the solubility of the plant extract upon encapsulation in NLCs (Kakran et al., 2012b).

Furthermore, *in vitro* release studies revealed a biphasic release profile of PTE and PSE from (PTE+PSE)-NLC. An initial burst release was observed over 24 hours, likely due to the release of unbound drug moieties. Subsequently, a sustained release phase was observed over seven days, suggesting the controlled release of the encapsulated drugs. The release kinetics were significantly influenced by the pH of the release medium, with a higher release rate observed in SIF medium (pH 7.4) compared to SGF medium (pH 1.2) (Figure 5.18). This pH-dependent release behavior is advantageous for targeted drug delivery to the gastrointestinal tract and systemic circulation.

The *in vivo* antidiabetic study evaluated the therapeutic efficacy of (PTE+PSE)-NLC compared to single-extract NLCs, free plant extracts, and glibenclamide. Results indicated that (PTE+PSE)-NLC significantly reduced FBGL to levels comparable to normal control mice (Table 5.14). The encapsulation of both plant extracts in NLCs resulted in a 31.28-fold greater reduction in FBGL compared to the free form of the extracts. This synergistic effect was further evidenced by the fact that the FBGL inhibition was 96.5% for (PTE+PSE)-NLC, 82.7% for PTE-NLC, and 86.6% for PSE-NLC (Figure 5.20).

The *in vivo* antinephritic activity of (PTE+PSE)-NLC was equally impressive. The formulation significantly reduced kidney weight, KHI, Scr, and BUN levels, while maintaining normal body weight. This was in stark contrast to the untreated diabetic group, which exhibited kidney enlargement due to inflammation, a hallmark of early diabetic nephropathy (Nazar, 2014). The (PTE+PSE)-NLC-treated group effectively prevented this inflammation, maintaining kidney

size and weight comparable to healthy control mice (Figure 5.21). Moreover, (PTE+PSE)-NLC significantly raised Alb levels and markedly reduced the elevated Scr and BUN levels, indicating improved renal function (Table 5.16).

Histopathological analysis of thin sections from pancreatic and kidney tissues further supported the therapeutic efficacy of (PTE+PSE)-NLC. The formulation demonstrated restorative and regenerative effects on pancreatic  $\beta$ -cells and kidney podocytes, as evidenced by the increased number of healthy cells and reduced pathological features in the treated groups (Figures 5.23 and 5.24). These findings underscore the potential of (PTE+PSE)-NLC as a promising therapeutic agent for diabetic nephropathy.

The (PTE+PSE)-NLC formulation demonstrated significant therapeutic potential in treating diabetic nephropathy, effectively reducing elevated blood glucose levels, restoring kidney function, and minimizing inflammation. Its enhanced bioavailability and synergistic effects make it a promising candidate for managing diabetes-related kidney complications.

## **5.D. CONCLUSION**

This study successfully demonstrated the therapeutic potential of nanostructured lipid carriers (NLCs) loaded with *Pueraria tuberosa* extract (PTE) and *Pterocarpus santalinus* extract (PSE) in managing diabetic nephropathy. The formulation effectively reduced elevated blood glucose levels, restored kidney function, and minimized inflammation, showcasing its promising potential as a novel therapeutic approach. The synergistic effects of PTE and PSE, when encapsulated in NLCs, significantly enhanced their bioavailability and therapeutic efficacy compared to their free forms. The biphasic release profile of the encapsulated extracts, with an initial burst release followed by sustained release, further contributed to the observed therapeutic benefits.

Moreover, the NLC formulation exhibited excellent physicochemical properties, ensuring its stability and biocompatibility. The successful encapsulation of the plant extracts into the NLCs, resulting in a crystalline-to-amorphous conversion, enhanced their solubility and bioavailability. This study provides compelling evidence for the efficacy of (PTE+PSE)-NLC in treating diabetic nephropathy. The formulation holds significant promise as a potential therapeutic option for managing this complex disease and improving the quality of life for patients with diabetes.

# Chapter VI

## Summary

## 6. SUMMARY

Diabetes can cause severe kidney damage known as diabetic nephropathy (DN), which is a leading cause of cardiovascular death and end-stage renal disease (ESRD). DN is clinically characterized by decreased kidney function, increased urinary albumin excretion, and kidney inflammation, particularly in its early stages. Current management strategies for DN focus on four key areas: reducing cardiovascular risk, glycemic control, blood pressure regulation, and inhibition of the RAAS. ACE inhibitors or ARBs treatments may slow the advancement of diabetic nephropathy, but they do not cure it. Moreover, prolonged use of these drugs is associated with significant costs and adverse side effects.

In response to these challenges, there is growing interest in natural products derived from plants as alternative therapies for DN. These natural compounds have demonstrated potential in lowering blood glucose and lipid levels, while also providing antioxidant properties that may help mitigate diabetes-related complications. In this context, four promising compounds with antioxidant, anti-inflammatory, antidiabetic, and nephroprotective properties were selected: curcumin (CUR) from *Curcuma longa*, epigallocatechin gallate (EGCG) from *Camellia sinensis* leaves, *Pueraria tuberosa* extract (PTE) from tubers, and *Pterocarpus santalinus* extract (PSE) from heartwood. However, their clinical use is limited due to low bioavailability, poor solubility, and chemical instability, necessitating the development of advanced drug delivery systems to enhance therapeutic efficacy.

In one study, CUR and EGCG were encapsulated in a shellac and locust bean gum matrix to form CESL-NP. A novel RP-HPLC method was established and confirmed according to ICH guidelines to simultaneously quantify the CUR and EGCG in this nanoformulation. Characterization studies revealed nanoparticles in the nanoscale range, spherical in shape, and uniformly dispersed with no aggregation. The encapsulation of CUR and EGCG within the nanoparticle matrix converted their crystalline forms into an amorphous state, enhancing

solubility. The drug release kinetics for CUR followed the first-order model in SGF and the Korsmeyer-Peppas model in SIF, with a release exponent ( $n$ ) below 0.43, indicating Fickian diffusion. For EGCG, the release followed the Higuchi model in both media, with release exponent values between 0.43 and 0.85, indicating non-Fickian diffusion.

*In vivo* studies demonstrated the antidiabetic and antinephritic potential of CESL-NP at a dose of 20 mg/kg, significantly reducing fasting blood glucose levels (FBGL), kidney size, kidney hypertrophy index (KHI), serum creatinine (Scr), and blood urea nitrogen (BUN). CESL-NP also normalized body weight and albumin levels. CESL-NP reduced FBGL by 38.68-folds compared to free CUR and EGCG, indicating improved bioavailability. Histopathological analysis further confirmed the regenerative effects of CESL-NP on pancreatic beta cells and islets of Langerhans, along with the restoration of damaged kidney podocytes.

In another study, PTE and PSE were co-encapsulated in nanostructured lipid carriers [(PTE+PSE)-NLC], using Compritol 888 ATO as the solid lipid and triolein as the liquid lipid. A new RP-HPLC method was also developed and validated for the simultaneous quantification of puerarin from PTE and pterostilbene from PSE. The resulting (PTE+PSE)-NLC formulation demonstrated a loading capacity of 10.1% for PTE and 9.92% for PSE, with entrapment efficiencies of 91.74% and 92.47%, respectively. Morphological studies confirmed nanoparticles in the 90-110 nm range, with spherical shape and narrow size distribution. The conversion of PTE and PSE from crystalline to amorphous form, as revealed by FTIR, DSC, and XRD analyses, contributed to improved solubility and stability. *In vitro* drug release studies demonstrated sustained release for PTE, following the Higuchi model in SGF and the Korsmeyer–Peppas model in SIF. The release exponent ( $n$ ) values for PTE ranged between 0.43 and 0.85, indicating non-Fickian diffusion. For PSE, the release kinetics followed the Hixon–Crowell model in SGF and the Korsmeyer–Peppas model in SIF, with  $n$  values below 0.43, suggesting Fickian diffusion.

*In vivo* antidiabetic studies demonstrated that the (PTE+PSE)-NLC formulation at 200 mg/kg significantly reduced FBGL, with a 96.5% reduction by the end of the eight-week study, outperforming both PSE-NLC and PTE-NLC. The formulation showed a 31.28-fold improvement in bioavailability compared to the free extract mixture. Histopathological evaluation revealed substantial regeneration of pancreatic beta cells and restoration of islet volume.

In antinephritic studies, (PTE+PSE)-NLC maintained normal kidney size and significantly reduced elevated kidney hypertrophy index, serum creatinine, and blood urea nitrogen levels. It also restored albumin levels to normal. Histological analysis of kidney tissues confirmed the protective effects of the formulation, reversing diabetes-induced pathological changes and restoring cellular integrity.

In conclusion, the encapsulation of CUR, EGCG, PTE, and PSE within biopolymeric nanoparticles and nanostructured lipid carriers significantly improved their bioavailability. By enhancing solubility and stability, these nanoformulations facilitated sustained drug release, potentially reducing the frequency of dosing and improving patient adherence. These findings underscore the promising potential of these innovative delivery systems for the treatment of diabetes and its related complications.

# References

- Abd El-Hameed, A.M., 2020. Polydatin-loaded chitosan nanoparticles ameliorates early diabetic nephropathy by attenuating oxidative stress and inflammatory responses in streptozotocin-induced diabetic rat. *J. Diabetes Metab. Disord.* 19, 1599–1607. <https://doi.org/10.1007/s40200-020-00699-7>
- Abdel-Mageid, A.D., Abou-Salem, M.E.S., Salaam, N.M.H.A., El-Garhy, H.A.S., 2018. The potential effect of garlic extract and curcumin nanoparticles against complication accompanied with experimentally induced diabetes in rats. *Phytomedicine* 43, 126–134. <https://doi.org/10.1016/j.phymed.2018.04.039>
- Abdel-moneum, R., Abdel-Rashid, R.S., 2023. Bile salt stabilized nanovesicles as a promising drug delivery technology: A general overview and future perspectives. *J. Drug Deliv. Sci. Technol.* 79. <https://doi.org/10.1016/j.jddst.2022.104057>
- Abdulmalek, S., Eldala, A., Awad, D., Balbaa, M., 2021. Ameliorative effect of curcumin and zinc oxide nanoparticles on multiple mechanisms in obese rats with induced type 2 diabetes. *Sci. Rep.* 11, 1–22. <https://doi.org/10.1038/s41598-021-00108-w>
- Aburahma, M.H., Badr-Eldin, S.M., 2014. Compritol 888 ATO: A multifunctional lipid excipient in drug delivery systems and nanopharmaceuticals. *Expert Opin. Drug Deliv.* 11, 1865–1883. <https://doi.org/10.1517/17425247.2014.935335>
- Adhikary, L., Chow, F., Nikolic-Paterson, D.J., Stambe, C., Dowling, J., Atkins, R.C., Tesch, G.H., 2004. Abnormal p38 mitogen-activated protein kinase signalling in human and experimental diabetic nephropathy. *Diabetologia* 47, 1210–1222. <https://doi.org/10.1007/s00125-004-1437-0>
- Adugna, B.Y., Adinew, G.M., Getahun, K.A., Gurmu, A.E., Berhie, A.Y., Awoke, T., Desta, G., 2022. Evaluation of the Antidiabetic Activity of Hydromethanolic Roots Extracts of *Rumex abyssinicus* Jacq: (Polygonaceae) in Swiss Albino Mice. *Evidence-based Complement. Altern. Med.* 2022. <https://doi.org/10.1155/2022/5193250>
- Ahmadi, R., Pishghadam, S., Mollaamine, F., Monfared, M.R.Z., 2013. Comparing the effects of ginger and glibenclamide on dihydroxybenzoic metabolites produced in Stz-induced diabetic rats. *Int. J. Endocrinol. Metab.* 11, 1–5. <https://doi.org/10.5812/ijem.10266>
- Ahmaditabar, P., Momtazi-Borojeni, A.A., Rezayan, A.H., Mahmoodi, M., Sahebkar, A., Mellat, M., 2017. Enhanced Entrapment and Improved in Vitro Controlled Release of N-Acetyl

- Cysteine in Hybrid PLGA/Lecithin Nanoparticles Prepared Using a Nanoprecipitation/Self-Assembly Method. *J. Cell. Biochem.* 118, 4203–4209. <https://doi.org/10.1002/jcb.26070>
- Ahmed, H., Ali Shah, S., Rashid, A., Ayaz, S., Rahat, S., Author, C., 2023. Phyto-Pharmacological Studies On Ethanolic Extract Of *Pueraria Tuberosa* And Its Effect On Spermatozoa Parameters. *J. Popul. Ther. Clin. Pharmacol.* 30, 1044–1061.
- Ajiboye, A.L., Nandi, U., Galli, M., Trivedi, V., 2021. Olanzapine loaded nanostructured lipid carriers via high shear homogenization and ultrasonication. *Sci. Pharm.* 89. <https://doi.org/10.3390/scipharm89020025>
- Akbarzadeh, A., Norouzian, D., Mehrabi, M.R., Jamshidi, S., Farhangi, A., Allah Verdi, A., Mofidian, S.M.A., Lame Rad, B., 2007. Induction of diabetes by Streptozotocin in rats. *Indian J. Clin. Biochem.* 22, 60–64. <https://doi.org/10.1007/BF02913315>
- Alahmer, S., El-Noss, M., Farid, A., 2024. Preparation of chitosan nanoparticles loaded with *Balanites aegyptiaca* extract for treatment of streptozotocin-induced diabetes in rats. *Int. J. Biol. Macromol.* 262. <https://doi.org/10.1016/j.ijbiomac.2024.130061>
- Albertini, B., Passerini, N., González-Rodríguez, M.L., Perissutti, B., Rodriguez, L., 2004. Effect of Aerosil® on the properties of lipid controlled release microparticles. *J. Control. Release* 100, 233–246. <https://doi.org/10.1016/j.jconrel.2004.08.013>
- Alghananim, A., Özalp, Y., Mesut, B., Serakinci, N., Özsoy, Y., Güngör, S., 2020. A solid ultra fine self-nanoemulsifying drug delivery system (S-snedds) of deferasirox for improved solubility: Optimization, characterization, and in vitro cytotoxicity studies. *Pharmaceuticals* 13, 1–25. <https://doi.org/10.3390/ph13080162>
- Alhazza, I.M., Ebaid, H., Omar, M.S., Hassan, I., Habila, M.A., Al-Tamimi, J., Sheikh, M., 2022. Supplementation with selenium nanoparticles alleviates diabetic nephropathy during pregnancy in the diabetic female rats. *Environ. Sci. Pollut. Res.* 29, 5517–5525. <https://doi.org/10.1007/s11356-021-15905-z>
- Almasian, A., Najafi, F., Eftekhari, M., Shams Ardekani, M.R., Sharifzadeh, M., Khanavi, M., 2021. Preparation of Polyurethane/Pluronic F127 Nanofibers Containing Peppermint Extract Loaded Gelatin Nanoparticles for Diabetic Wounds Healing: Characterization, in Vitro, and in Vivo Studies. *Evidence-based Complement. Altern. Med.* 2021. <https://doi.org/10.1155/2021/6646702>

- Al-Obaidy, S.S.M., Greenway, G.M., Paunov, V.N., 2021. Enhanced antimicrobial action of chlorhexidine loaded in shellac nanoparticles with cationic surface functionality. *Pharmaceutics* 13, 1–15. <https://doi.org/10.3390/pharmaceutics13091389>
- Alomari, G., Al-Trad, B., Hamdan, S., Aljabali, A., Al-Zoubi, M., Bataineh, N., Qar, J., Tambuwala, M.M., 2020. Gold nanoparticles attenuate albuminuria by inhibiting podocyte injury in a rat model of diabetic nephropathy. *Drug Deliv. Transl. Res.* 10, 216–226. <https://doi.org/10.1007/s13346-019-00675-6>
- Alomari, G., Al-Trad, B., Hamdan, S., Aljabali, A.A.A., Al Zoubi, M.S., Al-Batanyeh, K., Qar, J., Eaton, G.J., Alkaraki, A.K., Alshaer, W., Haifawi, S., Jemon, K., Chellappan, D.K., Dua, K., Tambuwala, M.M., 2021. Alleviation of diabetic nephropathy by zinc oxide nanoparticles in streptozotocin-induced type 1 diabetes in rats. *IET Nanobiotechnology* 15, 473–483. <https://doi.org/10.1049/nbt2.12026>
- Alonso-Sande, M., Teijeiro-Osorio, D., Remuñán-López, C., Alonso, M.J., 2009. Glucomannan, a promising polysaccharide for biopharmaceutical purposes. *Eur. J. Pharm. Biopharm.* 72, 453–462. <https://doi.org/10.1016/j.ejpb.2008.02.005>
- Alqarni, M.H., Haq, N., Alam, P., Abdel-Kader, M.S., Foudah, A.I., Shakeel, F., 2021. Solubility data, Hansen solubility parameters and thermodynamic behavior of pterostilbene in some pure solvents and different (PEG-400 + water) cosolvent compositions. *J. Mol. Liq.* 331. <https://doi.org/10.1016/j.molliq.2021.115700>
- Amann, B., Tinzmann, R., Angelkort, B., 2003. ACE Inhibitors Improve Diabetic Nephropathy Through Suppression of Renal MCP-1. *Diabetes Care* 26.
- Amiri-Rigi, A., Kesavan Pillai, S., Naushad Emmambux, M., 2023. Development of hemp seed oil nanoemulsions loaded with ascorbyl palmitate: Effect of operational parameters, emulsifiers, and wall materials. *Food Chem.* 400. <https://doi.org/10.1016/j.foodchem.2022.134052>
- Anandalakshmi, K., Venugobal, J., Ramasamy, V., 2016. Characterization of silver nanoparticles by green synthesis method using *Petalium murex* leaf extract and their antibacterial activity. *Appl. Nanosci.* 6, 399–408. <https://doi.org/10.1007/s13204-015-0449-z>
- Anilkumar, K., Reddy, G. V., Azad, R., Yarla, N.S., Dharmapuri, G., Srivastava, A., Kamal, M.A., Pallu, R., 2017. Evaluation of Anti-Inflammatory Properties of Isoorientin Isolated from

Tubers of *Pueraria tuberosa*. *Oxid. Med. Cell. Longev.* 2017. <https://doi.org/10.1155/2017/5498054>

Ansari, M., Sadarani, B., Majumdar, A., 2019. Colon targeted beads loaded with pterostilbene: Formulation, optimization, characterization and in vivo evaluation. *Saudi Pharm. J. SPJ Off. Publ. Saudi Pharm. Soc.* 27, 71–81. <https://doi.org/10.1016/j.jsps.2018.07.021>

Arayne, M.S., Sultana, N., Zuberi, M.H., 2006. Development and validation of RP-HPLC method for the analysis of metformin. *Pak. J. Pharm. Sci.* 19, 231–235.

Aree, T., Jongrungruangchok, S., 2016. Enhancement of antioxidant activity of green tea epicatechins in  $\beta$ -cyclodextrin cavity: Single-crystal X-ray analysis, DFT calculation and DPPH assay. *Carbohydr. Polym.* 151, 1139–1151. <https://doi.org/10.1016/j.carbpol.2016.05.113>

Aruna, M.R., Kumar, D.J.M., Senbagam, D., Senthilkumar, B., 2016. Investigation on phytochemical and antimicrobial properties of tuber extracts of *Pueraria tuberosa* linn. *J. Pure Appl. Microb* 10, 1573–1578.

Aruna, M.R., Kumar, M., Senbagam, D., Senthilkumar, B., 2016. Investigation on Phytochemical and Antimicrobial Properties of *Acorus Calamus* Extract. *J. Archaeol. Egypt/Egyptology* 10, 1573–1578.

Arunakumara, K.K.I.U., Walpola, B.C., Subasinghe, S., Yoon, M.H., 2011. *Pterocarpus santalinus* linn. f. (Rath handun): A review of its botany, uses, phytochemistry and pharmacology. *J. Korean Soc. Appl. Biol. Chem.* 54, 495–500. <https://doi.org/10.3839/jksabc.2011.076>

Asgary, S., Rafieian-Kopaei, M., Shamsi, F., Najafi, S., Sahebkar, A., 2014. Biochemical and histopathological study of the anti-hyperglycemic and anti-hyperlipidemic effects of cornelian cherry (*Cornus mas* L.) in alloxan-induced diabetic rats. *J. Complement. Integr. Med.* 11, 63–69. <https://doi.org/10.1515/jcim-2013-0022>

Aswathy, S.R., Muhas, C., Sruthy S., A., P. V., D.S., U., G., 2022. Validation and Application of Rp-Hplc Method for Quantification of Enrofloxacin in Pure and Veterinary Dosage Forms. *Int. J. Pharm. Pharm. Sci.* 14, 42–47. <https://doi.org/10.22159/ijpps.2022v14i2.43053>

Atkinson, M.A., Eisenbarth, G.S., Michels, A.W., 2014. Type 1 diabetes. *Lancet* 383, 69–82. [https://doi.org/10.1016/S0140-6736\(13\)60591-7](https://doi.org/10.1016/S0140-6736(13)60591-7)

- Awazu, M., Ishikura, K., Hida, M., Hoshiya, M., 1999. Mechanisms of mitogen-activated protein kinase activation in experimental diabetes. *J. Am. Soc. Nephrol.* 10, 738–745. <https://doi.org/10.1681/asn.v104738>
- Ayodele, O.E., Alebiosu, C.O., Salako, B.L., 2004. Diabetic nephropathy - A review of the natural history, burden, risk factors and treatment. *J. Natl. Med. Assoc.* 96, 1445–1454.
- Ayubi, M., Karimi, M., Abdpour, S., Rostamizadeh, K., Parsa, M., Zamani, M., Saedi, A., 2019. Magnetic nanoparticles decorated with PEGylated curcumin as dual targeted drug delivery: Synthesis, toxicity and biocompatibility study. *Mater. Sci. Eng. C* 104. <https://doi.org/10.1016/j.msec.2019.109810>
- Azamthulla, M., Balasubramanian, R., Kavimani, S., 2013. Acute and sub-acute toxicity of *Pterocarpus santalinus* heartwood extracts in rats. *Int. J. Front. Sci. Technol.* 1, 99–113.
- Azamthulla, M., Balasubramanian, R., S, K., 2015a. A review on *Pterocarpus santalinus* Linn. *World J. Pharm. Res.* 4, 282–292. <https://doi.org/10.20959/wjpr202317-29690>
- Azamthulla, M., Rajkapoor, B., S, K., 2015b. A review on *Pterocarpus santalinus* linn. *World J. Pharm. Res.* 4, 282–292.
- Azmi, N.A.N., Hasham, R., Ariffin, F.D., Elgharbawy, A.A.M., Salleh, H.M., 2020. Characterization, stability assessment, antioxidant evaluation and cell proliferation activity of virgin coconut oil-based nanostructured lipid carrier loaded with *Ficus deltoidea* extract. *Cosmetics* 7, 1–15. <https://doi.org/10.3390/cosmetics7040083>
- Bacon, J.L., Tomich, P.G., 2017. *Obstetrics and Gynecology: Maintenance of Knowledge, Obstetrics and Gynecology Clinics of North America.* [https://doi.org/10.1016/s0889-8545\(17\)30056-6](https://doi.org/10.1016/s0889-8545(17)30056-6)
- Badar, A., Pachera, S., Ansari, A.S., Kumar Lohiya, N., 2019. Nano Based Drug Delivery Systems: Present and Future Prospects. *Nanomedicine Nanotechnol. J.* 2, 121.
- Balakumar, P., Arora, M.K., Ganti, S.S., Reddy, J., Singh, M., 2009. Recent advances in pharmacotherapy for diabetic nephropathy: Current perspectives and future directions. *Pharmacol. Res.* 60, 24–32. <https://doi.org/10.1016/j.phrs.2009.02.002>

- Bao, H., Li, L., Zhang, H., 2008. Influence of cetyltrimethylammonium bromide on physicochemical properties and microstructures of chitosan-TPP nanoparticles in aqueous solutions. *J. Colloid Interface Sci.* 328, 270–277. <https://doi.org/10.1016/j.jcis.2008.09.003>
- Barak, S., Mudgil, D., 2014. Locust bean gum: Processing, properties and food applications-A review. *Int. J. Biol. Macromol.* 66, 74–80. <https://doi.org/10.1016/j.ijbiomac.2014.02.017>
- BarathManiKanth, S., Kalishwaralal, K., Sriram, M., Pandian, S.B.R.K., Youn, H. seop, Eom, S.H., Gurunathan, S., 2010. Anti-oxidant effect of gold nanoparticles restrains hyperglycemic conditions in diabetic mice. *J. Nanobiotechnology* 8, 1–15. <https://doi.org/10.1186/1477-3155-8-16>
- Barthelemy, P., Laforêt, J.P., Farah, N., Joachim, J., 1999. Compritol® 888 ATO: An innovative hot-melt coating agent for prolonged-release drug formulations. *Eur. J. Pharm. Biopharm.* 47, 87–90. [https://doi.org/10.1016/S0939-6411\(98\)00088-5](https://doi.org/10.1016/S0939-6411(98)00088-5)
- Bartosikova, L., Necas, J., 2018. Epigallocatechin gallate: A review. *Vet. Med. (Praha)*. 63, 443–467. <https://doi.org/10.17221/31/2018-VETMED>
- Beloqui, A., Solinís, M.Á., Rodríguez-Gascón, A., Almeida, A.J., Prát, V., 2016. Nanostructured lipid carriers: Promising drug delivery systems for future clinics. *Nanomedicine Nanotechnology, Biol. Med.* 12, 143–161. <https://doi.org/10.1016/j.nano.2015.09.004>
- Benz, K., Amann, K., 2011. Endothelin in diabetic renal disease. *Endothel. Ren. Physiol. Dis.* 172, 139–148. <https://doi.org/10.1159/000328695>
- Bessa, S.S.E.D., Hussein, T.A., Morad, M.A., Amer, A.M., 2012. Urinary platelet-derived growth factor-BB as an early marker of nephropathy in patients with type 2 diabetes: An Egyptian study. *Ren. Fail.* 34, 670–675. <https://doi.org/10.3109/0886022X.2012.674438>
- Bhagwat, D.A., D'Souza, J.I., 2012. Formulation and evaluation of solid self micro emulsifying drug delivery system using aerosil 200 as solid carrier. *Int. Curr. Pharm. J.* 1, 414–419. <https://doi.org/10.3329/icpj.v1i12.12451>
- Bharti, R., Chopra, B.S., Raut, S., Khatri, N., 2021. *Pueraria tuberosa*: A Review on Traditional Uses, Pharmacology, and Phytochemistry. *Front. Pharmacol.* 11. <https://doi.org/10.3389/fphar.2020.582506>

- Bhattacharjee, J., Verma, G., Aswal, V.K., Date, A.A., Nagarsenker, M.S., Hassan, P.A., 2010. Tween 80– sodium deoxycholate mixed micelles: Structural characterization and application in doxorubicin delivery. *J. Phys. Chem. B* 114, 16414–16421.
- Bhawana, Basniwal, R.K., Buttar, H.S., Jain, V.K., Jain, N., 2011. Curcumin Nanoparticles: Preparation, Characterization, and Antimicrobial Study. *J. Agric. Food Chem.* 59, 2056–2061. <https://doi.org/10.1021/jf104402t>
- Bhutia, G.T., De, A.K., Bera, T., 2022. Validation, stability studies, and simultaneous estimation of co-encapsulated curcumin, epigallocatechin gallate nanoformulation by RP-HPLC method. *Int. J. Appl. Pharm.* 14, 186–195. <https://doi.org/10.22159/ijap.2022v14i6.45818>
- Blahova, J., Martiniakova, M., Babikova, M., Kovacova, V., Mondockova, V., Omelka, R., 2021. Pharmaceutical drugs and natural therapeutic products for the treatment of type 2 diabetes mellitus, *Pharmaceuticals*. <https://doi.org/10.3390/ph14080806>
- Braz, L., Grenha, A., Corvo, M.C., Lourenço, J.P., Ferreira, D., Sarmento, B., Rosa da Costa, A.M., 2018. Synthesis and characterization of Locust Bean Gum derivatives and their application in the production of nanoparticles. *Carbohydr. Polym.* 181, 974–985. <https://doi.org/10.1016/j.carbpol.2017.11.052>
- Braz, L., Grenha, A., Ferreira, D., Rosa da Costa, A.M., Gamazo, C., Sarmento, B., 2017. Chitosan/sulfated locust bean gum nanoparticles: In vitro and in vivo evaluation towards an application in oral immunization. *Int. J. Biol. Macromol.* 96, 786–797. <https://doi.org/10.1016/j.ijbiomac.2016.12.076>
- Bulle, S., Reddyvari, H., Nallanchakravarthula, V., Vaddi, D.R., 2016. Therapeutic potential of *Pterocarpus santalinus* L.: An update. *Pharmacogn. Rev.* 10, 43–49. <https://doi.org/10.4103/0973-7847.176575>
- Burin, V.M., Arcari, S.G., Costa, L.L.F., Bordignon-Luiz, M.T., 2011. Determination of some phenolic compounds in red wine by RP-HPLC: Method development and validation. *J. Chromatogr. Sci.* 49, 647–651. <https://doi.org/10.1093/chrscl/49.8.647>
- Cadete, A., Figueiredo, L., Lopes, R., Calado, C.C.R., Almeida, A.J., Goncalves, L.M.D., 2012. Development and characterization of a new plasmid delivery system based on chitosan-sodium

- deoxycholate nanoparticles. Eur. J. Pharm. Sci. 45, 451–458. <https://doi.org/10.1016/j.ejps.2011.09.018>
- Carvalho, G.C., Marena, G.D., Karnopp, J.C.F., Jorge, J., Sábio, R.M., Martines, M.A.U., Bauab, T.M., Chorilli, M., 2022. Cetyltrimethylammonium bromide in the synthesis of mesoporous silica nanoparticles: General aspects and in vitro toxicity. Adv. Colloid Interface Sci. 307. <https://doi.org/10.1016/j.cis.2022.102746>
- Castelli, F., Puglia, C., Sarpietro, M.G., Rizza, L., Bonina, F., 2005. Characterization of indomethacin-loaded lipid nanoparticles by differential scanning calorimetry. Int. J. Pharm. 304, 231–238. <https://doi.org/10.1016/j.ijpharm.2005.08.011>
- Çelebier, M., Reçber, T., Koçak, E., Altinöz, S., 2013. RP-HPLC method development and validation for estimation of rivaroxaban in pharmaceutical dosage forms. Brazilian J. Pharm. Sci. 49, 359–366.
- Chakrawarti, L., Agrawal, R., Dang, S., Gupta, S., Gabrani, R., 2016. Therapeutic effects of EGCG: a patent review. Expert Opin. Ther. Pat. 26, 907–916. <https://doi.org/10.1080/13543776.2016.1203419>
- Chan, J.M., Zhang, L., Yuet, K.P., Liao, G., Rhee, J.W., Langer, R., Farokhzad, O.C., 2009. PLGA-lecithin-PEG core-shell nanoparticles for controlled drug delivery. Biomaterials 30, 1627–1634. <https://doi.org/10.1016/j.biomaterials.2008.12.013>
- Chandrashekar, K., Juncos, L.A., 2014. Endothelin antagonists in diabetic nephropathy: Back to basics. J. Am. Soc. Nephrol. 25, 869–871. <https://doi.org/10.1681/ASN.2014020174>
- Chaudhury, A., Duvoor, C., Reddy Dendi, V.S., Kraleti, S., Chada, A., Ravilla, R., Marco, A., Shekhawat, N.S., Montales, M.T., Kuriakose, K., Sasapu, A., Beebe, A., Patil, N., Musham, C.K., Lohani, G.P., Mirza, W., 2017. Clinical Review of Antidiabetic Drugs: Implications for Type 2 Diabetes Mellitus Management. Front. Endocrinol. (Lausanne). 8. <https://doi.org/10.3389/fendo.2017.00006>
- Chauhan, N.S., Gupta, N.K., Sharma, V., Dixit, V.K., 2011. Spectrofluorimetric estimation of puerarin in *Pueraria tuberosa*. Acta Pol. Pharm. - Drug Res. 68, 453–456.
- Chavan, R.B., Modi, S.R., Bansal, A.K., 2015. Role of solid carriers in pharmaceutical performance of solid supersaturable SEDDS of celecoxib. Int. J. Pharm. 495, 374–384. <https://doi.org/10.1016/j.ijpharm.2015.09.011>

- Chen, D., Han, S., Zhu, Y., Hu, F., Wei, Y., Wang, G., 2018. Kidney-targeted drug delivery via rhein-loaded polyethyleneglycol-co-polycaprolactone-co-polyethylenimine nanoparticles for diabetic nephropathy therapy. *Int. J. Nanomedicine* 13, 3507–3527. <https://doi.org/10.2147/IJN.S166445>
- Chen, D.Q., Hu, H.H., Wang, Y.N., Feng, Y.L., Cao, G., Zhao, Y.Y., 2018. Natural products for the prevention and treatment of kidney disease. *Phytomedicine* 50, 50–60. <https://doi.org/10.1016/j.phymed.2018.09.182>
- Chen, H., Brahmabhatt, S., Gupta, A., Sharma, A.C., 2005. Duration of streptozotocin-induced diabetes differentially affects p38-mitogen-activated protein kinase (MAPK) phosphorylation in renal and vascular dysfunction. *Cardiovasc. Diabetol.* 4, 1–13. <https://doi.org/10.1186/1475-2840-4-3>
- Chen, L.H., Doyle, P.S., 2022. Thermogelling Hydroxypropyl Methylcellulose Nanoemulsions as Templates to Formulate Poorly Water-Soluble Drugs into Oral Thin Films Containing Drug Nanoparticles. *Chem. Mater.* 34, 5194–5205. <https://doi.org/10.1021/acs.chemmater.2c00801>
- Chen, W., Zhao, Z., Zhao, S., Zhang, L., Song, Q., 2020. Resveratrol and Puerarin loaded polymeric nanoparticles to enhance the chemotherapeutic efficacy in spinal cord injury. *Biomed. Microdevices* 22. <https://doi.org/10.1007/s10544-020-00521-4>
- Cheng, A.Y.Y., Fantus, I.G., 2005. Oral antihyperglycemic therapy for type 2 diabetes mellitus. *Can. Med. Assoc. J.* 172, 213–226. <https://doi.org/10.1503/cmaj.1031414>
- Cheng, W., Dong, S., Wang, E., 2003. Synthesis and Self-Assembly of Cetyltrimethylammonium Bromide-Capped Gold Nanoparticles. *Langmuir* 19, 9434–9439. <https://doi.org/10.1021/la034818k>
- Ching, Y.C., Gunathilake, T.M.S.U., Chuah, C.H., Ching, K.Y., Singh, R., Liou, N.S., 2019. Curcumin/Tween 20-incorporated cellulose nanoparticles with enhanced curcumin solubility for nano-drug delivery: characterization and in vitro evaluation. *Cellulose* 26, 5467–5481. <https://doi.org/10.1007/s10570-019-02445-6>
- Chirio, D., Gallarate, M., Peira, E., Battaglia, L., Serpe, L., Trotta, M., 2011. Formulation of curcumin-loaded solid lipid nanoparticles produced by fatty acids coacervation technique. *J. Microencapsul.* 28, 537–548. <https://doi.org/10.3109/02652048.2011.590615>

- Cho, T.J., Hackley, V.A., 2010. Fractionation and characterization of gold nanoparticles in aqueous solution: Asymmetric-flow field flow fractionation with MALS, DLS, and UV-Vis detection. *Anal. Bioanal. Chem.* 398, 2003–2018. <https://doi.org/10.1007/s00216-010-4133-6>
- Chung, S.S.M., Ho, E.C.M., Lam, K.S.L., Chung, S.K., 2003. Contribution of polyol pathway to diabetes-induced oxidative stress. *J. Am. Soc. Nephrol.* 14, 233–236. <https://doi.org/10.1097/01.asn.0000077408.15865.06>
- Cirri, M., Maestrini, L., Maestrelli, F., Mennini, N., Mura, P., Ghelardini, C., Mannelli, L.D.C., 2018. Design, characterization and in vivo evaluation of nanostructured lipid carriers (NLC) as a new drug delivery system for hydrochlorothiazide oral administration in pediatric therapy. *Drug Deliv.* 25, 1910–1921. <https://doi.org/10.1080/10717544.2018.1529209>
- Crasto, W., Patel, V., Davies, M.J., Khunti, K., 2021. Prevention of Microvascular Complications of Diabetes. *Endocrinol. Metab. Clin. North Am.* 50, 431–455. <https://doi.org/10.1016/j.ecl.2021.05.005>
- Craven, P.A., Studer, R.K., Negrete, H., DeRubertis, F.R., 1995. Protein kinase C in diabetic nephropathy. *J. Diabetes Complications* 9, 241–245. [https://doi.org/10.1016/1056-8727\(95\)80012-4](https://doi.org/10.1016/1056-8727(95)80012-4)
- Crucho, C.I.C., Barros, M.T., 2017. Polymeric nanoparticles: A study on the preparation variables and characterization methods. *Mater. Sci. Eng. C* 80, 771–784. <https://doi.org/10.1016/j.msec.2017.06.004>
- Danafar, H., Davaran, S., Rostamizadeh, K., Valizadeh, H., Hamidi, M., 2014. Biodegradable m-PEG/PCL core-shell micelles: Preparation and characterization as a sustained release formulation for curcumin. *Adv. Pharm. Bull.* 4, 501–510. <https://doi.org/10.5681/apb.2014.074>
- Daoud, S., Schinzel, R., Neumann, A., Loske, C., Fraccarollo, D., Diez, C., Simm, A., 2001. Advanced Glycation Endproducts: Activators of Cardiac Remodeling in Primary Fibroblasts from Adult Rat Hearts. *Mol. Med.* 7, 543–551. <https://doi.org/10.1007/bf03401860>
- Davinelli, S., Sapere, N., Zella, D., Bracale, R., Intrieri, M., Scapagnini, G., 2012. Pleiotropic protective effects of phytochemicals in Alzheimer’s disease. *Oxid. Med. Cell. Longev.* 2012. <https://doi.org/10.1155/2012/386527>

- Davitt, C.J.H., Lavelle, E.C., 2015. Delivery strategies to enhance oral vaccination against enteric infections. *Adv. Drug Deliv. Rev.* 91, 52–69. <https://doi.org/10.1016/j.addr.2015.03.007>
- De, A.K., Bera, T., 2021. Analytical method development, validation and stability studies by RP-HPLC method for simultaneous estimation of andrographolide and curcumin in co-encapsulated nanostructured lipid carrier drug delivery system. *Int. J. Appl. Pharm.* 13, 73–86. <https://doi.org/10.22159/ijap.2021v13i5.42181>
- Debata, J., Kumar, S., Jha, S.K., Khan, A., 2017. A New RP-HPLC method development and validation of dapagliflozin in bulk and tablet dosage form. *Int J Drug Dev Res* 9, 48–51.
- DeFronzo, R.A., Ferrannini, E., Groop, L., Henry, R.R., Herman, W.H., Holst, J.J., Hu, F.B., Kahn, C.R., Raz, I., Shulman, G.I., Simonson, D.C., Testa, M.A., Weiss, R., 2015. Type 2 diabetes mellitus. *Nat. Rev. Dis. Prim.* 1, 1–23. <https://doi.org/10.1038/nrdp.2015.19>
- Deng, W., Wang, H., Wu, B., Zhang, X., 2019. Selenium-layered nanoparticles serving for oral delivery of phytomedicines with hypoglycemic activity to synergistically potentiate the antidiabetic effect. *Acta Pharm. Sin. B* 9, 74–86. <https://doi.org/10.1016/j.apsb.2018.09.009>
- Devendra, D., Liu, E., Eisenbarth, G.S., 2004. Type 1 diabetes: Recent developments. *Br. Med. J.* 328, 750–754. <https://doi.org/10.1136/bmj.328.7442.750>
- Devi, P.R., Rambabu, K., 2022. Rapid determination of carboplatin and docetaxel using RP-HPLC with PDA detector. *Int. J. Appl. Pharm.* 14, 186–192.
- Devi, R., Agarwal, S., 2019. Some Multifunctional Lipid Excipients and Their Pharmaceutical Applications. *Int. J. Pharm. Pharm. Sci.* 11, 1–7. <https://doi.org/10.22159/ijpps.2019v11i9.34194>
- Dkhil, M.A., Zrieq, R., Al-Quraishy, S., Abdel Moneim, A.E., 2016. Selenium nanoparticles attenuate oxidative stress and testicular damage in streptozotocin-induced diabetic rats. *Molecules* 21. <https://doi.org/10.3390/molecules21111517>
- Doost, A.S., Muhammad, D.R.A., Stevens, C. V., Dewettinck, K., Van der Meeren, P., 2018. Fabrication and characterization of quercetin loaded almond gum-shellac nanoparticles prepared by antisolvent precipitation. *Food Hydrocoll.* 83, 190–201. <https://doi.org/10.1016/j.foodhyd.2018.04.050>

- Doost, A.S., Nikbakht Nasrabadi, M., Kassozi, V., Dewettinck, K., Stevens, C. V., Van der Meeren, P., 2019. Pickering stabilization of thymol through green emulsification using soluble fraction of almond gum – Whey protein isolate nano-complexes. *Food Hydrocoll.* 88, 218–227. <https://doi.org/10.1016/j.foodhyd.2018.10.009>
- Dora, C.P., Singh, S.K., Kumar, S., Datusalia, A.K., Deep, A., 2010. Development and characterization of nanoparticles of glibenclamide by solvent displacement method. *Acta Pol. Pharm. - Drug Res.* 67, 283–290.
- Dounousi, E., Duni, A., Leivaditis, K., Vaios, V., Eleftheriadis, T., Liakopoulos, V., 2015. Improvements in the management of diabetic nephropathy. *Rev. Diabet. Stud.* 12, 119–133. <https://doi.org/10.1900/RDS.2015.12.119>
- Dronavalli, S., Duka, I., Bakris, G.L., 2008. The pathogenesis of diabetic nephropathy. *Nat. Clin. Pract. Endocrinol. Metab.* 4, 444–452. <https://doi.org/10.1038/ncpendmet0894>
- Dung, D.T.K., Hai, T.H., Phuc, L.H., Long, B.D., Vinh, L.K., Truc, P.N., 2009. Preparation and characterization of magnetic nanoparticles with chitosan coating. *J. Phys. Conf. Ser.* 187. <https://doi.org/10.1088/1742-6596/187/1/012036>
- Dunlop, M., 2000. Aldose reductase and the role of the polyol pathway in diabetic nephropathy. *Kidney Int.* 58, 3–12. <https://doi.org/10.1046/j.1523-1755.2000.07702.x>
- Duong, V.A., Nguyen, T.T.L., Maeng, H.J., Chi, S.C., 2019. Nanostructured lipid carriers containing ondansetron hydrochloride by cold high-pressure homogenization method: Preparation, characterization, and pharmacokinetic evaluation. *J. Drug Deliv. Sci. Technol.* 53. <https://doi.org/10.1016/j.jddst.2019.101185>
- Duran-Salgado, M.B., 2014. Diabetic nephropathy and inflammation. *World J. Diabetes* 5, 393. <https://doi.org/10.4239/wjd.v5.i3.393>
- Eleazu, C.O., Eleazu, K.C., Chukwuma, S., Essien, U.N., 2013. Review of the mechanism of cell death resulting from streptozotocin challenge in experimental animals, its practical use and potential risk to humans. *J. Diabetes Metab. Disord.* 12, 1–7. <https://doi.org/10.1186/2251-6581-12-60>
- El-Far, M., Essam, A., El-Senduny, F.F., Abd El-Azim, A.O., Yahia, S., El-Sherbiny, I.M., 2022. Potential use of nanoformulated ascorbyl palmitate as a promising anticancer agent: First

comparative assessment between nano and free forms. *J. Drug Deliv. Sci. Technol.* 78. <https://doi.org/10.1016/j.jddst.2022.103920>

El-Far, Y.M., Zakaria, M.M., Gabr, M.M., El Gayar, A.M., El-Sherbiny, I.M., Eissa, L.A., 2016. A newly developed silymarin nanoformulation as a potential antidiabetic agent in experimental diabetes. *Nanomedicine* 11, 2581–2602. <https://doi.org/10.2217/nnm-2016-0204>

Elmowafy, M., Samy, A., Raslan, M.A., Salama, A., Said, R.A., Abdelaziz, A.E., El-Eraky, W., El Awdan, S., Viitala, T., 2016. Enhancement of Bioavailability and Pharmacodynamic Effects of Thymoquinone Via Nanostructured Lipid Carrier (NLC) Formulation. *AAPS PharmSciTech* 17, 663–672. <https://doi.org/10.1208/s12249-015-0391-0>

El-Say, K.M., El-Sawy, H.S., 2017. Polymeric nanoparticles: Promising platform for drug delivery. *Int. J. Pharm.* 528, 675–691. <https://doi.org/10.1016/j.ijpharm.2017.06.052>

Emerich, D.F., Thanos, C.G., 2003. Nanotechnology and medicine. *Expert Opin. Biol. Ther.* 3, 655–663. <https://doi.org/10.1517/14712598.3.4.655>

Es-haghi, A., Soltani, M., Tabrizi, M.H., Noghondar, M.K., Khatamian, N., Naeeni, N.B., Kharaghani, M., 2024. The effect of EGCG/tyrosol-loaded chitosan/lecithin nanoparticles on hyperglycemia and hepatic function in streptozotocin-induced diabetic mice. *Int. J. Biol. Macromol.* 267. <https://doi.org/10.1016/j.ijbiomac.2024.131496>

Fahmy, U.A., L. Alaofi, A., Awan, Z.A., Alqarni, H.M., Alhakamy, N.A., 2020. Optimization of Thymoquinone-Loaded Coconut Oil Nanostructured Lipid Carriers for the Management of Ethanol-Induced Ulcer. *AAPS PharmSciTech* 21. <https://doi.org/10.1208/s12249-020-01693-1>

Farag, Y., Leopold, C.S., 2011. Development of shellac-coated sustained release pellet formulations. *Eur. J. Pharm. Sci.* 42, 400–405. <https://doi.org/10.1016/j.ejps.2011.01.006>

Fernandes, S.M., Cordeiro, P.M., Watanabe, M., da Fonseca, C.D., Vattimo, M. de F.F., 2016. The role of oxidative stress in streptozotocin-induced diabetic nephropathy in rats. *Arch. Endocrinol. Metab.* 60, 443–449. <https://doi.org/10.1590/2359-3997000000188>

Flyvbjerg, A., 2000. Putative pathophysiological role of growth factors and cytokines in experimental diabetic kidney disease. *Diabetologia* 43, 1205–1223. <https://doi.org/10.1007/s001250051515>

- Fonseca, D.P., Khalil, N.M., Mainardes, R.M., 2017. Bovine serum albumin-based nanoparticles containing resveratrol: Characterization and antioxidant activity. *J. Drug Deliv. Sci. Technol.* 39, 147–155. <https://doi.org/10.1016/j.jddst.2017.03.017>
- Forbes, J.M., Cooper, M.E., Oldfield, M.D., Thomas, M.C., 2003. Role of advanced glycation end products in diabetic nephropathy. *J. Am. Soc. Nephrol.* 14, S254-8. <https://doi.org/10.1097/01.asn.0000077413.41276.17>
- Forbes, J.M., Fukami, K., Cooper, M.E., 2007. Diabetic nephropathy: Where hemodynamics meets metabolism. *Exp. Clin. Endocrinol. Diabetes* 115, 69–84. <https://doi.org/10.1055/s-2007-949721>
- Fornoni, A., Ijaz, A., Tejada, T., Lenz, O., 2008. Role of inflammation in diabetic nephropathy. *Curr. Diabetes Rev.* 4, 10–17. <https://doi.org/10.2174/157339908783502361>
- Fricker, G., Kromp, T., Wendel, A., Blume, A., Zirkel, J., Rebmann, H., Setzer, C., Quinkert, R.O., Martin, F., Müller-Goymann, C., 2010. Phospholipids and lipid-based formulations in oral drug delivery. *Pharm. Res.* 27, 1469–1486. <https://doi.org/10.1007/s11095-010-0130-x>
- Gagliardi, A., Paolino, D., Iannone, M., Palma, E., Fresta, M., Cosco, D., 2018. Sodium deoxycholate-decorated zein nanoparticles for a stable colloidal drug delivery system. *Int. J. Nanomedicine* 13, 601–614. <https://doi.org/10.2147/IJN.S156930>
- Ganesan, P., Narayanasamy, D., 2017. Lipid nanoparticles: Different preparation techniques, characterization, hurdles, and strategies for the production of solid lipid nanoparticles and nanostructured lipid carriers for oral drug delivery. *Sustain. Chem. Pharm.* 6, 37–56. <https://doi.org/10.1016/j.scp.2017.07.002>
- Ganugula, R., Nuthalapati, N.K., Dwivedi, S., Zou, D., Arora, M., Friend, R., Sheikh-Hamad, D., Basu, R., Kumar, M.N.V.R., 2023. Nanocurcumin combined with insulin alleviates diabetic kidney disease through P38/P53 signaling axis. *J. Control. Release* 353, 621–633. <https://doi.org/10.1016/j.jconrel.2022.12.012>
- Gao, Z., Han, Y., Hu, Y., Wu, X., Wang, Y., Zhang, X., Fu, J., Zou, X., Zhang, J., Chen, X., Jose, P.A., Lu, X., Zeng, C., 2016. Targeting HO-1 by epigallocatechin-3-gallate reduces contrast-induced renal injury via anti-oxidative stress and anti-inflammation pathways. *PLoS One* 11. <https://doi.org/10.1371/journal.pone.0149032>

- Garg, S., Garg, A., 2018. Encapsulation of Curcumin in Silver Nanoparticle for Enhancement of Anticancer Drug Delivery. *Int. J. Pharm. Sci. Res.* 9, 1160. [https://doi.org/10.13040/IJPSR.0975-8232.9\(3\).1160-66](https://doi.org/10.13040/IJPSR.0975-8232.9(3).1160-66)
- Gasco, M.R., 1993. Method for producing solid lipid microspheres having a narrow size distribution.
- Giannouli, M., Karagkiozaki, V., Pappa, F., Moutsios, I., Gravalidis, C., Logothetidis, S., 2018. Fabrication of quercetin-loaded PLGA nanoparticles via electrohydrodynamic atomization for cardiovascular disease. *Mater. Today Proc.* 5, 15998–16005. <https://doi.org/10.1016/j.matpr.2018.05.044>
- Gil, N., Goldberg, R., Neuman, T., Garsen, M., Zcharia, E., Rubinstein, A.M., Van Kuppevelt, T., Meirovitz, A., Pisano, C., Li, J.P., Van Der Vlag, J., Vlodaysky, I., Elkin, M., 2012. Heparanase is essential for the development of diabetic nephropathy in mice. *Diabetes* 61, 208–216. <https://doi.org/10.2337/db11-1024>
- Ginter, E., Simko, V., 2013. Type 2 Diabetes Mellitus, Pandemic in 21st Century, in: Ahmad, S.I. (Ed.), *Diabetes: An Old Disease, a New Insight*. Springer New York, New York, NY, pp. 42–50. [https://doi.org/10.1007/978-1-4614-5441-0\\_6](https://doi.org/10.1007/978-1-4614-5441-0_6)
- Giuliani, L.M., Pegoraro, N.S., Camponogara, C., Osmari, B.F., de Bastos Brum, T., Reolon, J.B., Rechia, G.C., Oliveira, S.M., Cruz, L., 2022. Locust bean gum-based hydrogel containing nanocapsules for 3,3'-diindolylmethane delivery in skin inflammatory conditions. *J. Drug Deliv. Sci. Technol.* 78. <https://doi.org/10.1016/j.jddst.2022.103960>
- Goh, S.Y., Cooper, M.E., 2008. The role of advanced glycation end products in progression and complications of diabetes. *J. Clin. Endocrinol. Metab.* 93, 1143–1152. <https://doi.org/10.1210/jc.2007-1817>
- Górnicka, J., Mika, M., Wróblewska, O., Siudem, P., Paradowska, K., 2023. Methods to Improve the Solubility of Curcumin from Turmeric. *Life* 13, 1–13. <https://doi.org/10.3390/life13010207>
- Goyal, S.N., Reddy, N.M., Patil, K.R., Nakhate, K.T., Ojha, S., Patil, C.R., Agrawal, Y.O., 2016. Challenges and issues with streptozotocin-induced diabetes - A clinically relevant animal model to understand the diabetes pathogenesis and evaluate therapeutics. *Chem. Biol. Interact.* 244, 49–63. <https://doi.org/10.1016/j.cbi.2015.11.032>

- Gulotta, A., Saberi, A.H., Nicoli, M.C., McClements, D.J., 2014. Nanoemulsion-based delivery systems for polyunsaturated ( $\omega$ -3) oils: formation using a spontaneous emulsification method. *J. Agric. Food Chem.* 62, 1720–1725.
- Guo, Y., Jiang, N., Zhang, L., Yin, M., 2020. Green synthesis of gold nanoparticles from *Fritillaria cirrhosa* and its anti-diabetic activity on Streptozotocin induced rats. *Arab. J. Chem.* 13, 5096–5106. <https://doi.org/10.1016/j.arabjc.2020.02.009>
- Gutiérrez, R.M.P., Gómez, J.T., Urby, R.B., Soto, J.G.C., Parra, H.R., 2022. Evaluation of Diabetes Effects of Selenium Nanoparticles Synthesized from a Mixture of Luteolin and Diosmin on Streptozotocin-Induced Type 2 Diabetes in Mice. *Molecules* 27. <https://doi.org/10.3390/molecules27175642>
- Ha, E.S., Lee, S.K., Choi, D.H., Jeong, S.H., Hwang, S.J., Kim, M.S., 2020. Application of diethylene glycol monoethyl ether in solubilization of poorly water-soluble drugs. *J. Pharm. Investig.* 50, 231–250. <https://doi.org/10.1007/s40005-019-00454-y>
- Ha, H., Hwang, I.A., Park, J.H., Lee, H.B., 2008. Role of reactive oxygen species in the pathogenesis of diabetic nephropathy. *Diabetes Res. Clin. Pract.* 82, 42–45. <https://doi.org/10.1016/j.diabres.2008.09.017>
- Ha, H., Kim, K.H., 1992. Amelioration of diabetic microalbuminuria and lipid peroxidation by captopril. *Yonsei Med. J.* 33, 217–223.
- Ha, H., Kim, K.H., 1999. Pathogenesis of diabetic nephropathy: The role of oxidative stress and protein kinase C. *Diabetes Res. Clin. Pract.* 45, 147–151. [https://doi.org/10.1016/S0168-8227\(99\)00044-3](https://doi.org/10.1016/S0168-8227(99)00044-3)
- Haider, M., Abdin, S.M., Kamal, L., Orive, G., 2020. Nanostructured lipid carriers for delivery of chemotherapeutics: A review. *Pharmaceutics* 12. <https://doi.org/10.3390/pharmaceutics12030288>
- Halim, M.E., Misra, A., 2011. The effects of the aqueous extract of *Pterocarpus santalinus* heartwood and vitamin E supplementation in streptozotocin-induced diabetic rats. *J. Med. Plant Res.* 5, 398–409.
- Hami, Z., 2021. A Brief Review on Advantages of Nano-based Drug Delivery Systems. *Ann. Mil. Heal. Sci. Res.* 19, 1–6. <https://doi.org/10.5812/amh.112274>

- Harding, J.L., Pavkov, M.E., Magliano, D.J., Shaw, J.E., Gregg, E.W., 2019. Global trends in diabetes complications: a review of current evidence. *Diabetologia* 62, 3–16. <https://doi.org/10.1007/s00125-018-4711-2>
- Hashemzadeh, N., Jouyban, A., 2022. Review of Pharmaceutical Applications of Diethylene Glycol Monoethyl Ether. *J. Pharm. Pharm. Sci.* 25, 349–353. <https://doi.org/10.18433/jpps32921>
- Hata, A., Chen, Y.-G., 2016. TGF- $\beta$  Signaling from Receptors to Smads. *Cold Spring Harb. Perspect. Biol.* 8. <https://doi.org/10.1101/cshperspect.a022061>
- He, Z., King, G.L., 2004. Microvascular complications of diabetes. *Endocrinol. Metab. Clin. North Am.* 33, 215–238. <https://doi.org/10.1016/j.ecl.2003.12.003>
- Hedayati, R., Jahanshahi, M., Attar, H., 2012. Fabrication and characterization of albumin-acacia nanoparticles based on complex coacervation as potent nanocarrier. *J. Chem. Technol. Biotechnol.* 87, 1401–1408. <https://doi.org/10.1002/jctb.3758>
- Hillyer, J.F., Albrecht, R.M., 2001. Gastrointestinal persorption and tissue distribution of differently sized colloidal gold nanoparticles. *J. Pharm. Sci.* 90, 1927–1936. <https://doi.org/10.1002/jps.1143>
- Hoher, B., Schwarz, A., Reinbacher, D., Jacobi, J., Lun, A., Priem, F., Bauer, C., Neumayer, H.-H., Raschack, M., 2001. Effects of Endothelin Receptor Antagonists on the Progression of Diabetic Nephropathy. *Nephron* 87, 161–169. <https://doi.org/10.1159/000045906>
- Houacine, C., Adams, D., Singh, K.K., 2020. Impact of liquid lipid on development and stability of trimyristin nanostructured lipid carriers for oral delivery of resveratrol. *J. Mol. Liq.* 316. <https://doi.org/10.1016/j.molliq.2020.113734>
- Hu, K., Huang, Xiaoxia, Gao, Y., Huang, Xulin, Xiao, H., McClements, D.J., 2015. Core-shell biopolymer nanoparticle delivery systems: Synthesis and characterization of curcumin fortified zein-pectin nanoparticles. *Food Chem.* 182, 275–281. <https://doi.org/10.1016/j.foodchem.2015.03.009>
- Hu, K., McClements, D.J., 2014. Fabrication of surfactant-stabilized zein nanoparticles: A pH modulated antisolvent precipitation method. *Food Res. Int.* 64, 329–335. <https://doi.org/10.1016/j.foodres.2014.07.004>

- Hu, Q., Jiang, L., Yan, Q., Zeng, J., Ma, X., Zhao, Y., 2023. A natural products solution to diabetic nephropathy therapy. *Pharmacol. Ther.* 241. <https://doi.org/10.1016/j.pharmthera.2022.108314>
- Hu, Q., Qu, C., Xiao, X., Zhang, W., Jiang, Y., Wu, Z., Song, D., Peng, X., Ma, X., Zhao, Y.L., 2021. Flavonoids on diabetic nephropathy: advances and therapeutic opportunities. *Chin. Med.* 16, 1–17. <https://doi.org/10.1186/s13020-021-00485-4>
- Huang, A., Zhou, Q., Liu, J., Fei, B., Sun, S., 2008. Distinction of three wood species by Fourier transform infrared spectroscopy and two-dimensional correlation IR spectroscopy. *J. Mol. Struct.* 883–884, 160–166. <https://doi.org/10.1016/j.molstruc.2007.11.061>
- Huang, D., Refaat, M., Mohammedi, K., Jayyousi, A., Al Suwaidi, J., Abi Khalil, C., 2017. Macrovascular Complications in Patients with Diabetes and Prediabetes. *Biomed Res. Int.* 2017. <https://doi.org/10.1155/2017/7839101>
- Huang, J., Huang, K., Lan, T., Xie, X., Shen, X., Liu, P., Huang, H., 2013. Curcumin ameliorates diabetic nephropathy by inhibiting the activation of the SphK1-S1P signaling pathway. *Mol. Cell. Endocrinol.* 365, 231–240. <https://doi.org/10.1016/j.mce.2012.10.024>
- Huang, T.W., Ho, Y.C., Tsai, T.N., Tseng, C.L., Lin, C., Mi, F.L., 2020. Enhancement of the permeability and activities of epigallocatechin gallate by quaternary ammonium chitosan/fucoidan nanoparticles. *Carbohydr. Polym.* 242. <https://doi.org/10.1016/j.carbpol.2020.116312>
- Hunsicker, L.G., 2004. Emerging Trends for Prevention and Treatment of Diabetic Nephropathy: Blockade of the RAAS and BP Control. *J. Manag. Care Pharm.* 10, 12–17.
- Hussain, A., Attique, F., Naqvi, S.A.R., Ali, A., Ibrahim, M., Hussain, H., Zafar, F., Iqbal, R.S., Ayub, M.A., Assiri, M.A., 2022. Nanoformulation of Curcuma longa root extract and evaluation of its dissolution potential. *ACS omega* 8, 1088–1096.
- Hussain, Y., Alam, W., Ullah, H., Dacrema, M., Daglia, M., Khan, H., Arciola, C.R., 2022. Antimicrobial Potential of Curcumin: Therapeutic Potential and Challenges to Clinical Applications. *Antibiotics* 11. <https://doi.org/10.3390/antibiotics11030322>
- ICH, 2005. Validation of Analytical Procedures: Text and Methodology Q2(R1), in: International Conference on Harmonisation of Technical Requirements for Registration of Pharmaceuticals for Human Use. pp. 541–545. [https://doi.org/10.1007/978-3-642-35099-3\\_86](https://doi.org/10.1007/978-3-642-35099-3_86)

- Imran, M., Titilayo, B., Adil, M., Liyan-Zhang, Mehmood, Q., Mustafa, S.H., Shen, Q., 2024. Ascorbyl palmitate: A comprehensive review on its characteristics, synthesis, encapsulation and applications. *Process Biochem.* 142, 68–80. <https://doi.org/10.1016/j.procbio.2024.04.015>
- Isbrucker, R.A., Edwards, J.A., Wolz, E., Davidovich, A., Bausch, J., 2006. Safety studies on epigallocatechin gallate (EGCG) preparations. Part 2: Dermal, acute and short-term toxicity studies. *Food Chem. Toxicol.* 44, 636–650. <https://doi.org/10.1016/j.fct.2005.11.003>
- Iso, K., Tada, H., Kuboki, K., Inokuchi, T., 2001. Long-term effect of epalrestat, an aldose reductase inhibitor, on the development of incipient diabetic nephropathy in Type 2 diabetic patients. *J. Diabetes Complications* 15, 241–244. [https://doi.org/10.1016/S1056-8727\(01\)00160-X](https://doi.org/10.1016/S1056-8727(01)00160-X)
- Jana, S., Sen, K.K., 2017. Chitosan — Locust bean gum interpenetrating polymeric network nanocomposites for delivery of aceclofenac. *Int. J. Biol. Macromol.* 102, 878–884. <https://doi.org/10.1016/j.ijbiomac.2017.04.097>
- Javadzadeh, Y., Adibkia, K., Hamed, H., 2015. Transcutol® (Diethylene Glycol Monoethyl Ether): A Potential Penetration Enhancer, in: *Percutaneous Penetration Enhancers Chemical Methods in Penetration Enhancement: Modification of the Stratum Corneum*. pp. 195–204. <https://doi.org/10.1007/978-3-662-47039-8>
- Jayaramudu, T., Varaprasad, K., Pyarasani, R.D., Reddy, K.K., Akbari-Fakhrabadi, A., Carrasco-Sánchez, V., Amalraj, J., 2021. Hydroxypropyl methylcellulose-copper nanoparticle and its nanocomposite hydrogel films for antibacterial application. *Carbohydr. Polym.* 254. <https://doi.org/10.1016/j.carbpol.2020.117302>
- Jeon, J., Kim, J.H., Lee, C.K., Oh, C.H., Song, H.J., 2014. The antimicrobial activity of (-)-epigallocatechin-3-gallate and green tea extracts against *Pseudomonas aeruginosa* and *Escherichia coli* isolated from skin wounds. *Ann. Dermatol.* 26, 564–569. <https://doi.org/10.5021/ad.2014.26.5.564>
- Jia, L.J., Zhang, D.R., Li, Z.Y., Feng, F.F., Wang, Y.C., Dai, W.T., Duan, C.X., Zhang, Q., 2010. Preparation and characterization of silybin-loaded nanostructured lipid carriers. *Drug Deliv.* 17, 11–18. <https://doi.org/10.3109/10717540903431586>
- Jia, T., Rao, J., Zou, L., Zhao, S., Yi, Z., Wu, B., Li, L., Yuan, H., Shi, L., Zhang, C., Gao, Y., Liu, S., Xu, H., Liu, H., Liang, S., Li, G., 2018. Nanoparticle-encapsulated curcumin inhibits

diabetic neuropathic pain involving the P2Y<sub>12</sub> receptor in the dorsal root ganglia. *Front. Neurosci.* 11. <https://doi.org/10.3389/fnins.2017.00755>

Jin, Z., Cui, W., Zhang, F., Wang, F., Cheng, S., Fu, Y., Huang, A., 2022. Rapid Identification for the Pterocarpus Bracelet by Three-Step Infrared Spectrum Method. *Molecules* 27. <https://doi.org/10.3390/molecules27154793>

Joshi, M., Patravale, V., 2006. Formulation and evaluation of nanostructured lipid carrier (NLC)-based gel of valdecoxib. *Drug Dev. Ind. Pharm.* 32, 911–918. <https://doi.org/10.1080/03639040600814676>

Joshi, M., Patravale, V., 2008. Nanostructured lipid carrier (NLC) based gel of celecoxib. *Int. J. Pharm.* 346, 124–132. <https://doi.org/10.1016/j.ijpharm.2007.05.060>

Joshi, R.P., Negi, G., Kumar, A., Pawar, Y.B., Munjal, B., Bansal, A.K., Sharma, S.S., 2013. SNEDDS curcumin formulation leads to enhanced protection from pain and functional deficits associated with diabetic neuropathy: An insight into its mechanism for neuroprotection. *Nanomedicine Nanotechnology, Biol. Med.* 9, 776–785. <https://doi.org/10.1016/j.nano.2013.01.001>

Joye, I.J., McClements, D.J., 2014. Biopolymer-based nanoparticles and microparticles: Fabrication, characterization, and application. *Curr. Opin. Colloid Interface Sci.* 19, 417–427. <https://doi.org/https://doi.org/10.1016/j.cocis.2014.07.002>

Kakran, M., Sahoo, N.G., Li, L., Judeh, Z., 2012a. Fabrication of quercetin nanoparticles by anti-solvent precipitation method for enhanced dissolution. *Powder Technol.* 223, 59–64. <https://doi.org/10.1016/j.powtec.2011.08.021>

Kakran, M., Sahoo, N.G., Tan, I.L., Li, L., 2012b. Preparation of nanoparticles of poorly water-soluble antioxidant curcumin by antisolvent precipitation methods. *J. Nanoparticle Res.* 14. <https://doi.org/10.1007/s11051-012-0757-0>

Kamel, A.H., Ezzat, S., Ahmed, M.A., Amr, A.E.G.E., Almehezia, A.A., Al-Omar, M.A., 2020. Modified potentiometric screen-printed electrodes based on imprinting character for sodium deoxycholate determination. *Biomolecules* 10, 1–12. <https://doi.org/10.3390/biom10020251>

Kanesaki, Y., Suzuki, D., Uehara, G., Toyoda, M., Katoh, T., Sakai, H., Watanabe, T., 2005. Vascular endothelial growth factor gene expression is correlated with glomerular

neovascularization in human diabetic nephropathy. *Am. J. Kidney Dis.* 45, 288–294. <https://doi.org/10.1053/j.ajkd.2004.09.020>

Kar, N., Chakraborty, S., De, A.K., Ghosh, S., Bera, T., 2017. Development and evaluation of a cedrol-loaded nanostructured lipid carrier system for in vitro and in vivo susceptibilities of wild and drug resistant *Leishmania donovani* amastigotes. *Eur. J. Pharm. Sci.* 104, 196–211. <https://doi.org/10.1016/j.ejps.2017.03.046>

Kardani, K., Gurav, N., Solanki, B., Patel, P., Patel, B., 2013. RP-HPLC method development and validation of gallic acid in Polyherbal tablet formulation. *J. Appl. Pharm. Sci.* 3, 37–42. <https://doi.org/10.7324/JAPS.2013.3508>

Kashihara, N., Haruna, Y., K. Kondeti, V., S. Kanwar, Y., 2010. Oxidative Stress in Diabetic Nephropathy. *Curr. Med. Chem.* 17, 4256–4269. <https://doi.org/10.2174/092986710793348581>

Katsarou, A., Gudbjörnsdóttir, S., Rawshani, A., Dabelea, D., Bonifacio, E., Anderson, B.J., Jacobsen, L.M., Schatz, D.A., Lernmark, A., 2017. Type 1 diabetes mellitus. *Nat. Rev. Dis. Prim.* 3, 1–18. <https://doi.org/10.1038/nrdp.2017.16>

Kaul, K., Tarr, J.M., Ahmad, S.I., Kohner, E.M., Chibber, R., 2013. Introduction to Diabetes Mellitus, in: Ahmad, S.I. (Ed.), *Diabetes: An Old Disease, a New Insight*. Springer New York, New York, NY, pp. 1–11. [https://doi.org/10.1007/978-1-4614-5441-0\\_1](https://doi.org/10.1007/978-1-4614-5441-0_1)

Kaur, P., Kumar, M., Parkash, J., Reasad, D.N., 2019. Oral hypoglycemic drugs: An overview. *J. Drug Deliv. Ther.* 9, 770–777.

Khan, S., Shaharyar, M., Fazil, M., Baboota, S., Ali, J., 2016. Tacrolimus-loaded nanostructured lipid carriers for oral delivery – Optimization of production and characterization. *Eur. J. Pharm. Biopharm.* 108, 277–288. <https://doi.org/10.1016/j.ejpb.2016.07.017>

Kharat, S.N., Mendhulkar, V.D., 2016. Synthesis, characterization and studies on antioxidant activity of silver nanoparticles using *Elephantopus scaber* leaf extract. *Mater. Sci. Eng. C. Mater. Biol. Appl.* 62, 719–724. <https://doi.org/10.1016/j.msec.2016.02.024>

Kifle, Z.D., Yesuf, J.S., Atnafie, S.A., 2020. Evaluation of in vitro and in vivo anti-diabetic, anti-hyperlipidemic and anti-oxidant activity of flower crude extract and solvent fractions of

- hagenia abyssinica (Rosaceae). J. Exp. Pharmacol. 12, 151–167. <https://doi.org/10.2147/JEP.S249964>
- Kim, T.H., Jiang, H.H., Youn, Y.S., Park, C.W., Tak, K.K., Lee, S., Kim, H., Jon, S., Chen, X., Lee, K.C., 2011. Preparation and characterization of water-soluble albumin-bound curcumin nanoparticles with improved antitumor activity. Int. J. Pharm. 403, 285–291. <https://doi.org/10.1016/j.ijpharm.2010.10.041>
- Kondeti, V.K., Badri, K.R., Maddirala, D.R., Thur, S.K.M., Fatima, S.S., Kasetti, R.B., Rao, C.A., 2010. Effect of *Pterocarpus santalinus* bark, on blood glucose, serum lipids, plasma insulin and hepatic carbohydrate metabolic enzymes in streptozotocin-induced diabetic rats. Food Chem. Toxicol. 48, 1281–1287. <https://doi.org/10.1016/j.fct.2010.02.023>
- Korsmeyer, R.W., Gurny, R., Doelker, E., Buri, P., Peppas, N.A., 1983. Mechanisms of solute release from porous hydrophilic polymers. Int. J. Pharm. 15, 25–35. [https://doi.org/10.1016/0378-5173\(83\)90064-9](https://doi.org/10.1016/0378-5173(83)90064-9)
- Krongrawa, W., Sangnim, T., Piriayaprasarth, S., Patomchaivivat, V., Sriamornsak, P., Limmatvapirat, C., Limmatvapirat, S., 2024. Optimizing shellac nanoparticle fabrication: Influence of formulation and process parameters. Mater. Lett. 366, 136511. <https://doi.org/10.1016/j.matlet.2024.136511>
- Kumar, R., Kumar, M., Luthra, G., 2023. Fundamental approaches and applications of nanotechnology: A mini review. Mater. Today Proc. <https://doi.org/10.1016/j.matpr.2022.12.172>
- Kumari, M., Sharma, N., Manchanda, R., Gupta, N., Syed, A., Bahkali, A.H., Nimesh, S., 2021. PGMD/curcumin nanoparticles for the treatment of breast cancer. Sci. Rep. 11, 1–17. <https://doi.org/10.1038/s41598-021-81701-x>
- Kwon, H.J., Hong, Y.K., Kim, K.H., Han, C.H., Cho, S.H., Choi, J.S., Kim, B.W., 2006. Methanolic extract of *Pterocarpus santalinus* induces apoptosis in HeLa cells. J. Ethnopharmacol. 105, 229–234. <https://doi.org/10.1016/j.jep.2005.10.025>
- Lan, H.Y., 2012. Transforming growth factor- $\beta$ /Smad signalling in diabetic nephropathy. Clin. Exp. Pharmacol. Physiol. 39, 731–738. <https://doi.org/10.1111/j.1440-1681.2011.05663.x>

- Langham, R.G., Kelly, D.J., Maguire, J., Dowling, J.P., Gilbert, R.E., Thomson, N.M., 2003. Over-expression of platelet-derived growth factor in human diabetic nephropathy. *Nephrol. Dial. Transplant.* 18, 1392–1396. <https://doi.org/10.1093/ndt/gfg177>
- Lasoń, E., Sikora, E., Ogonowski, J., 2013. Influence of process parameters on properties of nanostructured lipid carriers (NLC) formulation. *Acta Biochim. Pol.* 60, 773–777. [https://doi.org/10.18388/abp.2013\\_2056](https://doi.org/10.18388/abp.2013_2056)
- Li, J., Chang, C., Zhai, J., Yang, Y., Yu, H., 2021. Ascorbyl palmitate effects on the stability of curcumin-loaded soybean phosphatidylcholine liposomes. *Food Biosci.* 41. <https://doi.org/10.1016/j.fbio.2021.100923>
- Li, K., Teng, C., Min, Q., 2020. Advanced Nanovehicles-Enabled Delivery Systems of Epigallocatechin Gallate for Cancer Therapy. *Front. Chem.* 8, 1–9. <https://doi.org/10.3389/fchem.2020.573297>
- Li, M., Deng, L., Xu, G., 2021. METTL14 promotes glomerular endothelial cell injury and diabetic nephropathy via m6A modification of  $\alpha$ -klotho. *Mol. Med.* 27. <https://doi.org/10.1186/s10020-021-00365-5>
- Li, Q., Cai, T., Huang, Y., Xia, X., Cole, S.P.C., Cai, Y., 2017. A review of the structure, preparation, and application of NLCs, PNPs, and PLNs. *Nanomaterials* 7, 1–25. <https://doi.org/10.3390/nano7060122>
- Li, Wenqing, Li, Wei, Wan, Y., Wang, L., Zhou, T., 2022. Preparation, characterization and releasing property of antibacterial nano-capsules composed of  $\epsilon$ -PL-EGCG and sodium alginate-chitosan. *Int. J. Biol. Macromol.* 204, 652–660. <https://doi.org/10.1016/j.ijbiomac.2022.01.123>
- Lim, A.K.H., Tesch, G.H., 2012. Inflammation in diabetic nephropathy. *Mediators Inflamm.* 2012. <https://doi.org/10.1155/2012/146154>
- Limmatvapirat, S., Nunthanid, J., Luangtana-Anan, M., Puttipipatkachorn, S., 2005. Effect of alkali treatment on properties of native shellac and stability of hydrolyzed shellac. *Pharm. Dev. Technol.* 10, 41–46. <https://doi.org/10.1081/PDT-200035897>
- Lin, X., Li, X., Zheng, L.Q., Yu, L., Zhang, Q., Liu, W., 2007. Preparation and characterization of monocaprato nanostructured lipid carriers. *Colloids Surfaces A Physicochem. Eng. Asp.* 311, 106–111. <https://doi.org/10.1016/j.colsurfa.2007.06.003>

- Liu, C., Wu, K., Gao, H., Li, J., Xu, X., 2022. Current Strategies and Potential Prospects for Nanoparticle-Mediated Treatment of Diabetic Nephropathy. *Diabetes, Metab. Syndr. Obes. Targets Ther.* 15, 2653–2673. <https://doi.org/10.2147/DMSO.S380550>
- Liu, H., Feng, J., Tang, L., 2022. Early renal structural changes and potential biomarkers in diabetic nephropathy. *Front. Physiol.* 13, 1–8. <https://doi.org/10.3389/fphys.2022.1020443>
- Liu, X.H., Luo, X.H., Lu, S.X., Zhang, J.C., Cao, W.L., 2007. A novel cetyltrimethyl ammonium silver bromide complex and silver bromide nanoparticles obtained by the surfactant counterion. *J. Colloid Interface Sci.* 307, 94–100. <https://doi.org/10.1016/j.jcis.2006.11.051>
- Liu, Y., Yang, G., Baby, T., Tengjisi, Chen, D., Weitz, D.A., Zhao, C., 2020. Stable Polymer Nanoparticles with Exceptionally High Drug Loading by Sequential Nanoprecipitation. *Angew. Chemie* 132, 4750–4758. <https://doi.org/10.1002/ange.201913539>
- Logeswari, P., Silambarasan, S., Abraham, J., 2015. Synthesis of silver nanoparticles using plants extract and analysis of their antimicrobial property. *J. Saudi Chem. Soc.* 19, 311–317. <https://doi.org/10.1016/j.jscs.2012.04.007>
- Lorenzati, B., Zucco, C., Miglietta, S., Lamberti, F., Bruno, G., 2010. Oral hypoglycemic drugs: Pathophysiological basis of their mechanism of action. *Pharmaceuticals* 3, 3005–3020. <https://doi.org/10.3390/ph3093005>
- Lozano-Maneiro, L., Puente-García, A., 2015. Renin-angiotensin-aldosterone system blockade in diabetic nephropathy. Present evidences. *J. Clin. Med.* 4, 1908–1937. <https://doi.org/10.3390/jcm4111908>
- Lu, X.Y., Wu, D.C., Li, Z.J., Chen, G.Q., 2011. Polymer nanoparticles, in: *Progress in Molecular Biology and Translational Science*. Elsevier Inc., pp. 299–323. <https://doi.org/10.1016/B978-0-12-416020-0.00007-3>
- Lüdtke, F.L., Stahl, M.A., Grimaldi, R., Bruno Soares Forte, M., Lúcia Gigante, M., Paula Badan Ribeiro, A., 2022. Optimization of high pressure homogenization conditions to produce nanostructured lipid carriers using natural and synthetic emulsifiers. *Food Res. Int.* 160. <https://doi.org/10.1016/j.foodres.2022.111746>
- Luo, C., Okubo, T., Nangrejo, M., Edirisinghe, M., 2015. Preparation of polymeric nanoparticles by novel electrospray nanoprecipitation. *Polym. Int.* 64, 183–187. <https://doi.org/10.1002/pi.4822>

- Luo, C.F., Yuan, M., Chen, M.S., Liu, S.M., Zhu, L., Huang, B.Y., Liu, X.W., Xiong, W., 2011. Pharmacokinetics, tissue distribution and relative bioavailability of puerarin solid lipid nanoparticles following oral administration. *Int. J. Pharm.* 410, 138–144. <https://doi.org/10.1016/j.ijpharm.2011.02.064>
- Luo, Q., Li, Kai, Xu, J., Li, Kun, Zheng, H., Liu, L., Zhang, H., Sun, Y., 2016. A Novel Biobased Sodium Shellac for Wrapping Disperse Multiscale Emulsion Particles. *J. Agric. Food Chem.* 64, 9374–9380. <https://doi.org/10.1021/acs.jafc.6b04417>
- Ma, J.Y., Hasham, R., Rasid, Z.I.A., Noor, N.M., 2021. Formulation and characterization of nanostructured lipid carrier encapsulate lemongrass oil using ultrasonication technique. *Chem. Eng. Trans.* 83, 475–480. <https://doi.org/10.3303/CET2183080>
- Madriwala, B., Jays, J., 2022. Analytical method development and validation for estimation of residual solvents in gliclazide using gas chromatography. *Int. J. Curr. Pharm. Res.* 14, 68–73.
- Mahler, R.J., Adler, M.L., 1999. Clinical review 102: Type 2 diabetes mellitus: Update on diagnosis, pathophysiology, and treatment. *J. Clin. Endocrinol. Metab.* 84, 1165–1171. <https://doi.org/10.1210/jcem.84.4.5612>
- Mahmood, A., Rapalli, V.K., Gorantla, S., Waghule, T., Singhvi, G., 2022. Dermatokinetic assessment of luliconazole-loaded nanostructured lipid carriers (NLCs) for topical delivery: QbD-driven design, optimization, and in vitro and ex vivo evaluations. *Drug Deliv. Transl. Res.* 12, 1118–1135. <https://doi.org/10.1007/s13346-021-00986-7>
- Maji, A.K., Mahapatra, S., Banerjee, D., 2014a. In-vivo immunomodulatory potential of standardized *Pueraria tuberosa* extract and its isoflavonoids. *Int. J. Pharm. Pharm. Sci.* 6, 861–867.
- Maji, A.K., Pandit, S., Banerji, P., Banerjee, D., 2014b. *Pueraria tuberosa*: A review on its phytochemical and therapeutic potential. *Nat. Prod. Res.* 28, 2111–2127. <https://doi.org/10.1080/14786419.2014.928291>
- Maji, R., Dey, N.S., Satapathy, B.S., Mukherjee, B., Mondal, S., 2015. Preparation and characterization of tamoxifen citrate loaded nanoparticles for breast cancer therapy. *Int. J. Nanomedicine* 9, 3107–3118. <https://doi.org/10.2147/IJN.S63535>
- Malviya, A., Gupta, R., Porte, S.M., 2016. Critical Review On Vidarikand (*Pueraria tuberosa* Dc.)-An Ayurvedic Herb. *Int. J. Ayurveda Pharma Res.* 4, 46–52.

- Mane, P.B., Antre, R. V, Oswal, R.J., 2012. Antidiabetic Drugs: An Overview. *Int. J. Pharm. Chem. Sci.* 1, 301–306.
- Manikandan, D.B., Sridhar, A., Krishnasamy Sekar, R., Perumalsamy, B., Veeran, S., Arumugam, M., Karuppaiah, P., Ramasamy, T., 2021. Green fabrication, characterization of silver nanoparticles using aqueous leaf extract of *Ocimum americanum* (Hoary Basil) and investigation of its in vitro antibacterial, antioxidant, anticancer and photocatalytic reduction. *J. Environ. Chem. Eng.* 9, 104845. <https://doi.org/10.1016/j.jece.2020.104845>
- Manjunatha, B.K., 2006. Hepatoprotective activity of *Pterocarpus santalinus* L.f., an endangered medicinal plant. *Indian J. Pharmacol.* 38, 25–28.
- Manjunatha, S. B., Biradar, D.P., Aladakatti, Y.R., 2016. Nanotechnology and its applications in agriculture: A review. *J. Farm Sci.* 29, 1–13.
- Mansoori, G.A., Soelaiman, T.A.F., 2005. Nanotechnology - An introduction for the standards community. *J. ASTM Int.* 2, 17–38. <https://doi.org/10.1520/JAI13110>
- Mansour, I., Thajudeen, B., 2017. Overview of Diabetic Nephropathy, in: *Managing Diabetic Nephropathies in Clinical Practice*. Springer International Publishing, Cham, pp. 1–21. [https://doi.org/10.1007/978-3-319-08873-0\\_1](https://doi.org/10.1007/978-3-319-08873-0_1)
- Maraschin, J. de F., 2013. Classification of Diabetes, in: Ahmad, S.I. (Ed.), *Diabetes: An Old Disease, a New Insight*. Springer New York, New York, NY, pp. 12–19. [https://doi.org/10.1007/978-1-4614-5441-0\\_2](https://doi.org/10.1007/978-1-4614-5441-0_2)
- Marquele-Oliveira, F., Torres, E.C., Barud, H. da S., Zoccal, K.F., Faccioli, L.H., Hori, J.I., Berretta, A.A., 2016. Physicochemical characterization by AFM, FT-IR and DSC and biological assays of a promising antileishmania delivery system loaded with a natural Brazilian product. *J. Pharm. Biomed. Anal.* 123, 195–204. <https://doi.org/10.1016/j.jpba.2016.01.045>
- Mašková, E., Kubová, K., Raimi-Abraham, B.T., Vllasaliu, D., Vohlídalová, E., Turánek, J., Mašek, J., 2020. Hypromellose – A traditional pharmaceutical excipient with modern applications in oral and oromucosal drug delivery. *J. Control. Release* 324, 695–727. <https://doi.org/10.1016/j.jconrel.2020.05.045>
- Matar, G.H., Andac, M., 2021. Antibacterial efficiency of silver nanoparticles-loaded locust bean gum/polyvinyl alcohol hydrogels. *Polym. Bull.* 78, 6095–6113. <https://doi.org/10.1007/s00289-020-03418-7>

- 
- Mauer, S.M., Steffes, M.W., Ellis, E.N., Sutherland, D.E., Brown, D.M., Goetz, F.C., 1984. Structural-functional relationships in diabetic nephropathy. *J. Clin. Invest.* 74, 1143–1155. <https://doi.org/10.1172/JCI111523>
- Mehmood, S., Maqsood, M., Mahtab, N., Khan, M.I., Sahar, A., Zaib, S., Gul, S., 2022. Epigallocatechin gallate: Phytochemistry, bioavailability, utilization challenges, and strategies. *J. Food Biochem.* 46, 1–27. <https://doi.org/10.1111/jfbc.14189>
- Mehta, D.R., Mehta, R.S., Bhatt, K.K., Shankar, M.B., 2005. RP-HPLC method for estimation of rabeprazole sodium in bulk and in tablet dosage form. *Indian Drugs* 42, 13–16.
- Mishra, S., Sarker, K., Ghosh, A., Saha, A., Sen, S., 2022. a Validated Stability Indicating Rp-Hplc Method for Estimation of Avapritinib in Bulk and Tablet Dosage Form. *Int. J. Appl. Pharm.* 14, 95–101. <https://doi.org/10.22159/ijap.2022v14i2.43432>
- Mogensen, C.E., Østerby, R., 1987. Structural and Functional Alterations in the Diabetic Kidney. *Vasc. Neurol. Complicat. Diabetes Mellit.* 2nd Int. Diabetes Conf. *Vasc. Neurol. Complicat. Diabetes Mellitus*, Florence, Novemb. 1985. <https://doi.org/10.1159/000413869>
- Mohan, T., Velusamy, P., Chakrapani, L.N., Srinivasan, A.K., Singh, A., Johnson, T., Periandavan, K., 2017. Impact of EGCG Supplementation on the Progression of Diabetic Nephropathy in Rats: An Insight into Fibrosis and Apoptosis. *J. Agric. Food Chem.* 65, 8028–8036. <https://doi.org/10.1021/acs.jafc.7b03301>
- Moheman, A., Husain, A., Siddiqi, K.S., 2011. Biosurfactant in planar chromatography of transition metal ions: Mixed micelles activated separations. *Tenside, Surfactants, Deterg.* 48, 275–280. <https://doi.org/10.3139/113.110130>
- Morigi, V., Tocchio, A., Bellavite Pellegrini, C., Sakamoto, J.H., Arnone, M., Tasciotti, E., 2012. Nanotechnology in Medicine: From Inception to Market Domination. *J. Drug Deliv.* 2012, 1–7. <https://doi.org/10.1155/2012/389485>
- Muhammad, D.R.A., Sedaghat Doost, A., Gupta, V., bin Sintang, M.D., Van de Walle, D., Van der Meeren, P., Dewettinck, K., 2020. Stability and functionality of xanthan gum–shellac nanoparticles for the encapsulation of cinnamon bark extract. *Food Hydrocoll.* 100. <https://doi.org/10.1016/j.foodhyd.2019.105377>

Nagavarma, B.V.N., Yadav, H.K.S., Ayaz, A., Vasudha, L.S., Shivakumar, H.G., 2012. Different techniques for preparation of polymeric nanoparticles- A review. *Asian J. Pharm. Clin. Res.* 5, 16–23.

Nagwani, S., Tripathi, Y.B., 2010. Amelioration of cisplatin induced nephrotoxicity by PTY: A herbal preparation. *Food Chem. Toxicol.* 48, 2253–2258. <https://doi.org/10.1016/j.fct.2010.05.057>

Nair, R.S., Morris, A., Billa, N., Leong, C.O., 2019. An Evaluation of Curcumin-Encapsulated Chitosan Nanoparticles for Transdermal Delivery. *AAPS PharmSciTech* 20, 1–13. <https://doi.org/10.1208/s12249-018-1279-6>

Narayan, S., Devi, R.S., Srinivasan, P., Devi, C.S.S., 2005. *Pterocarpus santalinus*: A traditional herbal drug as a protectant against ibuprofen induced gastric ulcers. *Phyther. Res.* 19, 958–962. <https://doi.org/10.1002/ptr.1764>

Naseri, N., Valizadeh, H., Zakeri-Milani, P., 2015. Solid lipid nanoparticles and nanostructured lipid carriers: Structure preparation and application. *Adv. Pharm. Bull.* 5, 305–313. <https://doi.org/10.15171/apb.2015.043>

Natesan, V., Kim, S.J., 2021. Diabetic nephropathy – A review of risk factors, progression, mechanism, and dietary management. *Biomol. Ther.* 29, 365–372. <https://doi.org/10.4062/biomolther.2020.204>

Nazar, C.M.J., 2014. Diabetic nephropathy; principles of diagnosis and treatment of diabetic kidney disease. *J. Nephroarmacology* 3, 15–20. <https://doi.org/10.1097/MAJ.0000000000000185>

Negi, J.S., Chattopadhyay, P., Sharma, A.K., Ram, V., 2013. Development of solid lipid nanoparticles (SLNs) of lopinavir using hot self nano-emulsification (SNE) technique. *Eur. J. Pharm. Sci.* 48, 231–239.

Nivedha, V.M., Priyadarshini, R., Rajeshkumar, S., Sinduja, P., 2021. Anti-diabetic and Antioxidant Activity of *Pterocarpus santalinus* and Stevia Herbal Formulation. *J. Pharm. Res. Int.* 33, 124–134. <https://doi.org/10.9734/jpri/2021/v33i62b35178>

Noh, H., King, G.L., 2007. The role of protein kinase C activation in diabetic nephropathy. *Kidney Int.* 72, S49–S53. <https://doi.org/10.1038/sj.ki.5002386>

- Olokoba, A.B., Obateru, O.A., Olokoba, L.B., 2012. Type 2 diabetes mellitus: A review of current trends. *Oman Med. J.* 27, 269–273. <https://doi.org/10.5001/omj.2012.68>
- Osicka, T.M., Yu, Y., Panagiotopoulos, S., Clavant, S.P., Kiriazis, Z., Pike, R.N., Pratt, L.M., Russo, L.M., Kemp, B.E., Comper, W.D., Jerums, G., 2000. Prevention of albuminuria by aminoguanidine or ramipril in streptozotocin-induced diabetic rats is associated with the normalization of glomerular protein kinase C. *Diabetes* 49, 87–93. <https://doi.org/10.2337/diabetes.49.1.87>
- Pal, V. kumar, Pal, Y., 2020. Analytical Method Development and Method Validation for Determination Assay and Content Uniformity of Levonorgestrel By Reversed-Phase Highperformance Liquid Chromatography. *Asian J. Pharm. Clin. Res.* 13, 101–107. <https://doi.org/10.22159/ajpcr.2020.v13i4.36771>
- Palk, L.E., 2018. Assessing and managing the acute complications of diabetes mellitus. *Nurs. Stand.* 34, 59–66. <https://doi.org/10.7748/ns.2018.e11250>
- Pandarekandy, S.T., Sreejesh, P.G., Thampi, B.S.H., Sreekumaran, E., 2017. Hypoglycaemic Effect of Glibenclamide: A Critical Study on the Basis of Creatinine and Lipid Peroxidation Status of Streptozotocin-induced Diabetic Rat. *Indian J. Pharm. Sci.* 79, 768–777. <https://doi.org/10.4172/pharmaceutical-sciences.1000290>
- Pandey, H., Srivastava, S., Kumar, A., Kumar, R., Bhusan Tripathi, Y., 2019a. Pharmacokinetics Study of Puerarin Absorption In Blood After Consumption Of *Pueraria Tuberosa* Water Extract (PTWE) By Rats. *Explor. Anim. Med. Res.* 9, 188–196.
- Pandey, H., Srivastava, S., Kumar, R., Tripathi, Y.B., 2018. Preclinical acute and repeated dose toxicity of *Pueraria tuberosa* (PTWE) on Charles foster rats. *Int. J. Pharm. Sci. Res.* 9, 4572–4581. [https://doi.org/10.13040/IJPSR.0975-8232.9\(11\).4572-81](https://doi.org/10.13040/IJPSR.0975-8232.9(11).4572-81)
- Pandey, H., Srivastava, S., Tripathi, Y.B., 2019b. Herbal tablet of *Pueraria tuberosa* water extract suppresses the alloxan induced liver damage and hyperglycemia in rats. *BioRxiv* 671594.
- Pandey, N., Tripathi, Y.B., 2010. Antioxidant activity of tuberosin isolated from *Pueraria tuberosa* Linn. *J. Inflamm.* 7, 1–8. <https://doi.org/10.1186/1476-9255-7-47>
- Papatheodorou, K., Banach, M., Bekiari, E., Rizzo, M., Edmonds, M., 2018. Complications of Diabetes 2017. *J. Diabetes Res.* 2018, 10–13. <https://doi.org/10.1155/2018/3086167>

- Parchwani, D., Upadhyah, A., 2012. Diabetic nephropathy: Progression and pathophysiology. *Int. J. Med. Sci. Public Heal.* 1, 59–70. <https://doi.org/10.5455/ijmsph.2012.1.59-70>
- Parhi, R., Suresh, P., 2012. Preparation and Characterization of Solid Lipid Nanoparticles-A Review. *Curr. Drug Discov. Technol.* 9, 2–16. <https://doi.org/10.2174/157016312799304552>
- Parsamanesh, N., Moossavi, M., Bahrami, A., Butler, A.E., Sahebkar, A., 2018. Therapeutic potential of curcumin in diabetic complications. *Pharmacol. Res.* 136, 181–193. <https://doi.org/10.1016/j.phrs.2018.09.012>
- Parveen, A., Jin, M., Kim, S.Y., 2018. Bioactive phytochemicals that regulate the cellular processes involved in diabetic nephropathy. *Phytomedicine* 39, 146–159. <https://doi.org/10.1016/j.phymed.2017.12.018>
- Patel, A., Heussen, P., Hazekamp, J., Velikov, K.P., 2011. Stabilisation and controlled release of silibinin from pH responsive shellac colloidal particles. *Soft Matter* 7, 8549–8555. <https://doi.org/10.1039/c1sm05853c>
- Patel, D., Dasgupta, S., Dey, S., Roja Ramani, Y., Ray, S., Mazumder, B., 2012. Nanostructured lipid carriers (NLC)-based gel for the topical delivery of aceclofenac: Preparation, characterization, and in vivo evaluation. *Sci. Pharm.* 80, 749–764. <https://doi.org/10.3797/scipharm.1202-12>
- Patlolla, R.R., Chougule, M., Patel, A.R., Jackson, T., Tata, P.N.V., Singh, M., 2010. Formulation, characterization and pulmonary deposition of nebulized celecoxib encapsulated nanostructured lipid carriers. *J. Control. Release* 144, 233–241. <https://doi.org/10.1016/j.jconrel.2010.02.006>
- Patra, J.K., Das, G., Fraceto, L.F., Campos, E.V.R., Rodriguez-Torres, M.D.P., Acosta-Torres, L.S., Diaz-Torres, L.A., Grillo, R., Swamy, M.K., Sharma, S., Habtemariam, S., Shin, H.S., 2018. Nano based drug delivery systems: Recent developments and future prospects. *J. Nanobiotechnology* 16, 1–33. <https://doi.org/10.1186/s12951-018-0392-8>
- Pedro, A.C., Maciel, G.M., Rampazzo Ribeiro, V., Haminiuk, C.W.I., 2020. Fundamental and applied aspects of catechins from different sources: a review. *Int. J. Food Sci. Technol.* 55, 429–442. <https://doi.org/10.1111/ijfs.14371>
- Pimentel-Moral, S., Teixeira, M.C., Fernandes, A.R., Borrás-Linares, I., Arráez-Román, D., Martínez-Férez, A., Segura-Carretero, A., Souto, E.B., 2019. Polyphenols-enriched Hibiscus

- sabdariffa extract-loaded nanostructured lipid carriers (NLC): Optimization by multi-response surface methodology. *J. Drug Deliv. Sci. Technol.* 49, 660–667. <https://doi.org/10.1016/j.jddst.2018.12.023>
- Pontes-Quero, G.M., Benito-Garzón, L., Pérez Cano, J., Aguilar, M.R., Vázquez-Lasa, B., 2021. Amphiphilic polymeric nanoparticles encapsulating curcumin: Antioxidant, anti-inflammatory and biocompatibility studies. *Mater. Sci. Eng. C* 121. <https://doi.org/10.1016/j.msec.2020.111793>
- Poulaki, V., Joussem, A.M., Mitsiades, N., Mitsiades, C.S., Iliaki, E.F., Adamis, A.P., 2004. Insulin-like growth factor-I plays a pathogenetic role in diabetic retinopathy. *Am. J. Pathol.* 165, 457–469. [https://doi.org/10.1016/S0002-9440\(10\)63311-1](https://doi.org/10.1016/S0002-9440(10)63311-1)
- Pourghasem, M., Shafi, H., Babazadeh, Z., 2015. Histological changes of kidney in diabetic nephropath. *Casp. J. Intern. Med.* 6, 120–127.
- Priyadarsini, K.I., 2014. The chemistry of curcumin: From extraction to therapeutic agent. *Molecules* 19, 20091–20112. <https://doi.org/10.3390/molecules191220091>
- Purves, T., Middlemas, A., Agthong, S., Jude, E.B., Boulton, A.J., Fernyhough, P., Tomlinson, D.R., 2001. A role for mitogen-activated protein kinases in the etiology of diabetic neuropathy. *FASEB J.* 15, 2508–2514. <https://doi.org/10.1096/fj.01-0253hyp>
- Qi, L.-W., Liu, E.-H., Chu, C., Peng, Y.-B., Cai, H.-X., Li, P., 2010. Anti-Diabetic Agents from Natural Products — An Update from 2004 to 2009. *Curr. Top. Med. Chem.* 10, 434–457. <https://doi.org/10.2174/156802610790980620>
- R.S, P., Bomb, K., Srivastava, R., Bandyopadhyaya, R., 2020. Dual drug delivery of curcumin and niclosamide using PLGA nanoparticles for improved therapeutic effect on breast cancer cells. *J. Polym. Res.* 27. <https://doi.org/10.1007/s10965-020-02092-7>
- Rabbani, S.I., Devi, K., Khanam, S., 2010. Protective role of glibenclamide against nicotinamide-streptozotocin induced nuclear damage in diabetic Wistar rats. *J. Pharmacol. Pharmacother.* 1, 18–23. <https://doi.org/10.4103/0976-500X.64531>
- Raghavendra, Mallikarjun, Vidya, M., 2013. Functions of kidney & artificial kidneys. *Int. J. Innov. Res. Electr. Electron. Instrum. Control Eng.* 1, 1–5.

- Raghuveer, P., Prameela Rani, A., 2020. Self Nano-emulsifying Drug Delivery System to Enhance Solubility and Dissolution of Candesartan Cilexetil. *Int. J. Pharm. Investig.* 10, 506–511. <https://doi.org/10.5530/ijpi.2020.4.88>
- Rajakumar, G., Rahuman, A.A., Priyamvada, B., Khanna, V.G., Kumar, D.K., Sujin, P.J., 2012. Eclipta prostrata leaf aqueous extract mediated synthesis of titanium dioxide nanoparticles. *Mater. Lett.* 68, 115–117. <https://doi.org/10.1016/j.matlet.2011.10.038>
- Rao, B.K., Giri, R., Kesavulu, M.M., Apparao, C., 2001. Effect of oral administration of bark extracts of *Pterocarpus santalinus* L. on blood glucose level in experimental animals. *J. Ethnopharmacol.* 74, 69–74. [https://doi.org/10.1016/S0378-8741\(00\)00344-5](https://doi.org/10.1016/S0378-8741(00)00344-5)
- Rao, N.M., Kumar, K.R., Bagyalakshmi, J., Ravi, T.K., Mogili, R., 2010. RP-HPLC method development and validation for estimation of Voglibose in bulk and tablet dosage forms. *Int. J. Res. Pharm. Sci* 1, 190–194.
- Rao, P.V., 2019. Nanobiotechnology Advances in Medicine, Agriculture and Other Important Areas: Applications and Future Perspectives. *Biotechnology* 18, 89–97. <https://doi.org/10.3923/biotech.2019.89.97>
- Raptis, A.E., Viberti, G., 2001. Pathogenesis of diabetic nephropathy. *Exp. Clin. Endocrinol. Diabetes* 109, S424±S437. <https://doi.org/10.1007/978-3-319-08873-0>
- Rayudu, S., Manoranjani, M., Reddy, R.S., 2022b. Analytical method development and validation of dexmethylphenidate and serdexmethylphenidate by using RP-HPLC in bulk and pharmaceutical dosage form. *Int. J. Appl. Pharm.* 14, 110–115.
- Reddy, C.S., Rao, B.T., 2021. Development and validation of a stability-indicating related substances of trandolapril by RP-HPLC and its degradation. *Int. J. Appl. Pharm.* 13, 115–121. <https://doi.org/10.22159/ijap.2021v13i5.42113>
- Rohini, K., Kalyani, C., Shankar, G., Sougata, G., Piyush, A., Parag, K., Balu, A.C., Kale, S.N., 2015. ZnO nanoparticles-red sandalwood conjugate: A promising anti-diabetic agent. *J. Nanosci. Nanotechnol.* 15, 4046–4051. <https://doi.org/10.1166/jnn.2015.10323>
- Rolim, W.R., Pelegriño, M.T., de Araújo Lima, B., Ferraz, L.S., Costa, F.N., Bernardes, J.S., Rodrigues, T., Brocchi, M., Seabra, A.B., 2019. Green tea extract mediated biogenic synthesis of silver nanoparticles: Characterization, cytotoxicity evaluation and antibacterial activity. *Appl. Surf. Sci.* 463, 66–74. <https://doi.org/10.1016/j.apsusc.2018.08.203>

- 
- Rosli, N.A., Hasham, R., Aziz, A.A., Aziz, R., 2015. Formulation and characterization of nanostructured lipid carrier encapsulated Zingiber zerumbet oil using ultrasonication technique. *J. Adv. Res. Appl. Mech.* ISSN 11, 16–23.
- Rossini, A.A., Like, A.A., Chick, W.L., Appel, M.C., Cahill, G.F., 1977. Studies of streptozotocin induced insulinitis and diabetes. *Proc. Natl. Acad. Sci. U. S. A.* 74, 2485–2489. <https://doi.org/10.1073/pnas.74.6.2485>
- Rudra, A., Deepa, R.M., Ghosh, M.K., Ghosh, S., Mukherjee, B., 2010. Doxorubicin-loaded phosphatidylethanolamine-conjugated nanoliposomes: In vitro characterization and their accumulation in liver, kidneys, and lungs in rats. *Int. J. Nanomedicine* 5, 811–823. <https://doi.org/10.2147/IJN.S13031>
- Ruggenti, P., Cravedi, P., Remuzzi, G., 2010. The RAAS in the pathogenesis and treatment of diabetic nephropathy. *Nat. Rev. Nephrol.* 6, 319–330. <https://doi.org/10.1038/nrneph.2010.58>
- Sadiah, S., Anwar, E., Djufri, M., Cahyaningsih, U., 2017. Preparation and characteristics of nanostructured lipid carrier (NLC) loaded red ginger extract using high pressure homogenizer method. *J. Pharm. Sci. Res.* 9, 1889–1893.
- Sagoo, M.K., Gnudi, L., 2018. Diabetic nephropathy: Is there a role for oxidative stress? *Free Radic. Biol. Med.* 116, 50–63. <https://doi.org/10.1016/j.freeradbiomed.2017.12.040>
- Sai, P.N., Venkateswarlu, B.S., Kumudhavalli, M. V, Muruganatham, V., 2021. Bio-analytical method development and validation for the simultaneous estimation of Decitabine and Cedazuridine in human plasma using LC-MS/MS. *Int J Appl Pharm* 13, 257–262.
- Salvi, V.R., Pawar, P., 2019. Nanostructured lipid carriers (NLC) system: A novel drug targeting carrier. *J. Drug Deliv. Sci. Technol.* 51, 255–267. <https://doi.org/10.1016/j.jddst.2019.02.017>
- Santhosh, S.B., Ragavendran, C., Natarajan, D., 2015. Spectral and HRTEM analyses of Annona muricata leaf extract mediated silver nanoparticles and its Larvicidal efficacy against three mosquito vectors Anopheles stephensi, Culex quinquefasciatus, and Aedes aegypti. *J. Photochem. Photobiol. B Biol.* 153, 184–190. <https://doi.org/10.1016/j.jphotobiol.2015.09.018>

- Santhoshkumar, J., Kumar, S.V., Rajeshkumar, S., 2017. Synthesis of zinc oxide nanoparticles using plant leaf extract against urinary tract infection pathogen. *Resour. Technol.* 3, 459–465. <https://doi.org/10.18799/24056529/2017/4/172>
- Santos, V. da S., Ribeiro, A.P.B., Santana, M.H.A., 2019. Solid lipid nanoparticles as carriers for lipophilic compounds for applications in foods. *Food Res. Int.* 122, 610–626. <https://doi.org/10.1016/j.foodres.2019.01.032>
- Sarkodie, J., Edoh, D., Sakyiamah, M., Appiah, A., Antwi, S., Nyarko, A., Owusu, P., Debrah, P., Jackson, N., Amoateng, P., 2013. Comparative study of the hypoglycaemic property of aqueous extract of *Mangifera indica* leaves in streptozotocin-induced diabetic rats and genetic diabetic mice. *South pacific J. Pharma Bio Sci.* 1, 37–42.
- Sarkodie, J., Edoh, D., Sakyiamah, M., Appiah, A., Antwi, S., Nyarko, A., Owusu, P., Debrah, P., Jackson, N., Amoateng, P., 2013. Comparative study of the hypoglycaemic property of aqueous extract of *Mangifera indica* leaves in streptozotocin-induced diabetic rats and genetic diabetic mice. *South pacific J. Pharma Bio Sci.* 1, 37–42.
- Sarmiento, B., Ferreira, D., Veiga, F., Ribeiro, A., 2006. Characterization of insulin-loaded alginate nanoparticles produced by ionotropic pre-gelation through DSC and FTIR studies. *Carbohydr. Polym.* 66, 1–7. <https://doi.org/10.1016/j.carbpol.2006.02.008>
- Sathiyabama, M., Indhumathi, M., Amutha, T., 2020. Preparation and characterization of curcumin functionalized copper nanoparticles and their application enhances disease resistance in chickpea against wilt pathogen. *Biocatal. Agric. Biotechnol.* 29. <https://doi.org/10.1016/j.bcab.2020.101823>
- Satirapoj, B., 2010. Review on pathophysiology and treatment of diabetic kidney disease. *J. Med. Assoc. Thai.* 93, 228–241.
- Satirapoj, B., Adler, S.G., 2014. Comprehensive approach to diabetic nephropathy. *Kidney Res. Clin. Pract.* 33, 121–131. <https://doi.org/10.1016/j.krcp.2014.08.001>
- Satirapoj, B., Adler, S.G., 2015. Prevalence and Management of Diabetic Nephropathy in Western Countries. *Kidney Dis.* 1, 61–70. <https://doi.org/10.1159/000382028>
- Satpathy, S., Patra, A., Ahirwar, B., Delwar Hussain, M., 2018. Antioxidant and anticancer activities of green synthesized silver nanoparticles using aqueous extract of tubers of *Pueraria*

---

*tuberosa*. *Artif. Cells, Nanomedicine Biotechnol.* 46, S71–S85. <https://doi.org/10.1080/21691401.2018.1489265>

Sawale, P.D., Singh, R.R.B., Kapila, S., Arora, S., Rastogi, S., Rawat, A.K.S., 2013. Immunomodulatory and antioxidative potential of herb (*Pueraria tuberosa*) in mice using milk as the carrier. *Int. J. Dairy Technol.* 66, 202–206. <https://doi.org/10.1111/1471-0307.12011>

Schmid, H., Boucherot, A., Yasuda, Y., Henger, A., Brunner, B., Eichinger, F., Nitsche, A., Kiss, E., Bleich, M., Gröne, H.J., Nelson, P.J., Schlöndorff, D., Cohen, C.D., Kretzler, M., 2006. Modular activation of nuclear factor- $\kappa$ B transcriptional programs in human diabetic nephropathy. *Diabetes* 55, 2993–3003. <https://doi.org/10.2337/db06-0477>

Scott, T.L., 2010. *Invasive plant medicine: the ecological benefits and healing abilities of invasives*. Simon and Schuster.

Sedaghat Doost, A., Kassozi, V., Grootaert, C., Claeys, M., Dewettinck, K., Van Camp, J., Van der Meeren, P., 2019. Self-assembly, functionality, and in-vitro properties of quercetin loaded nanoparticles based on shellac-almond gum biological macromolecules. *Int. J. Biol. Macromol.* 129, 1024–1033. <https://doi.org/10.1016/j.ijbiomac.2019.02.071>

Selby, N.M., Taal, M.W., 2020. An updated overview of diabetic nephropathy: Diagnosis, prognosis, treatment goals and latest guidelines. *Diabetes, Obes. Metab.* 22, 3–15. <https://doi.org/10.1111/dom.14007>

Sesharao, M., Madhavarao, V., 2018. A new validated simultaneous reversed-phase high-performance liquid chromatography assay method for estimation of two flavones (Baicalein and chrysin) in API drugs. *Asian J. Pharm. Clin. Res.* 11, 351–356. <https://doi.org/10.22159/ajpcr.2018.v11i1.21174>

Shafi, S., Tabassum, N., Ahmad, F., 2012. Diabetic nephropathy and herbal medicines. *Int. J. Phytopharm.* 3, 10–17.

Shah, M., Chuttani, K., Mishra, A.K., Pathak, K., 2011. Oral solid compritol 888 ATO nanosuspension of simvastatin: Optimization and biodistribution studies. *Drug Dev. Ind. Pharm.* 37, 526–537. <https://doi.org/10.3109/03639045.2010.527983>

Shaikh, J., Ankola, D.D., Beniwal, V., Singh, D., Kumar, M.N.V.R., 2009. Nanoparticle encapsulation improves oral bioavailability of curcumin by at least 9-fold when compared to

curcumin administered with piperine as absorption enhancer. *Eur. J. Pharm. Sci.* 37, 223–230. <https://doi.org/10.1016/j.ejps.2009.02.019>

Shariare, M.H., Afnan, K., Iqbal, F., Altamimi, M.A., Ahamad, S.R., Aldughaim, M.S., Alanazi, F.K., Kazi, M., 2020. Development and Optimization of Epigallocatechin-3-Gallate (EGCG) Nano Phytosome Using Design of Experiment (DoE) and Their In Vivo Anti-Inflammatory Studies. *Molecules* 25, 1–16. <https://doi.org/10.3390/MOLECULES25225453>

Sharma, A., Baldi, A., 2018. Nanostructured Lipid Carriers: A Review. *J. Dev. Drugs* 7, 1–12. <https://doi.org/10.4172/2329-6631.1000187>

Sharma, Ajay, Thakur, M., Kumar, A., Gautam, M., Kumari, S., Pathania, D., Sharma, Arush, 2023. Efficient photodegradation of fast sulphon black and crystal violet dyes from water systems using locust bean gum (LBG)-encapsulated zirconium-based nanoparticles and antibacterial activity. *Nanotechnol. Environ. Eng.* 8, 859–877. <https://doi.org/10.1007/s41204-023-00341-w>

Sharma, P., Singh, S.K., Pandey, N.K., Rajesh, S.Y., Bawa, P., Kumar, B., Gulati, M., Singh, S., Verma, S., Yadav, A.K., Wadhwa, S., Jain, S.K., Gowthamarajan, K., Malik, A.H., Gupta, S., Khursheed, R., 2018. Impact of solid carriers and spray drying on pre/post-compression properties, dissolution rate and bioavailability of solid self-nanoemulsifying drug delivery system loaded with simvastatin. *Powder Technol.* 338, 836–846. <https://doi.org/10.1016/j.powtec.2018.07.092>

Shen, S., Wang, F., Fernandez, A., Hu, W., 2020. Role of platelet-derived growth factor in type II diabetes mellitus and its complications. *Diabetes Vasc. Dis. Res.* 17. <https://doi.org/10.1177/1479164120942119>

Shi, H., Ratner, B.D., 2000. Template recognition of protein-imprinted polymer surfaces. *J. Biomed. Mater. Res.* 49 1, 1–11.

Shiadeh, S.N.R., Khodaverdi, E., Maleki, M.F., Eisvand, F., Nazari, A., Zarqi, J., Hadizadeh, F., Kamali, H., 2022. A sustain-release lipid-liquid crystal containing risperidone based on glycerol monooleate, glycerol dioleate, and glycerol trioleate: In-vitro evaluation and pharmacokinetics in rabbits. *J. Drug Deliv. Sci. Technol.* 70. <https://doi.org/10.1016/j.jddst.2022.103257>

- Shirazi, A.S., Varshochian, R., Rezaei, M., Ardakani, Y.H., Dinarvand, R., 2021. SN38 loaded nanostructured lipid carriers (NLCs); preparation and in vitro evaluations against glioblastoma. *J. Mater. Sci. Mater. Med.* 32, 78.
- Shiromani, S., Patil, M.M., Nallamuthu, I., R, R., Singsit, D., Anand, T., 2023. Shellac/caseinate as a composite nanocarrier for improved bioavailability of quercetin. *Food Hydrocoll. Heal.* 3, 100113. <https://doi.org/10.1016/j.fhfh.2022.100113>
- Shradha, T., Shailesh, W., Surendra, G., 2020. Nateglinide silica lipid hybrid particles for improved solubility. *Indian drugs* 57.
- Shukla, R., Pandey, N., Banerjee, S., Tripathi, Y.B., 2017. Effect of extract of *Pueraria tuberosa* on expression of hypoxia inducible factor-1 $\alpha$  and vascular endothelial growth factor in kidney of diabetic rats. *Biomed. Pharmacother.* 93, 276–285. <https://doi.org/10.1016/j.biopha.2017.06.045>
- Siepmann, J., Peppas, N.A., 2012. Modeling of drug release from delivery systems based on hydroxypropyl methylcellulose (HPMC). *Adv. Drug Deliv. Rev.* 64, 163–174. <https://doi.org/10.1016/j.addr.2012.09.028>
- Singh, A., Suki, M., Sharma, R., Ingle, P., 2020. Applications of Nanotechnology: A Review. *Int. J. Adv. Res. Chem. Sci.* 7, 16–32. <https://doi.org/10.20431/2349-0403.0702004>
- Singh, M., Singh, S., Prasad, S., Gambhir, I.S., 2008. Nanotechnology in medicine and antibacterial effect of silver nanoparticles. *Dig. J. Nanomater. Biostructures* 3, 115–122.
- Singh, R., Alavi, N., Singh, A.K., Leehey, D.J., 1999. Role of angiotensin II in glucose-induced inhibition of mesangial matrix degradation. *Diabetes* 48, 2066–2073. <https://doi.org/10.2337/diabetes.48.10.2066>
- Singh, R.M., Saini, P.K., Mathur, S.C., Singh, G.N., Lal, B., 2010. Development and validation of a RP-HPLC method for estimation of montelukast sodium in bulk and in tablet dosage form. *Indian J. Pharm. Sci.* 72, 235.
- Singh, V.P., Bali, A., Singh, N., Jaggi, A.S., 2014. Advanced glycation end products and diabetic complications. *Korean J. Physiol. Pharmacol.* 18, 1–14. <https://doi.org/10.4196/kjpp.2014.18.1.1>

Singhvi, G., Singh, M., 2011. Review: In vitro Drug Release Characterization Models. *Int. J. Pharm. Stud. Res.* 2, 77–84.

Sisay, W., Andargie, Y., Molla, M., 2022. Antidiabetic Activity of Hydromethanolic Extract of Crude *Dorstenia barnimiana* Root: Validation of In Vitro and In Vivo Antidiabetic and Antidyslipidemic Activity. *J. Exp. Pharmacol.* 14, 59–72. <https://doi.org/10.2147/JEP.S343735>

Skyler, J.S., 2004. Diabetes Mellitus: Pathogenesis and Treatment Strategies. *J. Med. Chem.* 47, 4113–4117. <https://doi.org/10.1021/jm0306273>

Skyler, J.S., Bakris, G.L., Bonifacio, E., Darsow, T., Eckel, R.H., Groop, L., Groop, P.H., Handelsman, Y., Insel, R.A., Mathieu, C., McElvaine, A.T., Palmer, J.P., Pugliese, A., Schatz, D.A., Sosenko, J.M., Wilding, J.P.H., Ratner, R.E., 2017. Differentiation of diabetes by pathophysiology, natural history, and prognosis. *Diabetes* 66, 241–255. <https://doi.org/10.2337/db16-0806>

Soetikno, V., Suzuki, K., Veeraveedu, P.T., Arumugam, S., Lakshmanan, A.P., Sone, H., Watanabe, K., 2013. Molecular understanding of curcumin in diabetic nephropathy. *Drug Discov. Today* 18, 756–763. <https://doi.org/10.1016/j.drudis.2013.04.009>

Soldatos, G., Cooper, M.E., 2008. Diabetic nephropathy: Important pathophysiologic mechanisms. *Diabetes Res. Clin. Pract.* 82, 75–79. <https://doi.org/10.1016/j.diabres.2008.09.042>

Soleimani, V., Sahebkar, A., Hosseinzadeh, H., 2018. Turmeric (*Curcuma longa*) and its major constituent (curcumin) as nontoxic and safe substances: Review. *Phyther. Res.* 32, 985–995. <https://doi.org/10.1002/ptr.6054>

Songsurang, K., Praphairaksit, N., Siraleartmukul, K., Muangsin, N., 2011. Electrospray fabrication of doxorubicin-chitosan-tripolyphosphate nanoparticles for delivery of doxorubicin. *Arch. Pharm. Res.* 34, 583–592. <https://doi.org/10.1007/s12272-011-0408-5>

Souto, E.B., Müller, R.H., 2006. Investigation of the factors influencing the incorporation of clotrimazole in SLN and NLC prepared by hot high-pressure homogenization. *J. Microencapsul.* 23, 377–388. <https://doi.org/10.1080/02652040500435295>

- Sri, D.E., Arivarasu, L., Rajeshkumar, S., Thangavelu, L., 2021. *Pterocarpus santalinus* Ethanolic Extract Preparation and Its Free Radical Scavenging Activity. *J. Pharm. Res. Int.* 33, 425–432. <https://doi.org/10.9734/jpri/2021/v33i61a35704>
- Srivastava, S., Pandey, H., Singh, S.K., Tripathi, Y.B., 2019. Anti-oxidant, anti-apoptotic, anti-hypoxic and anti-inflammatory conditions induced by PTY-2 against STZ-induced stress in islets. *Biosci. Trends* 13, 382–393. <https://doi.org/10.5582/bst.2019.01181>
- Stella, J., Krishnamoorthy, P., Mohamed, A.J., Anand, M., 2011. Free Radical Scavenging and Antibacterial Evaluation of *Pterocarpus Santalinus* Leaf In-Vitro Study. *Int. J. Pharm. Sci. Res.* 2, 1204.
- Strippoli, G.F.M., Craig, M., Schena, F.P., Craig, J.C., 2005. Antihypertensive agents for primary prevention of diabetic nephropathy. *J. Am. Soc. Nephrol.* 16, 3081–3091. <https://doi.org/10.1681/ASN.2004080634>
- Studer, R.K., Negrete, H., Craven, P.A., DeRubertis, F.R., 1995. Protein kinase C signals thromboxane induced increases in fibronectin synthesis and TGF- $\beta$  bioactivity in mesangial cells. *Kidney Int.* 48, 422–430. <https://doi.org/10.1038/ki.1995.310>
- Sullivan, D.W., Gad, S.C., Julien, M., 2014. A review of the nonclinical safety of Transcutol®, a highly purified form of diethylene glycol monoethyl ether (DEGEE) used as a pharmaceutical excipient. *Food Chem. Toxicol.* 72, 40–50. <https://doi.org/10.1016/j.fct.2014.06.028>
- Sumner, J.P., Aylott, J.W., Monson, E., Kopelman, R., 2002. A fluorescent PEBBLE nanosensor for intracellular free zinc. *Analyst* 127, 11–16. <https://doi.org/10.1039/b108568a>
- Sun, Y.M., Su, Y., Li, J., Wang, L.F., 2013. Recent advances in understanding the biochemical and molecular mechanism of diabetic nephropathy. *Biochem. Biophys. Res. Commun.* 433, 359–361. <https://doi.org/10.1016/j.bbrc.2013.02.120>
- Sundar, S., Kundu, J., Kundu, S.C., 2010. Biopolymeric nanoparticles. *Sci. Technol. Adv. Mater.* 11, 014104. <https://doi.org/10.1088/1468-6996/11/1/014104>
- Sura, R.S., Subrahmanyam, C.V.S., Rachamalla, S.S., 2022. Bioanalytical Rp-Hplc Method Development and Validation of Clopidogrel Bisulfate in Wistar Rat Plasma and Its Application To Pharmacokinetic Study. *Int. J. Appl. Pharm.* 14, 106–111. <https://doi.org/10.22159/ijap.2022v14i1.43328>

- Surendiran, A., Sandhiya, S., Pradhan, S.C., Adithan, C., 2009. Novel applications of nanotechnology in medicine. *Indian J. Med. Res.* 130, 689–701.
- Sutherland, K., Del Río, J.C., 2014. Characterisation and discrimination of various types of lac resin using gas chromatography mass spectrometry techniques with quaternary ammonium reagents. *J. Chromatogr. A* 1338, 149–163. <https://doi.org/10.1016/j.chroma.2014.02.063>
- Talarico, L., Consumi, M., Leone, G., Tamasi, G., Magnani, A., 2021. Solid lipid nanoparticles produced via a coacervation method as promising carriers for controlled release of quercetin. *Molecules* 26, 1–14. <https://doi.org/10.3390/molecules26092694>
- Thomas, A., 2000. Fats and Fatty Oils, in: *Ullmann's Encyclopedia of Industrial Chemistry*. John Wiley & Sons, Ltd, p. 48. [https://doi.org/https://doi.org/10.1002/14356007.a10\\_173](https://doi.org/https://doi.org/10.1002/14356007.a10_173)
- Thomas, M.C., Brownlee, M., Susztak, K., Sharma, K., Jandeleit-Dahm, K.A.M., Zoungas, S., Rossing, P., Groop, P.H., Cooper, M.E., 2015. Diabetic kidney disease. *Nat. Rev. Dis. Prim.* 1, 1–20. <https://doi.org/10.1038/nrdp.2015.18>
- Thombare, N., Kumar, S., Kumari, U., Sakare, P., Yogi, R.K., Prasad, N., Sharma, K.K., 2022. Shellac as a multifunctional biopolymer: A review on properties, applications and future potential. *Int. J. Biol. Macromol.* 215, 203–223. <https://doi.org/10.1016/j.ijbiomac.2022.06.090>
- Thrall, J.H., 2004. Nanotechnology and Medicine. *Radiology* 230, 315–318. <https://doi.org/10.1148/radiol.2302031698>
- Throckmorton, D.C., Brogden, A.P., Min, B., Rasmussen, H., Kashgarian, M., 1995. PDGF and TGF- $\beta$  mediate collagen production by mesangial cells exposed to advanced glycosylation end products. *Kidney Int.* 48, 111–117. <https://doi.org/10.1038/ki.1995.274>
- Tiwari, A., Khan, S.A., Kher, R.S., Dhoble, S.J., 2014. Synthesis, characterization and optical studies of highly luminescent ZnS nanoparticles associated with hypromellose matrix as a green and novel stabilizer. *Luminescence* 29, 637–641. <https://doi.org/10.1002/bio.2597>
- Tomic, D., Shaw, J.E., Magliano, D.J., 2022. The burden and risks of emerging complications of diabetes mellitus. *Nat. Rev. Endocrinol.* 18, 525–539. <https://doi.org/10.1038/s41574-022-00690-7>

- Tomizawa, H., Aramaki, Y., Fujii, Y., Kara, T., Suzuki, N., Yachi, K., Kikuchi, H., Tsuchiya, S., 1993. Uptake of phosphatidylserine liposomes by rat Peyer's patches following intraluminal administration. *Pharm. Res.* 10, 549–552.
- Tong, F., Liu, S., Yan, B., Li, X., Ruan, S., Yang, S., 2017. Quercetin nanoparticle complex attenuated diabetic nephropathy via regulating the expression level of ICAM-1 on endothelium. *Int. J. Nanomedicine* 12, 7799–7813. <https://doi.org/10.2147/IJN.S146978>
- Tu, L., Yi, Y., Wu, W., Hu, F., Hu, K., Feng, J., 2013. Effects of particle size on the pharmacokinetics of puerarin nanocrystals and microcrystals after oral administration to rat. *Int. J. Pharm.* 458, 135–140. <https://doi.org/10.1016/j.ijpharm.2013.10.001>
- Tufro, A., Veron, D., 2012. VEGF and Podocytes in Diabetic Nephropathy. *Semin. Nephrol.* 32, 385–393. <https://doi.org/10.1016/j.semnephrol.2012.06.010>
- Tundisi, L.L., Mostaço, G.B., Carricondo, P.C., Petri, D.F.S., 2021. Hydroxypropyl methylcellulose: Physicochemical properties and ocular drug delivery formulations. *Eur. J. Pharm. Sci.* 159. <https://doi.org/10.1016/j.ejps.2021.105736>
- Twigg, S.M., Cao, Z., McLennan, S. V., Burns, W.C., Brammar, G., Forbes, J.M., Cooper, M.E., 2002. Renal connective tissue growth factor induction in experimental diabetes is prevented by aminoguanidine. *Endocrinology* 143, 4907–4915. <https://doi.org/10.1210/en.2002-220619>
- Tzeng, W.S., Teng, W.L., Huang, P.H., Lin, T.C., Yen, F.L., Shiue, Y.L., 2021. Pterostilbene nanoparticles downregulate hypoxia-inducible factors in hepatoma cells under hypoxic conditions. *Int. J. Nanomedicine* 16, 867–879. <https://doi.org/10.2147/IJN.S282172>
- Ucisik, M.H., Küpcü, S., Schuster, B., Sleytr, U.B., 2013. Characterization of CurcuEmulsomes: Nanoformulation for enhanced solubility and delivery of curcumin. *J. Nanobiotechnology* 11, 1–13. <https://doi.org/10.1186/1477-3155-11-37>
- Ugandar, R., Nilugal, K.C., Lyn, L.D., 2015. In-vitro and In-vivo evaluation of directly compressed tablets of simvastatin with soy lecithin. *World J. Pharm. Res.* 4, 2693–2718.
- Üner, M., 2006. Preparation, characterization and physico-chemical properties of solid lipid nanoparticles (SLN) and nanostructured lipid carriers (NLC): Their benefits as colloidal drug carrier systems. *Pharmazie* 61, 375–386.

- Üner, M., Wissing, S.A., Yener, G., Müller, R.H., 2005. Solid lipid nanoparticles (SLN) and nanostructured lipid carriers (NLC) for application of ascorbyl palmitate. *Pharmazie* 60, 577–582.
- Vaishnavi, V., Sadasivuni, K.K., Ponnamma, D., Golla, N., 2020. Green synthesis of silver nanoparticles from *Pterocarpus santalinus* leaf broth and their antibacterial and antioxidant activities, in: *Macromolecular Symposia*. p. 2000079.
- Vallon, V., Komers, R., 2011. Pathophysiology of the Diabetic Kidney. *Compr. Physiol.* 1, 1175–1232. <https://doi.org/10.1002/cphy.c100049>.Pathophysiology
- Varela-Fernández, R., García-Otero, X., Díaz-Tomé, V., Regueiro, U., López-López, M., González-Barcia, M., Isabel Lema, M., Javier Otero-Espinar, F., 2022. Lactoferrin-loaded nanostructured lipid carriers (NLCs) as a new formulation for optimized ocular drug delivery. *Eur. J. Pharm. Biopharm.* 172, 144–156. <https://doi.org/10.1016/j.ejpb.2022.02.010>
- Vasavada, N., Agarwal, R., 2005. Role of oxidative stress in diabetic nephropathy. *Adv. Chronic Kidney Dis.* 12, 146–154. <https://doi.org/10.1053/j.ackd.2005.01.001>
- Venkatesan, A., Roy, A., Kulandaivel, S., Natesan, V., Kim, S.J., 2022. p-Coumaric Acid Nanoparticles Ameliorate Diabetic Nephropathy via Regulating mRNA Expression of KIM-1 and GLUT-2 in Streptozotocin-Induced Diabetic Rats. *Metabolites* 12. <https://doi.org/10.3390/metabo12121166>
- Verhulst, M.J.L., Loos, B.G., Gerdes, V.E.A., Teeuw, W.J., 2019. Evaluating all potential oral complications of diabetes mellitus. *Front. Endocrinol. (Lausanne)*. 10. <https://doi.org/10.3389/fendo.2019.00056>
- Vijayanand, P., Jyothi, V., Aditya, N., Mounika, A., 2018. Development and Characterization of Solid Lipid Nanoparticles Containing Herbal Extract: In Vivo Antidepressant Activity. *J. Drug Deliv.* 2018, 1–7. <https://doi.org/10.1155/2018/2908626>
- Villegas, I., Sánchez-Fidalgo, S., De La Lastra, C.A., 2008. New mechanisms and therapeutic potential of curcumin for colorectal cancer. *Mol. Nutr. Food Res.* 52, 1040–1061. <https://doi.org/10.1002/mnfr.200700280>
- Wahab, N.A., Yevdokimova, N., Weston, B.S., Roberts, T., Li, X.J., Brinkman, H., Mason, R.M., 2001. Role of connective tissue growth factor in the pathogenesis of diabetic nephropathy. *Biochem. J.* 359, 77–87. <https://doi.org/10.1042/0264-6021:3590077>

- Wang, Q. yue, Guan, Q. hua, Chen, F. qin, 2009. The changes of platelet-derived growth factor-BB (PDGF-BB) in T2DM and its clinical significance for early diagnosis of diabetic nephropathy. *Diabetes Res. Clin. Pract.* 85, 166–170. <https://doi.org/10.1016/j.diabres.2009.05.008>
- Wang, W., Li, K., Bai, D., Wu, J., Xiao, W., 2024. Pterostilbene: a potential therapeutic agent for fibrotic diseases. *Inflammopharmacology* 32, 975–989. <https://doi.org/10.1007/s10787-024-01440-z>
- Wang, Y., Ma, Yi, Ma, Yingying, Du, Y., Liu, Z., Zhang, D., Zhang, Q., 2012. Formulation and pharmacokinetics evaluation of puerarin nanocrystals for intravenous delivery. *J. Nanosci. Nanotechnol.* 12, 6176–6184. <https://doi.org/10.1166/jnn.2012.6436>
- Wardani, G., Nugraha, J., Mustafa, M.R., Sudjarwo, S.A., 2022. Antioxidative Stress and Anti-Inflammatory Activity of Fucoidan Nanoparticles against Nephropathy of Streptozotocin-Induced Diabetes in Rats. *Evidence-based Complement. Altern. Med.* 2022. <https://doi.org/10.1155/2022/3405871>
- Wilmer, W.A., Dixon, C.L., Hebert, C., 2001. Chronic exposure of human mesangial cells to high glucose environments activates the p38 MAPK pathway. *Kidney Int.* 60, 858–871. <https://doi.org/10.1046/j.1523-1755.2001.060003858.x>
- Wolf, G., Ziyadeh, F.N., 2007. Cellular and molecular mechanisms of proteinuria in diabetic nephropathy. *Nephron - Physiol.* 106, 26–31. <https://doi.org/10.1159/000101797>
- Wong, C.K., Ho, A.W.Y., Tong, P.C.Y., Yeung, C.Y., Kong, A.P.S., Lun, S.W.M., Chan, J.C.N., Lam, C.W.K., 2007. Aberrant activation profile of cytokines and mitogen-activated protein kinases in type 2 diabetic patients with nephropathy. *Clin. Exp. Immunol.* 149, 123–131. <https://doi.org/10.1111/j.1365-2249.2007.03389.x>
- Wong, C.Y., Martinez, J., Dass, C.R., 2016. Oral delivery of insulin for treatment of diabetes: status quo, challenges and opportunities. *J. Pharm. Pharmacol.* 68, 1093–1108. <https://doi.org/10.1111/jphp.12607>
- Wu, J., Li, K., Zhou, M., Gao, H., Wang, W., Xiao, W., 2024. Natural compounds improve diabetic nephropathy by regulating the TLR4 signaling pathway. *J. Pharm. Anal.* 14, 100946. <https://doi.org/https://doi.org/10.1016/j.jpha.2024.01.014>

- Wu, J., Yan, L.J., 2015. Streptozotocin-induced type 1 diabetes in rodents as a model for studying mitochondrial mechanisms of diabetic  $\beta$  cell glucotoxicity. *Diabetes, Metab. Syndr. Obes. Targets Ther.* 8, 181–188. <https://doi.org/10.2147/DMSO.S82272>
- Wu, M., Jin, J., Jin, P., Xu, Y., Yin, J., Qin, D., Wang, K., Du, Q., 2017. Epigallocatechin gallate- $\beta$ -lactoglobulin nanoparticles improve the antitumor activity of EGCG for inducing cancer cell apoptosis. *J. Funct. Foods* 39, 257–263. <https://doi.org/10.1016/j.jff.2017.10.038>
- Wu, W., Hu, W., Han, W.B., Liu, Y.L., Tu, Y., Yang, H.M., Fang, Q.J., Zhou, M.Y., Wan, Z.Y., Tang, R.M., Tang, H.T., Wan, Y.G., 2018. Inhibition of Akt/mTOR/p70S6K signaling activity with Huangkui capsule alleviates the early glomerular pathological changes in diabetic nephropathy. *Front. Pharmacol.* 9, 1–17. <https://doi.org/10.3389/fphar.2018.00443>
- Xie, H., Liu, C., Gao, J., Shi, J., Ni, F., Luo, X., He, Y., Ren, G., Luo, Z., 2021. Fabrication of Zein-Lecithin-EGCG complex nanoparticles: Characterization, controlled release in simulated gastrointestinal digestion. *Food Chem.* 365. <https://doi.org/10.1016/j.foodchem.2021.130542>
- Xie, H., Sun, J., Chen, Y., Zong, M., Li, S., Wang, Y., 2015. EGCG Attenuates Uric Acid-Induced Inflammatory and Oxidative Stress Responses by Medicating the NOTCH Pathway. *Oxid. Med. Cell. Longev.* 2015. <https://doi.org/10.1155/2015/214836>
- Xie, J., Yang, F., Shi, X., Zhu, X., Su, W., Wang, P., 2013. Improvement in solubility and bioavailability of puerarin by mechanochemical preparation. *Drug Dev. Ind. Pharm.* 39, 826–835. <https://doi.org/10.3109/03639045.2012.664147>
- Xu, H., Hou, Z., Zhang, H., Kong, H., Li, X., Wang, H., Xie, W., 2013. An efficient trojan delivery of tetrandrine by poly(N-vinylpyrrolidone)-block-poly( $\epsilon$ -caprolactone) (PVP-b-PCL) nanoparticles shows enhanced apoptotic induction of lung cancer cells and inhibition of its migration and invasion. *Int. J. Nanomedicine* 9, 231–242. <https://doi.org/10.2147/IJN.S55541>
- Yadav, D., Pandey, V., Srivastava, S., Kumar, M., Bhusan Tripathi, Y., 2019. Methanolic extract of *Pueraria tuberosa* Linn ameliorates renal injury and oxidative stress in rats with alloxan-induced diabetes. *J. Emerg. Technol. Innov. Res.* 6, 557–574.
- Yamagishi, S., Matsu, T., 2010. Advanced glycation end products, oxidative stress and diabetic nephropathy. *Oxid. Med. Cell. Longev.* 3, 101–108.

- Yang, X., 2019. Design and optimization of crocetin loaded PLGA nanoparticles against diabetic nephropathy via suppression of inflammatory biomarkers: a formulation approach to preclinical study. *Drug Deliv.* 26, 849–859. <https://doi.org/10.1080/10717544.2019.1642417>
- Yang, Y., Zhang, Z., Li, S., Ye, X., Li, X., He, K., 2014. Synergy effects of herb extracts: Pharmacokinetics and pharmacodynamic basis. *Fitoterapia* 92, 133–147. <https://doi.org/10.1016/j.fitote.2013.10.010>
- Yaribeygi, H., Simental-Mendía, L.E., Butler, A.E., Sahebkar, A., 2019. Protective effects of plant-derived natural products on renal complications. *J. Cell. Physiol.* 234, 12161–12172. <https://doi.org/10.1002/jcp.27950>
- Yen, F.L., Wu, T.H., Tzeng, C.W., Lin, L.T., Lin, C.C., 2010. Curcumin nanoparticles improve the physicochemical properties of curcumin and effectively enhance its antioxidant and antihepatoma activities. *J. Agric. Food Chem.* 58, 7376–7382. <https://doi.org/10.1021/jf100135h>
- Yonashiro, H., Higashi, K., Morikawa, C., Ueda, K., Itoh, T., Ito, M., Masu, H., Noguchi, S., Moribe, K., 2018. Morphological and Physicochemical Evaluation of Two Distinct Glibenclamide/Hypromellose Amorphous Nanoparticles Prepared by the Antisolvent Method. *Mol. Pharm.* 15, 1587–1597. <https://doi.org/10.1021/acs.molpharmaceut.7b01122>
- Yoon, S.P., Maeng, Y.H., Hong, R., Lee, B.R., Kim, C.G., Kim, H.L., Chung, J.H., Shin, B.C., 2014. Protective effects of epigallocatechin gallate (EGCG) on streptozotocin-induced diabetic nephropathy in mice. *Acta Histochem.* 116, 1210–1215. <https://doi.org/10.1016/j.acthis.2014.07.003>
- Younes, M., Aquilina, G., Castle, L., Engel, K.H., Fowler, P., Frutos Fernandez, M.J., Fürst, P., Gürtler, R., Husøy, T., Manco, M., Mennes, W., Moldeus, P., Passamonti, S., Shah, R., Barmaz, S., Smeraldi, C., Tard, A., Vianello, G., Rincon, A.M., Gundert-Remy, U., 2020. Opinion on the re-evaluation of ascorbyl palmitate (E 304i) as a food additive in foods for infants below 16 weeks of age and the follow-up of its re-evaluation as a food additive for uses in foods for all population groups. *EFSA J.* 18. <https://doi.org/10.2903/j.efsa.2020.6153>
- Yu, C.C., Du, Y.J., Li, J., Li, Y., Wang, L., Kong, L.H., Zhang, Y.W., 2022. Neuroprotective Mechanisms of Puerarin in Central Nervous System Diseases: Update. *Aging Dis.* <https://doi.org/10.14336/AD.2021.1205>

- Yuan, Y., He, N., Dong, L., Guo, Q., Zhang, X., Li, B., Li, L., 2021a. Multiscale Shellac-Based Delivery Systems: From Macro: From Nanoscale. *ACS Nano* 15, 18794–18821. <https://doi.org/10.1021/acsnano.1c07121>
- Yuan, Y., Zhang, S., Ma, M., Xu, Y., Wang, D., 2022. Delivery of curcumin by shellac encapsulation: Stability, bioaccessibility, freeze-dried redispersibility, and solubilization. *Food Chem. X* 15, 100431. <https://doi.org/10.1016/j.fochx.2022.100431>
- Yuan, Y., Zhang, X., Pan, Z., Xue, Q., Wu, Y., Li, Y., Li, B., Li, L., 2021b. Improving the properties of chitosan films by incorporating shellac nanoparticles. *Food Hydrocoll.* 110, 106164. <https://doi.org/10.1016/j.foodhyd.2020.106164>
- Zain, M., Awan, F.R., 2014. Renin Angiotensin Aldosterone System (RAAS): Its biology and drug targets for treating diabetic nephropathy. *Pak. J. Pharm. Sci.* 27, 1379–1391.
- Zanetti-Ramos, B.G., Fritzen-Garcia, M.B., de Oliveira, C.S., Pasa, A.A., Soldi, V., Borsali, R., Creczynski-Pasa, T.B., 2009. Dynamic light scattering and atomic force microscopy techniques for size determination of polyurethane nanoparticles. *Mater. Sci. Eng. C* 29, 638–640. <https://doi.org/10.1016/j.msec.2008.10.040>
- Zangeneh, M.M., Goodarzi, N., Zangeneh, A., Tahvilian, R., Najafi, F., 2018. Amelioration of renal structural changes in STZ-induced diabetic mice with ethanolic extract of *Allium saralicum* R.M. Fritsch. *Comp. Clin. Path.* 27, 861–867. <https://doi.org/10.1007/s00580-018-2674-9>
- Zhang, G., Zhang, J., 2018. Enhanced oral bioavailability of EGCG using pH-sensitive polymeric nanoparticles: Characterization and in vivo investigation on nephrotic syndrome rats. *Drug Des. Devel. Ther.* 12, 2509–2518. <https://doi.org/10.2147/DDDT.S172919>
- Zhang, H., Chen, B., Banfield, J.F., 2010. Particle size and pH effects on nanoparticle dissolution. *J. Phys. Chem. C* 114, 14876–14884.
- Zhang, J., Nie, S., Martinez-zaguilan, R., Sennoune, S.R., Wang, S., 2016. Formulation, characteristics and antiatherogenic bioactivities of CD36-targeted epigallocatechin gallate (EGCG)-loaded nanoparticles. *J. Nutr. Biochem.* 30, 14–23.
- Zhang, W.-H., Chen, Y., Gao, L.-M., Cao, Y.-N., 2021. Neuroprotective role of epigallocatechin-3-gallate in acute glaucoma via the nuclear factor- $\kappa$ B signalling pathway. *Exp. Ther. Med.* 22, 1–9. <https://doi.org/10.3892/etm.2021.10669>

Zhang, Y., Li, Y., Zhao, X., Zu, Y., Wang, W., Wu, W., Zhong, C., Wu, M., Li, Z., 2016. Preparation, characterization and bioavailability of oral puerarin nanoparticles by emulsion solvent evaporation method. *RSC Adv.* 6, 69889–69901. <https://doi.org/10.1039/c6ra08413c>

Zhang, Y., Ren, S., Ji, Y., Liang, Y., 2019. Pterostilbene Ameliorates Nephropathy Injury in Streptozotocin-Induced Diabetic Rats. *Pharmacology* 104, 71–80. <https://doi.org/10.1159/000500293>

Zhang, Z., Feng, S.S., 2006. The drug encapsulation efficiency, in vitro drug release, cellular uptake and cytotoxicity of paclitaxel-loaded poly(lactide)-tocopheryl polyethylene glycol succinate nanoparticles. *Biomaterials* 27, 4025–4033. <https://doi.org/10.1016/j.biomaterials.2006.03.006>

Zhang, Z., Sha, X., Shen, A., Wang, Y., Sun, Z., Gu, Z., Fang, X., 2008. Polycation nanostructured lipid carrier, a novel nonviral vector constructed with triolein for efficient gene delivery. *Biochem. Biophys. Res. Commun.* 370, 478–482. <https://doi.org/10.1016/j.bbrc.2008.03.127>

Zhao, Q., Luan, X., Zheng, M., Tian, X.H., Zhao, J., Zhang, W.D., Ma, B.L., 2020. Synergistic mechanisms of constituents in herbal extracts during intestinal absorption: Focus on natural occurring nanoparticles. *Pharmaceutics* 12. <https://doi.org/10.3390/pharmaceutics12020128>

Zhong, Y., Ma, C.M., Shahidi, F., 2012. Antioxidant and antiviral activities of lipophilic epigallocatechin gallate (EGCG) derivatives. *J. Funct. Foods* 4, 87–93. <https://doi.org/10.1016/j.jff.2011.08.003>

Zhong, Y., Shahidi, F., 2011. Lipophilized Epigallocatechin Gallate (EGCG) Derivatives as Novel Antioxidants. *J. Agric. Food Chem.* 59, 6526–6533. <https://doi.org/10.1021/jf201050j>

Zimmet, P., Alberti, K.G., Magliano, D.J., Bennett, P.H., 2016. Diabetes mellitus statistics on prevalence and mortality: Facts and fallacies. *Nat. Rev. Endocrinol.* 12, 616–622. <https://doi.org/10.1038/nrendo.2016.105>

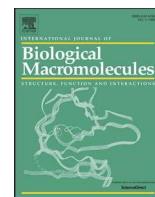
Signature of Candidate:

Gyancho Tshering Bhutia



Contents lists available at ScienceDirect

## International Journal of Biological Macromolecules

journal homepage: [www.elsevier.com/locate/ijbiomac](http://www.elsevier.com/locate/ijbiomac)

# Shellac and locust bean gum coacervated curcumin, epigallocatechin gallate nanoparticle ameliorates diabetic nephropathy in a streptozotocin-induced mouse model

Gyamcho Tshering Bhutia<sup>a</sup>, Asit Kumar De<sup>b</sup>, Manas Bhowmik<sup>c</sup>, Tanmoy Bera<sup>a,\*</sup><sup>a</sup> Laboratory of Nanomedicine, Division of Pharmaceutical Biotech., Department of Pharmaceutical Technology, Jadavpur University, Kolkata 700 032, West Bengal, India<sup>b</sup> Department of Chemistry, Jadavpur University, Kolkata 700032, West Bengal, India<sup>c</sup> Pharmaceutics Research laboratory II, Department of Pharmaceutical Technology, Jadavpur University, Kolkata 700 032, West Bengal, India

## ARTICLE INFO

## Keywords:

Diabetic nephropathy  
Curcumin  
Epigallocatechin gallate  
Bioavailability  
Shellac-locust bean gum nanoparticles  
Biopolymer

## ABSTRACT

Curcumin and epigallocatechin gallate have the disadvantage of low aqueous solubility and first-pass metabolism, resulting in limited bioavailability. This work aimed to enhance oral bioavailability by forming gastric pH-stable shellac nanoparticles containing curcumin and epigallocatechin gallate using locust bean gum by anti-solvent precipitation (CESL-NP). The nanoparticles were characterized by their particle size, morphology, zeta potential, gastric pH stability, release profile, drug loading, and entrapment efficiency. The findings showed that a network of hydrolyzed shellac, locust bean gum, curcumin, and epigallocatechin gallate successfully entrapped individual particles inside a complex system. The morphological investigation of the CESL-NP formulation using FESEM, TEM, and AFM revealed the presence of spherical particles. FTIR, DSC, and XRD analysis revealed that curcumin and epigallocatechin gallate were amorphous due to their bond interactions with the matrix. Streptozotocin-treated mice, upon treatment with CESL-NP, showed kidney and pancreatic improvements with normalized kidney hypertrophy index and histopathology, maintained biochemical parameters, increased beta cell count, and a 38.68-fold higher blood glucose level inhibition were observed when compared to free-(CUR + EGCG). This research affirms that the shellac-locust bean gum complex shows potential for the sustained oral delivery of curcumin and epigallocatechin gallate, specifically for treating diabetic nephropathy.

## 1. Introduction

Diabetes mellitus (DM) is a metabolic disease of the pancreas characterized by persistent hyperglycemia. It is a chronic disease caused due to damage of pancreatic beta cells or by deficiency of insulin production or insulin resistance. DM is a primary global public health concern, impacting about 400 million people globally [1]. Type 2 diabetes mellitus (T2DM), the prevalent variant of diabetes, is associated with insulin resistance and is projected to affect a global population of 8 billion people by 2025 [2]. T2DM complications encompass nephropathy, retinopathy, neuropathy, as well as renal and cardiovascular disorders. Type 1 diabetes mellitus is an autoimmune condition targeting pancreatic cells, resulting in diminished or disrupted insulin production. Conversely, T2DM arises from the dysfunction of pancreatic beta cells, which impairs insulin utilization [3].

Diabetic nephropathy (DN) is the predominant complication of DM, affecting about 40 % of patients with diabetes [4]. DN is the leading contributor to end-stage renal disease (ESRD), and this complex process involves numerous pathways [5]. It has been reported that DN therapy correlates with the reduction of oxidative stress and the reinforcement of the host's antioxidant defence system [6]. Inflammatory cytokines, such as interleukin, play a crucial role in the onset and treatment of DN [7].

Conventional treatments have primarily concentrated on lowering blood glucose levels but have proven ineffective in addressing the related problems [7]. Given the limitations of current antidiabetic medications, there is an urgent need to investigate alternative treatments. Identifying novel therapeutic targets and treatments that influence the development of DN holds significant clinical importance [8]. There is considerable interest in using herbal medications as therapeutic options for managing diabetes and its complications [9]. Natural plant-

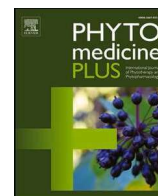
\* Corresponding author.

E-mail address: [proftanmoybera@gmail.com](mailto:proftanmoybera@gmail.com) (T. Bera).<https://doi.org/10.1016/j.ijbiomac.2024.132369>

Received 5 November 2023; Received in revised form 7 May 2024; Accepted 12 May 2024

Available online 13 May 2024

0141-8130/© 2024 Elsevier B.V. All rights are reserved, including those for text and data mining, AI training, and similar technologies.



## Evaluation of the antidiabetic and antinephritic effects of *Pueraria tuberosa* and *Pterocarpus santalinus* extracts co-encapsulated in nanostructured lipid carriers in streptozotocin-induced mouse model

Gyamcho Tshering Bhutia<sup>a</sup>, Asit Kumar De<sup>b</sup>, Manas Bhowmik<sup>c</sup>, Pavia Bera<sup>d</sup>,  
Tanmoy Bera<sup>a,\*</sup>

<sup>a</sup> Laboratory of Nanomedicine, Division of Pharmaceutical Biotech., Department of Pharmaceutical Technology, Jadavpur University, Kolkata 700 032, West Bengal, India

<sup>b</sup> Department of Chemistry, Jadavpur University, Kolkata 700032, West Bengal, India

<sup>c</sup> Pharmaceutics Research laboratory II, Department of Pharmaceutical Technology, Jadavpur University, Kolkata 700 032, West Bengal, India

<sup>d</sup> College of Engineering, 4202 East Fowler Avenue, ENG 030, University of South Florida, Tampa, FL 33620, USA

### ARTICLE INFO

#### Keywords:

Diabetic nephropathy  
*Pueraria tuberosa* extract  
*Pterocarpus santalinus* extract  
Bioavailability  
Nanostructured lipid carrier system  
Herbal compounds

### ABSTRACT

**Background:** Diabetic nephropathy (DN) causes significant morbidity and mortality, leading to substantial psycho-economic costs. New strategies and medications are needed to manage DN more effectively.

**Purpose:** The antidiabetic and antinephritic properties of *Pueraria tuberosa* and *Pterocarpus santalinus* have been demonstrated in previous studies. However, poor oral bioavailability has limited their clinical application. A nanostructured lipid carrier (NLC) formulation was created and tested to address this problem. The promising experimental results suggest that this formulation holds potential for further clinical exploration.

**Study design:** The *in vivo* study evaluated the therapeutic potential of NLCs loaded with hydroalcoholic extracts of *P. tuberosa* tubers (PTE) and *P. santalinus* heartwood (PSE) in managing DN over eight weeks in streptozotocin (STZ)-induced diabetic mice.

**Methods:** The protective effects of PTE and PSE were evaluated in mice at a dose of 80 mg/kg body weight. Two weeks after STZ treatment, animals with blood sugar levels above 250 mg/dL were identified as diabetic and showed signs of nephritis. In these diabetic mice, PTE-NLC and PSE-NLC, individually and in their combined form (PTE+PSE)-NLC, were assessed for their hypoglycemic and nephroprotective effects. Animals were sacrificed for histopathological and biochemical analysis after eight weeks of therapy. Nanoparticles were characterized by their morphology, zeta potential, drug loading capacity, particle size, and release profile.

**Results:** In STZ-induced diabetic mice, treatment with (PTE+PSE)-NLC significantly improved pancreas and kidney health. It restored the kidney hypertrophy index, stabilized biochemical parameters, enhanced histopathological outcomes, and increased beta-cell count. Additionally, (PTE+PSE)-NLC led to a 30.53-fold more significant reduction in blood glucose levels than free (PTE+PSE) extracts.

**Conclusion:** Our findings highlight the potential of the NLC formulation of *P. tuberosa* and *P. santalinus* extracts in treating diabetic nephropathy. The bioactive compounds in these extracts play a crucial role in their antidiabetic and antinephritic effects, marking significant progress in the field.

**Abbreviations:** ACE, angiotensin converting enzyme; AFM, atomic force microscopy; Alb, albumin; AR, analytical reagent; ARBs, angiotensin II receptor blockers; BUN, blood urea nitrogen; CTAB, cetyltrimethylammonium bromide; DAD, diode array detector; DLS, dynamic light scattering; DM, diabetes mellitus; DN, diabetic nephropathy; DSC, differential scanning calorimeter; EE, entrapment efficiency; ECM, extracellular matrix; ESRD, end-stage renal disease; FESEM, field emission scanning electron microscopy; FBGL, fasting blood glucose level; FTIR, fourier transform infrared; GLI, glibenclamide; GLUT 4, glucose transporter 4; H&E, hematoxylin and eosin; HPLC, high performance liquid chromatography; IAEC, institutional animal ethics committee; ICH, international conference on harmonization; IP, intraperitoneal; KHI, kidney hypertrophy index; KW, kidney weight; LC, loading capacity; LOQ, limit of quantification; LOD, limit of detection; MMP-9, matrix metalloproteinase-9; NLC, nanostructured lipid carrier; PPAR $\gamma$ , peroxisome proliferator-activated  $\gamma$ ; PSE, *Pterocarpus santalinus* extract; PTE, *Pueraria tuberosa* extract; RT, retention time; RSD, relative standard deviation; Scr, serum creatinine; SGF, simulated gastric fluid; SIF, simulated intestinal fluid; SLN, solid lipid nanoparticle; STZ, streptozotocin; TEM, transmission electron microscopy; XRD, x-ray diffraction.

\* Correspondence author at: Laboratory of Nanomedicine, Department of Pharmaceutical Technology, Jadavpur University, Kolkata-700032, West Bengal, India.

E-mail address: [proftanmoybera@gmail.com](mailto:proftanmoybera@gmail.com) (T. Bera).

<https://doi.org/10.1016/j.phyplu.2025.100742>

Available online 19 January 2025

2667-0313/© 2025 The Authors. Published by Elsevier B.V. This is an open access article under the CC BY-NC license (<http://creativecommons.org/licenses/by-nc/4.0/>).

## VALIDATION, STABILITY STUDIES, AND SIMULTANEOUS ESTIMATION OF CO-ENCAPSULATED CURCUMIN, EPIGALLOCATECHIN GALLATE NANOFORMULATION BY RP-HPLC METHOD

GYAMCHO TSHERING BHUTIA<sup>1</sup> , ASIT KUMAR DE<sup>2</sup>, TANMOY BERA<sup>1\*</sup> 

<sup>1</sup>Laboratory of Nanomedicine, Division of Pharmaceutical Biotechnology, Department of Pharmaceutical Technology, Jadavpur University, Kolkata 700032, West Bengal, India, <sup>2</sup>Department of Chemistry, Jadavpur University, Kolkata 700032, West Bengal, India  
Email: prof.tanmoybera@gmail.com

Received: 13 Jul 2022, Revised and Accepted: 25 Aug 2022

### ABSTRACT

**Objective:** A new reverse-phase high-performance liquid chromatography (RP-HPLC) method was developed to simultaneously determine curcumin and epigallocatechin gallate (EGCG) in novel nanoformulation.

**Methods:** The high-performance liquid chromatography (HPLC) method was achieved by using a Thermo Scientific Hypersil Base Deactivated Silica (BDS) C18 column (25 cm X 4.6 mm, 5 µm) at 35 °C column oven temperature. The chromatographic procedure was performed with a mobile phase of acetonitrile and 0.025 M (pH 4.0) potassium dihydrogen phosphate (KH<sub>2</sub>PO<sub>4</sub>) buffer by gradient mode of elution. The injection volume was 20 µl, and the flow rate was 1.5 ml/min, with ultraviolet (UV) detection using a diode array detector (DAD) at a 268 nm isosbestic wavelength.

**Results:** Drug entrapment efficiency studies were performed with co-encapsulated EGCG and curcumin nanoformulation, which were found to be 94.35 % and 95.12 %, respectively. This shows that the developed method is highly effective. EGCG and curcumin were eluted at 3.9 min and 10.7 min, respectively. The linearity range was 25-175 µg/ml for EGCG and 12.5-100 µg/ml for curcumin. The correlation coefficient was 0.991 for EGCG and 0.999 for curcumin from the linearity curve, which indicates that the method can produce good sensitivity. Forced degradation studies were conducted in acidic, basic, oxidative, thermal, photolytic, and UV stress conditions, where all the degradation peaks were monitored.

**Conclusion:** The developed method was linear, simple, rapid, robust, and precise. It could be used to quantify EGCG and curcumin simultaneously in various nanoformulations for *in vivo* and *in vitro* applications.

**Keywords:** RP-HPLC method, UV detection, EGCG, Curcumin, Nanoformulation

© 2022 The Authors. Published by Innovare Academic Sciences Pvt Ltd. This is an open access article under the CC BY license (<https://creativecommons.org/licenses/by/4.0/>)  
DOI: <https://dx.doi.org/10.22159/ijap.2022v14i6.45818>. Journal homepage: <https://innovareacademics.in/journals/index.php/ijap>

### INTRODUCTION

A compound is considered bioactive if it directly affects living organisms after administration. These effects may be therapeutic or toxicological [1]. Bioactive compounds boost anti-inflammatory and antioxidant properties while lowering platelet aggregation, circulating LDL (low-density lipoprotein), and tumor growth [2]. In epidemiological studies, higher vegetable consumption has been linked to a lower risk of chronic illnesses, including cardiovascular disease, cancer, and age-related impaired functioning [3]. These health benefits are assumed to be attributed to bioactive compounds, micronutrients, and macronutrients, found in vegetables [4]. The therapeutic properties of these compounds, such as curcumin (from turmeric), allicin (from garlic), and catechin (from tea), assist in preventing diseases such as diabetes, cancer, and degenerative neurological disorders [5]. However, limited stability due to susceptibility to light, temperature, poor solubility, oxygen, and low bioavailability are all issues that restrict their use in pharmaceutical formulations [6]. Increasing the solubility and stability of bioactive compounds, as well as their bioactivity and bioavailability, can be done by nanoformulation with hydrophilic carriers [7]. Bioactive compounds can be encapsulated to nanoparticles to improve their targeting ability, efficiency, and specificity. It can also extend the presence of therapeutic substances in the bloodstream and enhance cellular absorption, and provide synergistic effects when multiple drugs are used together [8].

Curcumin is the major phytochemical in the rhizome of *Curcuma longa* L. (Zingiberaceae), generally known as turmeric [9]. Turmeric is a plant that has been used for medical purposes since 4000 BC in India's Vedic civilization. It was utilized as a culinary spice and had religious importance [10]. It has been shown that curcumin has antioxidant, anticancer, wound healing, anti-inflammatory, antimutagenic, antimicrobial, and antiviral properties [11]. Fig. 1 depicts the chemical structure of curcumin.

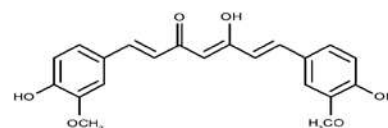


Fig. 1: Chemical structure of curcumin

Green tea is derived from the leaves of the Eastern Asian plant *Camilla sinensis* [12]. Catechin is a significant component of green tea. Catechin is a common term for four different substances: epigallocatechin (EGC), epigallocatechin gallate (EGCG), epicatechin gallate (ECG), and epicatechin (EC) [13]. EGCG is a polyphenol organic molecule in green tea that has been demonstrated to have therapeutic properties such as antioxidative, antifungal, anticancer, antiviral, and antimicrobial activities [14]. Fig. 2 depicts the chemical structure of EGCG.

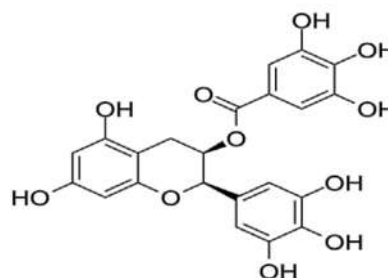


Fig. 2: Chemical structure of EGCG



3<sup>rd</sup> International Conference on Bioprocess for Sustainable Environment and Energy-2022



*Certificate of participation*

This is to certify that  
**Gyamcho Tshering Bhutia**

from **Jadavpur University, Kolkata**

has participated and presented poster entitled

*A validated stability studies indicating RP-HPLC method development for simultaneous determination of EGCG and curcumin in nanoformulation*

in online mode in the 3<sup>rd</sup> International Conference on Bioprocess for Sustainable Environment and Energy - 2022 organized by the National Institute of Technology Rourkela, India during June 20-24, 2022.

*Angana Sarkar*

Prof. Angana Sarkar  
Organizing Secretary  
ICBSEE- 2022, NIT Rourkela

*Kasturi Dutta*

Prof. Kasturi Dutta  
Organizing Secretary  
ICBSEE- 2022, NIT Rourkela

*Kunal Pal*

Prof. Kunal Pal  
Conference Chairman  
NIT Rourkela

*Santanu Paria*

Prof. Santanu Paria  
Dean SRICCE  
NIT Rourkela



3<sup>rd</sup> International Conference  
on



Bioprocess for Sustainable Environment and Energy-India-2022

**CERTIFICATE FOR BEST POSTER**

This is to certify that

*Gyamcho Tshering Bhutia*

is awarded the **Best Poster**  
for the research paper titled

*A Validated Stability Studies Indicating RP-HPLC Method Development for Simultaneous Determination of EGCG and Curcumin in Nanoformulation*

at the  
**'International Conference on Bioprocess for Sustainable Environment and Energy (ICBSEE)- India- 2022'**  
held on 20-24 June, 2022 at National Institute of Technology, Rourkela

*Angana Sarkar*

Prof. Angana Sarkar  
Organizing Secretary  
ICBSEE-2022, NIT Rourkela

*Kasturi Dutta*

Prof. Kasturi Dutta  
Organizing Secretary  
ICBSEE 2022, NIT Rourkela

*Kunal Pal*

Prof. Kunal Pal  
Conference Chairman  
ICBSEE-2022, NIT Rourkela

*Santanu Paria*

Prof. Santanu Paria  
Dean, SCRICCE  
NIT Rourkela

INTERNATIONAL SEMINAR ON  
"EMERGING FIELDS OF RESEARCH IN BIOTECHNOLOGY &  
BIOMEDICINE"



CERTIFICATE OF APPRECIATION

THIS CERTIFICATE RECOGNIZES THE CONTRIBUTION OF

Prof./Dr./Mr./Ms./Miss Gyancho Ishering Bhutia

as Invited Speaker/Chair Person/Co-Chair Person/Evaluator/Delegate/Presenter(Oral/Poster)  
In the International Seminar Jointly Organized by Dr. V. Ravi Chandran Centre for Advanced  
Research in Pharmaceutical Sciences, Jadavpur University, Kolkata, India &  
Indian Association of Pharmaceutical Scientists and Technologists (IAPST), Kolkata, India.  
held at Jadavpur University, Kolkata, India on 16 November 2022.

Prof. Dr. Biswajit Mukherjee  
Coordinator,  
Dr. V. Ravi Chandran Centre for  
Advanced Research in  
Pharmaceutical Sciences, Jadavpur  
University, Kolkata, India.



Dr. N. Udapa  
President,  
Indian Association of  
Pharmaceutical Scientists  
and Technologists (IAPST),  
Kolkata, India.

6<sup>th</sup> International Conference

C. No : AEDS/CIABASSD/019/2022

On  
Current Issues in Agricultural, Biological & Applied Sciences  
for Sustainable Development  
(CIABASSD-2022)  
(June 11-13, 2022)

Organized by



Department & Directorate of Extension Education,  
Uttar Banga Krishi Vishwavidyalaya, Pundibari, West Bengal, India



ICAR- National Agricultural Higher  
Education Project (NAHEP)-IG



KALIMPONG  
SCIENCE CENTRE  
Kalimpong Science Centre  
Deolo, Kalimpong, W.B.



Agro Environmental Development Society (AEDS)  
Majhra Ghat, Rampur, U.P, India  
(www.aeds.org)



The Himalayan Scientific  
Society for Fundamental and  
Applied Research, Kalimpong

Certificate of Presentation

This is to certify that Prof./Dr./Er/Mr./Mrs./Ms. Gyancho Ishering Bhutia

From Dept. of Pharm Tech., Jadavpur University, Kolkata

has presented a paper (oral/poster) entitled "Evaluation of the antidiabetic potential of Nanof ormulation of curcumin and EGCG in diabetic nephropathy"

authored by Gyancho Ishering Bhutia, Dr. Tanmay Bera

in the 6<sup>th</sup> International Conference on "Current Issues in Agricultural, Biological & Applied Sciences for Sustainable Development (CIABASSD-2022)" Held on June 11-13, 2022 at Kalimpong Science Centre, Deolo, Kalimpong, West Bengal, India.

Prof. Prabhakar Kumar Pal  
Organizing Chairman  
(CIABASSD-2022)

Dr. B. B. Gurung  
Head & Curator  
Kalimpong Science Centre

Dr. Chhatrapal Singh  
Organizing Secretary  
(CIABASSD-2022)

Prof. Sajeed Ali  
Jt. Organizing Secretary  
(CIABASSD-2022)

SI No: IISER/AF/M2/ 78

Date: 11/01/2023

INDIAN INSTITUTE OF SCIENCE EDUCATION & RESEARCH - KOLKATA  
ANIMAL FACILITY



**This Certificate Is Presented To**

Mr/Ms/Mrs/Dr Gyamcho Tshering Bhutia

For Successfully Completing **Module -2**  
“Hands on Training On Basics of Animal Handling (Mice) & Research”  
Organized by Indian Institute of Science Education & Research Kolkata,  
Animal Facility, From 5<sup>th</sup> of January to 14<sup>th</sup> of January, 2023.

*Rupak Datta*

**Prof Rupak Datta**  
**Facility In charge**

IISER KOLKATA



ANIMAL FACILITY

*Jayasri Das Sarma*

**Prof Jayasri Das Sarma**  
**Coordinator**

सीएसआईआर- भारतीय रासायनिक जीवविज्ञान संस्थान

4, राजा एस.सी. मल्लिक रोड, जादवपुर, कोलकाता-700 032, भारत

CSIR-Indian Institute of Chemical Biology

4, Raja S. C. Mullick Road, Jadavpur, Kolkata-700 032, INDIA



भारत का नवाधार इंजन  
The Innovation Engine of India



CSIR Innovation Cell Kolkata

प्रमाणपत्र / CERTIFICATE

Reg. No. : IICB/23-24/Aug/SDP/IICB-HPLC/0007



IICB  
Translational  
Research Unit  
of Excellence

यह प्रमाणित किया जाता है कि श्री / सुश्री / डॉ ग्याम्छो छिरीड भुटिया (आधार संख्या 2804 9389 5814)

ने इस संस्थान द्वारा 31 जुलाई 2023 से 11 अगस्त 2023 तक आयोजित कौशल विकास कार्यक्रम में थ्योरी एंड हैंड्स-ऑन-ट्रैनिंग के अंतर्गत “हाई परफॉरमैन्स लिक्विड क्रोमैटोग्राफी (एच.पी.एल.सी) (कोड- IICB-HPLC)”

सर्टिफिकेट कोर्स को सफलतापूर्वक सम्पूर्ण किया है।

This is to certify that Mr./Ms./Dr. Gyamcho Tshering Bhutia (Aadhaar No. 2804 9389 5814) has successfully completed the certificate course in the Skill Development Program on Theory & Hands-on-Training in **High Performance Liquid Chromatography (HPLC) (Code – IICB-HPLC)**

conducted by this Institute from 31<sup>st</sup> July 2023 to 11<sup>th</sup> August 2023

*[Signature]*  
पाठ्यक्रम समन्वयक  
Course Coordinator  
CSIR-IICB

*[Signature]*  
नोडल अधिकारी  
Nodal Officer  
Skill Development Cell CSIR-IICB

*[Signature]*  
निदेशक  
Director  
CSIR-IICB